AERODYNAMIC DESIGN, ANALYSIS, AND VALIDATION OF A SUPERSONIC INFLATABLE DECELERATOR

A Thesis
Presented to
The Academic Faculty

by

Ian Gauld Clark

In Partial Fulfillment
of the Requirements for the Degree
Doctor of Philosophy in the
School of Aerospace Engineering

Georgia Institute of Technology
August 2009

AERODYNAMIC DESIGN, ANALYSIS, AND VALIDATION OF A SUPERSONIC INFLATABLE DECELERATOR

Approved by:

Dr. Robert D. Braun, Advisor
School of Aerospace Engineering
Georgia Institute of Technology

Dr. F. McNeil Cheatwood
Atmospheric Flight and Entry Systems Branch
NASA Langley Research Center

Dr. Juan R. Cruz
Atmospheric Flight and Entry Systems Branch
NASA Langley Research Center

Dr. Stephen M. Ruffin
School of Aerospace Engineering
Georgia Institute of Technology

Professor David Spencer
School of Aerospace Engineering
Georgia Institute of Technology

Date Approved: 2 July 2009

ACKNOWLEDGEMENTS

There are many who have helped and supported me throughout my academic career and without whom I would have never come this far. First, I would like to thank my advisor, Robert Braun, who has provided unlimited leadership, wisdom, and pragmatism to me. I could not have wished for a better mentor to my graduate studies. I would like to thank Juan Cruz for his willingness and patience in helping me complete my research. You have served as an exceptional role model to a young engineer and have shown me a level of expertise that I will long strive to achieve. I also wish to thank the other members of my committee, Stephen Ruffin, David Spencer, and Neil Cheatwood, whose guidance has been invaluable and greatly appreciated.

This research was completed with the assistance of numerous individuals throughout the NASA community. I would like to thank Chuck Player, Monica Hughes, and NASA's PAIDAE program for affording me the opportunity to conduct the wind tunnel test portion of this research. I would also like to thank the staff of the Glenn Research Center and Langley Research Center wind tunnels for their assistance in executing those tests. I would like to thank Scott Murman, Artem Dyakonov, and Pieter Buning for their assistance in developing the computational portion of this research.

Lastly, I would like to thank all of the members of the Georgia Tech community who helped see me through my 10 year stay, especially my colleagues in the Space Systems Design Lab who provide a much needed distraction to the rigors of academia.

TABLE OF CONTENTS

LIST OF TABLES

LIST OF FIGURES

LIST OF SYMBOLS OR ABBREVIATIONS

A	Area
ADDPEP	Aerodynamic Deployable Decelerator Performance Evaluation Program
AIAA	American Institute of Aeronautics and Astronautics
AUSMPW+	Advection Upstream Splitting Method, Pressure Weighted
CFD	Computational Fluid Dynamics
CFL	Courant-Friedrichs-Lewis Condition
DGB	Disk Gap Band
D	Diameter or drag
EDL	Entry, Descent, and Landing
IAD	Inflatable Aerodynamic Decelerator
IRDT	Inflatable Reentry Descent Technology
IRVE	Inflatable Reentry Vehicle Experiment
LaRC	Langley Research Center
LAURA	Langley Aerothermodynamic Upwind Relaxation Algorithm
LUPWT	Langley Unitary Plan Wind Tunnel
m	Mass
MER	Mars Exploration Rover
MPF	Mars Pathfinder
MSL	Mars Science Laboratory
MSR	Mars Sample Return
N	Stress resultant
NASA	National Aeronautics and Space Administration
OML	Outer Mold Line
PAIDAE	Program to Advance Inflatable Decelerators for Atmospheric Entry
PEPP	Planetary Entry Parachute Program
POST	Program to Optimize Simulated Trajectories
P	Load or non-dimensional membrane pressure

p	Pressure
q	Dynamic pressure
r	Radius
R	Non-dimensional radial coordinate
Re	Reynolds number
RMS	Root mean square
SST	Shear Stress Transport
T	Tension or Temperature
V	Velocity
X	Non-dimensional axial coordinate
Z	Tension shell shape parameter

Greek Symbols

α	Angle of attack or ratio of circumferential stress to meridional stress
β	Ballistic coefficient
γ	Entry flight path angle or ratio of specific heats
Δ	Change in parameter
η	Burble fence ratio
ϕ	Meridional coordinate
ρ	Density
σ	Stress
θ	Cone angle or circumferential coordinate

Subscripts

a	Aeroshell
b	Base
∞	Value in the free stream
iso	isotensoid
t	Torus
TC	Tension Cone
ts	Tension shell

SUMMARY

Since the 1970s, NASA has relied on the use of rigid aeroshells and supersonic parachutes to enable robotic mission to Mars. These technologies are constrained by size and deployment condition limitations that limit the payload they can deliver to the surface of Mars. One candidate technology envisioned to replace the supersonic parachute is the supersonic inflatable aerodynamic decelerator (IAD). This dissertation presents an overview of work performed in maturing a particular type of IAD, the tension cone. The tension cone concept consists of a flexible shell of revolution that is shaped so as to remain under tension and resist deformation. Work completed on maturing the concept and presented in this dissertation falls into three categories: systems design, wind tunnel testing, and computational fluid dynamics validation.

Systems analyses that evaluated trajectory impacts of a supersonic IAD demonstrated several key advantages. Using a near-term Mars robotic mission as a baseline, supersonic IADs were shown to allow the landing of larger payloads at higher elevations relative to a system using parachutes alone. Increases in payload of over 700 kg (a 40% increase in payload mass) were estimated for IAD systems. Further increases in mass were shown to be possible by using a two-stage IAD and subsonic parachute system. Significant gains in landing site surface elevation and an insensitivity to entry system mass growth were also demonstrated.

A series of supersonic wind tunnel tests were conducted at the NASA Glenn and Langley Research Centers to characterize the behavior of a tension cone IAD at relevant Mach numbers. The tests were conducted on a particular tension cone configuration that was designed with the objective of eliminating unfavorable aerodynamic characteristics observed in prior wind tunnel testing, i.e. the presence of embedded shocks and flow separation along the surface. Testing of both rigid force and moment models and pressure models demonstrated the new design to have favorable performance including drag coefficients between 1.4 and 1.5 and static stability at angles of attack from 0 to 20. A separate round of tests conducted on flexible tension cone models showed the system to be free of aeroelastic instability. Deployment tests conducted on an inflatable model demonstrated rapid, stable inflation in a supersonic environment. Structural modifications incorporated on the models were seen to reduce inflation pressure requirements by a factor of nearly two. Through this test program, this new tension cone IAD design was shown to be a credible option for a future flight system.

A key objective of the wind tunnel test program was to gather data useful for validation of aerodynamic and structural analysis methods. Validation of CFD analyses for predicting aerodynamic IAD performance was completed and the results are presented. Inviscid CFD analyses are seen to provide drag predictions accurate to within 6%. Viscous analyses performed show excellent agreement with measured pressure distributions and flow field characteristics. Comparisons between laminar and turbulent solutions indicate the likelihood of a turbulent boundary layer at high supersonic Mach numbers and large angles of attack.

CHAPTER I

MOTIVATION, BACKGROUND, AND STUDY OBJECTIVES

1.1 Motivation

Towards the end of the 1960s, NASA began several technology development programs aimed at maturing deceleration technologies for use in planetary atmosphere entries. Research into entry body shapes and supersonic parachutes was undertaken with the objective of enabling the successful landing of a spacecraft on the surface of Mars. Although the initial beneficiaries of these efforts were the two Viking landers, the developed technologies became the foundation for every subsequent Mars entry vehicle. Over the past 30 years incremental improvements in aeroshell and parachute technologies have allowed for a gradual increase in Mars landed mass. However, these improvements are rapidly reaching their limits [14]. The latest mission in development, the 2011 Mars Science Laboratory (MSL), is being designed to land an 850 kg rover at a surface elevation of at least one kilometer. To do this, MSL will require the largest diameter aeroshell (4.5 m) and the largest diameter supersonic parachute (21.5 m) ever flown on Mars (see Table 1). Furthermore, parachute deployment is planned at a higher Mach number and dynamic pressure than on any previous Mars mission. This system may be near the limits of current parachute technology and later missions attempting further increases in landed mass will be faced with a difficult decision: either attempt to extrapolate current decelerator technology further beyond the tested and validated flight regime, or invest in a new, costly technology development program.

One promising technology path first researched in the 1960's involves the use of a supersonic inflatable aerodynamic decelerator (IAD). Prior systems studies, including the one provided in this thesis, that have examined the use of a supersonic IAD have shown that this technology provides significant improvement in landed mass, landing elevation, and entry corridor versus traditional parachute systems.

Maturing the IAD as a viable technology for entry, descent, and landing applications will

Table 1: Summary of prior parachute usage on Mars missions.

Mission	Diameter (m)	Area (m^2)	Deployment Mach Number	Deployment q_∞ (Pa)	Landed Mass (kg)
Viking I	16.15	205.0	1.1	321	612
Viking II	16.15	205.0	1.1	378	612
MPF	12.5	122.7	1.57	585	370
MER-A	14.1	156.1	1.77	725	539
MER-B	14.1	156.1	1.77	750	539
Phoenix	11.7	107.5	1.2	430	364
MSL	21.5	363.1	2.2	750	850

require a considerable amount of testing and analysis. Computational analysis methods have advanced immensely since the Viking era but are only recently being applied towards the study of IADs. The present day standard for aerodynamic performance evaluation entails the use of high-fidelity computational fluid dynamics (CFD) tools. Acquiring confidence in these tools requires extensive validation against data attained at conditions similar to those that will be experienced in flight. To date, this degree of validation has been absent in the codes used to analyze supersonic IADs.

1.2 Description and Functions

An inflatable aerodynamic decelerator is a deployable device primarily designed to provide aerodynamic drag. This increased drag can be used for the purpose of either deceleration or increased stability. The outer mold line of an IAD is maintained by internal pressure which may come from either an onboard pressurization system or through ram-air inlets. The key difference between an IAD and a parachute is that IADs are generally limited to mostly-closed surfaces (for the purpose of pressurization), whereas parachutes maintain an open surface. Further classification of IADs can be made by considering the regime in which they operate (supersonic vs. hypersonic/entry) and how they are integrated to the entry vehicle (attached vs. trailing). Historically, IADs have often been referred to as ballutes, a term which originated with a particular type of entry IAD, the Goodyear Ballute [39], but has more recently been used in reference to any entry IAD.

Supersonic inflatable aerodynamic decelerators provide two key functions: deceleration and stability. The former is achieved by decreasing the entry vehicle's ballistic coefficient, the ratio of the inertial to drag effects on the vehicle. Specifically, this is achieved by greatly increasing the frontal area of the entry vehicle while maintaining a reasonably large drag coefficient. Depending on when the IAD is deployed, this can allow the entry vehicle to decelerate at a higher altitude, which in turn can enable landings at greater elevations or can increase the timeline associated with staging events. Several such examples are provided in Chapter 2.

The second main function of a supersonic IAD is to improve the static stability of an entry vehicle. For attached IAD configurations, this is a result of the IAD extending past the aftbody of the entry vehicle and shifting the center of pressure backwards. Since the IAD is much lighter than the entry vehicle, the center of mass does not shift appreciably and the static margin is increased. Shown in Figure 1 are the pitching moments versus angle of attack for two attached IAD configurations. When compared against a basic 60^0 cone, the IADs provide a 4x improvement in C_{m_α}. The improvement in stability is even larger for IADs that are deployed in a trailing configuration well behind the entry vehicle.

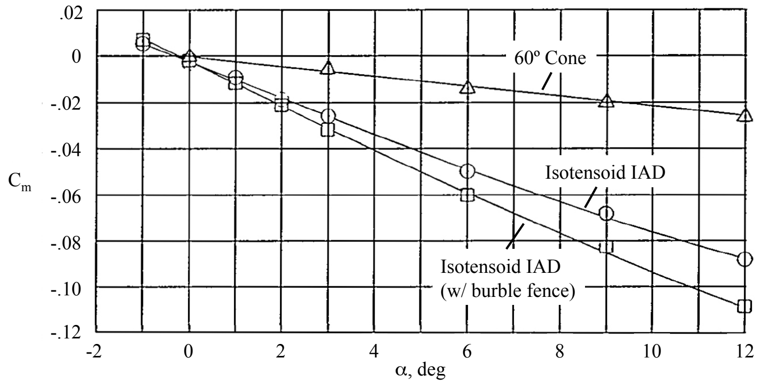

Figure 1: Pitching moment vs. angle of attack for a 60^0 cone and an attached isotensoid IAD at Mach 3.0, $Re \approx 3 \text{ x } 10^6$. Note: Center of gravity referenced at base of conical forebody. (Adapted from [24])

Aside from their primary functions, supersonic IADs have several other advantages when compared against the traditional means of deceleration: rigid aeroshells and supersonic parachutes. When compared to parachutes, IADs offer improved drag performance and can be deployed at higher Mach numbers and dynamic pressures. Also, whereas rigid aeroshells are limited by launch vehicle fairing dimensions, IADs are stowed and not nearly as constrained by fairing size.

1.3 Configurations

The concept of an inflatable aerodynamic decelerator can be traced back to the early 1960's when NASA was beginning to develop robotic planetary exploration missions which would require atmospheric deceleration. During this time a variety of IAD configurations were explored with distinguishing characteristics that included the mounting approach (e.g. attached or trailing), inflation method (on-board inflation system versus ram-air), and shape (e.g. spherical or conical). Some of the first wind-tunnel experiments were performed as early as 1961 by McShera, who explored drag and stability characteristics of a simple spherical balloon in both free-flight and when towed behind a payload [50]. Around the same time, an investigation of using a towed cone as a decelerator was performed by Charczenko [19] at Mach numbers up to 4.65. Another early configuration was proposed in 1962 by the Goodyear Aerospace Corporation, which coined the term ballute from the contraction of balloon and parachute. Shown in Figure 2 is an early variant of the Goodyear ballute. Subsequent variations included a ring near the base that was used to provide additional stability at subsonic velocities by inducing separated flow.

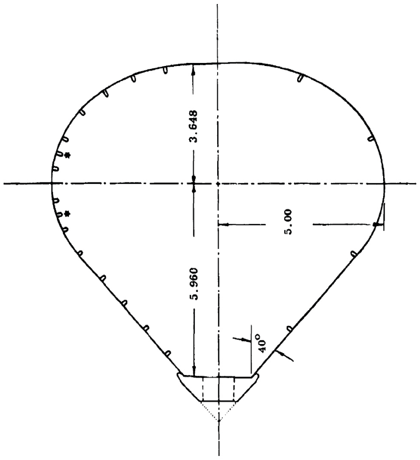

Figure 2: Early variant of the Goodyear ballute configuration [39].

In 1963 McShera followed up his earlier tests of a simple towed sphere with increasingly more complex shapes [52]. These included two ram-air inflated configurations, shown in Figure 3, and three closed configurations requiring a separate inflation system, shown in

Figure 4. It is of note that these appear to be the first published tests in which ram-air was used to pressurize the IAD.

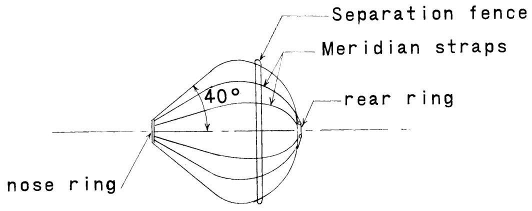

80° cone balloon with front inlet

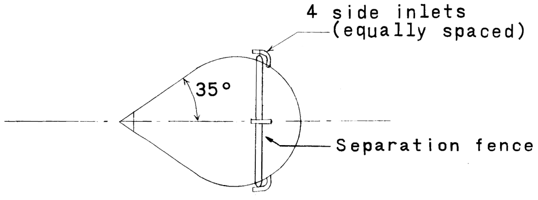

70° cone balloon with side inlets

Figure 3: Early ram-air inflated aerodynamic decelerator configurations [52].

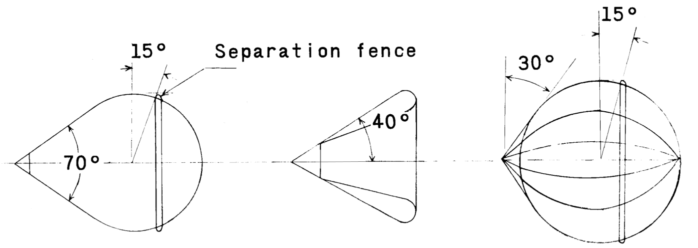

70° cone balloon 80° cone Sphere

Figure 4: Early IAD configurations requiring a separate inflation system [52].

Following the initial aerodynamic studies of McShera, Charczenko, and Goodyear, two primary shapes emerged that would garner a majority of subsequent IAD research efforts. The first of these was formulated by Houtz [34] and centered around the concept of an isotensoid IAD shape with fabric stresses that would be uniform in all directions. Beginning with an input pressure distribution, Houtz was able to derive a set of differential equations that governed a family of shapes exhibiting constant fabric stress. Once an initial shape was derived, wind tunnel models could be fabricated and tested to attain an actual pressure distribution. This in turn could be passed back through Houtz's equations to arrive at a refined, iterated isotensoid shape. Additional iteration was possible, though typically not required. Examples of the isotensoid shapes possible under this method are provided in Figure 5. Of note is that the concept of an isotensoid structure was actually used in the development of the original Goodyear ballutes, however, the more general formulation of Houtz did not appear until a few years later.

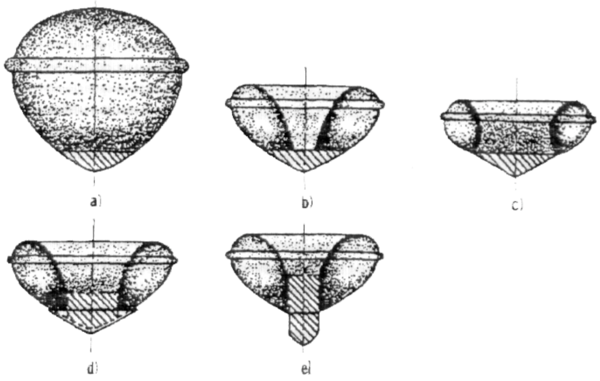

Figure 5: Example isotensoid IAD shapes [54].

Another configuration studied concurrently with the isotensoid shape was the tension cone. The tension cone concept, shown in Figure 6, consists of a flexible shell that is uniquely shaped so as to remain under tension and thus resist shape deformation. The shape itself is analytically derived on the basis of a predefined pressure distribution and an assumed constant ratio of circumferential to meridional stress. The tension in the shell is resisted at one end by a rigid forebody and at the other end by a compression ring, in some cases consisting of an inflated torus. Note that "tension cone" and "tension shell" are terms often used interchangeably in the literature. However, in the context of this thesis, the term "tension cone" corresponds to the entry device as a whole while "tension shell" refers to the axisymmetric portion between the rigid forebody and compression ring.

The initial theoretical development for the tension cone concept was developed by Anderson et al. in 1965 [3]. Starting from linear membrane theory, Anderson derived a set of equations that could be used to solve for a unique tension shell shape when given an initial axisymmetric pressure distribution. As with the isotensoid concept, iteration on the shape

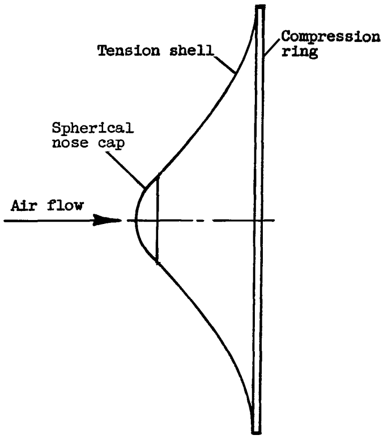

Figure 6: Typical tension cone decelerator [66].

was possible by first assuming a pressure distribution, testing that shape, and then passing the measured pressure distribution back through the analysis to arrive at a refined shape. In his initial work, Anderson expanded the tension shell relations for cases assuming both Newtonian and uniform pressure distributions. It should be noted that although derivation of a tension shell shape requires an initial pressure distribution, the linear membrane theory formulation implies that the shape is in fact insensitive to changes in dynamic pressure. The tension cone relations also allow one to solve for the circumferential and merdional stress resultants at any point along the shell, again assuming that the ratio of stress resultants is constant. For a given pressure distribution, multiple tension shell curvatures are possible depending on the values of several shape parameters. A sample of several possible tension shell shapes is shown in Figure 7. Though the plotted shapes lack a blunt nose or a rounded shoulder, tension shell theory does not exclude these features. Additional details of the tension shell formulation are provided in Appendix B.

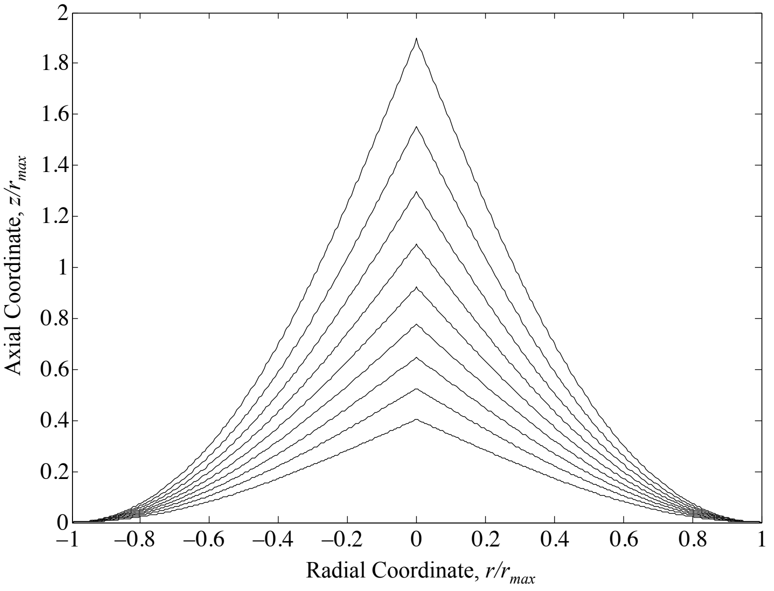

Figure 7: Example range of possible tension shell shapes.

1.4 Prior System Studies

In conjunction with the development and early testing of supersonic inflatable aerodynamic decelerators in the 1960's, efforts were initiated to analyze the flight regimes in which they would be favorable over traditional parachutes. For example, an extensive study was contracted by the Air Force prior to a series of atmospheric flight tests to examine the feasibility of using inflatable decelerators for recovery of rocket boosters, instrument data packages, and emergency escape capsules [1]. Though focused mostly on hypersonic deployments of trailing decelerators, the study encompassed analytical estimates of aerodynamic and aerothermodynamic performance for a range of trailing configurations, inflation systems studies, and materials investigations. The study concluded that a ram-air inflated, isotensoid design with a 40° cone angle and a 10% burble fence was optimal for the conditions considered. Thermal constraints of temperatures as high as 1500 °F had the investigators exploring cloths woven of nickel-based alloys and subsequently coated to reduce porosity. Initial testing indicated favorable structural and leakage performance even after prolonged (∼20–60 minute) exposure to temperatures in that range.

Later work by Anderson et al. recognized that the mass of a given decelerator was dependent on the loading, and thus dynamic pressure, at which it would be flown [2]. With that in mind, mass estimating relationships were developed for several different concepts as a function of size and loading. These estimates were then scaled by each concept's drag area contribution, yielding a decelerator ballistic coefficient. Results from this analysis approach are shown in Figure 8, where the abscissa is a function of the required drag area and dynamic pressure condition and the ordinate is the decelerator ballistic coefficient. In general, for a given dynamic pressure and drag area combination, a lower value of decelerator ballistic coefficient indicates a more mass efficient decelerator. Although the trailing isotensoid configuration performed poorly in Anderson's analysis, the attached isotensoid decelerator (AID) configuration showed promise in cases that require large drag areas or are exposed to high dynamic pressures. Additionally, the contours of parachute performance shown in Figure 8 would likely encounter Mach number limitations at the larger values of $q(C_D A)^{1/2}$, limitations that IADs do not exhibit. These results highlight a key aspect of supersonic

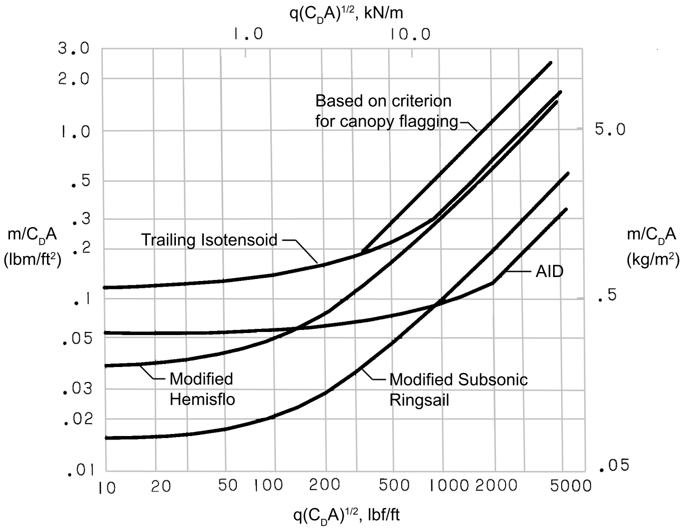

Figure 8: Decelerator ballistic coefficient as a function of a required drag area/dynamic pressure combination (adapted from [2]).

inflatable decelerators, that they perform well in supersonic environments but traditional parachutes tend to provide a more efficient solution in the subsonic regime.

Recognizing that parachutes are more mass efficient closer to terminal conditions, Bohon and Miserentino evaluated entry systems that utilized both an AID device and a terminal parachute [13]. Of note is that these analyses were performed assuming the 3.5 m diameter, 70° sphere cone aeroshell of the Viking lander. Results comparing a combined parachute and AID system mass to landed payload mass for a Martian atmospheric entry are shown in Table 2. Total decelerator system masses of 3.4% to 12.3% of the entry mass were estimated using the relations derived from [2]. Overall, Bohon and Miserentino concluded that inclusion of the supersonic AID allowed for deployment restrictions on the terminal parachute to be relaxed, leading to a potential increase in landed mass.

More recent systems studies have come to similar conclusions regarding the advantages of combined supersonic IAD/subsonic parachute decelerator systems. Brown, et al. examined a hypercone for application to a Mars lander [15]. Though similar in shape to a tension cone, the hypercone does not appear to be specifically derived on the basis of tension shell theory. A parametric mass model that included estimates for an inflatable torus was used to study the impact of the attachment angle on the total decelerator mass with the result that

Table 2: Mass breakdown for a parachute and combined parachute/AID decelerator system [13].

System variable	Deceleration system					
	Parachute		AID + parachute			
$m_t/(C_DA)_e$, slugs/ft^2	0.32	0.4	0.32	0.4	0.5	0.6
Entry mass, lbm	1720	2150	1720	2150	2690	3220
Aeroshell + ablator, lbm	175	185	175	185	196	205
Residual mass, lbm	1304	1712	1304	1712	2226	2731
Deployment conditions:						
AID q_∞, lbf/ft^2			18	47	75	86
AID M			2.3	4.1	5.0	5.0
Parachute q_∞, lbf/ft^2	17	23.6	8.5	8.5	8.5	8.5
Parachute M	2.3	2.5	1.5	1.5	1.5	1.5
Decelerator size, ft:						
AID, D			18	21	26	41
Parachute, D_o	55	61.5	55	61.5	68.8	75.5
Decelerator mass, lbm:						
AID			18	32	78	300
Parachute	69	120	42	57	76	96
Total decelerator mass, lbm	69	120	60	89	154	396
Retropropulsion mass, lbm	110	138	110	138	172	206
Landed-payload mass, lbm	1125	1454	1134	1485	1900	2129

an angle between 55° and 60° was considered optimal. An examination of potential systems for use in inflating the torus concluded that a system using vaporized liquid hydrogen had the greatest efficiency. Of systems with some degree of space flight heritage, solid propellant based gas generators were calculated as having the greatest ratio of inflation gas mass to inflation system mass. Total decelerator system mass estimates made for a 4 MT Mars lander concluded that a two-stage system employing a subsonic parachute was the most efficient. Significant contributors to the IAD system mass included the hypercone braids (17%), inflation system (16%), and inflation gas (14%), with the remaining mass comprised of straps, liners, coating mass, and other miscellaneous items. The total IAD system mass yielded a 3.8% mass fraction (IAD system mass to lander mass).

Aerothermal aspects of supersonic IADs have mostly been neglected in literature, likely due to an assumption of negligible heating at supersonic conditions. A notable exception is a study by Faurote and Burgess[28] that sought to characterize the aerothermal environment for an Attached Inflatable Decelerator deployed at either Earth or Mars. Convective heat rates were attained by using boundary layer equations based on the local similarity concept. Conditions at the edge of the boundary layer were approximated by assuming a given distribution of pressure coefficient along with isentropic expansion through a normal shock. Both laminar and turbulent heating relations were used, with transition based on a local length Reynolds number of 200,000. Transient temperature estimates were calculated using a simple one-dimensional heat conduction approach. The study concluded that deployment of an Attached Inflatable Decelerator at Mars was possible at Mach numbers up to 8.0 and ballistic coefficients of 110 kg/m^2 (the highest Mach and lowest ballistic coefficients considered) using technologies available at the time. Deployments at Earth were limited to Mach 5.8 due to material thermal limits. Earlier attempts at aerothermal analysis, such as those performed for the 1962 Air Force study [1], used a similar approach though with simpler boundary layer relations or relied on a prescribed heat transfer coefficient distribution attained from wind tunnel testing.

1.5 Wind Tunnel and Ground Tests

1.5.1 Early Tests

Some of the earliest ground based testing on IADs was performed by McShera on simple-shape trailing configurations [50],[52]. Of the five designs evaluated, McShera notes that all but the front inlet ram-air model were quite stable and lacked dynamic oscillations across a broad range of payload trailing distances. In the case of the front inlet configuration, full inflation was never achieved and a mass-flow pulsation phenomena developed which subsequently led to vibratory fabric loading and eventual material failure. This behavior was eventually alleviated by the addition of a porous screen over the inlet and by adding cups to channel the flow into the IAD. Drag coefficients for all five models varied between 0.6 and 1.1.

1.5.2 Isotensoid Testing

The isotensoid shape saw extensive ground based testing beginning in the 1960's and into the mid-1970's. Wind tunnel tests at Mach 10 on the trailing Goodyear ballute were performed as early as 1962 for the purpose of acquiring heating and pressure distributions for a variety of trailing distances [39]. These tests demonstrated a reduction in heat transfer rates of up to half with the presence of the leading payload, although this came at the expense of a nearly equally large decrease in drag coefficient.

Concepts designed and fabricated by the Goodyear Corporation, referred to as attached inflatable decelerators (AIDs), saw extensive theoretical development and testing [6]. Typical design characteristics for these concepts are shown in Figure 9 and include a burble fence, gored construction, and coated fabric.

The burble fence generally added another 5–10% to the maximum diameter of the AID model and served to provide constant point flow separation. Even though models incorporating the burble fence often provided lower drag coefficients, the fence was shown to be required for stability in the transonic and subsonic flight regimes [54]. These models were fabricated using Nomex coated with Viton to reduce porosity. The first sets of supersonic wind tunnel tests were performed on a 5 ft. diameter model, including a 5% burble fence, at

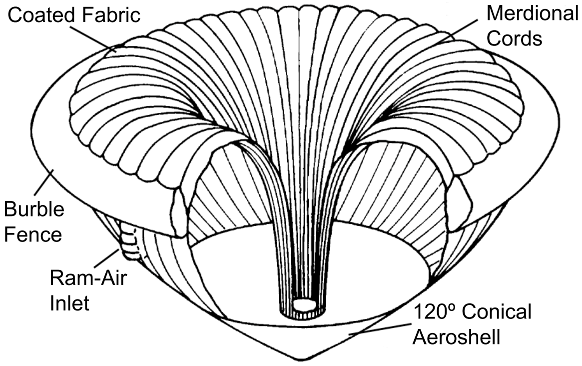

Figure 9: Design characteristics of the Goodyear AID concept (adapted from [54]).

Mach numbers of 2.2 and 3.0 and a dynamic pressure of 120 psf [54]. Initial canopy deployment was assisted by a water-alcohol mixture that would vaporize at low pressure, providing the initial canopy pressurization and exposing the ram-air inlets to the free-stream. Test data showed excellent agreement with the theoretical methods used to predict performance and inflation behavior. A drag coefficient of 1.14 was reported at Mach 3.0, versus a modified Newtonian prediction of 1.16. The ratio of internal pressure to dynamic pressure was observed as 1.87, versus a predicted value of 2.0 based on isentropic flow relations. Additionally, the measured shape differed from prediction in only the axial direction, where the measured depth value of 26.5 inches slightly exceeded the predicted depth of 24.85 inches. These results led the program to conclude that AID model performance was readily predictable. Other results of interest included full inflation times between 0.17 and 0.27 seconds, insensitivity of the axial force coefficient to angle of attack variations of up to 5 degrees, and lack of an opening load overshoot commonly encountered during parachute inflation. Though not specifically mentioned, this latter characteristic was likely due to the flow rate into the canopy decreasing as the internal pressure approached twice the dynamic pressure.

Follow-on wind tunnel tests on the AID configuration expanded the testing envelope to higher Mach numbers and lower dynamic pressures. Using the same 120° conical aeroshell and 5 foot diameter configuration as before, one test achieved successful deployment at a Mach number of 4.4 and dynamic pressure of 74.5 psf [12]. The test continued for a total of 66 minutes and included variations in dynamic pressure from 36 to 117 psf and angle of attack from 0 to 10 degrees. Steady, flutter-free behavior was reported at all conditions. Additional tests examined small variations in the general AID shape, the impact of varying burble fence size, and the sensitivity of the aerodynamics to Reynolds number [24] at a Mach 3.0 test condition. Those effects were explored using both deployable models and solid models instrumented with pressure ports. A summary of the drag coefficients reported is provided in Table 3. The drag coefficient is seen to vary by only 1% across an order of magnitude increase in Reynolds number. Furthermore, whereas the addition of the burble fence lowered drag performance on Model 1, it actually improved performance on Model 2. Predictions of drag using modified Newtonian theory produced estimates within 10% of those measured experimentally.

Pressure distributions on the five models tested are shown in Figure 10. Models with a burble fence are seen to exhibit a sharp pressure rise just in front of the burble fence. The authors note that this is likely due to the presence of separated flow behind a weak shock on the surface of the model. For Shape 2, the larger burble fence is able to move the sonic point further towards the back of the model and retain high pressure over more of the surface, thus the higher measured drag coefficients.

The significant research and development program surrounding the AID concept effectively ended in the mid 1970's. Though not discussed in program literature, the likely reason for this was the launch of the Viking probes to Mars and the subsequent absence of a mission requiring a supersonic decelerator other than a parachute. The AID concept was never incorporated into a planetary mission. However, it did find use as a stabilizer in munitions deployment programs managed by the U.S. Air Force [30].

Table 3: Drag coefficients of AID configuration at Mach 3.0 [24].

Model Shape	Burble Fence Height, h/r_b	C_D at $\alpha = 0^\circ$				
		Force Test Models		Pressure Distribution Models	Newtonian Theory	
		$Re \approx 1.1x10^6$	$Re \approx 3.0x10^6$	$Re \approx 9.8x10^6$	$k = 2.000$	$k = 1.755$
1	0.00	0.871	0.856	0.873	0.920	0.810
1	0.15	0.811	0.792	0.790	1.000	0.880
2	0.00	1.136	1.123	1.121	1.350	1.180
2	0.10	1.230	1.210	1.172	1.395	1.225
2	0.20	1.330	1.300	1.319	1.483	1.302

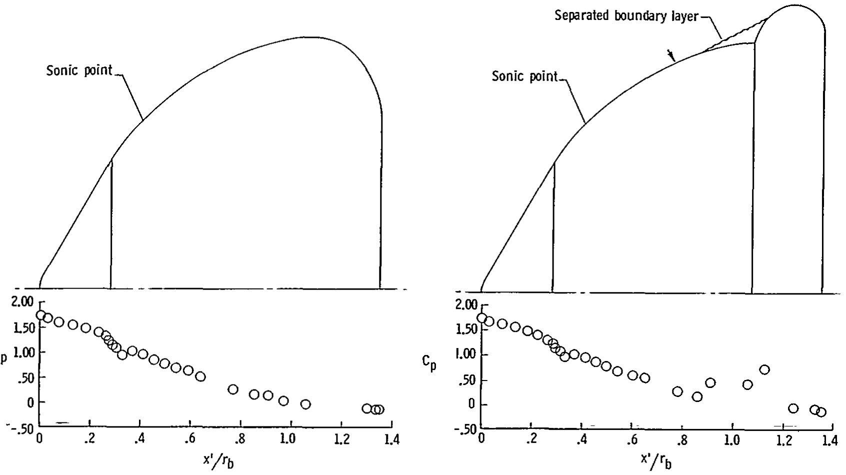

(a) Shape 1, $h/r_b = 0$.

(b) Shape 1, $h/r_b = 0.15$.

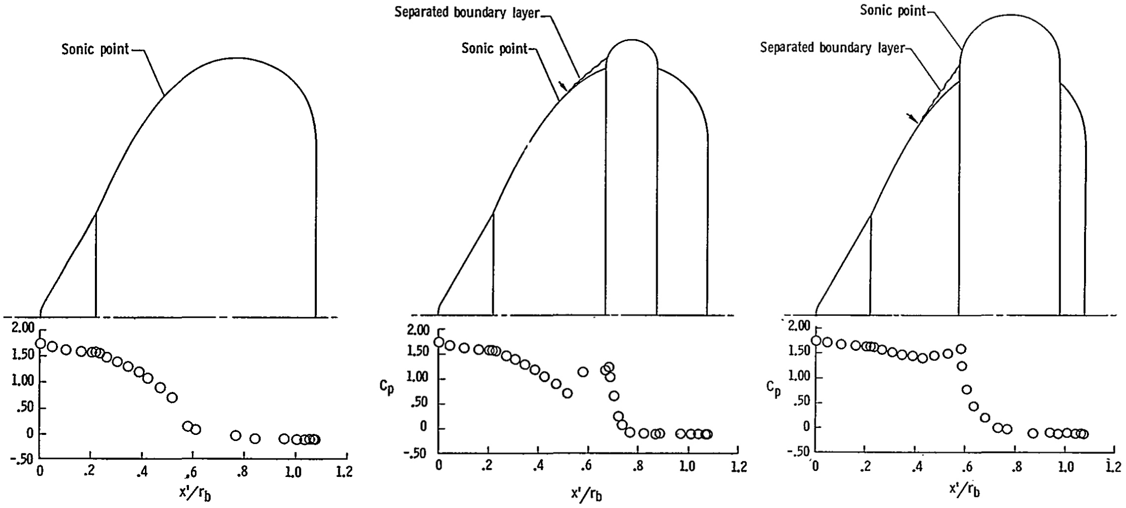

(c) Shape 2, $h/r_b = 0$.

(d) Shape 2, $h/r_b = 0.10$.

(e) Shape 2, $h/r_b = 0.20$.

Figure 10: Pressure distributions at Mach 3.0 and 0° angle of attack for various AID configurations [24].

1.5.3 Tension Cone Testing

Shortly after Anderson published his initial paper detailing tension shell theory, several sets of wind tunnel tests were performed on small scale tension cone models with the goal of exploring aerodynamic and stability characteristics in supersonic and hypersonic condtions. Most of the initial experiments involving the tension cone were performed for the purpose of exploring the capability of the tension cone as a rigid aeroshell. Hypersonic tests at Mach 20 [21], Mach 8 [38], and Mach 7 [64] examined static aerodynamics, pressure distributions, and heating profiles on rigid test articles. Most of the models tested at these conditions incorporated blunt noses and somewhat shallow cone angles. A common result in all hypersonic tests was the presence of an attached shock near the back of the tension shell, as shown in Figure 11. This is due to the combination of the concavity of the tension shell shape and the high Mach numbers of the tests. The attached shock produced a sharp pressure rise near the base of the model. Convective heat rates were also observed to increase considerably in the post-shock region with longer models seeing higher heat rates.

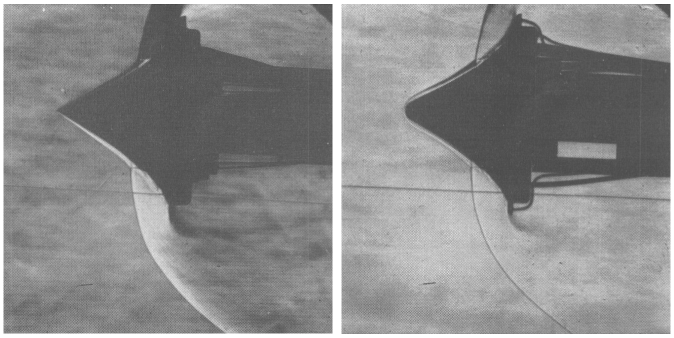
(a) (b)

Figure 11: Schlieren imagery of a pointed (a) and blunted nose (b) tension cone at Mach 8, $Re = 1.5 \text{ x } 10^6$, and 0° angle of attack [38].

The first tests of a tension cone at supersonic conditions were performed by Deveikis and Sawyer in 1966 [23]. A total of 13 different rigid tension cone models were tested with varying nose radii and cone angles. Though previous tests at hypersonic conditions consistently produced attached shocks, Deveikis and Sawyer were able to achieve a fully detached bow shock on models that incorporated a large enough cone angle, as shown in Figure 12.

Boundary layer flow separation was observed in conjunction with the attached shock. For smaller cone angle models (< 35°), larger nose radii produced more flow separation, though the opposite was true at greater cone angles. Many models that showed stable flow at zero angle of attack experienced leeward flow separation when tested at small angles of attack. However, the largest cone angle model, a 47° model, demonstrated no signs of flow separation for any combination of nose radius up to 40% of the base radius and angle of attack up to 12°. Drag coefficients as high as 1.55 were measured for large cone angles.

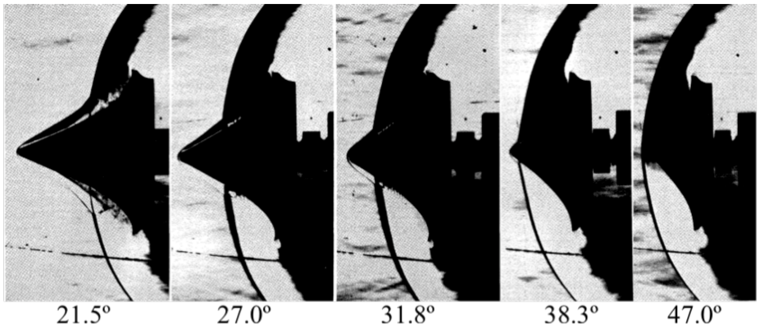

Figure 12: Effect of varying cone angle at Mach 3.0 (adapted from [23]).

Axial and normal force coefficients varied linearly with angle of attack. As long as the flow remain attached, static stability was achieved with a nearly constant value of pitching moment slope. A later set of tests conducted at similar conditions sought to improve flow stability by reducing the base radius and varying the shoulder radius, which in prior tests had always been a sharp corner [67]. The addition of small shoulder radii of approximately 5% of the base radius was observed to delay flow separation on several models, though at the expense of a reduced drag coefficient.

An investigation into the sensitivity of the derived tension shell shapes to pressure distribution was performed by Sawyer in 1970 [66]. Sawyer generated two separate sets of tension shell models. The first assumed a basic Newtonian pressure distribution. The second iterated on the Newtonian-derived shape using integral-relation theory [70] to produce a new shape. Though these two theories produce drastically different pressure distributions, the change in tension shell curvature is relatively small, as shown in Figure 13. The final integral-relation-derived shape was a product of successive iterations on shape and pressure

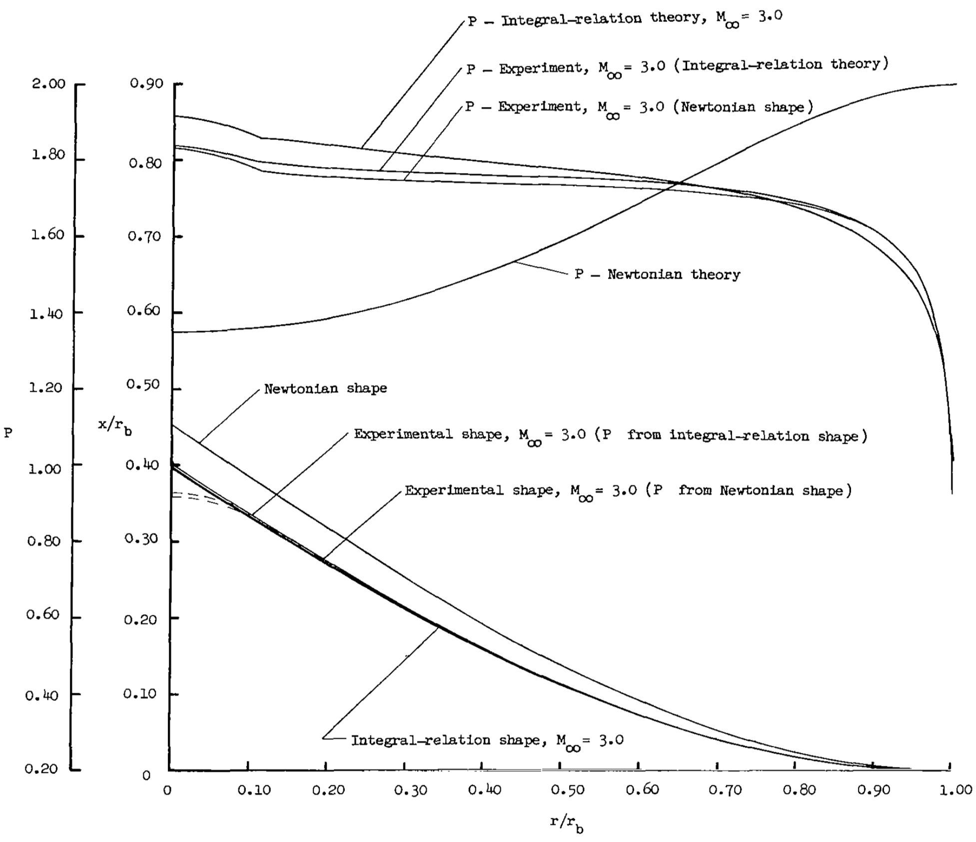

Figure 13: Impact of pressure distribution on tension shell curvature [67].

distribution, each of which produced very slight changes in total curvature. Results from wind tunnel tests of the two shapes demonstrated close agreement with the predictions by integral-relation theory. Measured values of pressure coefficient varied by less than 1% between the two models. Two new tension shell curves were derived based on the experimental pressure distributions but these were nearly identical to the original integral-relation-derived shape.

The agglomeration of historical wind tunnel tests on rigid tension cones can be used to draw several conclusions regarding their aerodynamics. Flow stability around the tension cone is primarily dependent on Mach number, cone angle, and angle of attack. It is also affected by the bluntness of the nose and the radius of the shoulder, though to a somewhat lesser degree. As long as the flow remains attached, the tension cone is statically stable and normal force varies nearly linearly with angle of attack. Drag performance of the tension cone is strongly dependent on the cone angle, with drag coefficients in the range of 1.2 to 1.6 at supersonic conditions.

Even though prior wind tunnel testing was limited to rigid models, the idea of a deployable tension cone has been around nearly as long as the concept itself. Seminal structural tests performed by Kyser were the first to investigate using an inflatable torus as the aft compression ring [42]. For his tests, Kyser fabricated inflatable tori with varying ratios of cross sectional radius to total radius by wrapping Dacron fiber around an elastomeric bladder. Kyser also used a combination of global buckling relations for inflated tori [31] and his own derivations of compressive stresses on the torus to predict required internal pressures. The predictions identified three primary modes of failure: local wrinkling (termed crippling) of the torus wall, in-plane buckling of the torus, and out-of-plane buckling of the torus. Though only briefly discussed, a key point made during his derivations involved the method of attachment of the torus to the tension shell. In particular, it was assumed that the tension shell was attached to the torus by fibers that extend around the back-side of the torus and are secured by a small-ring. Kyser's test configuration is shown in Figure 14. Two alternate attachment methods were considered and are shown in Figure 15. It was noted that in the case of method (a), the compressive stresses in the torus would be 50% greater than the nominal attachment method and thus require much more internal pressure to resist wrinkling. Attachment method (b) was discounted on the notion that the backside fibers would pull on and distort the forebody curvature of the tension shell.

Using a combination of toggle-harness and vacuum bag test apparatuses, Kyser's tests were observed to correlate well with theoretical predictions, as shown in Figure 16 for a slender torus. A notable exception to this was that out-of-plane buckling was not observed despite being predicted to occur at lower loading conditions than in-plane buckling. The implication of this result is that the torus need not be designed to resist the out-of-plane mode, thus allowing for a more slender and lighter torus. Tori constructed with larger cross sectional areas were observed to require greater loads than predicted for collapse, though generally by some fixed amount. Stout tori that were intentionally fabricated with more resin to stiffen the torus wall showed even greater offsets from the predicted collapse loads.

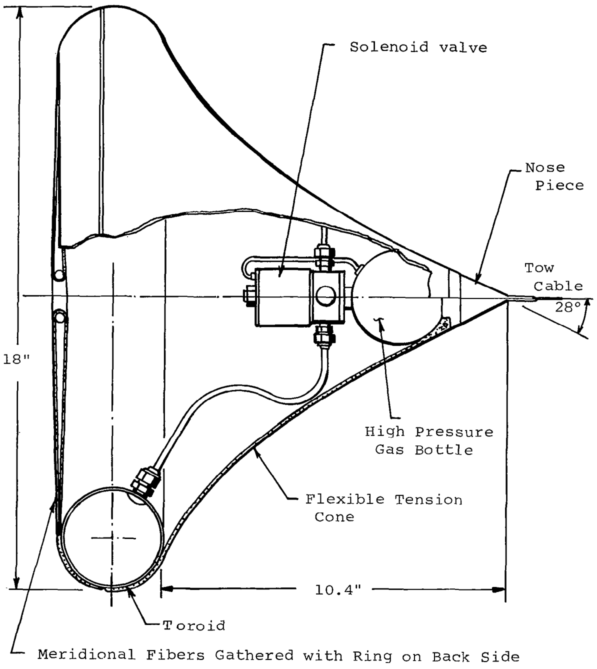

Figure 14: Tension cone configuration tested by Kyser [42].

1.6 Atmospheric Flight Tests

Flight tests of IADs at either hypersonic or supersonic conditions are relatively few in number and are limited to isotensoid based designs. As part of NASA's Planetary Entry Parachute Program (PEPP), Goodyear constructed an 18-foot (5.49-meter) diameter trailing isotensoid decelerator that was used in a 1967 sub-orbital rocket test [4]. The model was built using 48 gores of Nomex cloth for the canopy and included a burble fence with a height of 10% of the isotensoid diameter. The test article had a total mass of less than 19 kg, including bridle and riser lines. The payload mass was 93.5 kg, yielding a system mass fraction of approximately 17%. The technology development program included a pair of helicopter drop tests during which the decelerator was successfully deployed from a stowed configuration. Subsonic drag coefficients in excess of 1.2 were reported during these drop tests, though these were noted to be artificially high due to several reasons including a large coning angle during descent that would have produced some degree of lift by the decelerator. Supersonic testing of the article was performed at a deployment condition of Mach 3.15 and dynamic pressure of 38.5 psf (1843 Pa) [58]. However, the IAD failed to fully

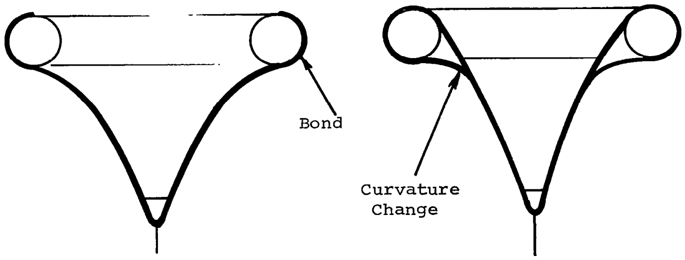

(a) (b)

Figure 15: Alternative torus/tension shell attachment methods considered by Kyser [42].

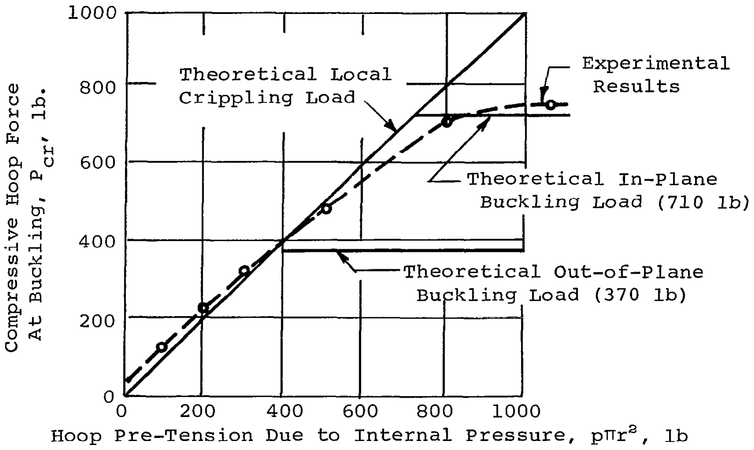

Figure 16: Experimental results of vacuum bag tests on a slender, filament wound torus [42].

inflate. In-flight video and post-test study of the test article showed that several of the ram-air inlets failed during deployment thus preventing a full inflation. It was postulated that severe flagging of envelope material during inflation caused the inlets to be shielded from the flow, thus prolonging the flagging further until the inlets and canopy began to tear [49].

A second flight test of a towed, isotensoid-based decelerator occurred in 1968 with much more success [72]. The ram-air inflated device measured 48-inches in diameter while the payload was an axisymmetric blunted cylinder with a base diameter of 18.21 inches. Sketches of both articles are provided in Figure 17. The trailing decelerator, including towline assembly, weighed 16.5 lbs while the payload was 184.5 lbs. Deployment of the decelerator occurred at a Mach number of 4.2 and dynamic pressure of 163 psf. The time to inflate to full size was reconstructed as 0.42 seconds. Time histories of tension in the towline showed a peak force nearly equal to the fully-deployed steady-state value. Stability assessments made with the help of on-board accelerometers, gyros, and video cameras indicated static and dynamic stability in both the pitch and yaw planes. Measured decelerator-only drag coefficients varied between 0.67 at Mach 4.2 to a peak of 1.45 at Mach 1.25. Subsonic drag coefficients were around 0.9.

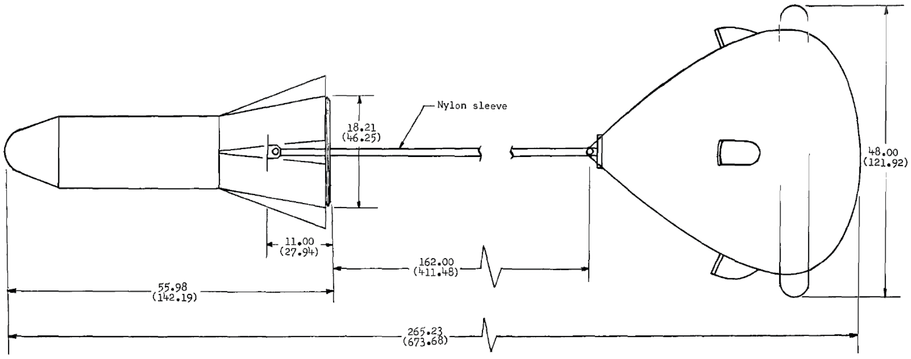

Figure 17: Sketches of the Mach 4.2 trailing isotensoid flight test configuration in dimensions of inches (cm). Note: not to scale. Adapted from [72].

Tests of trailing isotensoid IADs performed as part of the Air Force's Aerodynamic Deployable Decelerator Performance-Evaluation Program (ADDPEP) sought to explore different materials and burble fence characteristics [11]. Test conditions, summarized in Table 4, were achieved through the use of mutliple configurations of sounding rockets and included deployment conditions as high as Mach 9.75. With the exception of two tests, satisfactory deployment and inflation of the IAD was achieved. For the Mach 3.20 deployment, full inflation was never achieved due to the fabric coating changing state under the test environment, causing the Nomex to become too porous to maintain the needed internal pressure. Post-test examination indicated the coating failure was likely a result of an incomplete cure during fabrication. Partial inflation attributed to ram-air inlet structural failure also occurred for the Mach 4.12 deployment.

Though the emphasis on this review is for supersonic tests, many attempts at using IADs in hypersonic regimes have been made and deserve mention. These include the Inflatable Reentry Descent Technology (IRDT) [63] flight mission and the two follow on programs

Table 4: Summary of test conditions for ADDPEP trailing isotensoid IAD tests [11]. Note: conditions correspond to moment of initial line stretch.

Configuration			Test Conditions		
Diameter, ft (m)	Material	Burble Fence	Mach Number	Dynamic Pressure, psf (kPa)	Altitude, kft (km)
5.0 (1.524)	Nylon	10%	2.30	230.0 (11.0)	86.0 (26.2)
5.0 (1.524)	Nylon	10%	2.10	330.0 (15.8)	75.5 (23.0)
5.0 (1.524)	Nomex	10%, shielded	3.20	230.0 (11.0)	97.0 (29.6)
5.0 (1.524)	Nomex	None	4.12	284.0 (13.6)	101.0 (30.8)
5.0 (1.524)	Nomex	None	9.75	8.3 (0.4)	230.0 (70.1)

(IRDT-2 and IRDT-2R) as well as the Inflatable Reentry Vehicle Experiment (IRVE) [35]. Unfortunately, these three flight test opportunities were all largely unsuccessful with at least two failures, IRVE and IRDT, being attributed to separation issues with the launch vehicle. As of writing, a reflight of the IRVE mission is scheduled for 2009.

1.7 Objectives

The work submitted in this dissertation has three primary objectives. The first is to analyze the potential benefits that a supersonic IAD can provide for near-term robotic missions to Mars. Although prior systems studies have examined the application of supersonic IADs to robotic missions, nearly all of these assessments were conducted prior to the Viking program. Having first provided a summary of historical IAD development efforts, the current systems study allows for the inclusion of knowledge gained in EDL strategies as well as IAD design and aerodynamics over the past 30 years.

The use of computational tools for the analysis of supersonic IADs requires that the codes be validated. The second objective of this investigation is to acquire a data set useful for this purpose. This is achieved through the design and testing of an IAD configuration, the tension cone, that lacks the technical maturity of other configurations but whose structural design shows potential as a low mass decelerator. The design portion of this investigation develops a configuration that applies lessons learned from prior tension cone tests as well as an improved understanding of the tension cone shape trade space. The test portion of this investigation attains a data set that is capable of validating aerodynamic and structural analyses, and aeroelastic tools that couple these two forms of analysis.

The third objective of this investigation is to use the data acquired from testing to validate CFD tools for use in studying IAD aerodynamic performance. This involves the evaluation of multiple CFD tools with varying degrees of fidelity and complexity. These tools are used to generate predictions of flow field behavior, static aerodynamic characteristics, and surface pressure distributions. These predictions are compared against results from the test program. Conclusions regarding the accuracy of the computational methods applied are provided.

1.8 Summary of Contributions

The body of work presented herein advances the state of the art in supersonic inflatable aerodynamic decelerators by further maturing the tension cone configuration and validating the ability to computationally model its aerodynamic behavior. The following summary lists the contributions of this research.

The design of a tension cone IAD that advances the aerodynamic viability of the configuration: Prior testing of rigid tension cone models at supersonic conditions revealed the possibility of aerodynamic characteristics, such as embedded shocks and flow separation, that would prove detrimental for a flexible tension cone decelerator. This thesis presents a tension cone that is designed and demonstrated to be free of these characteristics. The design incorporates lessons learned from prior tests as well as further understanding of the tension cone shape trade space. Wind tunnel testing at relevant Mach numbers and Reynolds numbers shows that the flowfield around the shape is stable. The result is a shape that improves the viability of the tension cone concept.

The first testing of a flexible tension cone IAD at relevant Mach and Reynolds numbers: Previous supersonic testing of tension cone IADs has been on rigid models only. Testing of a flexible model provides a more suitable comparison of how a tension cone would perform in flight. These tests also provide the first investigation of how a tension cone behaves when inflated and deployed from a stowed configuration and how the shape behaves at non-zero angles of attack. A flexible, deployable model allows for insight into the inflation pressure required to produce a fully deployed shape and how the shape deforms when subject to insufficient pressure.

The validation of modern CFD codes for use in analyzing tension cone aerodynamic performance: Computational fluid dynamics is frequently used for predicting the performance of supersonic IADs but has yet to be specifically validated for that application. This research uses data acquired from wind tunnel testing of the tension cone to assess the capabilities of multiple CFD codes. Solutions are generated at several test conditions and compared against wind tunnel data. A code to code comparison evaluates each code's ability to match wind tunnel results. This work addresses issues regarding fidelity and grid topology requirements, promotes confidence in the suitability of these codes, and provides a path for development of more complex fluid-structure interaction codes.

CHAPTER II

MARS SUPERSONIC IAD ENTRY SYSTEMS STUDY

2.1 Overview of Systems Study

This chapter presents the results of a systems analysis of supersonic IADs. The objective of this investigation is to quantify the potential advantages offered by a supersonic IAD with respect to a baseline robotic Mars mission. Although prior systems studies have addressed the use of a supersonic IAD for a Mars mission, nearly all of these studies were performed prior to the Viking landings. This study is unique in that it analyzes supersonic IADs for use on a present day or near-term Mars robotic mission. Preliminary aerodynamic and structural analyses are conducted for two separate IAD configurations. Results from these analyses are used to quantify trajectory effects and provide mass estimates for an IAD system. Key sensitivities provide insight into areas of further research and technology development.

2.2 Mission Overview

A large rover mission is baselined for this investigation. Such a mission may take shape through either the Astrobiology Field Laboratory (AFL) or Mars Sample Return (MSR) flight projects. Envisioned as a follow-on rover mission to Mars Science Laboratory (MSL), a significant portion of the MSL entry, descent, and landing heritage is assumed [7]. The entry vehicle configuration, shown in Figure 18, is identical to that used by MSL. The rover mass is anticipated to be 10% to 25% higher than MSL, primarily due to accommodation of a more complex science payload [7] and the requirement for increased landing precision. For the purposes of this study, an entry mass of 4,200 kg is assumed (31% higher than MSL). It should be noted that this value yields a packing density of approximately 195 kg/m^3, or nearly 85% of the packing density achieved with the Mars Exploration Rovers, implying a complex and difficult packaging arrangement. The mission entry sequence is intended to mirror MSL in many respects, including the use of a center of mass offset to provide trim

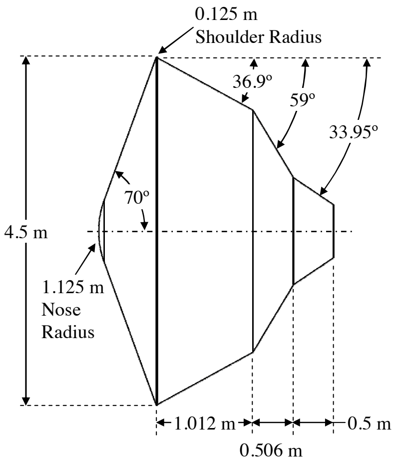

Figure 18: AFL Entry Capsule

at a non-zero angle of attack and subsequently an L/D of approximately 0.24. As in the MSL mission, hypersonic guidance via lift vector (bank angle) modulation is baselined. In the present study, a reference trajectory is modeled using a reference bank-angle profile, a relative entry flight path angle of -16.1°, and a relative entry velocity of 5.9 km/s. For this reference trajectory, the final stages of descent assume nominal deployment of a 23 m supersonic disk-gap-band (DGB) parachute at a Mach number of 2.3 and a dynamic pressure of 800 Pa. Note that these assumed DGB parachute deployment conditions are beyond those planned for MSL, which itself is beyond those successfully demonstrated to date. Upon inflation, the parachute rapidly decelerates the entry vehicle through transonic and into subsonic flight conditions. As with MSL, heatshield separation is assumed to occur upon reaching a Mach number of 0.7. The terminal descent portion of flight is performed using the MSL skycrane architecture. For MSL, powered descent initiation is dependent upon ground acquisition by a terminal descent sensor followed by measurement of the vehicles altitude and velocity [74]. Although no specific set of flight conditions define the point at which the descent engines are ignited, it was assumed that the earliest this event could occur is 20 seconds after heatshield jettison. For the reference trajectory, this occurs at an altitude of 7.3 km and a velocity of 112 m/s. The complete nominal AFL entry trajectory is shown in Figure 19, relative to that computed for MSL. Validation of the trajectory modeling was performed against simulations provided by the Jet Propulsion Laboratory for the AFL mission and by the NASA Langley Research Center for the MSL mission.

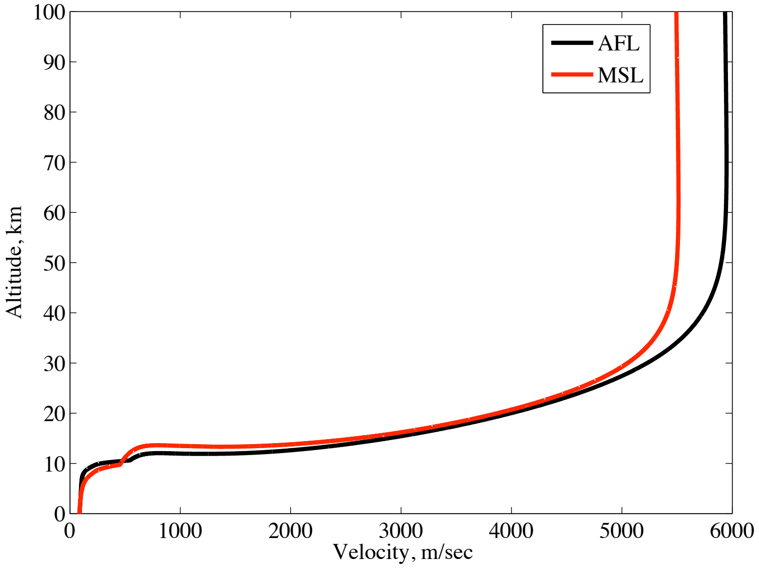

Figure 19: Nominal AFL and MSL entry trajectories.

2.2.1 IAD-Modified Mission

Two major variations to the reference mission profile are studied. The first consists of the elimination of the DGB parachute in favor of a supersonic inflatable aerodynamic decelerator. The objective in this case is to allow for significant deceleration earlier in the trajectory and consequently allow for landing at higher elevations than would otherwise be possible using a parachute alone.

Previous robotic Mars missions have limited parachute deployment to Mach numbers less than 2.1 due to the lack of deployment and initial inflation test data obtained at the Earth in Mars relevant conditions above this Mach number and the severe area oscillations that have been observed in DGB parachutes at Mach numbers above approximately 1.5. Historical testing of supersonic IADs has shown no area oscillation susceptibility due to Mach number effects. Thus, this analysis placed no such Mach restriction with the exception that deployment must occur at a Mach number less than 5 with the assumption that this would eliminate aerothermal heating considerations.

By design of the reference bank profile, as the entry vehicle slows to supersonic velocities, the lift vector may be returned to near vertical causing a small loft in the trajectory. The IAD modified mission takes advantage of this feature by waiting until the peak loft altitude is attained before initiating deployment. Entry flight path angle variation was also performed in an attempt to position this loft at Mach numbers and altitudes larger than for the reference trajectory.

2.2.2 Two-Stage IAD/Parachute Mission

Although IADs offer excellent aerodynamics in high Mach number, high dynamic pressure environments, this generally comes at the expense of a system that is more massive than a traditional parachute. Parachutes on the other hand perform very well in subsonic environments. Previous studies have shown that the optimal solution from a mass standpoint may be to incorporate a two-stage IAD-parachute system [13]. In this manner, the IAD can be deployed at high supersonic conditions, decelerate the vehicle to subsonic conditions, and then give way to a more efficient parachute system. The second alternative mission profile examines this concept by discarding the IAD at a Mach number of 0.9 and subsequently deploying a ringsail parachute.

2.2.3 Decelerator Configurations

Three types of aerodynamic decelerators are evaluated for this study: a supersonic tension cone IAD, a supersonic isotensoid IAD, and a subsonic ringsail parachute. The primary geometric parameters for a nominal tension cone are provided in Table 5 using notation described in Figure 20. The values of cone angle and torus radius ratio are identical to those used in the wind tunnel models discussed in Chapter 3. The radius of the aeroshell was chosen to be equivalent to that for the MSL and AFL missions. Note that scaling of the total IAD diameter was achieved by holding constant the radius of the aeroshell, the tension cone angle, and the ratio of tension shell to torus radii. Deployment of the tension cone occurs when the torus is rapidly pressurized using either a gas generator or pressure tank based inflation system. Detailed modeling of the inflation system and deployment dynamics are neglected for this conceptual design study.

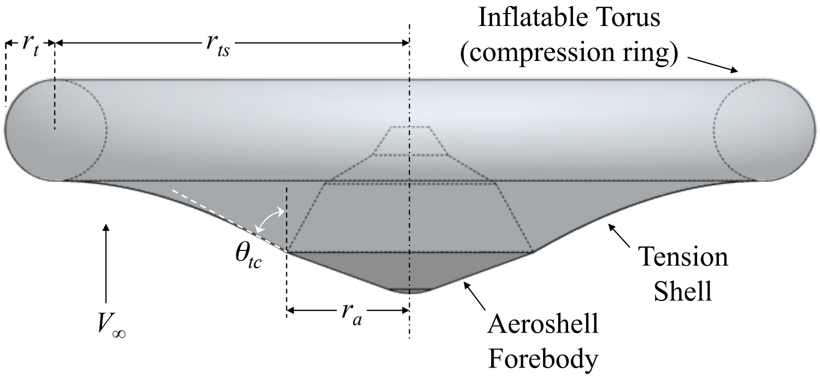

Figure 20: Baseline tension cone configuration for IAD systems study.

Table 5: Baseline tension cone geometry values for IAD systems study.

Parameter	Symbol	Dimension
Cone angle	θ_{tc}	60°
Torus radius ratio	r_{ts}/r_t	7
Aeroshell radius	r_a	2.25 m

The attached isotensoid configuration utilized in this study is shown in Figure 21 with the pertinent isotensoid parameters indicated in Table 6. Similar to the tension cone, the decelerator canopy half-angle (θ_{iso}) does not precisely match the aeroshell half-angle (θ_a) at the attach point. The deployment duration of the attached isotensoid is determined by the mass flow rate into the canopy through the ram-air inlets and out of the canopy due to material porosity. To a large degree these rates can be tailored by optimizing inlet area and material porosity to achieve a desired inflation rate that balances deceleration loads and inflation stability. Wind tunnel testing of the inflation process indicated inflation times on the order of 0.6 seconds for a 1.5 meter diameter device [54]. Based on a desire to minimize exposure to adverse transients, inflation times for full scale articles are expected to be of similar order and thus inflation of the isotensoid device is modeled as instantaneous.

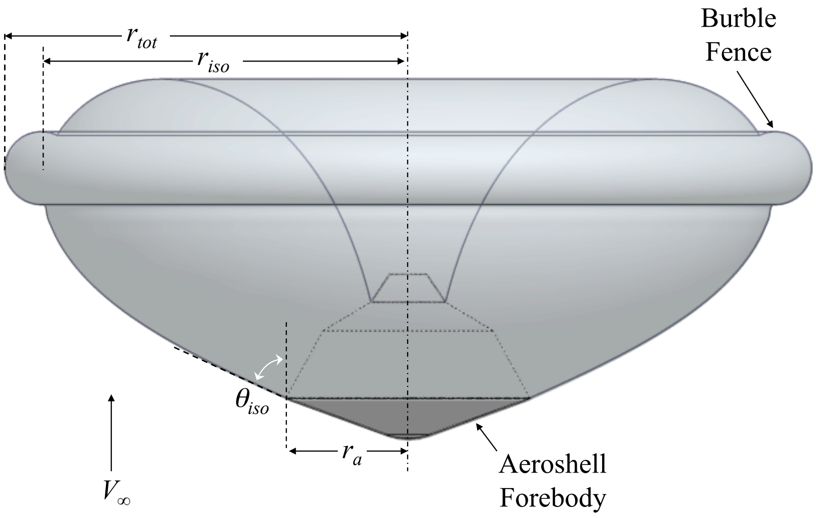

Figure 21: Baseline attached isotensoid configuration for IAD systems study.

Table 6: Baseline attached isotensoid geometry values for IAD systems study.

Parameter	Symbol	Dimension
Cone angle	θ_{iso}	65°
Total decelerator radius	r_{tot}	$1.1r_{iso}$
Aeroshell radius	r_a	2.25 m

A ringsail parachute was analyzed as a potential second-stage decelerator for its high subsonic drag coefficient, good stability characteristics, and relatively low mass per unit drag area [10]. Additionally, the ringsail canopy can be designed for optimum performance for a given flight condition, enabling ringsail configurations to achieve subsonic drag coefficients of 0.8 or better. Subsonic inflation of the parachute can be modeled as occurring linearly over a constant number of parachute diameters [10]. Even for a large parachute (> 20 m diameter) deployed at a velocity of 100 m/s, the inflation time is less than two seconds; thus in this analysis, the ringsail parachute inflation is also modeled as instantaneous.

2.3 Aerodynamic Model

An aerodynamic model for both the tension cone and attached isotensoid configurations was developed for use during trajectory simulations. The model incorporated drag versus Mach data attained from several wind tunnel tests of the attached isotensoid and tension cone configurations. The wind tunnel data corresponds to a collection of tests performed in the 1960's and 1970's as well as the more recent tests of the tension cone decelerator performed as part of this dissertation and discussed in Chapter 3. Data included in the attached isotensoid model was only for geometries incorporating a burble fence. Once the data was compiled, a curve fit was generated for each configuration, with a few data points being weighted more than others to account for their similarity to the reference configurations. The original data and the resulting fits are provided in Figure 22. Although the transonic data from TND3700 (Reference [33]) was acquired on a rigid model of a configuration somewhat different than for the other data points, that configuration was considerably less blunt than the rigid model used during testing at the LaRC Unitary tunnel. Thus, the TND3700 transonic data points are considered conservative versus how a more blunt tension cone would perform. Additional supersonic data on tension cones is available in the literature but was excluded from the drag model because of the large differences in configuration between those shapes and the one used in this study.

Historical testing on the attached isotensoid has been on predominantly similar geometries, with the largest differences being the cone angle of the aeroshell forebody (60° vs. 70°) and the size of the isotensoid in relation to the aeroshell. The transonic and higher-subsonic isotensoid data shown in Figure 22 is for the same configuration and the difference is attributed to one model being rigid while the other being flexible. As discussed in Reference [68], the isotensoid shape is due to a specific pressure distribution and testing at transonic and subsonic conditions caused the flexible isotensoid to take a more blunt shape, thus resulting in greater drag performance. It is assumed that this would also be the case in a flight environment and therefore the rigid isotensoid data was excluded from the aerodynamic model. No adjustment to the drag data was made to account for what would likely be a slight performance improvement in a CO_2 environment [41].

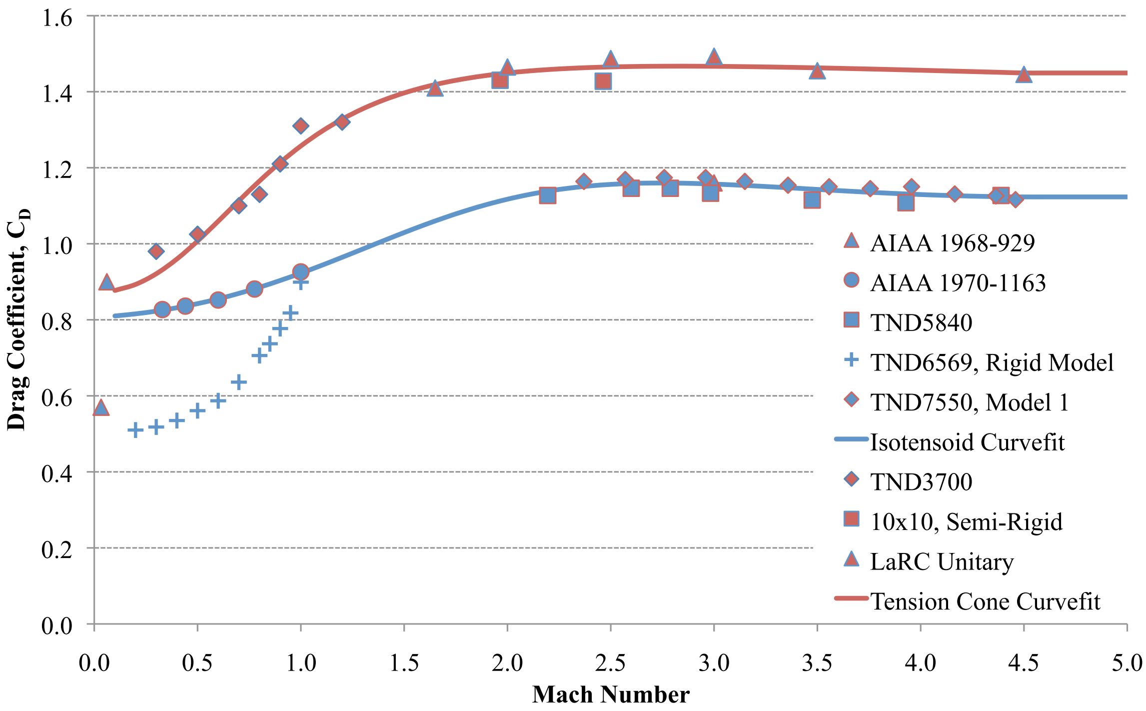

Figure 22: Summary of tension cone and attached isotensoid wind tunnel test data at a 0° angle of attack. Solid lines denote the corresponding curvefit used for later analyses. Note: TND numbers refer to NASA technical document numbers.

A comparison of the performance of the tension cone and isotensoid decelerator configurations versus other decelerator configurations is shown in Figure 23. The drag performance of the tension cone can be seen to be similar to that of a 60° sphere cone in the supersonic regime, though improved performance is estimated for subsonic conditions. A comparison between the two IAD types shows that the tension cone provides approximately 25% greater drag in the supersonic regime and a 10% or greater drag advantage in the subsonic regime. A portion of this difference can be attributed to the inclusion of the burble fence on the isotensoid shape. At supersonic conditions, the drag provided by the burble fence is small compared to the resulting increase in reference area. The trend of drag coefficient versus Mach number for the two inflatable decelerator configurations is more similar to a rigid aeroshell configuration than a trailing DGB parachute. As with a 60° or 70° sphere cone, the two IADs maintain nearly constant drag performance at increasing Mach number, while the parachute steadily decreases. Neither IAD configuration exhibits the decrease in drag coefficient in the transonic regime, often termed a transonic drag bucket, common to parachutes and other decelerators which trail an entry system. The lack of a drag bucket is a feature that may allow for the heatshield to be discarded much earlier in the trajectory as recontact with the entry vehicle is less likely.

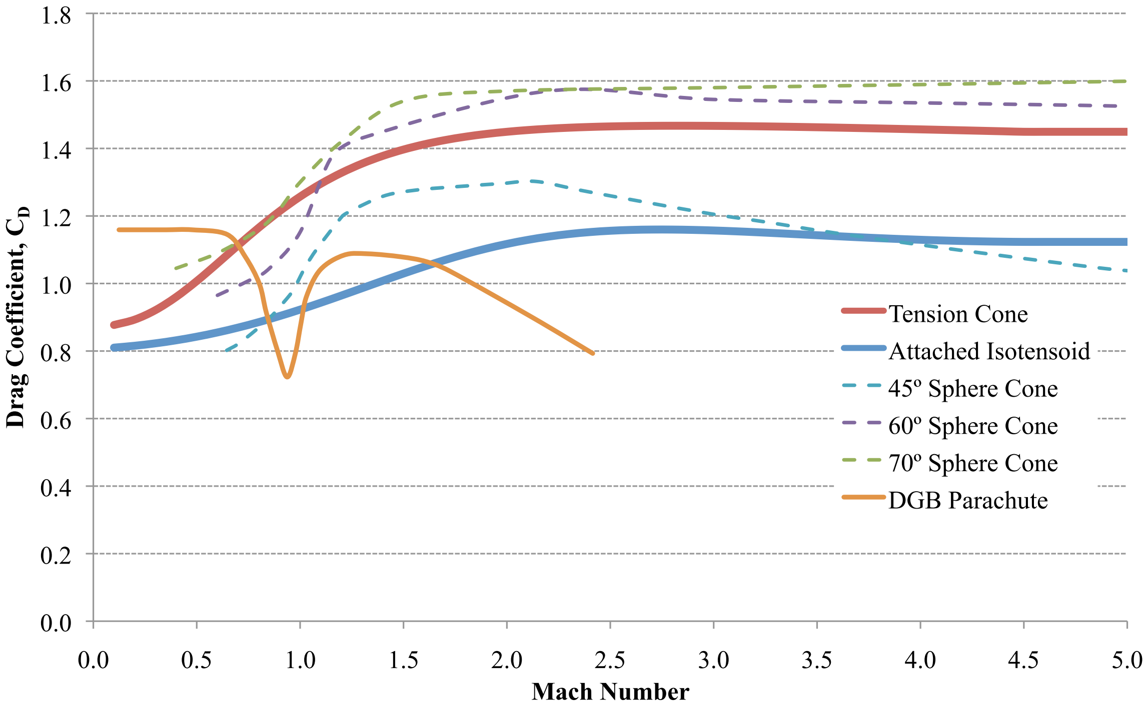

Figure 23: Comparison of drag coefficient vs Mach number for IADs and sphere cone aeroshells. Note: Drag coefficients non-dimensionalized using projected area. Data sources: 45° Sphere Cone [55]; 60° Sphere Cone [46],[73]; 70° Sphere Cone [25]; DGB Parachute [22]

2.4 Mass Model

Neither the tension cone nor isotensoid decelerators have been fabricated at scales comparable to flight-like devices. Thus, many uncertainties exist about the exact nature in which these articles would be fabricated, making mass estimation difficult. For this study an approach was utilized in which basic structural principles were combined with tension cone and isotensoid shape theory. The result is a preliminary estimate of the loads and stresses encountered by the two supersonic IADs. This in turn is combined with assumed material properties to derive thickness estimates and subsequently material mass estimates. A summary of the structural considerations and subsequent mass relations incorporated in the analysis is provided below for each configuration.

2.4.1 Tension Cone Mass Estimation

Mass estimates for the tension cone configuration were carried out using the first-order model described in Appendix A. For this model, key inputs are required in the areas of geometry, aerodynamics, material properties, and inflation gas parameters. Geometric parameters are based on the total diameter of the tension cone ($r_{ts} + r_t$) being sized and the values provided in Table 5. Values of other parameters required for mass estimation are provided in Table 7. The drag contribution of the tension cone was determined by subtracting off the drag contribution of the aeroshell from the total drag. The dynamic pressure chosen was based on the dynamic pressure at deployment for the 5.0 t entry case discussed later. For both IAD configurations, the textile portions of the decelerator were sized assuming the material properties of Vectran. Vectran was selected based on its high strength-to-weight ratio, good thermal resistance, and use on the Pathfinder and Mars Exploration Rover (MER) airbags. The same 200 denier Vectran material [71] used on the two MER landers was used in this study. The tension shell was sized assuming an areal density of uncoated Vectran whereas the torus portion of the tension cone was assumed to have the higher areal density of coated Vectran to account for the addition of a silicone coating to reduce porosity. The final areal density used in mass calculations was scaled linearly with the required tensile strength of the material, though with a minimum value of one-half the nominal areal density. The minimum value is used to account for the fact that there exists some limit as to how thin or how light Vectran can be manufactured. The inflation gas parameters are consistent with nitrogen gas operating at the maximum use temperature of Vectran [29].

Table 7: Key inputs to tension cone drag model.

Parameter		Value	
Aerodynamics			
$C_{D,total}$		1.45	
$C_{D,aeroshell}$		1.60	
Dynamic Pressure	q_∞	1500	Pa
Material Properties			
Vectran			
Strength	N_t	84940	N/m
Areal Density	ρ_{areal}	0.0915	kg/m^2
Coated Vectran			
Strength	N_t	84940	N/m
Areal Density	ρ_{areal}	0.1458	kg/m^2
Inflation Gas			
Temperature	T_{gas}	423	K
Specific Gas Constant	R_{gas}	297	N-m/kg-K

Both a tank system and a gas generator were investigated for the inflation system. Following the tank sizing guidelines in [36], the tank mass was estimated to be moderately higher than the mass of the inflation gas itself. Gas generators on the other hand are very similar in design to solid rocket motors, which typically yield more favorable mass fractions. For this study the gas generator was assumed to be an additional 1/3 the mass of the inflation gas.

The tension cone mass model detailed in Appendix A is considered to be conservative, a result reinforced by the testing of flexible tension cone models. As discussed in Chapter 3, predictions of the required inflation pressures were seen to be significantly higher than the required inflation pressures observed in test. To incorporate these lessons learned into the tension cone mass model, a modification to the required torus pressures was made. In particular, the required inflation pressures for models incorporating a structural modification (anti-torque panels) on the backside of the tension cone were on average 2.74 times less than those predicted for models without anti-torque panels. Thus, during mass estimation, the calculated inflation pressures were reduced by a similar factor. This in turn reduced the stresses on the torus and allowed for a reduction in material mass. A 25% increase in the tension shell mass was applied to account for the addition of anti-torque panels, though this had little effect on the total system mass.

The trajectory analyses performed focused on IAD diameters of 14, 17, 20, and 23 m. Mass estimates for tension cones of these sizes are provided in Table 8. The results in Table 8 demonstrate that the total tension cone mass increases rapidly with increasing diameter. Furthermore, the rate of mass increase is larger than the rate of increase in the square of the total diameter. In other words, larger tension cones will yield larger decelerator ballistic coefficients (decelerator mass divided by total drag area). Table 8 also provides the decelerator system mass fraction as a percentage of the nominal 4200 kg entry mass, which for even the largest tension cone is less than 9%.

Table 8: Tension cone mass for a range of diameters.

Tension Cone Diameter (m)		14	17	20	23
Geometry (m)					
Tension shell radius	r_{ts}	6.1250	7.4375	8.7500	10.0625
Torus radius	r_t	0.8750	1.0625	1.2500	1.4375
Aeroshell radius	r_a	2.25	2.25	2.25	2.25
Mass (kg)					
Tension Shell	m_{ts}	6.1	14.3	28.9	52.2
Torus	m_t	19.3	36.0	60.0	92.5
Inflation Gas	m_g	31.7	59.1	98.4	151.8
Gas generator		10.6	19.7	32.8	50.6
Total Mass (kg)	m_{tc}	**67.6**	**129.1**	**220.1**	**347.1**
Decelerator Ballistic Coefficient (kg/m^2)	β	0.303	0.392	0.483	0.576
Decelerator System Mass Fraction		0.016	0.031	0.052	0.083

The largest contributor to the rapidly increasing mass is the inflation gas, which in turn is driven primarily by torus pressure requirements, hence the desire for using anti-torque panels. The dominant driver of the calculated inflation pressure is the desire to eliminate wrinkling on the torus, which is considered a precursor to structural failure. Torus fabrication methods that are capable of tailoring the stresses in the torus or providing additional stiffness would likely reduce the system mass considerably.

2.4.2 Isotensoid Mass Estimation

Mass estimation for the attached isotensoid configuration was performed using the model of Reference [2]. As with the tension cone model, the isotensoid model sizes the device based upon first order estimates of the stresses encountered. Inputs to the model were kept consistent with those of [2] with the exception of the drag coefficient of the isotensoid, the deployment dynamic pressure, and the material properties. Values of these parameters, in the notation of [2], are shown in Table 9. The strength to weight ratios of the meridional cords and canopy fabric are based on those for uncoated and coated Vectran, respectively. As with the tension cone, a minimum gage areal density of no less than 50% the nominal value was applied. A summary of the mass estimation efforts for the isotensoid across the range of diameters used in this analysis is provided in Table 10.

Table 9: Key inputs into isotensoid mass model of [2].

Parameter	Symbol	Value	
Meridional Cord Strength to Mass Ratio	k_c	582579	N-m/kg
Fabric Strength to Mass Ratio	k_f	191920	N-m/kg
Decelerator Drag Coefficient	C_D	1.2	
Burble Fence Ratio	η	0.1	
Dynamic Pressure	q_∞	1500	Pa

Table 10: Isotensoid mass for a range of diameters.

Isotensoid Diameter (m)		14	17	20	23
Meridians					
Cord Length (m)	l_m	6.4	7.7	9.1	10.5
Cord Mass (kg)	m_m	12.4	20.9	33.1	49.3
Canopy					
Surface Area (m^2)	A_f	358	527	730	965
Canopy Mass (kg)	m_c	45.5	64.8	87.8	114.6
Total Mass (kg)	m_{iso}	**57.9**	**85.7**	**120.8**	**163.9**
Decelerator Ballistic Coefficient (kg/m^2)	β	0.313	0.315	0.321	0.329
Decelerator System Mass Fraction		0.014	0.020	0.029	0.039

Compared to the tension cone the isotensoid is estimated as having a lower mass for a given diameter. Much of this can be attributed to the ram-air inflation mechanism of the isotensoid that eliminates the requirement for an independent inflation system. That is, even though the isotensoid configuration has significantly greater material acreage, the increase in material mass is still less than the mass of the inflation system. Calculated decelerator system mass fractions very between 1.4% and 3.9%. From a mass perspective, should it be possible to reduce the inflation pressure requirement of the tension cone torus, the two concepts would become more equivalent in mass. Alternatively, a reduction in the peak dynamic pressure, which for supersonic IAD's generally occurs at deployment, would also favor the tension cone. An example of this is provided in Figure 24 where IAD mass is shown against drag area for several values of dynamic pressure. For a dynamic pressure of 1 kPa the tension cone is calculated to be more mass efficient up to drag areas of nearly 400 m^2. For comparison, the 4.5 m aeroshell has a drag area of about 25 m^2. A 0.5 kPa increase in dynamic pressure decreases the crossover point to a drag area of 230 m^2.

A caveat to the above mass estimates is reiterated due to the lack of any historical precedence in the manufacturing of IADs at these scales. This applies equally to both the tension cone and isotensoid mass estimates. Furthermore, the tension cone configuration evaluated likely does not constitute a mass optimal configuration. Increases in torus diameter or decreases in the attachment angle would reduce the system mass, though at the expense of a decrease in drag performance.

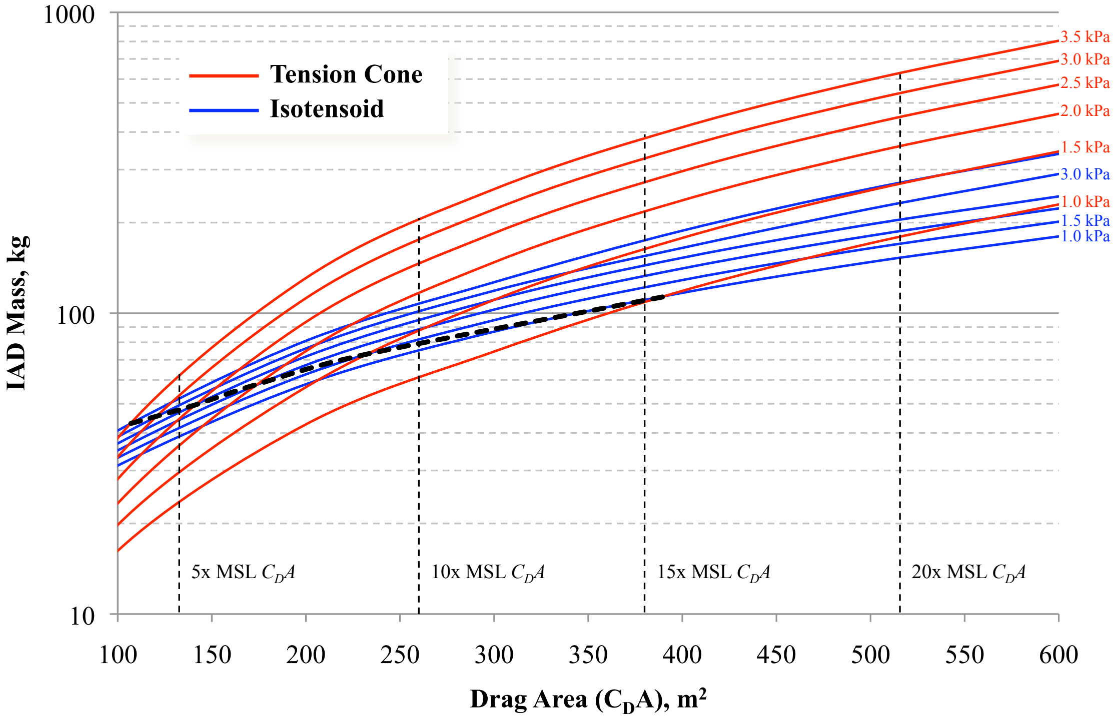

Figure 24: IAD mass versus drag area for dynamic pressure increments of 0.5 kPa. Dashed black line corresponds to the lower mass crossover point. MSL CD_A refers to the drag area of the nominal 4.5 m diameter, 70° aeroshell.

2.4.3 Parachute Mass Estimation

Mass estimates of a ringsail parachute were made using a linear regression of historical data from [26]. A mortar mass estimate was also attained using a linear regression of data provided in [27]. The results are the following relations:

$$m_p = 0.1055\frac{D_0\pi^2}{4} \tag{1}$$

$$m_{mortar} = 0.2355 m_p \tag{2}$$

where m_p is the parachute mass in kg, D_0 is the parachute nominal diameter in m, and m_{mortar} is the mortar mass in kg.

2.5 Trajectory Results

A key advantage of an IAD is its ability to increase drag area ($C_D A$) earlier in the descent profile, enabling deceleration at higher altitudes versus the traditional DGB parachute. Additionally, the lack of a transonic drag bucket may permit the entry vehicle to release its heatshield at any point after IAD inflation without risking recontact. Early heatshield separation reduces the mass being decelerated and allows for onboard altimeters to acquire the ground sooner. This latter capability allows for the initiation of propulsive descent at a higher altitude, enabling landing at higher surface elevations and/or additional time to perform pinpoint landing guidance.

Three degree of freedom trajectory simulations were performed using the Program to Optimize Simulated Trajectories (POST) [62]. For all trajectories, the entry phase up to the point of decelerator deployment employed the same reference bank-angle vs. Mach profile as the DGB reference trajectory used in this study. Three primary trades were evaluated: replacement of the nominal 23 m DGB with a supersonic IAD, replacement of the DGB with a two stage IAD-ringsail combination, and the impact of an additional 20% increase in entry system mass.

2.5.1 IAD and Baseline DGB System Comparison

The system impact of increasing IAD diameters versus the present Astrobiology Field Laboratory baseline 23 m DGB parachute was analyzed. Both IAD concepts were assessed. An initial comparison of the trajectories is provided in Figure 25, where IADs of varying diameters are shown deployed at the loft peak of the reference trajectory (∼Mach 3.3). Evident in Figure 25 is the rapid, near constant altitude deceleration that occurs after IAD deployment. This is followed by transition to an asymptotic terminal descent in which drag and gravitational forces are nearly equal and opposite and the vehicle is descending on a line of constant dynamic pressure. Terminal velocity is strongly dependent on the diameter of the IAD, with diameters between 14 m and 23 m shown in Figure 25. Given that the terminal velocity represents the velocity at which the entry vehicle would stage to propulsive terminal descent, a trade between IAD size and propellant mass arises. For example, a 14 m tension cone IAD provides a terminal velocity of 150 m/s at an altitude of 5 km, whereas a 20 m tension cone IAD provides a terminal velocity of 105 m/s at the same altitude. For reference, a 23 m DGB parachute deployed at Mach 2.3 results in a terminal velocity of 100 m/s at 5 km altitude. Clearly, a larger IAD reduces the velocity and thus the propellant required for terminal descent, though at the expense of a heavier IAD system.

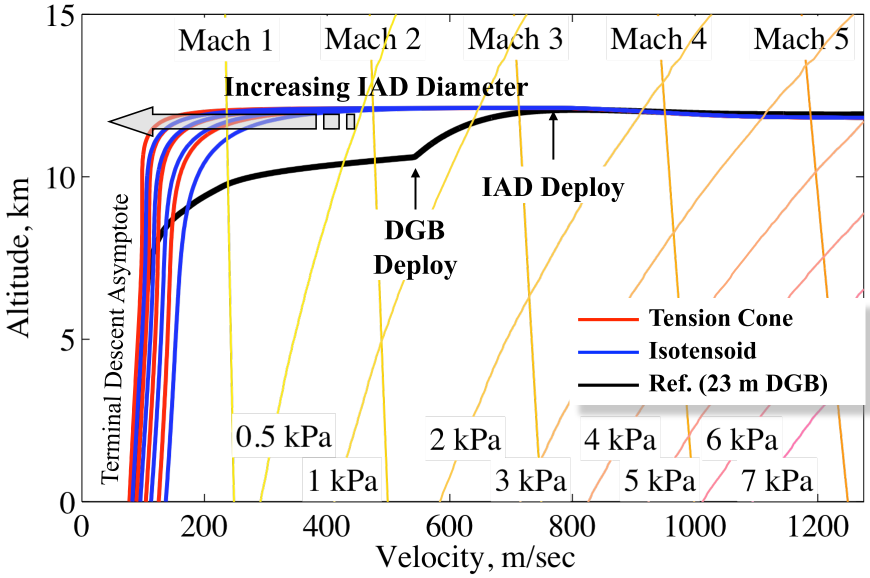

Figure 25: Comparison of reference trajectory and IAD-modified trajectories against contours of Mach and dynamic pressure (γ_{entry} = -16.1°).

Figure 25 demonstrates that a significant increase in altitude ($\geq$ 3 km) at subsonic velocities is possible with use of an IAD. Architecturally, this altitude increase can be used to provide either an increase in terminal descent timeline or the ability to land at higher surface elevations. In the latter case, all things being equal, increases in staging altitudes translate into equivalent increases in landed altitude. However, the nominal entry trajectory belies the greater impact that an IAD can provide as a result of its large deployment condition envelope. That is, the DGB reference trajectory places the loft peak at a Mach number of about 3.3 and dynamic pressure of 1.5 kPa, whereas a supersonic IAD is theoretically capable of deploying at higher Mach numbers and greater dynamic pressures. Thus, a more valid comparison can be made when the loft is repositioned. Retaining the reference bank profile, this is accomplished by entering at a shallower flight path angle. For a relative entry flight path angle of approximately -13.7° the loft peak occurs at Mach 5 and at a dynamic pressure nearly equivalent to before. The resulting trajectories are shown in Figure 26. Of note is that even moderately sized (14 m diameter) IADs can be used to attain subsonic velocities at altitudes nearly 10 km higher than the baseline DGB trajectory. This significant increase in altitude can be related to large increases in the timeline as well. Noting that the IAD transitions to a terminal descent asymptote at a very high altitude, and approximating the terminal velocity as 150 m/sec, every kilometer increase over the baseline DGB trajectory translates to about 7 more seconds of timeline. Thus, a 10 kilometer increase provides over a minute of additional timeline, a very sizable increase given that prior Mars entries, from atmospheric interface to touchdown, typically occurred over only six minutes.

Figure 26 shows that the improved drag performance of the tension cone provides additional advantages in altitude over the isotensoid design of $\sim$ 3-5 km. Deployment of the nominal 23 m DGB at a Mach number of 2.3 for this shallower entry results in an altitude loss of roughly a kilometer. Furthermore, the deployment dynamic pressure is an additional 10% greater than the reference condition. Lastly, it is worth noting that the shallower entry flight path angle also affords reductions in heating rates encountered by the entry vehicle, though at the expense of increased heat loads.

Although these trajectories do not represent optimized bank profiles they still demonstrate the expanded EDL system performance range that an IAD enables. If a steeper entry is desired, IADs still provide a considerable altitude advantage. An example of this scenario is provided in Figure 27, where the bank profile was adjusted to provide more lift throughout the entry and the relative entry angle was steepened to -19°. This trajectory provides 8-10 km in increased altitude (as measured at the Mach 1 condition) and nearly a minute of additional timeline. Deployment of the 23 m DGB parachute at Mach 2.3 for this entry condition is seen to provide additional altitude gain over the nominal case, though not nearly to the degree that an IAD provides. Parachute deployment at a higher Mach number and nominal dynamic pressure of 800 kPa would decrease this deficit to some degree.

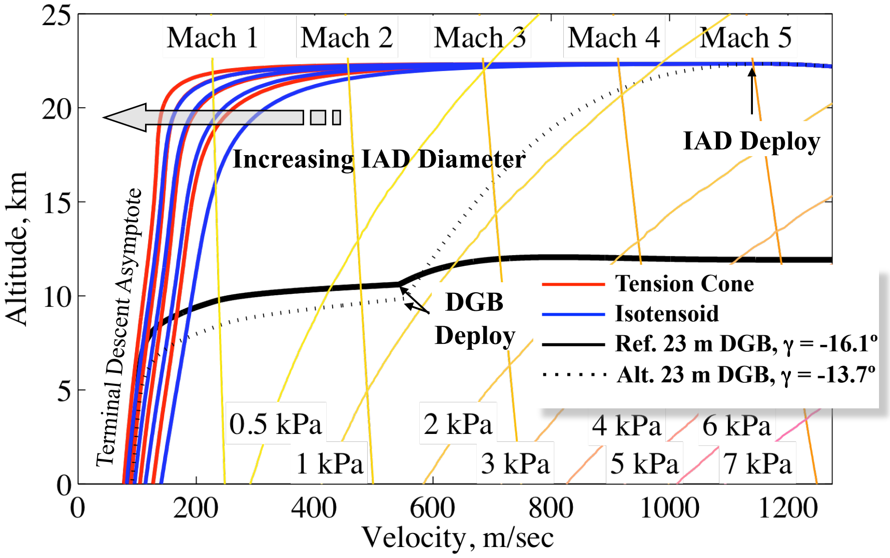

Figure 26: Trajectory comparison for IAD-modified trajectory with repositioned loft peak (γ_{entry} = -13.7°).

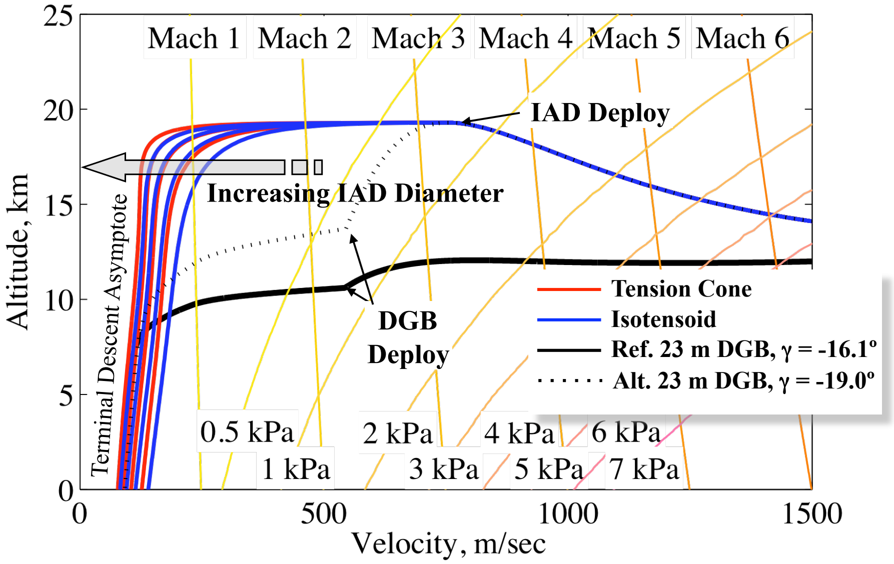

Figure 27: Trajectory comparison for steepened, lift up entry (γ_{entry} = -19°).

2.5.2 IAD and Two-stage System Comparisons

Use of an IAD clearly provides flexibility in terminal descent altitude and timeline; however a more massive IAD is required to achieve the same terminal velocity as a DGB parachute. Coupling a smaller IAD with a subsonic ringsail parachute would simultaneously allow for a lower terminal velocity, a lower IAD mass, and an increase in surface elevation capability. Although adding a second aerodynamic decelerator adds complexity and risk to the EDL sequence of events, the mass savings may serve as a mission enabler. To investigate this trade, a 14 m IAD coupled with a ringsail parachute with diameters between 20 and 29 m is analyzed. Ringsail deployment is assumed to occur at Mach 0.9. The results of this trajectory analysis are shown in Figure 28.

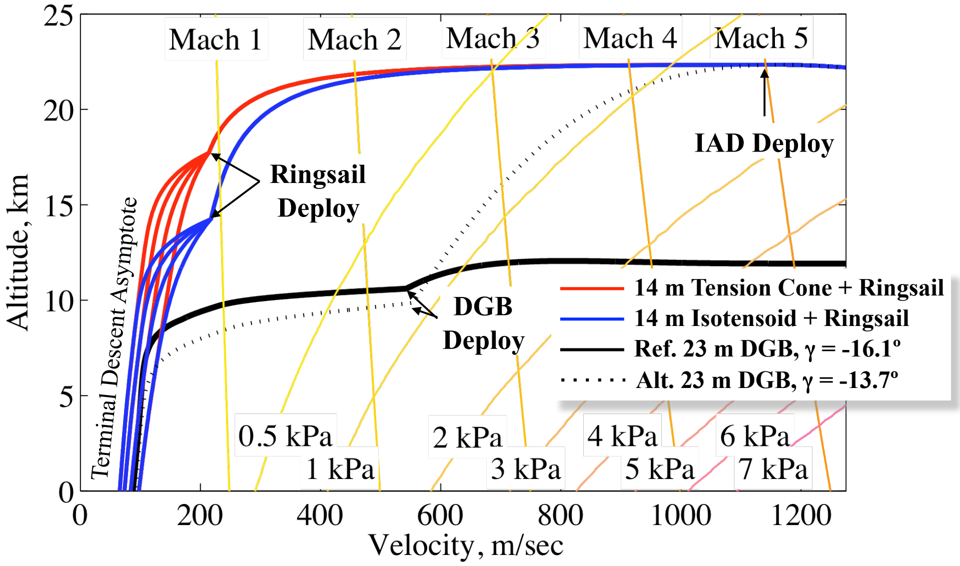

Figure 28: Hybrid trajectory comparison for various ringsail diameters (γ_{entry} = -13.7°).

Figure 28 shows a difference between the tension cone and isotensoid ringsail deployment altitude, which is expected due to the difference in drag coefficient of the two configurations. The two IAD trajectories eventually converge to the same terminal velocity given similar ringsail parachutes. With the addition of the subsonic ringsail, transitioning to propulsive descent at altitudes below 10 km does not require the improved drag performance of the tension cone. Lastly, the higher drag coefficient of a ringsail parachute provides for a

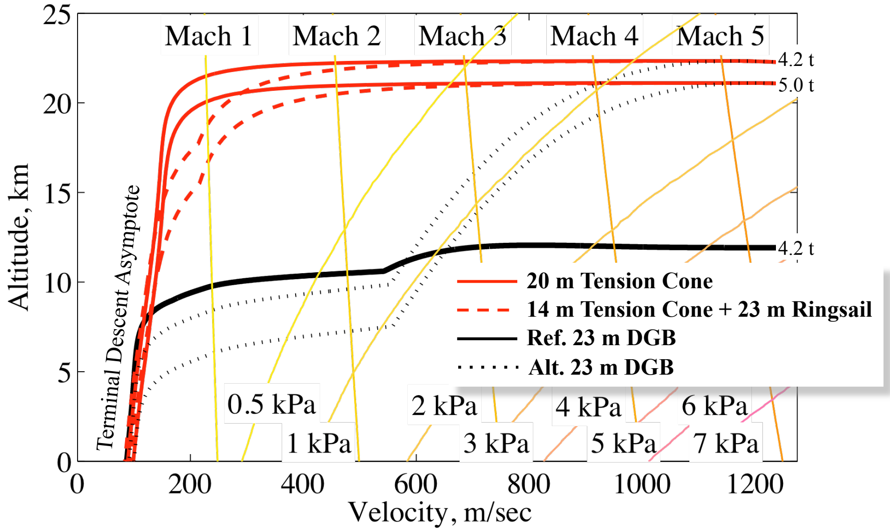

Figure 29: Trajectory comparison for two entry system masses (γ_{entry} = -13.7°).

moderate decrease in terminal velocity versus an equivalent diameter DGB.

2.5.3 Entry Mass Sensitivity

To investigate the sensitivity of the inflatable decelerator and hybrid systems to increasing mass, the tension cone configuration was analyzed for two entry masses: the baseline 4.2 t vehicle and a roughly 20% heavier 5 t vehicle. The 5 t entry mass corresponds to achieving the packing density of the MER vehicles within the larger 4.5 m diameter aeroshell. The results of this trajectory analysis are shown in Figure 29.

Figure 29 shows that an increase in mass acts to lower the altitude of the loft maneuver by about 2 km and thus lower the altitude of all subsequent EDL events. Although a decrease in altitude is undesirable, it illustrates that the tension cone is robust to entry system mass growth and still provides a significant altitude benefit versus the lower mass baseline DGB system. In addition, Figure 30 demonstrates that the two-stage 14 m tension cone IAD and ringsail system can deliver at least 20% more mass to approximately the same terminal velocity as the 23 m DGB reference mission. Figure 30 shows that both the tension cone and two-stage systems undergo about a 3 km decrease in propulsive staging altitude for a 20% increase in entry mass. However, this decrease in altitude does not endanger the mission for staging velocities above approximately 125 m/s. This staging velocity could be further reduced by baselining a larger diameter IAD or ringsail parachute.

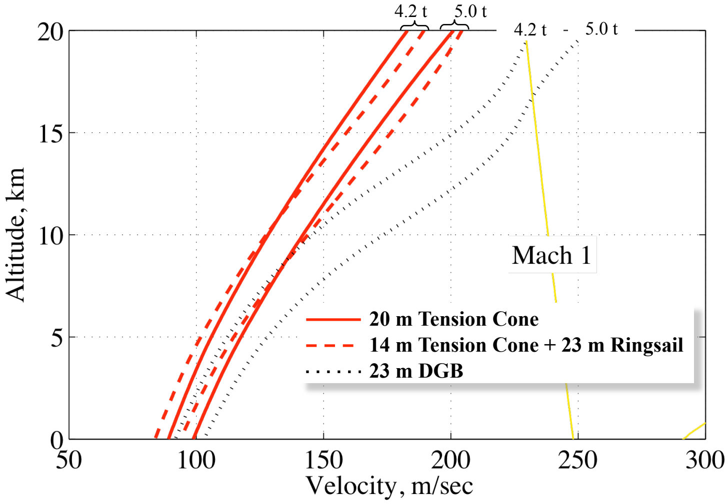

Figure 30: Staging altitudes for varying entry masses.

2.5.4 Mass and Trajectory Summary

A summary of the mass estimates for each decelerator combination is provided in Table 11. Of note, the smaller IADs are shown to be mass-competitive with the baseline 23 m DGB parachute.

Table 11: Mass summary of decelerator systems.

System Configuration	Diameter (m)	Mass (kg)		
		IAD	Parachute	Total
Baseline DGB	23	-	77	77
Tension Cone	14	104	-	68
	17	194	-	129
	20	326	-	220
	23	505	-	347
Isotensoid	14	50	-	58
	17	83	-	86
	20	122	-	121
	23	174	-	164
Tension Cone + Ringsail	14/20	68	41	109
	14/23	68	54	122
	14/26	68	69	137
	14/29	68	86	154
Isotensoid + Ringsail	14/20	58	41	99
	14/23	58	54	112
	14/26	58	69	127
	14/29	58	86	144

Examination of mass estimates alone does not adequately portray the system view. Rather, the mass contributions must be weighed against other benefits that the IAD may provide. In particular, the altitude and timeline discussed in previous sections must also be considered. One approach taken is to consider the velocity and altitude at which the decelerator system is jettisoned for transition to a propulsive terminal descent system. With this approach, a mission designer can effectively ask, “How large of a system do I need to achieve a specific altitude and velocity combination for staging purposes, and what is the mass contribution of that system?” The following outlines the approach and results from this type of analysis.

Each decelerator system is assessed based on two metrics: the delta mass (Δm_{sys}) of the deceleration system (both aerodynamic and propulsive) and the altitude at which propulsive descent was initiated. The delta mass represents the change in decelerator system mass from the baseline that is incurred as a result of moving to an IAD or IAD-parachute two-stage system. This delta includes the mass of the decelerator system and any additional propellant required as a result of staging at a higher velocity. The value of the delta mass is the difference between the combined IAD/ringsail/propellant mass and the baseline DGB mass. For trajectories incorporating an IAD, the altitude of terminal descent initiation was for the -13.7° entry flight path angle.

Five velocity conditions were selected to initiate propulsive descent ranging from 200 m/s to 100 m/s (propulsive descent is initiated at 110 m/s in the DGB reference trajectory). The altitude at which these velocity conditions are achieved will depend on the size of the IAD or parachute. Since mass is a function of size (i.e. diameter), the propulsive staging altitude is directly correlated to the IAD and parachute mass. The propellant mass required to null the remaining vehicle velocity is calculated via the rocket equation

$$m_{prop} = m_i \left[1 - \exp\left(\frac{-\Delta V}{g_0 I_{sp}}\right)\right] \tag{3}$$

where m_i is the initial vehicle mass, m_f is the final vehicle mass, m_{prop} is the propellant mass, ΔV is the required change in velocity, g_0 is the acceleration due to gravity of Earth ($g_0 = 9.81 m/s^2$), and I_{sp} is the specific impulse of the descent rocket engines, assumed to be 205 s based on the Viking terminal descent engines [56]. Note that the above calculation neglects gravity and thrust vectoring losses.

A summary of the delta propellant and delta system masses for each terminal velocity condition is provided in Table 12. From Table 12 it can be seen that nearly all configurations analyzed incurred mass increases over the baseline DGB system. However, the altitude at which propulsive descent can be initiated is significantly higher than the baseline configuration. For example, utilizing a 20 m isotensoid IAD and staging at 175 m/s will incur a 108 kg increase in decelerator system mass but will also yield a 9.2 km increase in staging altitude. Lower staging velocities yield lower system mass increases, though at the expense of a smaller improvement in staging altitude. For example, using the same 20 m isotensoid and staging at 150 m/s provides only a 4 km increase in staging altitude. This is due to the IAD having reached its terminal descent slope. In general, higher altitudes can be achieved by staging at higher velocities. Two-stage systems that include a subsonic ringsail parachute are shown to incur lower mass increases than the single IAD system, though typically with less altitude benefit. The most favorable situation for a two-stage system is shown to be for lower propulsive staging velocities. For example, a 14 m isotensoid coupled with a 29 m ringsail can provide a nearly 6 km altitude increase at a staging velocity of 100 m/s while only incurring a modest 51 kg increase in system mass. It is worth noting that the altitudes shown correspond to an upper limit and in some cases (e.g. to mitigate wind drift) lower altitudes may be preferred.

Table 12: System study metric summary for 4.2 t baseline case.

Staging Vel. (m/s)		200		175		150		125		100	
Δm_{prop}		143		104		65		24		-16	
Config.	**Diam. (m)**	**Staging Alt (km)**	Δm_{sys} **(kg)**	**Staging Alt (km)**	Δm_{sys} **(kg)**	**Staging Alt (km)**	Δm_{sys} **(kg)**	**Staging Alt (km)**	Δm_{sys} **(kg)**	**Staging Alt (km)**	Δm_{sys} **(kg)**
Baseline DGB	23	9.4	-	9.1	-	8.7	-	8.1	-	4.5	-
Tension Cone	14	16.2	134	10.9	95	5.3	55	-	-	-	-
	17	19.8	195	17.8	156	11.1	117	5.2	76	-	-
	20	21.1	286	20.4	247	17.6	208	9.7	167	3.4	127
	23	21.6	413	21.3	374	20.5	335	13.8	294	7.2	254
Isotensoid	14	11.3	124	6.6	85	1.9	45	-	-	-	-
	17	17.4	152	13.1	113	7.6	73	2.5	33	-	-
	20	20.0	187	18.3	148	12.7	108	7.0	68	1.2	28
	23	21.1	230	20.4	191	18.1	151	10.9	111	5.2	71
Tension Cone + Ringsail	14/20	18.5	175	16.4	136	11.5	96	6.3	56	0.6	15
	14/23	20.0	188	19.0	149	16.3	109	10.2	69	4.6	28
	14/26	20.7	203	20.1	164	19.0	124	14.0	84	7.9	44
	14/29	21.1	220	20.7	181	20.1	141	18.1	101	10.7	66
Isotensoid + Ringsail	14/20	18.2	165	16.2	126	11.6	86	6.3	46	0.6	6
	14/23	19.7	178	18.7	139	16.3	100	10.2	59	4.6	19
	14/26	20.4	193	19.8	154	18.8	115	14.1	74	7.9	34
	14/29	20.8	210	20.5	171	19.9	131	18.0	91	10.7	51

Table 12 provides a mission designer with insight into the trades available for using IADs and how they may impact the descent profile. Use of a single IAD system can yield significant altitude increases so long as the vehicle is designed to stage at higher terminal descent velocities. Staging at higher altitudes and velocities is desirable as it affords the ability to mitigate navigation errors through terrain-relative navigation and guidance, allows additional timeline margin for subsequent descent and landing events, and allows for landing at higher surface elevation sites. For the latter, all things being equal, a 1 km increase in staging altitude can be translated to an equivalent increase in the landing site elevation capability.

Although Table 12 clearly shows altitude and trajectory advantages that can be attained from a supersonic IAD, it should also be recognized that an increase in payload mass is also attainable. Because a supersonic IAD is reasonably insensitive to increases in entry mass (Figure 29), the IAD can accommodate an entry mass increase greater than the mass of the IAD itself. For example, an entry mass of 5 t can be decelerated to subsonic velocities at nearly the same altitude as a 4.2 t entry mass. Since the IAD system would constitute significantly less than the 800 kg increase in entry mass, the net effect is an increase in payload mass. With this in mind, the mass analysis performed for the 4.2 t entry case was also performed on a 5 t entry case. However, the previous metric of delta system mass has been replaced with a net increase in payload capability, corresponding to the difference between the increased entry mass and the mass of the IAD and additional propellant. The results from this trade are shown for two staging velocities in Figure 31, while the complete results for five staging velocities are provided in Table 13. It should be mentioned that in this context, increased payload mass does not necessarily represent an equivalent increase in rover mass or instrument mass. Rather, some of the payload increase will likely be consumed by increased structural masses, larger propellant tanks, etc. that result from an increased entry mass.

From Figure 31 it can be seen that payload increases of 700 kg or more are attainable with the use of an IAD system. For example, a hybrid 14 m tension cone and ringsail parachute system can provide a nearly 700 kg increase in payload mass at a staging altitude of 15 km. The greatest payload increases occur with smaller IADs and IADs coupled with a subsonic parachute. Larger, and more massive, IADs provide smaller increases in payload mass but enable higher staging altitudes. Comparing hybrid systems to single IAD systems shows that the hybrid system can move towards higher staging altitudes with less of an impact to the payload mass increase, though this advantage is lessened with increasing staging velocity.

Use of the nominal DGB parachute for this increased entry mass would require deployment at dynamic pressures of 1.1 kPa at Mach 2.3, a 33% increase in dynamic pressure beyond that planned for MSL. Although it may theoretically be possible to develop a parachute that would work for these increased masses, doing so would likely require a costly qualification program, similar to the Balloon Launch Decelerator Test Program undertaken for the Viking missions. Given the marginal increase in payload mass that such a program would ultimately afford, it may be more prudent to spend those resources qualifying a supersonic IAD, a technology that would enable a greater range of entry masses for future Mars systems.

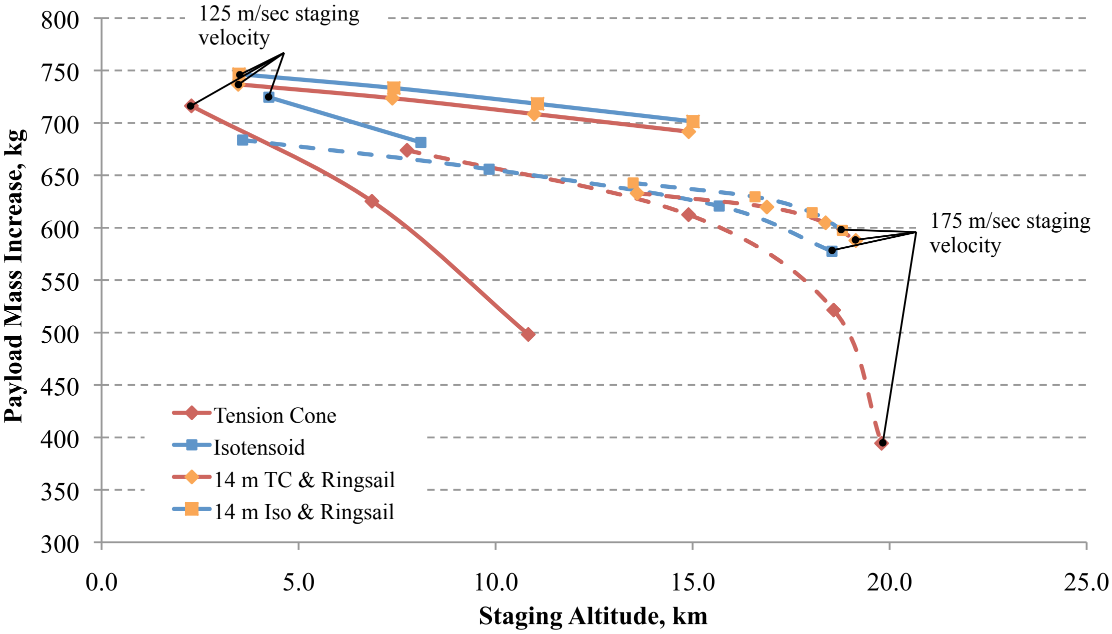

Figure 31: Payload increase for a range of staging altitudes and IAD configurations. Solid lines correspond to a 125 m/sec staging velocity while dashed lines correspond to a 175 m/sec staging velocity.

Table 13: Payload increases possible for a 5 t entry mass using various IAD configurations.

Staging Vel. (m/s)		200		175		150		125		100	
Δm_{prop}		186		136		84		32		-21	
Config.	**Diameter (m)**	**Staging Alt (km)**	Δm_{pl} **(kg)**	**Staging Alt (km)**	Δm_{pl} **(kg)**	**Staging Alt (km)**	Δm_{pl} **(kg)**	**Staging Alt (km)**	Δm_{pl} **(kg)**	**Staging Alt (km)**	Δm_{pl} **(kg)**
Tension Cone	14	13.3	623	7.8	674	2.3	725	-	-	-	-
	17	17.9	562	14.9	612	8.1	664	2.3	716	-	-
	20	19.5	471	18.6	521	13.8	573	6.9	625	0.4	678
	23	20.2	343	19.8	394	18.6	446	10.8	498	4.4	551
Isotensoid	14	8.2	633	3.6	684	-	-	-	-	-	-
	17	14.7	605	9.8	656	4.7	707	-	-	-	-
	20	18.1	570	15.7	621	9.6	672	4.2	725	-	-
	23	19.5	527	18.5	578	14.8	629	8.1	681	2.3	734
Tension Cone + Ringsail	14/20	16.4	582	13.6	633	8.5	685	3.5	737	-	-
	14/23	18.2	569	16.9	620	13.3	671	7.4	724	1.7	776
	14/26	19.1	554	18.4	605	16.8	656	11.0	709	5.1	761
	14/29	19.6	537	19.1	588	18.3	639	14.9	692	8.0	745
Isotensoid + Ringsail	14/20	16.1	592	13.5	643	8.6	694	3.5	747	-	-
	14/23	17.8	579	16.6	629	13.3	681	7.4	733	1.7	786
	14/26	18.7	563	18.0	614	16.6	666	11.1	718	5.1	771
	14/29	19.2	547	18.8	598	18.0	649	15.0	701	8.0	754

2.6 Summary

The objective of this system study was to demonstrate how the use of inflatable aerodynamic decelerators can provide a technology path to enable higher altitude and higher mass landing on the surface of Mars. Both a tension cone and isotensoid IAD configuration were investigated. Trajectories using IADs and IAD-parachute two-stage systems were compared to a nominal trajectory utilizing a traditional DGB parachute. Results from this performance analysis demonstrated the IADs ability to dramatically increase the altitudes at which the entry vehicle transitions to subsonic velocities. Additional improvement was possible when the reference entry flight path angle or entry bank angle profile was adjusted to allow for IAD deployment at higher Mach numbers and altitudes. Structural analyses, material properties, and historical regressions were used to generate first-order mass estimates for the decelerator systems so as to provide a complete representation of each system. These preliminary mass estimates showed the isotensoid configuration to be a lower mass solution, though potential exists to improve the mass performance of the tension cone. A large contributor to the mass of a tension cone system is the inflation system required for deployment, which in turn is largely sized based on the dynamic pressure at which the device inflates. Deployments at lower dynamic pressures were seen to favor the tension cone over the isotensoid.

Each of the decelerator systems were assessed based on two metrics: the mass of the IAD EDL system architecture relative to the reference DGB EDL system architecture and the altitude at which propulsive descent can be initiated for each system. Systems that incorporated only a single IAD were favorable at higher terminal propulsion staging velocities while systems that incorporated a two-stage IAD-parachute system were favorable at lower staging velocities. Because of their significant insensitivity to increased entry masses, IADs can also increase payload mass considerably. Increasing the entry mass by 800 kg above the 4.2 t DGB EDL architecture provided an increase in IAD payload mass of approximately 700 kg, particularly when coupled with use of a smaller IAD.

CHAPTER III

WIND TUNNEL TESTING

A key requirement of any decelerator development program is that the configuration be extensively tested at relevant conditions. Towards this end, a collaborative effort between NASA Langley Research Center (LaRC), the Georgia Institute of Technology, and ILC Dover Inc. was initiated. This effort was funded through the NASA Program to Advance Inflatable Decelerators for Atmospheric Entry (PAIDAE), a part of the Fundamental Aeronautics Program. The focus of the effort was a series of wind tunnel tests to explore the aerodynamic and structural performance of a specific tension cone configuration. The tests were divided into two separate sets, one that tested rigid models and one that tested flexible tension cone models. Data acquired from these tests will be used to validate computational methods for predicting IAD aerodynamic and structural performance.

Presented in this chapter is a review of the tension cone wind tunnel test program performed as part of this investigation and the results from that program. This section includes an overview of how the tested configuration was developed, the types of models tested, the conditions at which the tests were conducted, and the results from those tests. The test summaries and data are organized by test location, which corresponds to the types of models used. In particular, testing of the rigid tension cone models was conducted at the Langley Unitary Plan Wind Tunnel (LUPWT) while testing of the flexible articles was conducted at the Glenn Research Center 10- x 10-Foot Supersonic Wind Tunnel, henceforth referred to as the 10x10. Data tables of the static force and moment data and the surface pressure data presented in this chapter are provided in the Appendices.

3.1 Configuration Development

Development of the tension cone shape and configuration was achieved through careful consideration of prior tension shell wind tunnel tests as well as a thorough investigation of the tension shell shape trade space. A summary of basic tension shell theory and the results of a tension shell shape trade study are provided in the Appendices. This section presents a review of the iterative computation procedure used to arrive at the final tension cone shape definition.

3.1.1 Shape Definition

The final choice of tension cone dimensions and shape parameters was driven by several factors including the results of a trade space study, blockage concerns of the 10x10 test section, the loading limits of available wind tunnel balances, and the ease of manufacturing tori capable of withstanding the anticipated inflation pressures. The final shape parameters are provided in Table 14.

Table 14: Final shape parameters for wind tunnel model definition.

Quantity	**Value**
Area Ratio	10
r_{ts}/r_t	7
Attachment Angle, θ_{tc}	60°

The shape parameters define the relative size of the tension shell and torus but the curvature of the tension shell still requires a valid pressure distribution. The final curvature of the tension shell was arrived at through an iterative procedure that refined the tension shell shape through successive calculations of the surface pressure distribution. The initial tension shell was calculated assuming a Newtonian pressure distribution and then iterated on using inviscid computational fluid dynamics. For this task a Cartesian grid based solver, NASCART-GT, was used to generate 1st order, axisymmetric solutions of the pressures on the tension shell. The first iteration consisted of using the initial, Newtonian pressure derived tension shell geometry to calculate an inviscid pressure distribution, which in turn was used to generate a new tension shell shape. Subsequent iterations used the results of the prior iteration to generate a new pressure distribution and then a new tension shell. The results of these iterations are shown in Figure 32. It can be seen that although the Newtonian pressure distribution differs considerably from an inviscid aerodynamics pressure distribution, the resulting tension shell shapes do not differ significantly. Iterations on the 1st shape derived from inviscid pressure distributions produced maximum shape variations of less than 1% in the axial direction. Thus, only 3 total iterations were needed to converge on the final tension cone shape. Pressure contours for the final tension shell are shown in Figure 33 below. It should be noted that only the windward portion of the configuration shown in Figure 33 was considered relevant. Since the tension shell shape is dominated by the surface pressure distribution, zero aftbody pressure was assumed during shape generation, as was done in [68]. For computation, the aftbody was simplified by thickening the tension shell so as to expedite generation of the computational geometry and reduce the time required to produce a converged CFD solution. As a check of the suitability of using an inviscid approach to determine the tension shell curvature, a viscous solution of the Newtonian derived shape was computed using the Navier-Stokes aerothermodynamics code LAURA. Though this solution produced a slightly different pressure distribution, the derived tension shell differed from the final inviscid tension shell by less than 0.5% in the axial direction.

The above iterative process was used to determine the shape of the tension cone. However, the scale was determined by other considerations. In the case of the 10x10 models, the dimensions were limited by test section blockage and by the ease of manufacturing a textile pressurized torus. Larger models would produce more drag and require higher pressures inside the torus. Though test section blockage for the 10x10 seemed to indicate the possibility of using models up to 1 m in diameter, ease of manufacturing dictated the model be scaled to 60 cm in diameter. The diameter of the Unitary model was established based on a recent history of testing blunt body models in that facility. The final dimensions for the wind tunnel models are provided in Appendix C .

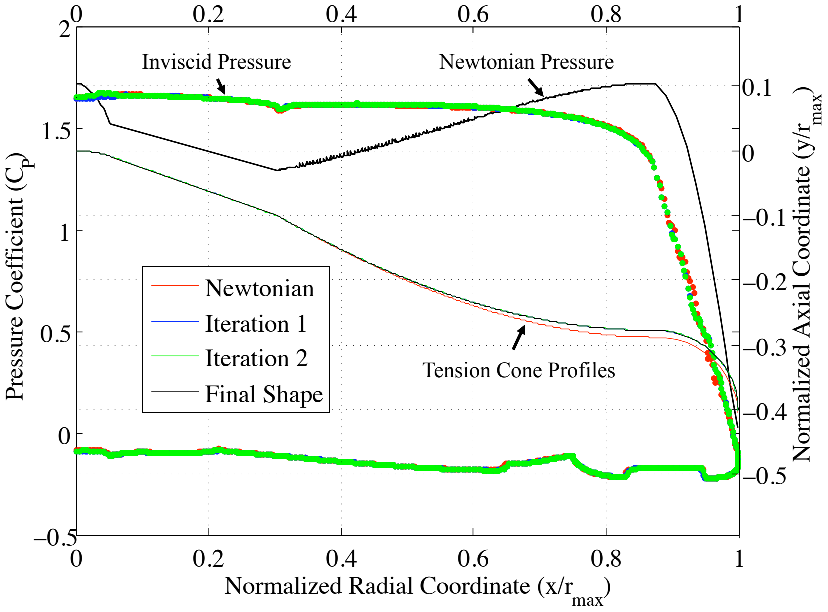

Figure 32: Pressure distributions used for development of the tension cone test configuration and the resulting tension cone profiles.

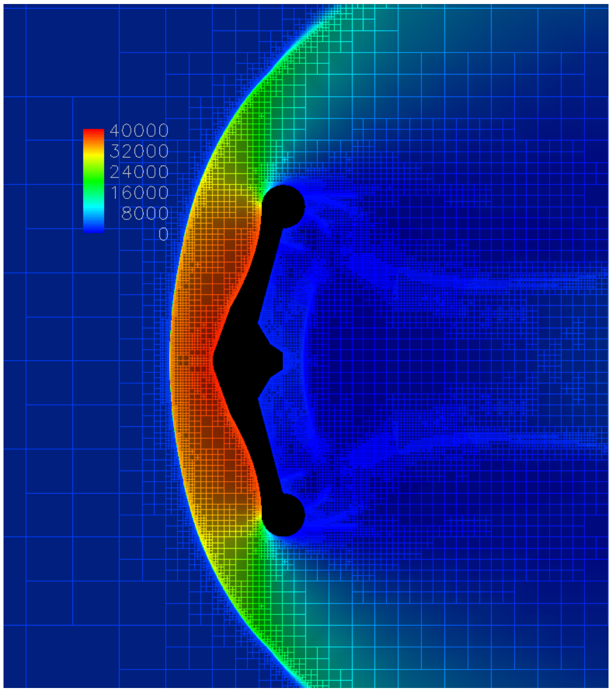

Figure 33: Pressure contours, in units of Pa, and computation grid of the final inviscid NASCART-GT CFD solution used for tension shell curvature definition.

3.2 Unitary Tunnel Testing

Testing conducted at the LUPWT was similar to prior tests of tension cone models in that it focused on rigid model aerodynamics. The goal of this set of wind tunnel tests was to acquire data useful for the characterization of a tension cone at relevant Mach numbers. The data gathered was used to validate the computational aerodynamic analyses presented in Chapter 4. The goals of the test were met by accomplishing five objectives:

1. Determine the static aerodynamic characteristics (e.g. lift, drag, pitching moment) of the tension cone.
2. Determine the shape and position of shock waves surrounding the tension cone.
3. Determine the stability of the flow around the tension cone.
4. Determine the pressure distribution along the surface of the tension cone.
5. Determine the relationship between the shape and position of shock waves surrounding the tension cone and the surface pressure distribution.

3.2.1 Model Description

The LUPWT portion of the test program entailed testing two different models, a force and moment model and a pressure model. The force and moment model was integrated with a six-component wind tunnel balance and used to attain static aerodynamic characteristics including force and moment coefficients. A profile of the model assembly is shown in Figure 34. Note that the outer mold line directly behind the tension cone represents the balance windshield. A balance windshield is commonly used in wind tunnel testing to prevent the balance from measuring loads other than those directly on the model. Dimensionally, the force and moment and pressure models were identical and were 6-inches in diameter, corresponding to a 1.07% scale model of a tension cone IAD attached to a 4.5 m diameter aeroshell. The complete model assembly outer mold lines of the two model types, including sting and windshield, were kept as similar as possible with the exception that for the pressure model a different sting was required and the wind shield was slightly ($\sim$ 0.14 in) further aft. The pressure model contained 82 pressure ports, arranged in three spokes of 27 ports plus one port at the nose. Included among the 27 ports were 4 ports on the backside of

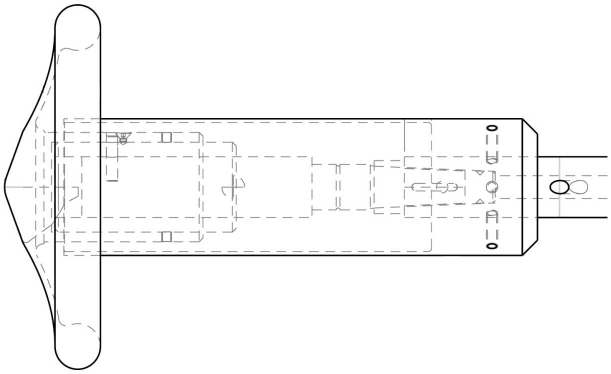

Figure 34: Wind tunnel model assembly of the force and moment model.

the pressure model, two on the torus and two on the backside of the tension shell. The radial distribution of the ports, shown in Figure 35, was derived based upon the predicted pressure distribution. The three spokes, shown in Figure 36, were located at 0°, 90°, and

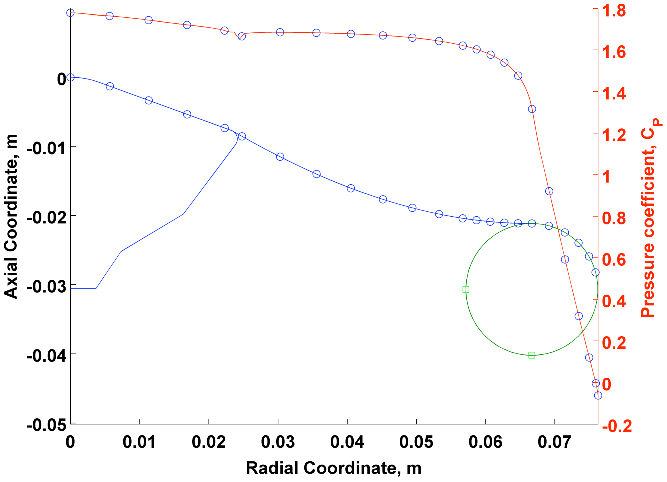

Figure 35: Radial distribution of pressure ports along the surface of the tension cone model. Note: two pressure ports, not shown, are located on the back side of the tension shell.

225° positions. Because the model can be rolled 180°, these three spokes effectively allowed for pressure readings at locations 45° apart.

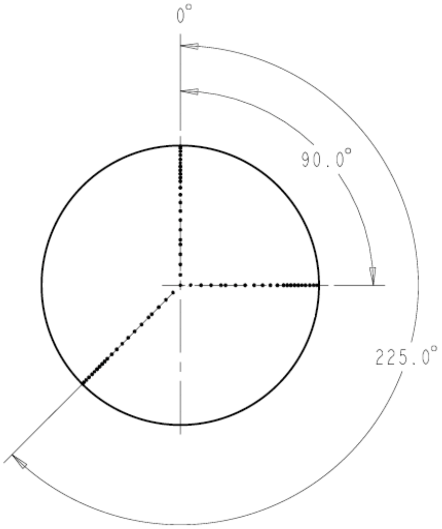

Figure 36: Location of the three pressure port spokes on the tension cone model (front view).

3.2.2 Test Procedure

Rigid model testing was conducted at the Langley Unitary Plan Wind Tunnel, located at NASA's Langley Research Center. The LUPWT includes two test sections, each 4- x 4-feet in size. Test section 1 is used for lower Mach number testing between 1.46 and 2.86. Test section 2 is capable of Mach numbers from 2.30 to 4.63 [37]. Figure 37 shows the model installed in the test section.

Figure 37: Tension cone model assembly within the LUPWT test section (shown with author).

Instrumentation common to both force and moment and pressure testing included schlieren video (at 24 fps) and still photography (at 16 megapixels) as well as three pressure transducers required to measure the windshield cavity pressures. Force and moment testing was conducted using Langley balance 2008, a six-component strain gauge balance. The pressure model required use of an additional 82 pressure transducers. The transducers consisted of a mix of 5 psi and 15 psi ESP modules. The 5 psi modules were used for the aftbody pressure ports and the pressure ports located at the maximum radius of the model. All other ports utilized 15 psi ESP modules.

For the force and moment model, data acquisition was performed at a sampling rate of 30 Hz over a duration of 2 seconds. Recorded values were an average of the 60 sampled values. The same sampling rate was used for the pressure model and averaging was extended to 30 seconds to data. Settling times of 10 seconds for the force and moment testing and

30 seconds for the pressure testing were used between each data point.

Data were attained at 8 different combinations of Mach and Reynolds number. These conditions are reported in Table 15. All but two conditions targeted a model Reynolds number of 1.0 x 10^6. The other two runs were performed at Reynolds numbers designed to match conditions of the 10x10 testing for comparison purposes. During testing of the pressure model a reduced set of angles of attack and sideslip were used due to the longer settling times required. The angle of attack and sideslip sequences are reported in Table 16. Angle of attack sweeps were conducted at a sideslip angle of 0° and vice versa. Measurements taken during sideslip sweeps were used for assessing the quality of the data. Tests conducted at Mach 1.65 were limited to a minimum angle of attack of -6° because of concerns with reflected shocks impinging on the model. Tests using the pressure model were conducted twice, once each at roll angles of 0° and 180° to allow for pressure readings in increments of 45°. It should be noted that the values provided in Tables 15 and 16 are nominal test conditions and do not account for variations in flow conditions or changes in angle of attack due to sting deflection and flow angularity. For the latter case, these variations were generally of less than a degree.

Table 15: Test matrix used for rigid tension cone model testing.

Mach Number	**Reynolds Num. (model)**	**Dynamic Press., psf**	**Total Press., psf**	**Static Press., psf**	**Total Temp., °F (R)**	**Static Temp., °F (R)**
1.65	1.00 x 10^6	456	1094	239	125 (585)	-81 (379)
2.00	1.00 x 10^6	449	1253	160	125 (585)	-135 (325)
2.00	6.91 x 10^5	311	861	111	125 (585)	-135 (325)
2.50	5.46 x 10^5	223	872	51.0	125 (585)	-200 (260)
2.50	1.00 x 10^6	410	1600	93.6	125 (585)	-200 (260)
3.00	1.00 x 10^6	357	2083	56.7	125 (585)	-251 (209)
3.50	1.00 x 10^6	304	2703	35.4	125 (585)	-290 (170)
4.50	1.00 x 10^6	229	4666	16.1	150 (610)	-339 (121)

Table 16: Angle of attack and angle of sideslip sequences used during testing.

Model	**Sting Angle of Attack, deg.**	**Sting Angle of Sideslip, deg.**
Force and Moment	0,1,2,3,4,5,6,7,8,9,10,11,12,13,14,15,16,17,18,19,20,16,12,8,4,0,-1,-2,-3,-4,-5,-6,-7,-8,-9,-10,-11,-12,-9,-6,-3,0	0,1,2,3,4,5,6,7,8,6,4,2,0,-1,-2,-3,-4,-5,-6,-7,-8,-6,-4,-2,0
Pressure	0,1,2,4,8,12,16,20,16,8,4,0,-1,-2,-4,-8,-12,-8,-4,0	0,4,8,4,0,-4,-8,-4,0

3.2.3 Data Reduction and Uncertainty Analysis

During data reduction, force and moment coefficients were calculated using a reference area calculated from the model total diameter. Pitching moment coefficients were calculated about the nose of the model using the total diameter as the reference length. Although this would not be the location of the actual center of mass, it nonetheless provides for easy translation of the data to an actual center of mass location.

A considerable effort was made to determine the test conditions at each data point as accurately as possible. Since the LUPWT utilizes an asymmetric nozzle, there is a measurable degree of non-uniformity of the flow across the test section. Reference [37] provides contours of flow angularity and Mach number variation across the test section at a variety of test conditions. From these contours estimates of the flow angularity and Mach number variation were calculated for each angle of attack using the position of the nose of the model in the test section. Further adjustments to the reported angle of attack were made to account for the deflection of the sting under aerodynamic loading. Calculation of the freestream dynamic pressure for each test condition was performed using the reported total pressure and corrected Mach number.

The application of the flow angularity and sting deflection corrections resulted in angle of attack sequences that differed for each of the Mach number test conditions. To facilitate comparison between Mach numbers and for data reporting purposes, force and moment data was further reduced to discrete values of angle of attack in one degree increments (e.g. 0°, 1°, 2°, etc.). This was achieved by fitting a smoothing spline to the C_A, C_N, and C_m data sets and reporting the spline values at each discrete angle of attack. Prior to fitting, the C_N and C_m data was offset so as to produce a value of zero at a 0° angle of attack, as would be expected from an axisymmetric model in a uniform flow. The offset value was determined by performing a linear fit of the data between angles of attack of -1.5° and 1.5°. A delta equal to the intercept of the linear fit was then applied to each data point, thus removing an element of bias in the data.

A base pressure correction was applied to the measured axial forces to produce a second value of axial force coefficient, $C_{A_{adj}}$. Visible in Figure 34 is that a small gap was present between the rear tension cone surface and the balance wind shield. As a result, the total axial force measured included a small portion that was due to pressures internal to the balance wind shield. To simplify subsequent computational analyses it was desired to reduce the measured portion of the model to only the forebody and the portion of the aftbody external to the wind shield. The force acting on the model internal to the windshield was calculated by averaging the aftbody pressures measured during testing of the pressure model and multiplying by the base area of the wind shield. The resulting force was added to the measured value of axial force and subsequently reduced to coefficient form. Based on preliminary calculations, a similar adjustment to the normal force and pitching moment coefficients was deemed unnecessary. Axial force data presented in this chapter is predominantly C_A data which is derived from the axial force measured by the balance while axial force data presented in Chapter 4 is predominantly $C_{A_{adj}}$ data.

An assessment of the total experimental uncertainty were based on combined estimates of the precision uncertainty and the bias uncertainty. The precision uncertainty constitutes random uncertainty in the measurements due to, for example, the accuracy of the measurement device or an inability to replicate test conditions exactly. Estimates of the precision uncertainty for the pressure data were made by examining the standard deviation of repeated measurements at similar test conditions. Estimates were developed for both the 15 psi and 5 psi modules at each combination of Mach number and Reynolds number. The precision uncertainty of the force and moment data was estimated by examining the standard deviation of the residuals of the smoothing splines.

The bias uncertainty constitutes systematic (non-random) error. Estimates of the bias uncertainty were through a Monte Carlo analysis that was performed to asses the impact of test condition and instrument uncertainty on the reported force, moment, and pressure coefficient values. The input parameters and distributions assumed are shown in Table 17. The Mach number uncertainty was estimated from data in Reference [37]. The total pressure uncertainty was estimated by comparing two separate measurements of total pressure reported by the facility. Pressure port uncertainty is based on the accuracy stated by the ESP manufacturer. Force and moment uncertainties were estimated from calibration data for the balance.

Both the precision and bias uncertainties were estimated at the 95% confidence level. Thus, the total uncertainty at a 95% confidence level is simply the root sum of squares of the bias and precision uncertainties. It is important to note that the uncertainties calculated are best estimates developed from available calibration data and test results and do not in fact represent known distributions. Furthermore, the confidence intervals refer to an individual observation and not, for example, the mean of a set of observations.

Table 17: Distributions used to estimate bias uncertainty for the LUPWT test series.

Parameter	**Std. Deviation**	**Distribution**
Mach Number		
Mach 1.65 – 2.0	$\frac{0.015}{\sqrt{3}}$	uniform
Mach 2.5 – 4.5	$\frac{0.010}{\sqrt{3}}$	uniform
Total Pressure, P_0	$\frac{0.10\%}{\sqrt{3}}$ of measured value	uniform
Port Pressure	$\frac{0.05\%}{\sqrt{3}}$ of full-scale	uniform
Axial Force	0.468 lb	normal
Normal Force	0.021 lb	normal
Pitching Moment	0.0825 in-lb	normal

3.2.4 Force and Moment Results

Provided in Figure 38 are results from the force and moment testing. Data tables of the Unitary force and moment results are provided in Appendix D. At all Mach numbers the axial force coefficient is nearly constant across the full 20° range of angle of attack. Variations of C_A with angle of attack are within 5% of their 0° AoA value. A small oscillation in axial force versus angle of attack is observable at the lowest Mach numbers. Normal force coefficients are also observed to behave nearly linearly as angle of attack is increased. Furthermore, the normal force coefficient can be seen to be almost completely independent of Mach number and exhibits a slope of approximately 0.00266 deg^{-1}. Pitching moment (Figure 38) was also observed to vary linearly with angle of attack and increased marginally with increasing Mach number. Pitching moment slope C_{m_α} about the nose of the model is approximately -0.00212 deg^{-1}. Referencing the pitching moment at the shoulder of the sphere cone forebody, a more probable location for the center of mass of a flight vehicle, produced a 0.2% increase (more positive) in C_{m_α} and static stability is maintained at all angles of attack. The center of pressure, shown in Figure 39, was calculated as lying aft of the nose at a distance of 80 – 135% of the model diameter, generally increasing with angle of attack and Mach number. An examination of the 0° axial force coefficient versus Mach number (Figure 40) shows reasonably constant performance with the drag peaking around Mach 2.5 before subsequently dropping off slightly at higher Mach numbers.

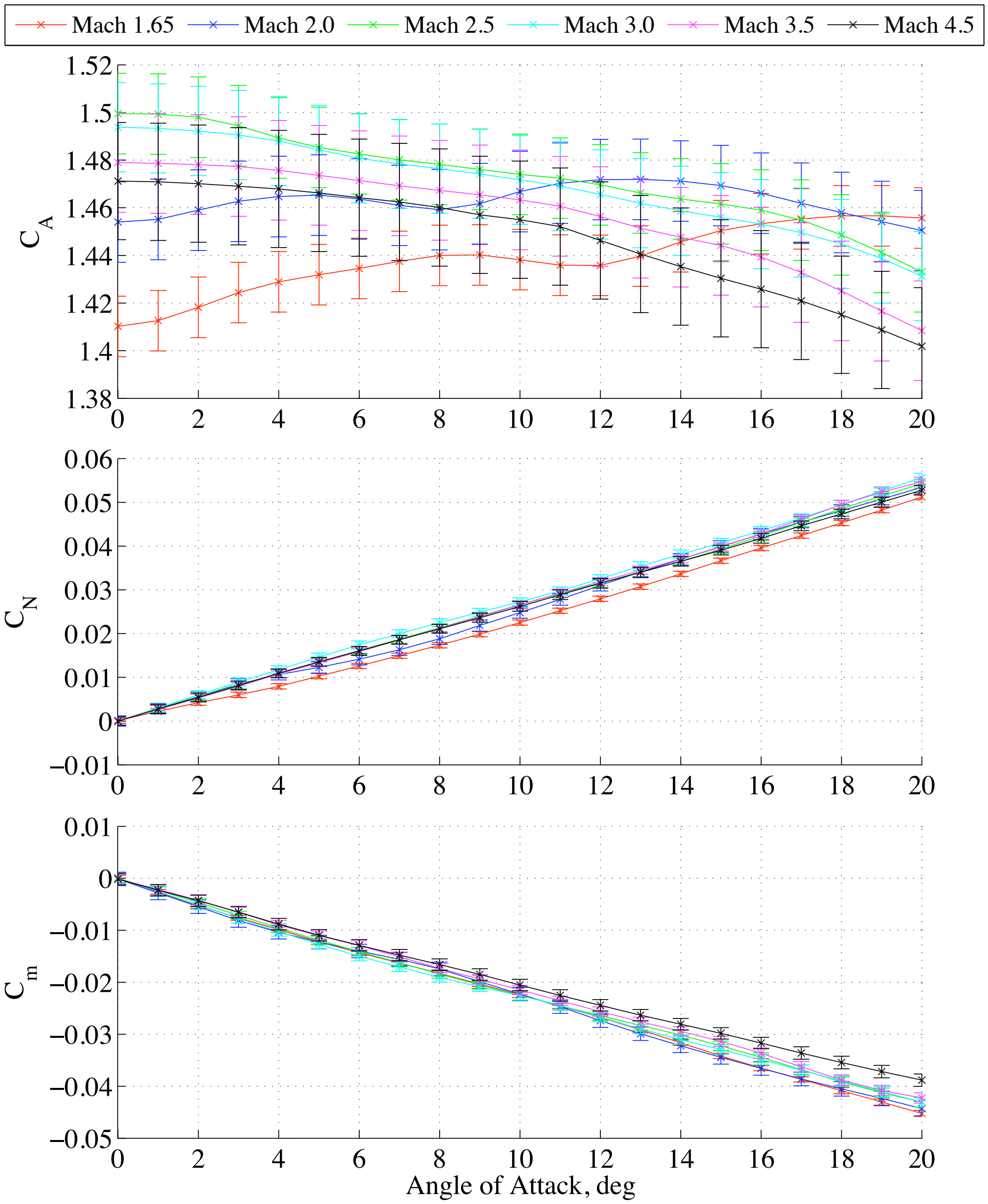

Figure 38: Axial, normal, and pitching moment coefficients measured by the LUPWT force and moment model at a Reynolds number of 1.0 x 10^6. Uncertainty bars correspond to 95% confidence intervals.

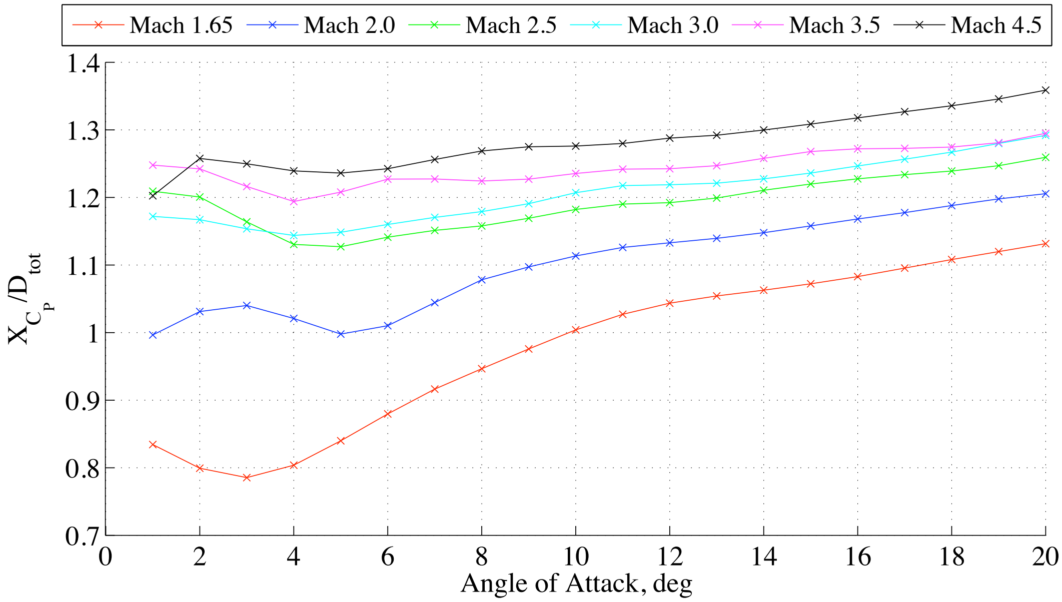

Figure 39: Axial location of the tension cone center of pressure (normalized by the model diamter) versus angle of attack for several Mach numbers.

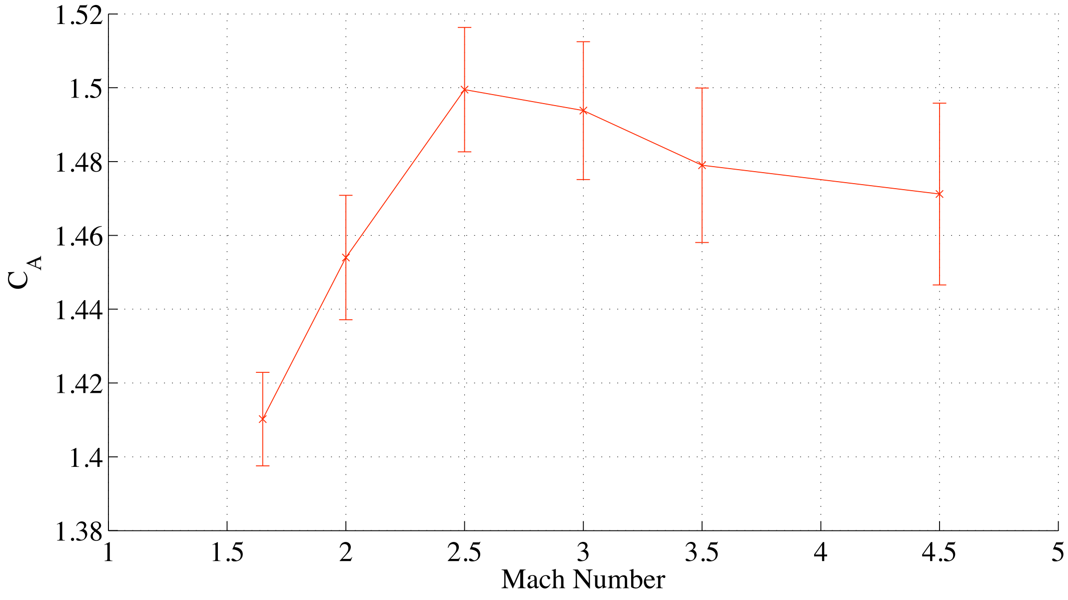

Figure 40: Drag coefficient of the LUPWT force and moment model versus Mach number at a 0° angle of attack and Reynolds number of 1.0 x 10^6.

3.2.5 Pressure Model Results

Provided in Figures 41 – 46 are the results from the pressure model testing. The data are presented such that each plot corresponds to a different spoke on the pressure model. Positive radial locations correspond to where the spokes lie with the model at a 0° roll angle. Data tables of the Unitary pressure model results are provided in Appendix E. Angles of attack shown on the data plots do not include flow angularity corrections, which are generally less than a degree. The corrected angles of attack are provided in Appendix E.

From the figures shown several observations can be made regarding the surface pressure distributions. Pressure distributions are seen to show the same general trends across all Mach numbers. Examination of pressures on the 0° spoke reveals the progression of the stagnation point across the model at angle of attack. In particular, at $\sim 12°$ angle of attack, the largest surface pressures are located on the windward conical portion of the forebody, while at $\sim 20°$ angle of attack they have progressed to the concave tension shell portion of the geometry. The change in pressure gradient seen in the vicinity of the ±20 mm location is due to the sphere cone portion of the forebody transitioning to the tension shell portion of the geometry. As the angle of attack is increased, this region can be seen to exhibit progressively larger adverse pressure gradients on the leeward side of the model. This effect becomes more pronounced with increasing Mach number and is largest for the Mach 4.5 case (Figure 46(a)). Although this would generally be a concern due to flow separation, it is believed that very little, if any, flow separation occurred for any Mach number. If large flow separation were to occur, it is likely that it would have an impact on the measured pitching moments of the model. However, the pitching moment slopes shown in Figure 38 are consistently linear at all Mach numbers and angles of attack. Schlieren imagery taken during testing, and shown later, did not reveal any leeward side flow separation. However, the free stream density was likely too low for this to be evidential. A physical explanation for the flow remaining attached is provided through use of CFD analysis in Chapter 4.

For a given Mach number, pressures on the aftbody of the model are nearly uniform throughout and little variation is seen with angle of attack. As Mach number increases, both aftbody and forebody pressure coefficients are seen to rise, though at differing rates. The latter result can be used to explain the rise in the 0° angle of attack axial force coefficient around Mach 2.5 – 3.0. In particular, a lag in the aftbody pressure rise as Mach number increases produces greater pressure differentials across the entire surface of the model, and thus greater total drag. This characteristic can be qualitatively seen by averaging the change in pressure coefficient across the forebody and aftbody separately as Mach number is increased, as is shown in Table 18. Between Mach numbers of 1.65 to 2.0 and 2.0 to 2.5, forebody pressures rise more than aftbody pressures, resulting in an increase in total drag. Between Mach 2.5 and 3.0, the two sets of pressures rise at approximately the same amount and the total drag remains mostly constant. As Mach number is increased further, aftbody pressures begin increasing more than forebody pressures and a drop in total drag results.

Table 18: Variation in aftbody and forebody pressure coefficients with increasing Mach number.

	Change in Mach Number				
	1.65 ⇒ 2.0	2.0 ⇒2.5	2.5 ⇒3.0	3.0 ⇒3.5	3.5 ⇒4.5
Forebody Avg. ΔC_P	0.077	0.081	0.055	0.021	0.035
Aftbody Avg. ΔC_P	0.034	0.056	0.065	0.040	0.065

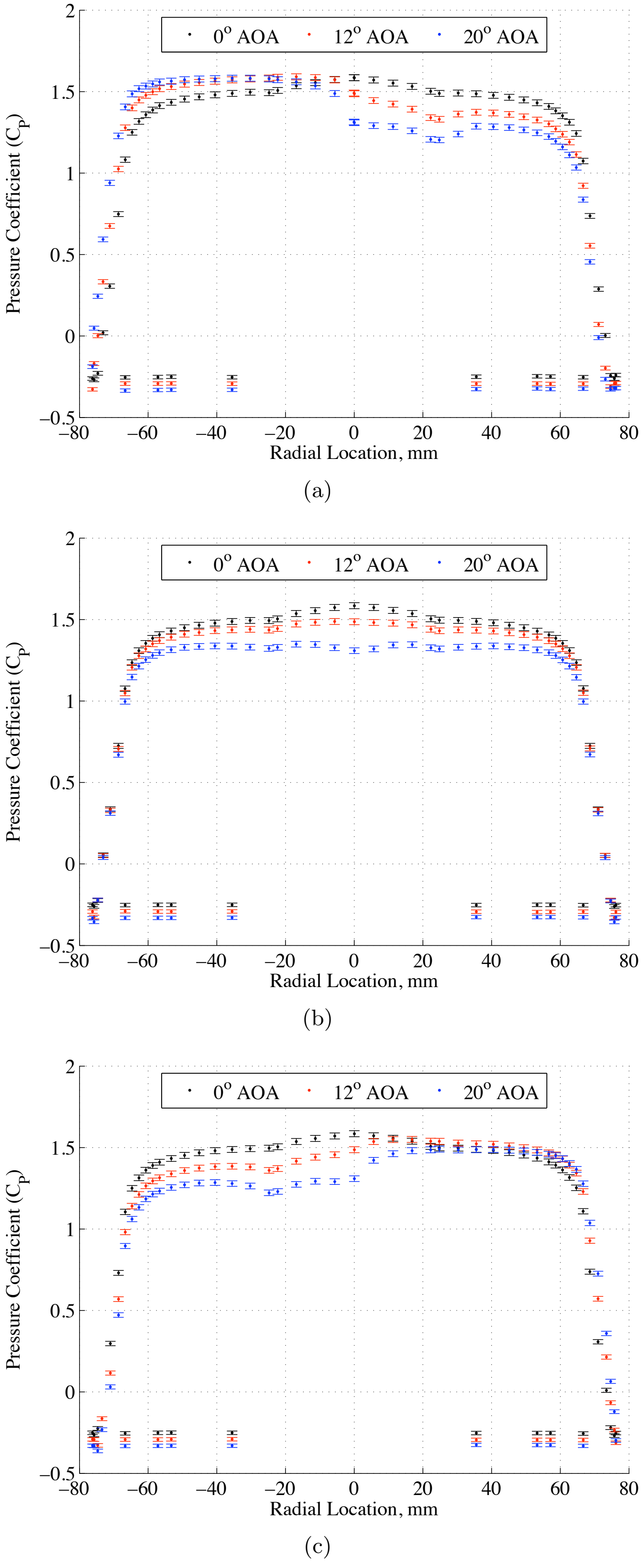

Figure 41: Pressure distributions at Mach 1.65 and a Reynolds number of 1.0 x 10^6 for the (a) 0°, (b) 90°, and (c) 225° spokes.

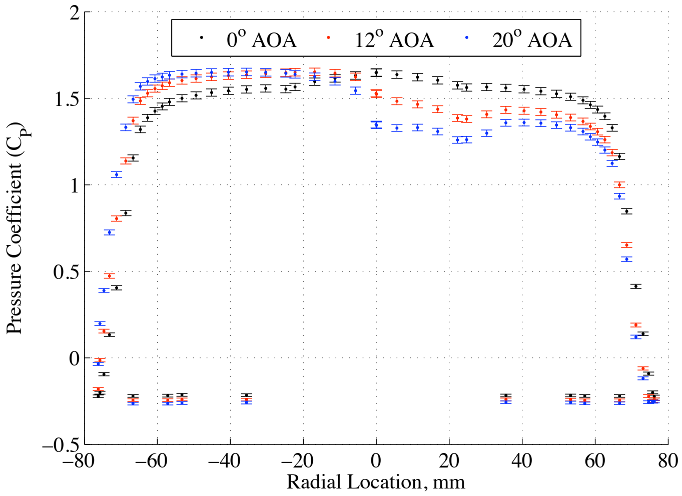

(a)

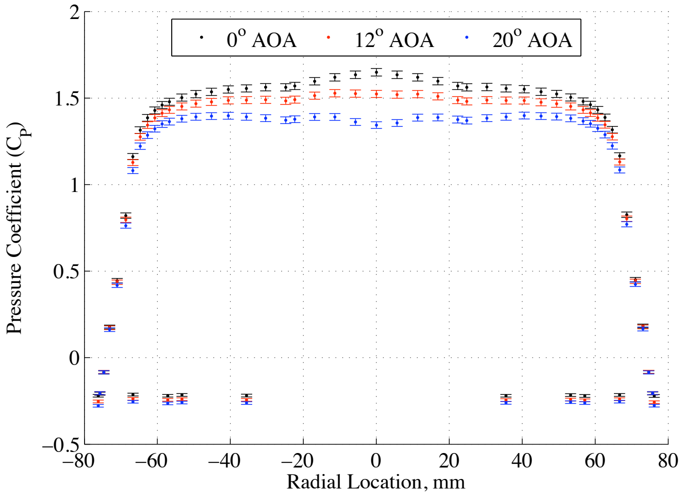

(b)

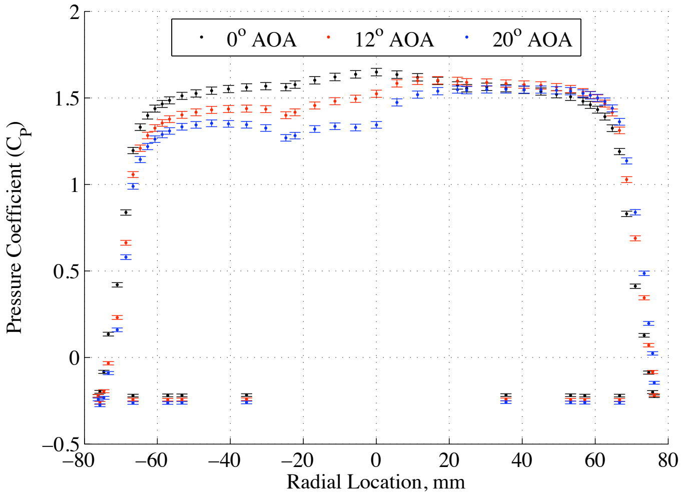

(c)

Figure 42: Pressure distributions at Mach 2.00 and a Reynolds number of 1.0 x 10^6 for the (a) 0°, (b) 90°, and (c) 225° spokes.

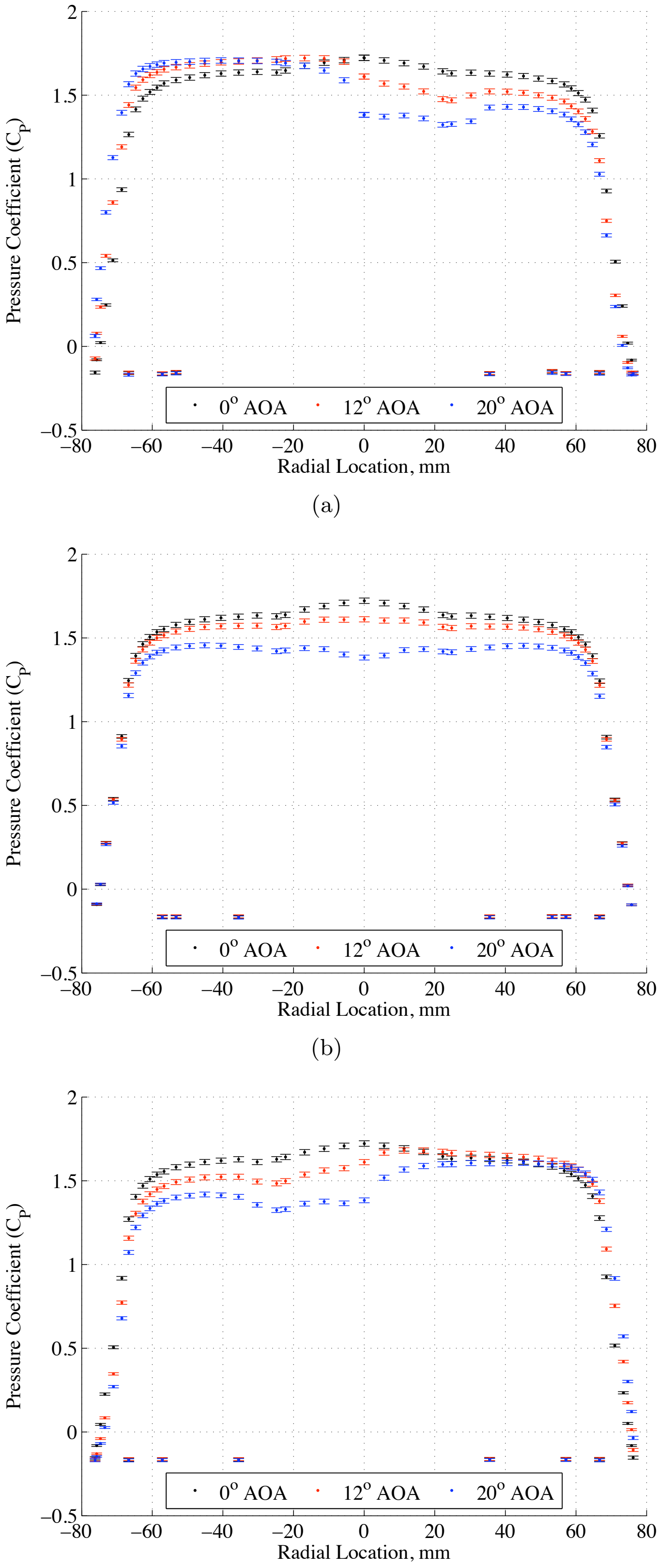

(a)

(b)

(c)

Figure 43: Pressure distributions at Mach 2.50 and a Reynolds number of 1.0 x 10^6 for the (a) 0°, (b) 90°, and (c) 225° spokes.

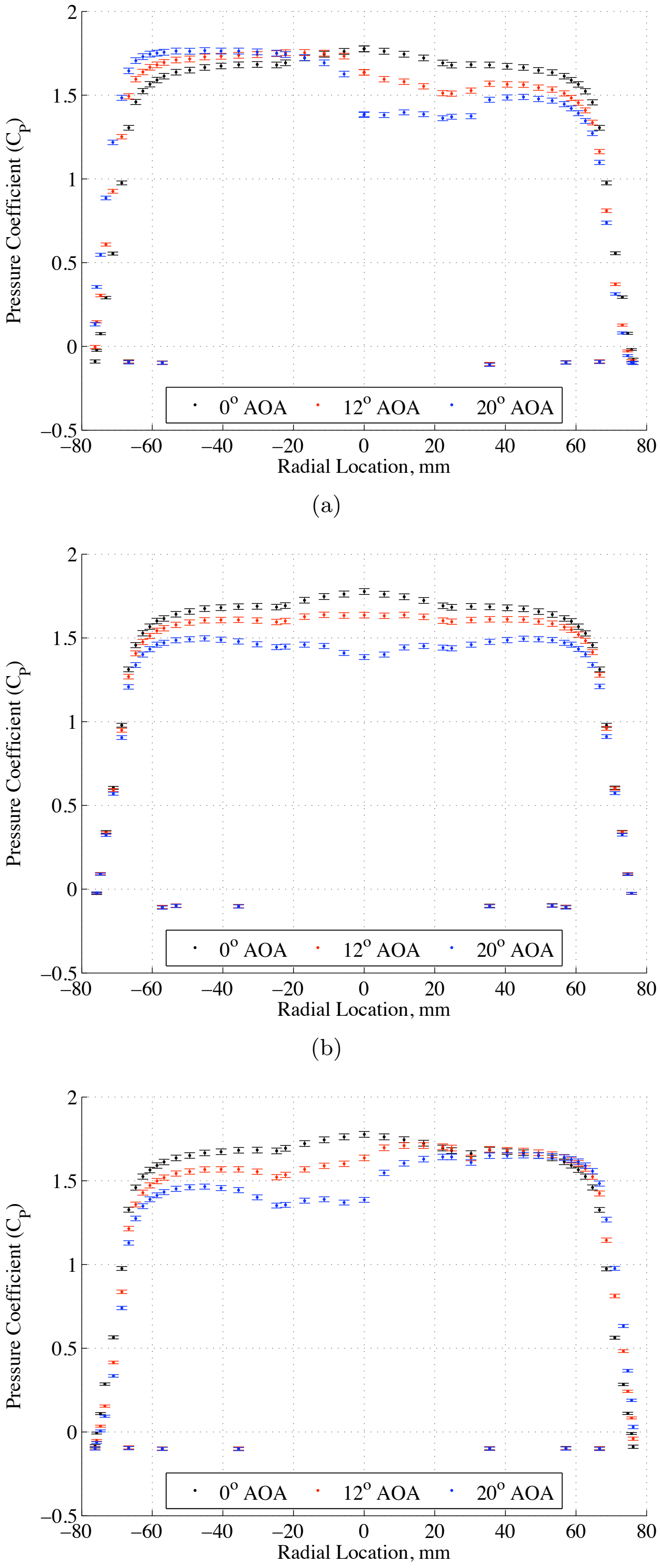

(a)

(b)

(c)

Figure 44: Pressure distributions at Mach 3.00 and a Reynolds number of 1.0 x 10^6 for the (a) 0°, (b) 90°, and (c) 225° spokes.

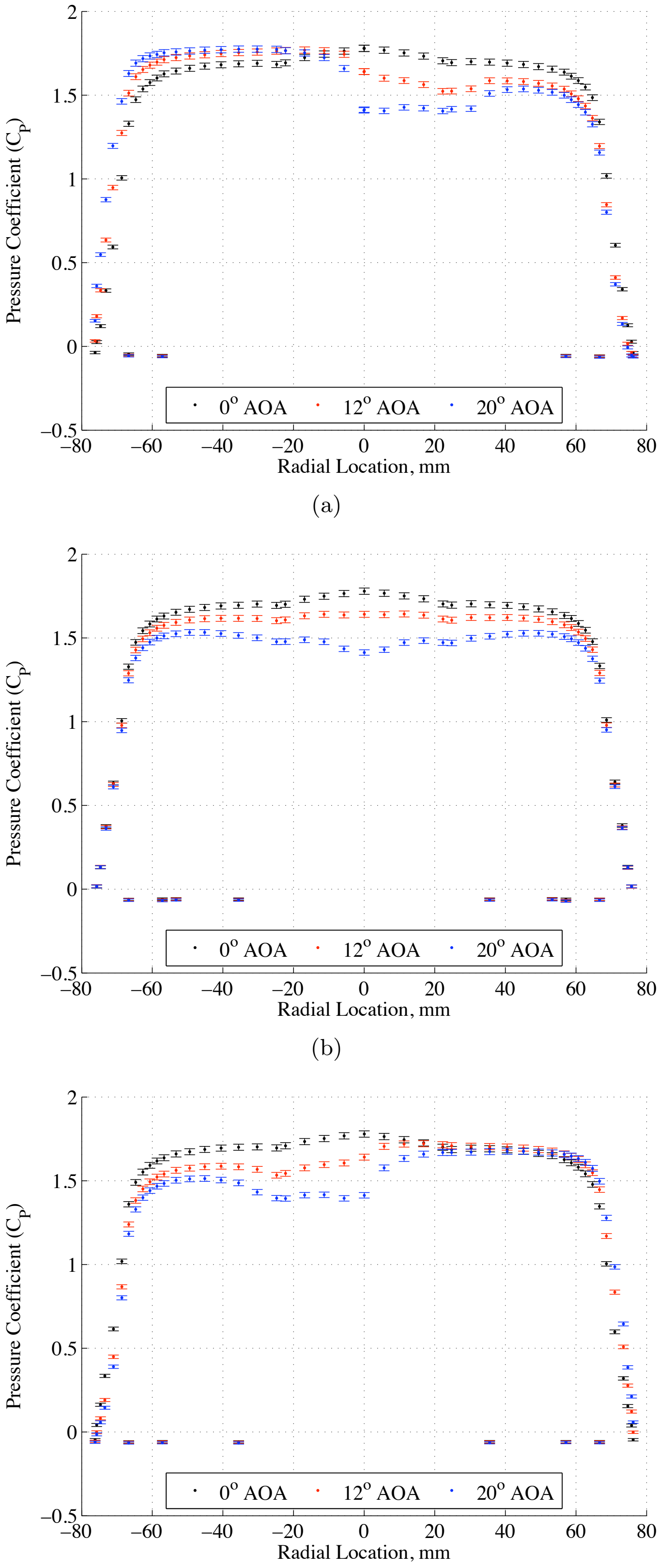

(a)

(b)

(c)

Figure 45: Pressure distributions at Mach 3.50 and a Reynolds number of 1.0 x 10^6 for the (a) 0°, (b) 90°, and (c) 225° spokes.

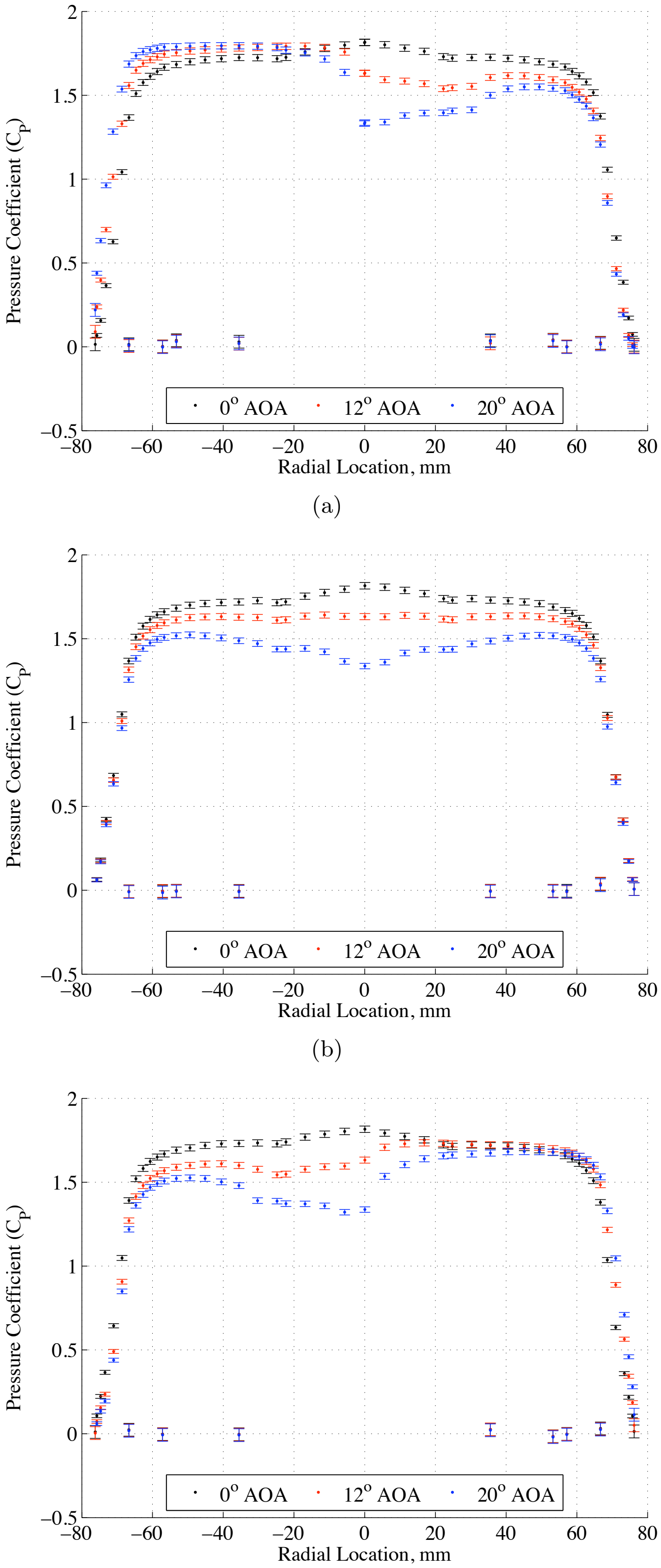

(a)

(b)

(c)

Figure 46: Pressure distributions at Mach 4.50 and a Reynolds number of 1.0 x 10^6 for the (a) 0°, (b) 90°, and (c) 225° spokes.

3.2.6 Flowfield Observations

Schlieren photographs of the model at Mach numbers of 1.65, 2.5, 3.5, and 4.50 are shown in Figures 47 – 50. Vertical bars present in each image are reinforcement beams on the door to the wind tunnel test section. Due to the orientation of the knife edge used for schlieren imaging, positive density gradients are shown as darker regions on the top half of each image and lighter regions on the bottom half. For each figure, three angles of attack are provided. Figure 48(a) shows a clear visualization of the flow field typical of the tension cone model. The bow shock is detached and exhibits no abrupt changes in curvature. A large change in contrast near the shoulder of the model indicates the approximate location of the sonic line attachment point. Expansion lines are easily distinguished on the shoulder and illustrate the flow accelerating around the shoulder of the model. A set of recompression shocks illustrate the extent of the wake region, although these are affected to some degree by the presence of the sting.

Of particular importance is that the flow appears to remain attached across the entire forebody of the model. Based on the surface pressure data shown in Figures 41 – 46, the most likely test condition to exhibit flow separation is the Mach 4.5, 20° angle of attack case shown in Figure 50(c). Although the image shows no apparent flow separation it is possible that the free stream density may have been too low at this test condition for separation to be visible. Schlieren video attained during testing shows the bow shock to be stationary at this condition. The first real disruption of the bow shock shape is barely visible in the form of a very small inflection on the leeward side.

The schlieren imagery is evidence that the extensive efforts of the configuration design phase were successful in preventing many of the flow instability issues that were observed in prior testing of tension cones (see Section 2.4). In particular, the choice of the 60° attachment angle produced a shape that is expected to be robust to flow instabilities throughout the supersonic regime, even at high Mach numbers.

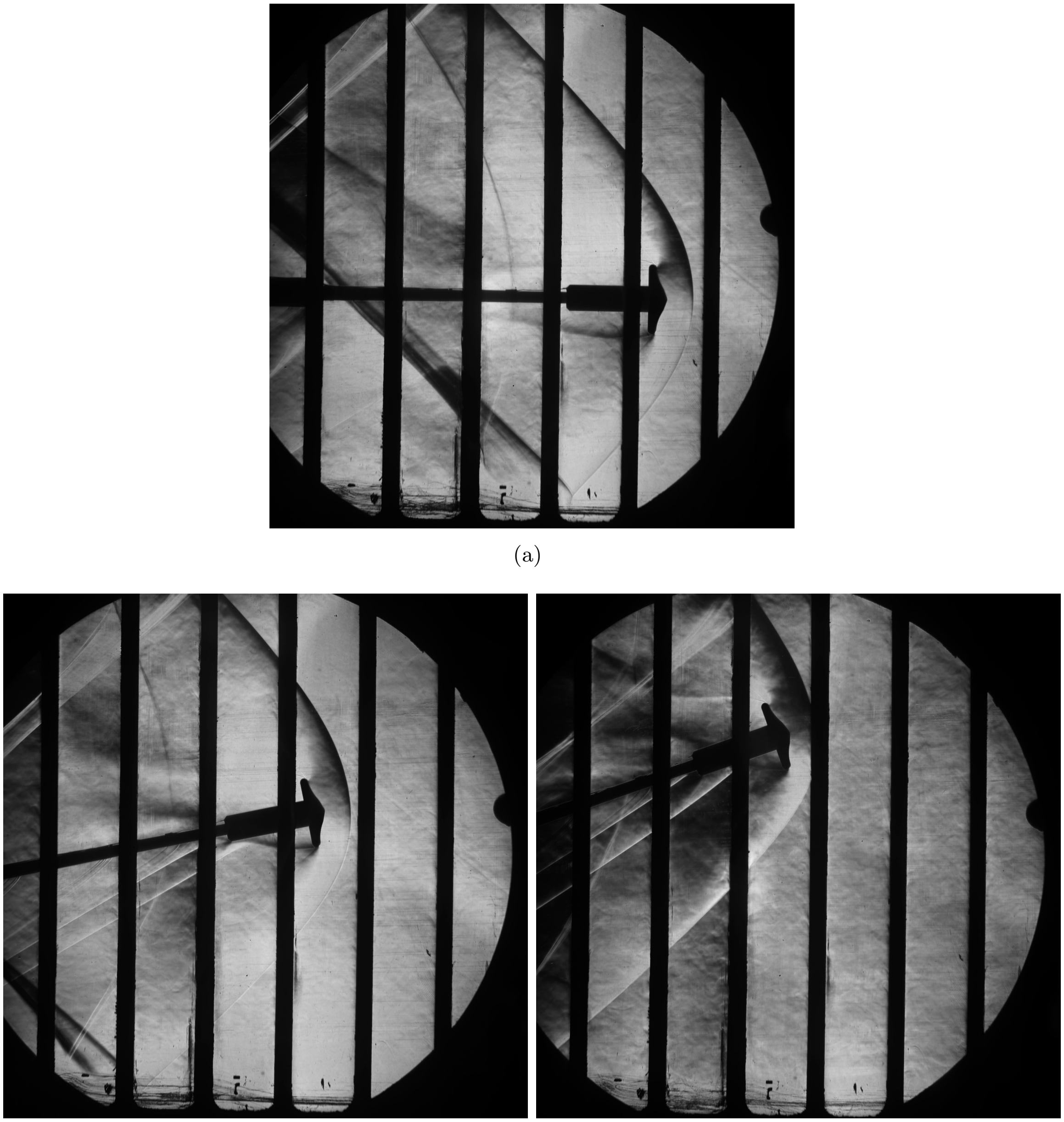

(a)

(b)

(c)

Figure 47: Schlieren imagery at Mach 1.65 and a Reynolds number of 1.0 x 10^6 for an angle of attack of (a) 0.3°, (b) 12.3°, and (c) 20.2°.

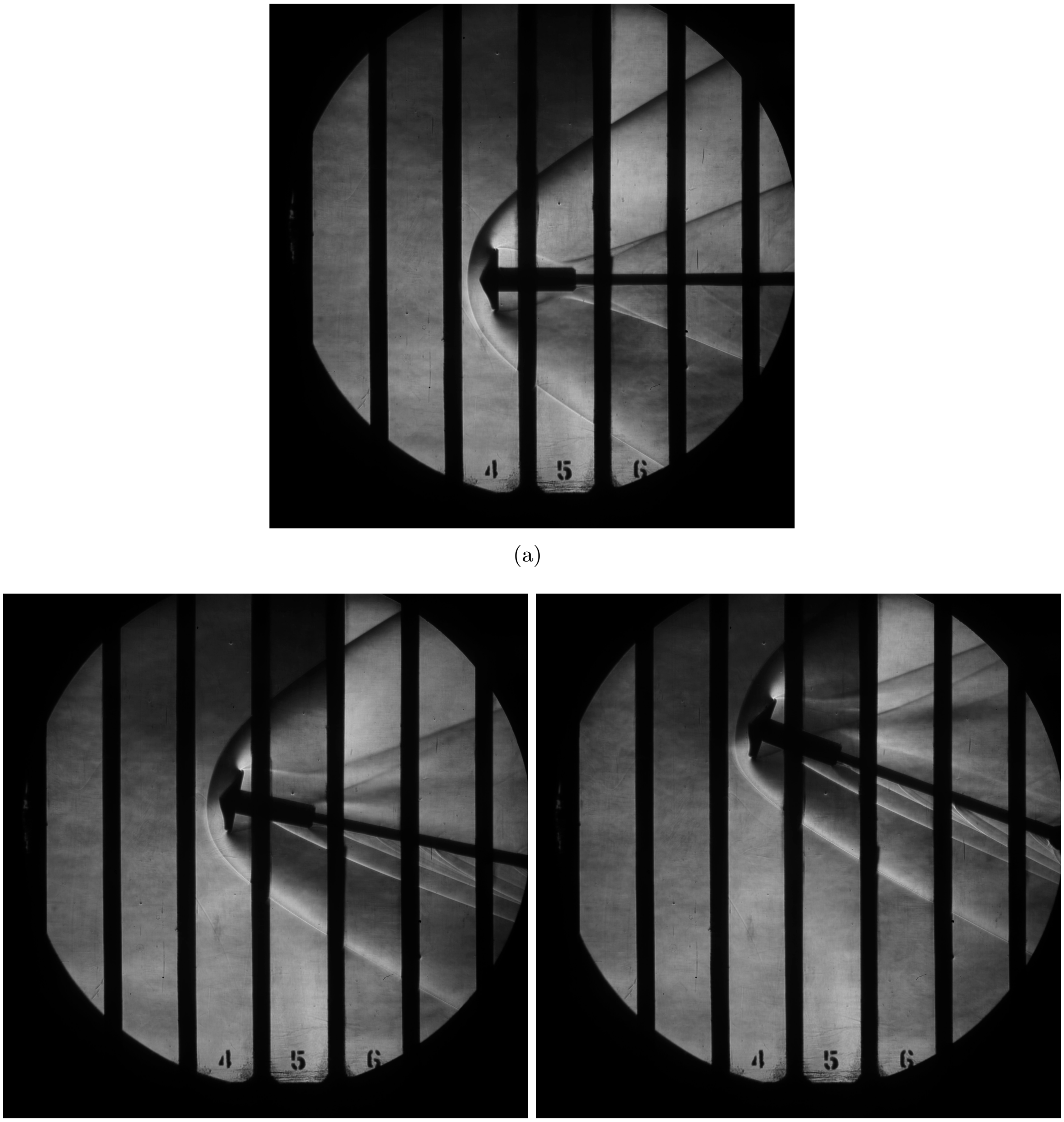

(a)

(b)

(c)

Figure 48: Schlieren imagery at Mach 2.5 and a Reynolds number of 1.0 x 10^6 for an angle of attack of (a) 0.3°, (b) 12.2°, and (c) 20.2°.

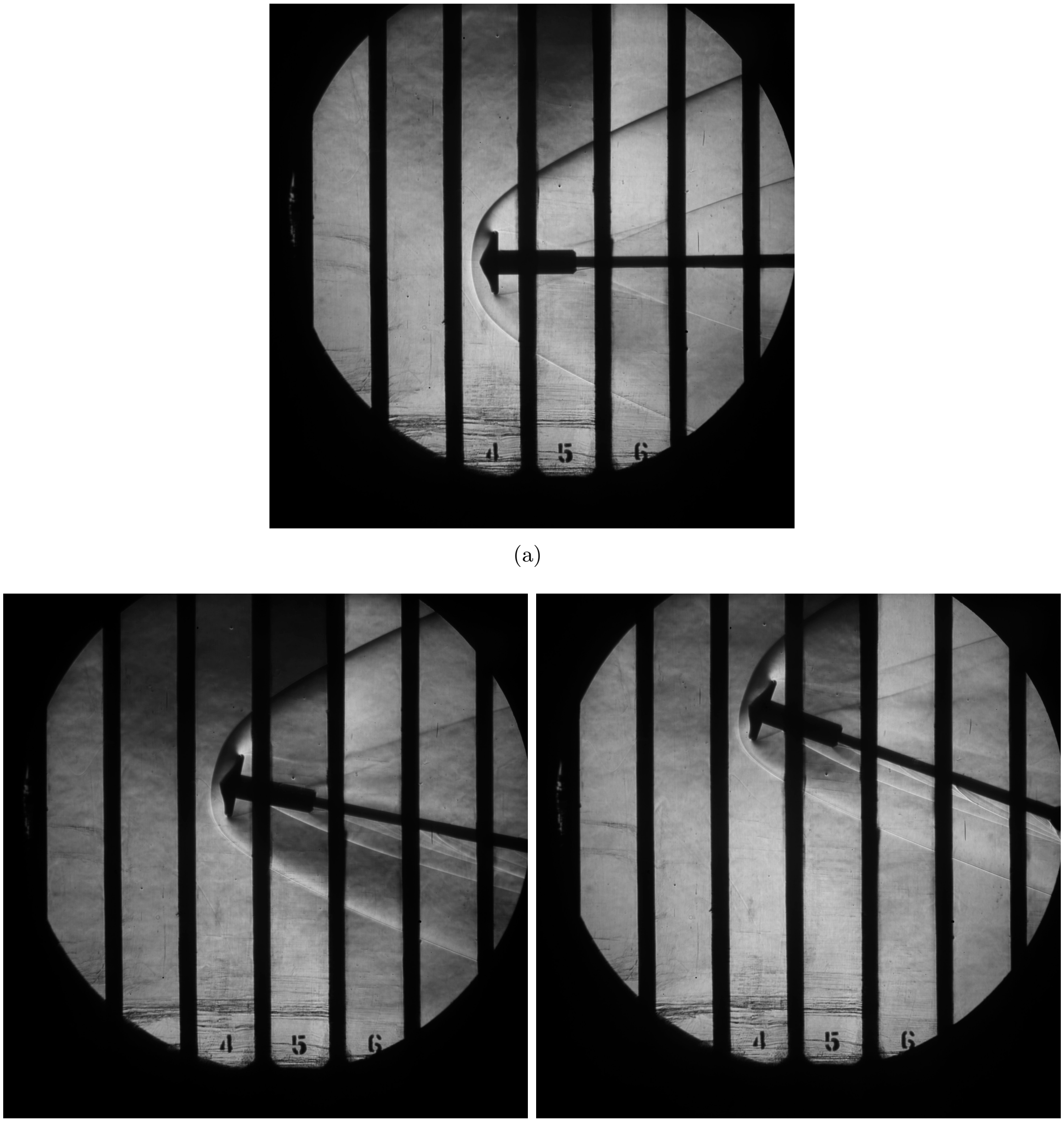

(a)

(b)

(c)

Figure 49: Schlieren imagery at Mach 3.5 and a Reynolds number of 1.0 x 10^6 for an angle of attack of (a) 0.2°, (b) 12.3°, and (c) 20.1°.

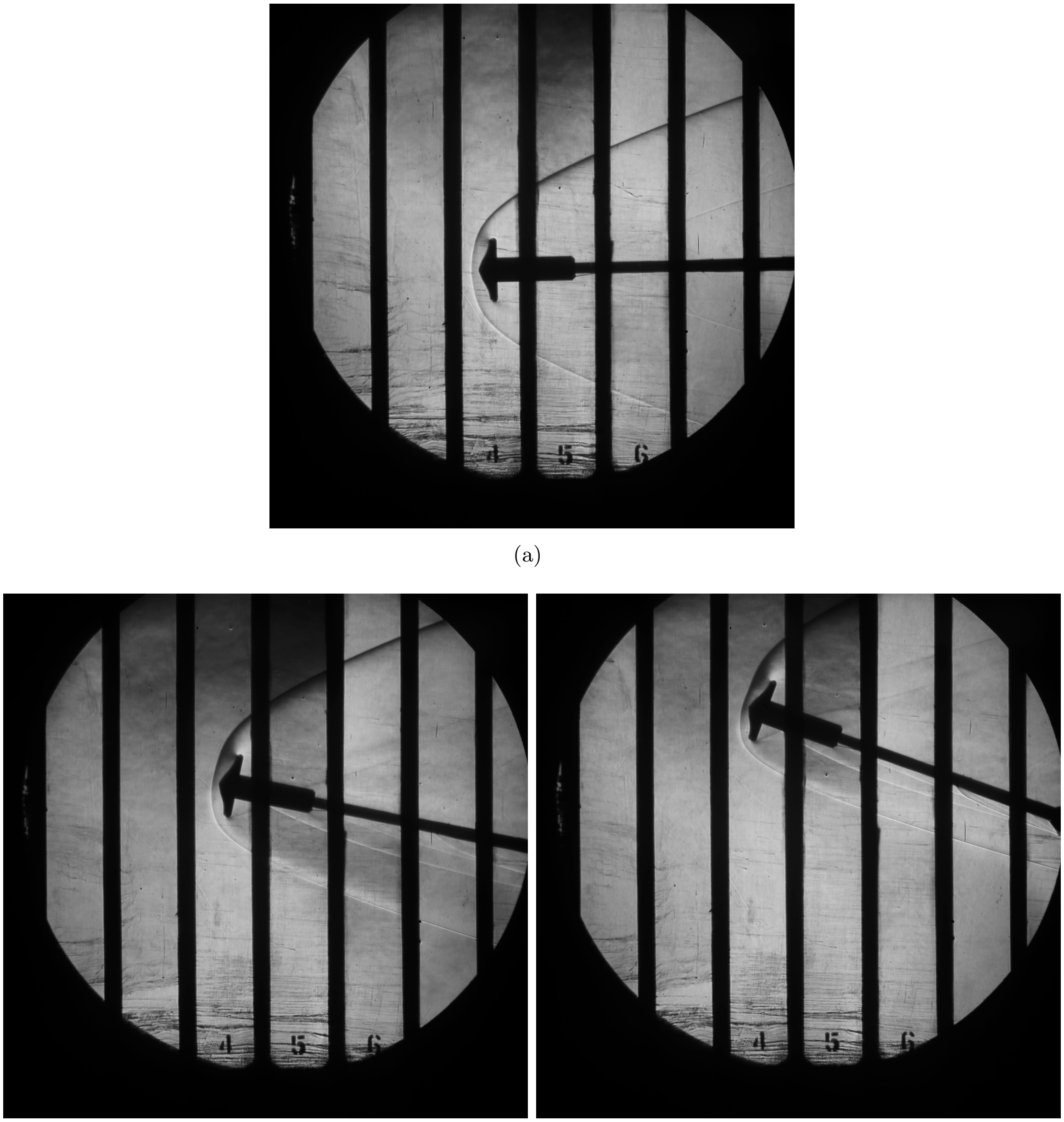

(a)

(b)

(c)

Figure 50: Schlieren imagery at Mach 4.5 and a Reynolds number of 1.0 x 10^6 for an angle of attack of (a) 0.0°, (b) 13.0°, and (c) 20.8°.

3.3 10- x 10-Foot Tunnel Testing

The second portion of the supersonic tension cone wind tunnel test program performed focused on testing of flexible articles. As with the rigid model testing, the goal of these tests was to acquire data useful for characterizing the behavior of a tension cone IAD at relevant Mach numbers. The data from flexible article testing will be used to provide an understanding of the aerodynamic behavior of the tension cone and to validate aerodynamic analyses. This test data will also be used by subsequent investigators to validate structural and aeroelastic analyses. The objectives that relate to these goals can be divided into two groups, qualitative and quantitative. Each group is enumerated below.

Qualitative Objectives

1. Determine the stability of the flow.
2. Determine the aeroelastic stability of the deployed tension cone IAD.
3. Characterize how deployment of the tension cone occurs.

Quantitative Objectives

1. Determine the static aerodynamic characteristics.
2. Determine the shape and position of shocks.
3. Determine the shape of the tension cone IAD under relevant aerodynamic loading.
4. Determine the time history of any unsteady forces and moments.
5. Determine the inflation pressure required for deployment from a stowed state.
6. Determine the time history of loads during deployment starting from a stowed state.
7. Determine the pressure required to eliminate localized wrinkling on the torus.
8. Determine the pressure required to maintain the torus in a non-buckled state.
9. Determine the pressure required to re-deploy the tension cone from a collapsed state.

This section of the thesis presents a description of the models used for testing, the procedure used to acquire data, and a summary of the data set acquired during testing.

3.3.1 Model Description

Testing of a flexible tension cone decelerator was performed using two distinct model types: a semi-rigid model and an inflatable model. Both model types are illustrated in Figure 51. Performing the test with two model types was done primarily for risk reduction reasons. Because there was no prior history of deploying a tension cone at supersonic conditions, the semi-rigid model was used to attain static aerodynamic data without the complexities of inflation. Due to the difficulties associated with fabricating flexible articles, both models were fabricated using a 16-segment torus, rather than a fully circular shape. The designed diameter of both types of models was 60 cm as measured from the flats of the tori segments.

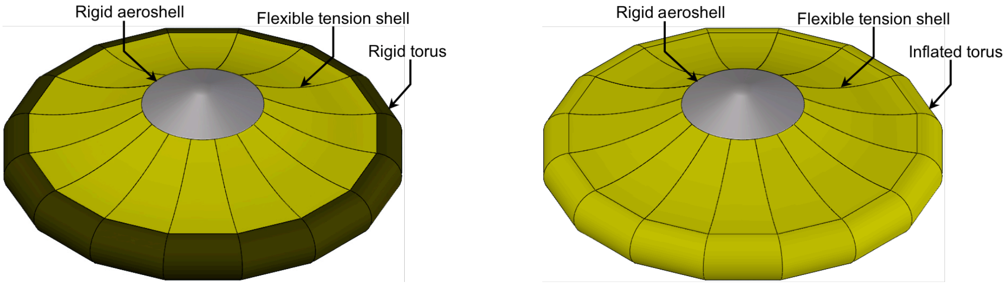

Figure 51: Semi-rigid (left) and inflatable (right) models.

3.3.1.1 Semi-Rigid Model

The semi-rigid model consisted of a textile tension shell attached to a 70° spherecone aeroshell and a rigid torus. The textile portion was comprised of 16 gores of urethane-coated kevlar. Gores were assembled using a welding process that melted each panel to a narrow strip of backing tape (also urethane-coated kevlar). Attachment of the tension shell to the rigid aeroshell was accomplished primarily by clamping the tension shell between the aeroshell and a separate backing plate. A silicone based adhesive was applied at the aeroshell/tension shell junction to provide a smooth interface.

The torus portion of the model was a lightweight, but rigid, torus. The torus was fabricated by laying fiberglass over pieces of foam bonded to a 1/8-inch thick aluminum ring. This process is outlined in Figure 52. Steps (b) and (c) of Figure 52 were repeated for a total of two layers of fiberglass. When completed, the rigid torus weighed less than 3 kg.

Attachment of the torus to the tension shell was achieved through use of a two-part epoxy.

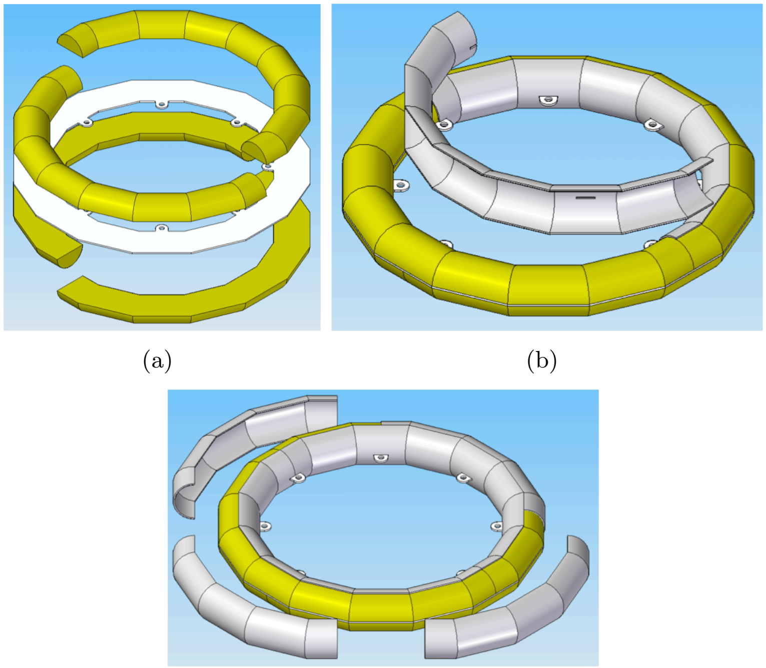
(a) (b)

(c)

Figure 52: Rigid torus assembly sequence: (a) Foam is bonded to aluminum ring. (b) Inner fiberglass layup. (c) Outer fiberglass layup.

One additional feature of the rigid torus model was a series of 8 tabs on the inner portion of the aluminum ring. During tunnel start-up and shut-down these tabs were used in conjunction with support hardware to hold the torus in a near-fixed position. The elements of this type of model are labeled in Figure 53.

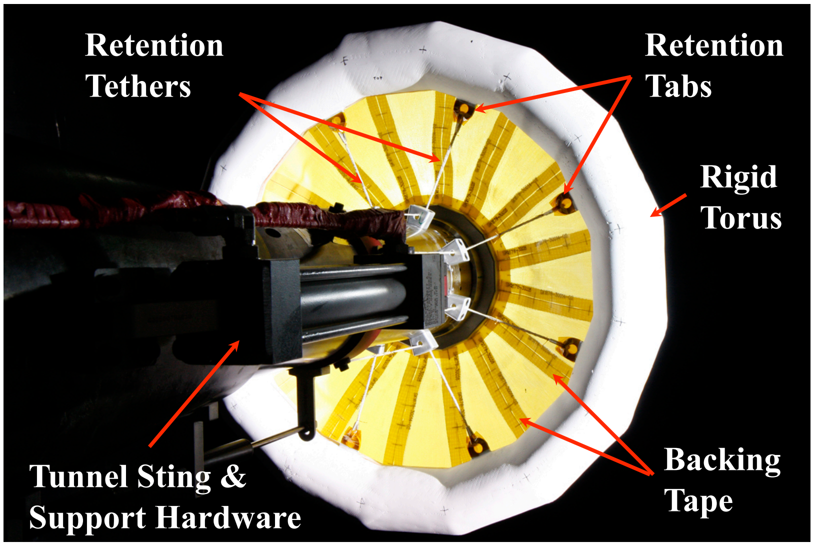

(a)

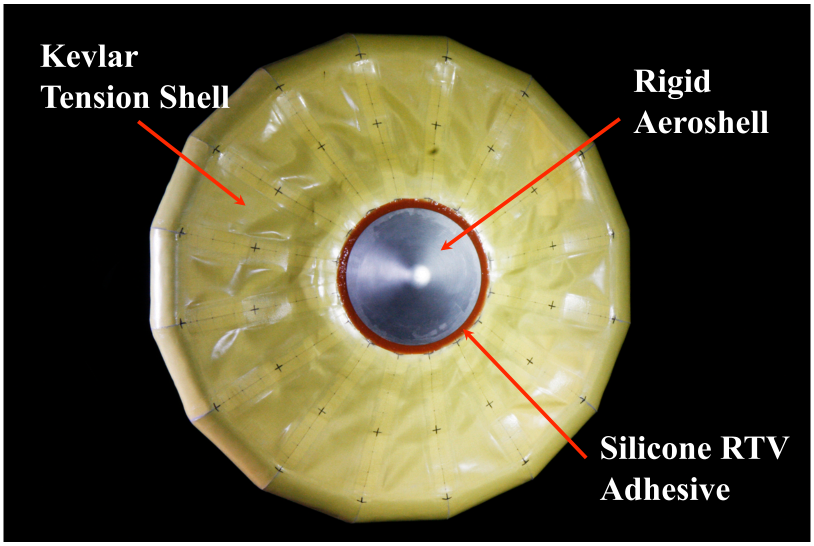

(b)

Figure 53: Semi-rigid model as installed in test section. a) aft view b) front view

3.3.1.2 Inflatable Model

The second model type, referred to as the inflatable model, replaces the rigid torus with a textile, inflatable torus. The inflatable torus was fabricated using the same urethane-coated kevlar as the tension shell. Inflation of the torus was achieved through two tubes located at the 3 o'clock and 9 o'clock positions on the back of the model. The inflation tubes were also constructed using kevlar to provide flexibility and allow for the model to be easily stowed.

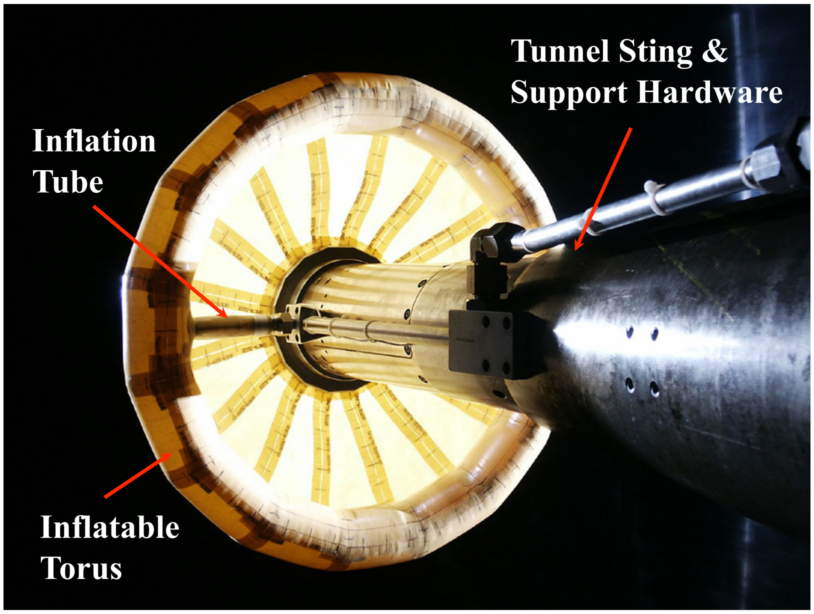

Figure 54: Aft view of the inflatable tension cone model installed in the test section.

Two variations of the inflatable model were used during testing. Due to pre-test concerns about the tension shell torquing the flexible torus and causing it to roll forward during testing, a series of panels were added. These anti-torque panels, shown in Figure 55, ran from the back of the inflatable torus to the base of the rigid aeroshell. During early testing of these two variations of inflatable models, differences in shape and aerodynamics were observed. As a result, the anti-torque panel modification was also applied to the semi-rigid model and both variants (with and without panels) were tested at similar conditions.

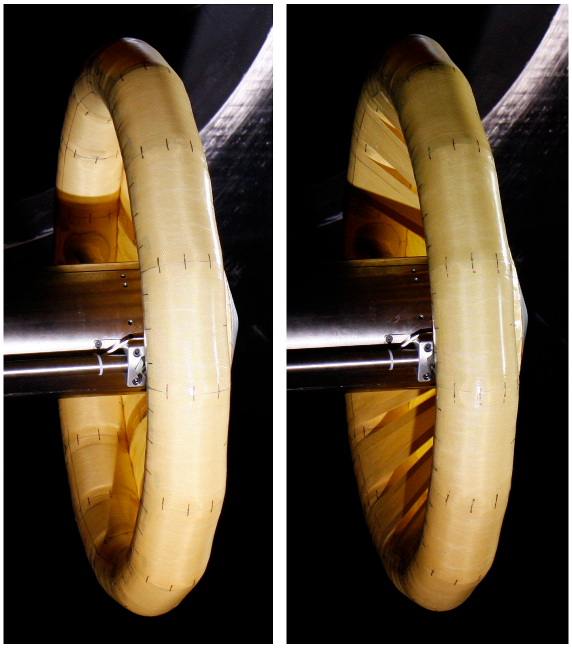

(a) (b)

Figure 55: Inflatable models a) without anti-torque panels and b) with anti-torque panels.

3.3.1.3 Support Hardware

Two pieces of support hardware were critical to the execution of the test: a rigid torus retention system and an inflation system. During tunnel start-up and shut-down, flow transients can produce very strong pressure oscillations, particularly in the time leading up to and during shock passage through the test section. A major concern for both models was securing their motion during this time and preventing unnecessary stresses on the models. For the semi-rigid model, a retention system was installed on the tunnel sting. This system consisted of a ring that actuated along the length of the sting. Attached to the ring were a series of tethers that were also attached to the retention tabs on the semi-rigid model. During tunnel start-up and shut-down operations the ring would be retracted aftwards, placing the tethers in tension and thus restricting the motion of the torus.

Pressurization of the inflatable model required an inflation system. This system was used to rapidly pressurize the model during deployment and to control the pressure inside the torus after the model was inflated. Air was provided via a large accumulator interfaced to the facility's high pressure system and charged prior to testing. A series of feed lines ran from the accumulator into the wind tunnel test section. Pressure and flow were controlled through a series of valves with the one closest to the model being within the wind tunnel strut. The system was designed so as to be capable of inflating the model to a pressure of 130 psid within 0.5 seconds.

3.3.2 Test Procedure

Testing of the two flexible types of tension shell IADs was conducted at the Abe Silverstein 10- x 10-foot Supersonic Wind Tunnel (10x10) at NASA's Glenn Research Center. The 10x10 is capable of supersonic operation from Mach 2.0 to 3.5. Operation of the tunnel in the Mach 2.5 - Mach 3.5 range requires the use of a second compressor. Consequently, the heat of compression raises the stagnation temperature of the flow from approximately 80°F to over 140°F. Concerns about melting of the urethane coating limited testing to the lower Mach number range of the facility. This decision was further justified by the lack of any significant Mach number effects being observed in prior testing at the Langley Unitary Plan Wind Tunnel. All testing on the inflatable model was conducted at Mach 2.5 while testing on the semi-rigid included a few runs at Mach 2.0.

Instrumentation used during the test included video, still photography, a force and moment balance, and a set of pressure transducers. Video of the test included standard video and high speed video shot at a minimum speed of 500 frames per second. Both sets of video provided front, side, and schlieren views while the standard video also provided a view of the back of the model. Still cameras provided views nearly identical to those of the high speed cameras, though at 10.1 megapixel resolution. Measurements of the torus pressure were made using a pair of Kulite pressure sensors located within the inflation tubes. Force and moment measurements were attained using the Ames Task Balance 2.5 MK16.

Data acquisition from the balance and pressure transducers was performed using two separate systems. The Dewetron system, used during deployments and pressure sweeps, was programmed to sample data a rate of 1000 Hz. The Escort system was capable of sampling at 500 Hz though only values averaged over 1 second were recorded.

The quantitative objectives for the semi-rigid model focused on gathering static aerodynamic data. The approximate test conditions at which the data were gathered are shown in Table 3.3.2. The angle of attack sequence used is shown in Table 20. Static aerodynamic coefficients were also acquired using the inflatable model, though at a reduced angle of attack sequence.

Table 19: Test matrix used for semi-rigid tension cone model testing.

Mach Number	**Reynolds Num. (model)**	**Dynamic Press., psf**	**Total Press., psf**	**Static Press., psf**	**Total Temp., °F (R)**	**Static Temp., °F (R)**
2.5	5.46×10^5	51.2	200	11.7	85.3 (545)	-217.4 (242.2)
2.5	1.00×10^6	94.7	370	21.6	85.3 (545)	-217.4 (242.2)
2.5	1.60×10^6	150	586	34.3	85.3 (545)	-217.4 (242.2)
2.5	2.13×10^6	200	781	45.7	85.3 (545)	-217.4 (242.2)
2.0	6.91×10^5	71.6	200	25.6	85.3 (545)	-156.9 (302.8)
2.0	1.00×10^6	104	292	37.3	85.3 (545)	-156.9 (302.8)
2.0	1.45×10^6	150	419	53.6	85.3 (545)	-156.9 (302.8)
2.0	1.93×10^6	200	559	71.4	85.3 (545)	-156.9 (302.8)

Table 20: Angle of attack sequences used during testing.

Model	**Sting Angle of Attack, deg.**
Semi-Rigid	0,2,4,6,9,12,15,18,15,12,9,6,4,3,0,-2,-4,-6,-4,-2,0
Inflatable	0,1,2,3,4,5,6,0,-3,-6,0

Operation of the inflatable model was focused on the deployment sequence and determination of required torus inflation pressures. Deployment of the inflatable model occurred from a stowed configuration, shown in Figure 56. Stowage of the inflatable model was achieved by first drawing a vacuum on the torus. The torus and tension shell were then wrapped around the sting and secured using a thin layer of Kapton film and Kapton tape. Once the tunnel was started and test conditions were achieved, the torus was rapidly pressurized, causing the Kapton film to break away and allowing the model to deploy. The pressure at which the torus was inflated to was controlled by establishing an equivalent pressure in a large reservoir that was part of the inflation system.

For determination of the torus pressures required to maintain shape, a pressure sweep sequence was employed. This procedure entailed starting with the inflatable model in a fully deployed state at the required freestream condition. The pressure in the torus would then be slowly lowered until the model reached a fully collapsed state. At this point, the torus would be slowly re-inflated until a fully deployed shape was again reached. Observations of wrinkling and buckling patterns as well as force and moment data were made throughout the pressure sweep sequence.

Tunnel conditions during deployment and pressure sweeps were designed to match those used during testing of the semi-rigid model. A total of 7 deployments were conducted, 2 each at dynamic pressures of ~51.2 psf and ~94.7 psf and three deployments at a dynamic pressure of ~150 psf. Torus pressure sweeps were conducted at each of these three dynamic pressures.

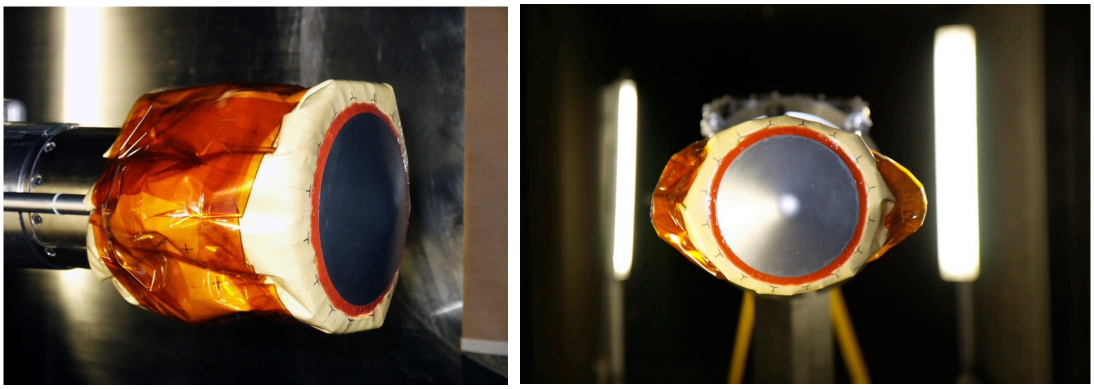
(a) (b)

Figure 56: Inflatable model in stowed configuration. (a) side view (b) front view

3.3.3 Data Reduction and Uncertainty Analysis

During data reduction, calculation of aerodynamic force and moment coefficients was performed using the as-measured (versus as-designed) values for the model diameter and model area. Pitching moments were referenced to the nose of the model using the as-measured diameter of the model as the reference length. Reported torus pressures are an average of the values reported by each of the two Kulite pressure sensors.

Difficulty was encountered in analyzing aerodynamic data from testing of the inflatable model due to the inflation tubes not being attached to the metric portion of the wind tunnel balance. Post-test analyses indicated that this had an impact on side and normal force measurements and likely influenced the axial force measurements as well. In general, side and normal force data from testing of the inflatable model is not presented with the exception of the deployment force time histories, for which it is provided for qualitative purposes. Pitching moment data from the inflation model was also considered heavily polluted by the inflation tubes restricting motion of the torus and thus is not presented.

An uncertainty analysis was conducted on the static aerodynamic data acquired with the inflatable and semi-rigid models. Uncertainty estimates for the inflation model were limited to C_A only and did not account for the possible effect of the inflation tubes. As with the analysis conducted on the Unitary data set, this analysis was divided into estimates of the precision uncertainty and the bias uncertainty. Precision uncertainties for the semi-rigid model were developed from repeated test runs and scaled with respect to dynamic pressure, with higher dynamic pressures resulting in lower uncertainty estimates. Precision uncertainties for the inflatable model were developed from repeated pressure sweeps and were also scaled with dynamic pressure. Estimates of the bias uncertainty were determined by Monte Carlo analyses that used the distributions shown in Table 21 as inputs. The Mach number and total pressure estimates were developed from data in Reference [5]. The force and moment estimates were developed from calibration data and from the wind-off zero data taken before and after each test.

Total uncertainties were estimated at the 95% confidence level.

Table 21: Distributions used to estimate bias uncertainty for the 10x10 test series.

Parameter	**Std. Deviation**	**Distribution**
Mach Number	0.008	normal
Total Pressure, P_0	0.40% of measured value	normal
Axial Force	(0.25% of measured value + 1 lb)/$\sqrt{3}$	uniform
Normal Force	(0.75% of measured value + 2 lb)/$\sqrt{3}$	uniform
Pitching Moment	(0.50% of measured value + 13 in-lb)/$\sqrt{3}$	uniform

3.3.4 Deployment Results

A total of seven tension cone deployments were performed at supersonic conditions. The first four deployments were performed using a conservative estimate of the required inflation pressure that assumed the torus was a membrane structure (Appendix A). Deployment of the inflatable model during these tests was observed to occur very rapidly and without any aeroelastic instabilities or dynamic motions of the torus. These pressures were sufficient to eliminate any signs of localized wrinkling on the surface of the torus. A typical history of the deployment loads for one of these runs, Run 25, is provided in Figure 57. Images corresponding to the indicated times are provided in Figure 58. Run 25 utilized a model incorporating anti-torque panels.

The sequence of events highlighted in Figure 57 correspond to initial torus pressurization (a), initial tension cone deployment (b), mid-deployment (c), and deployment completion (d). The delay between initial pressurization and tension cone deployment is caused by the restraining Kapton film not breaking until a sufficient level of torus pressure was achieved. At time (b), the Kapton begins breaking and the tension cone begins deployment. The rapid increase in torus volume that occurs during deployment results in a momentary drop in measured pressure that occurs around time (c). Examination of the axial force history reveals a rapid rise to a static value with very little overshoot observed. Some of the deployments were observed to have more significant overshoots in axial force, though a post-test examination of the data indicated that the overshoot was more likely due to the set-up of the inflation system.

Deployment initiation is considered to occur when the axial force begins a rapid increase

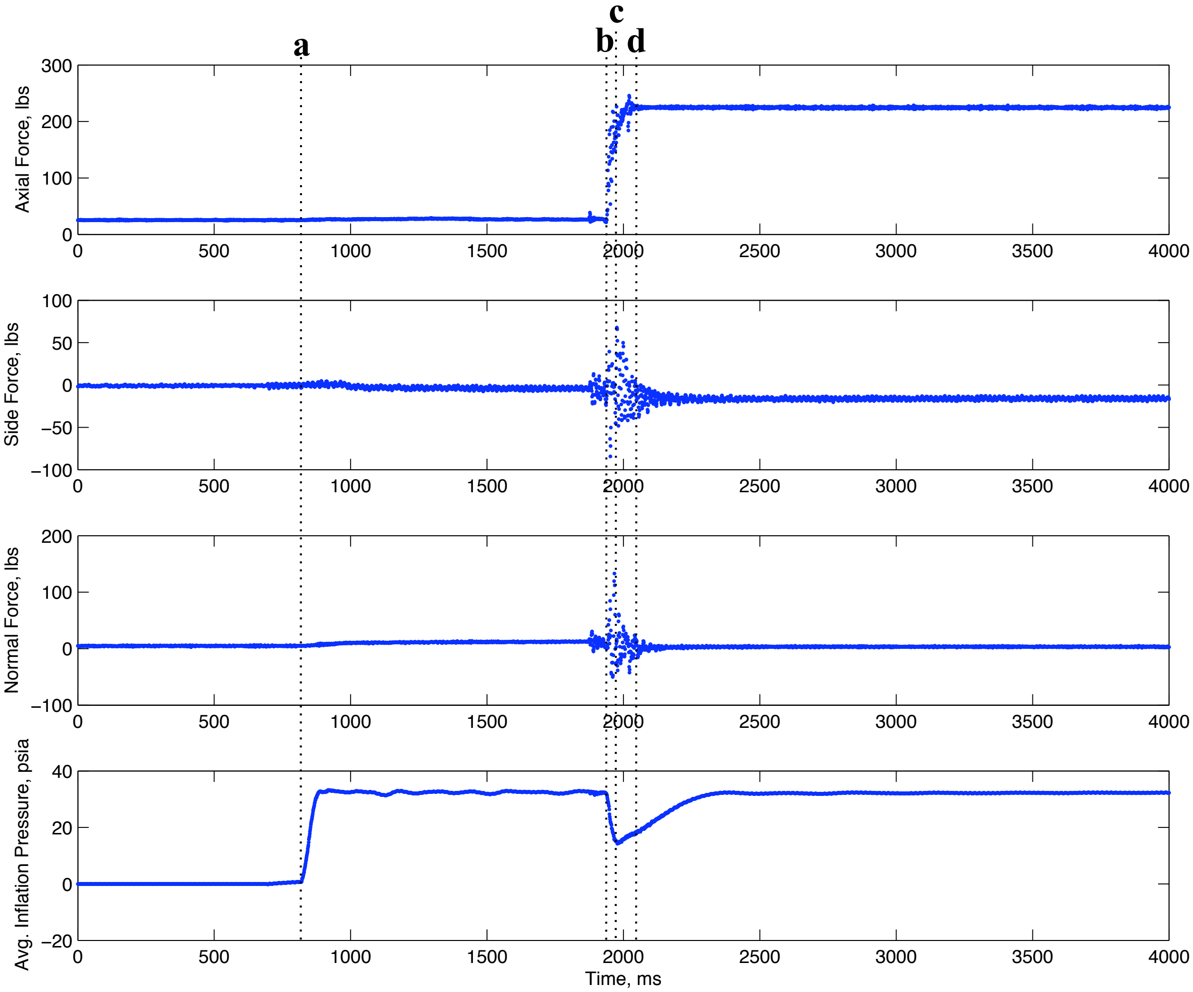

Figure 57: Force history during deployment of an inflatable model at a Mach number of 2.5 and dynamic pressure of ∼50 psf. Figure letters correspond to events shown in Figure 58.

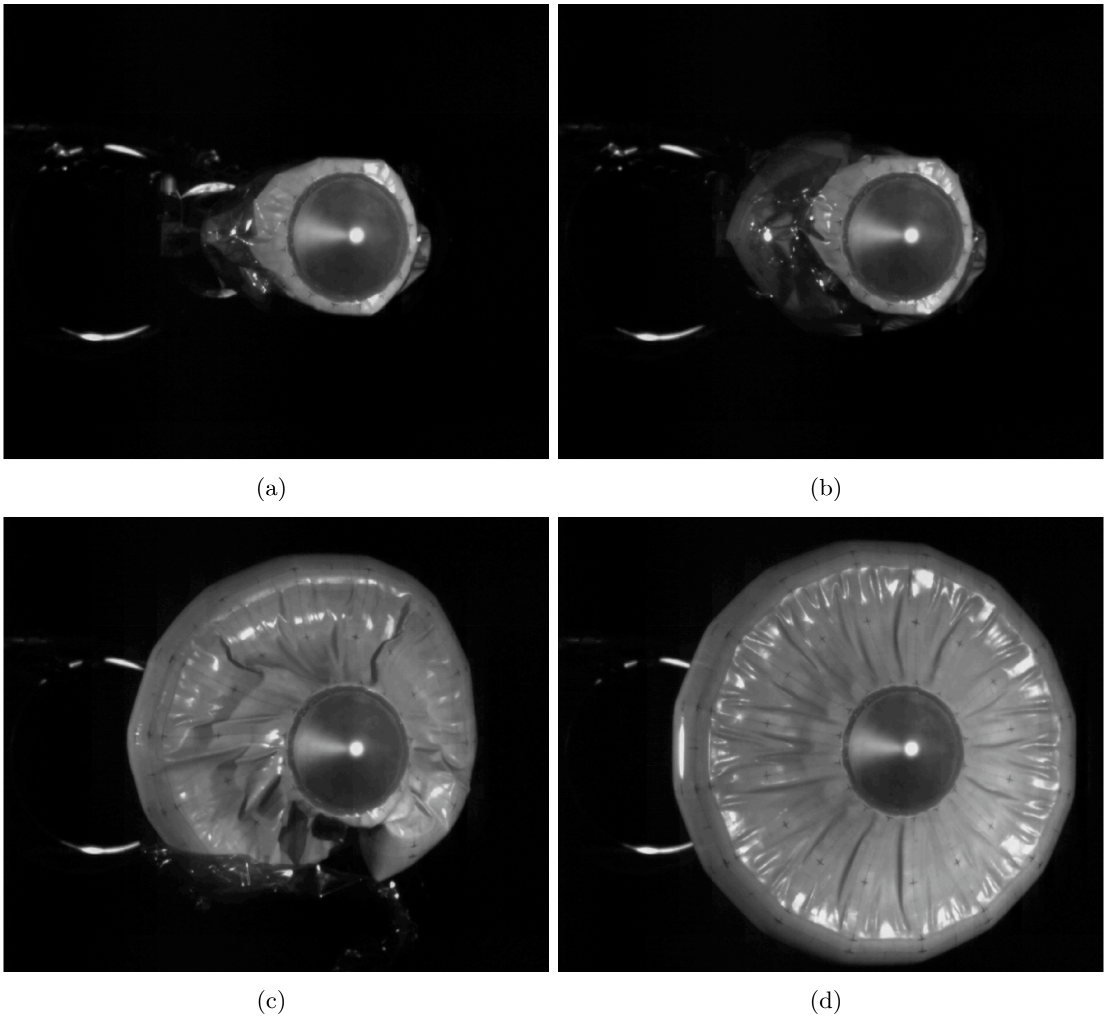

(a) (b)

(c) (d)

Figure 58: Deployment sequence images for an inflatable model at a Mach number of 2.5 and dynamic pressure of ∼50 psf. Figure letters correspond to events shown in Figure 57.

and deployment conclusion is determined at the first of 10 consecutive data points that are within 2% of the steady-state axial force. Using these guidelines, the deployment duration for Run 25 is calculated as 116 ms. The extremely short duration is attributable to two factors: the conservative estimate of the required inflation pressure (and the ability to rapidly deliver that inflation pressure) and the pre-pressurization of the torus that occurs before the Kapton restraint breaks.

Traces of the side and normal forces show periods of unsteadiness that occur concurrent with the axial force history. Very small changes in side and normal force are observable prior to deployment and additional oscillations are seen post deployment completion. The set-up of the inflation model prevented the inflation tubes from being isolated from the metric portion of the balance and this likely contributed to the measured side and normal forces. For example, a post-deployment offset of approximately 10 pounds side force is seen and could be explained by there being a slight difference in the length of the two inflation tubes.

Following completion of the first set of four deployments, a second round of deployments was conducted in which the targeted inflation pressure was set to a value considerably lower than estimated using the conservative equations of Appendix A. Based on a series of pressure sweeps that had already been completed, and the success of the first four deployments, an improved estimate of the pressure required to keep the torus fully inflated was available. The final three deployments were performed at torus pressures derived from a linear fit of the available pressure sweep data. The linear fit provided an estimation of the internal pressure required for a fully deployed torus at a given value of freestream dynamic pressure. This new estimate, plus a small margin of approximately 5-10%, was subsequently used to set the inflation system's target pressure. Although the first attempt at deployment at this lower-pressure estimate resulted in an incomplete inflation, a subsequent increase in inflation pressure revealed that the target pressure was off by only a few psi. Of interest, even though the model used in this first lower-pressure inflation did not fully inflate and remained in a buckled state, the model did not exhibit any observable oscillations.

The other two deployments at the reduced pressure estimates were successful at achieving a fully inflated torus. A force history of one of those deployments, Run 144, is provided in Figure 59 and images corresponding to the highlighted times are provided in Figure 60. Run 144 was conducted on a model incorporating anti-torque panels and at a dynamic pressure of ~150 psf.

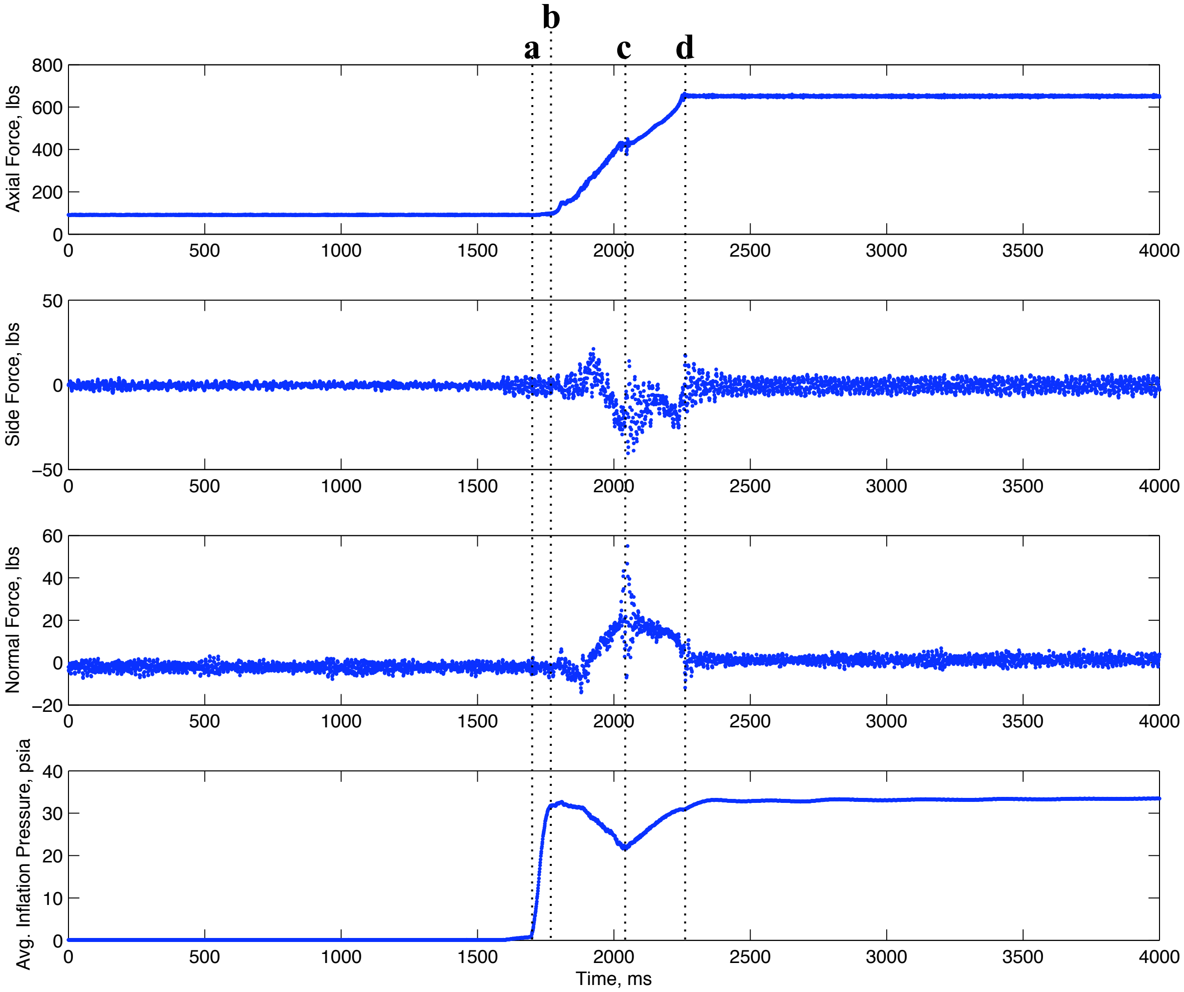

Figure 59: Force history during deployment of an inflatable model at a Mach number of 2.5 and dynamic pressure of ~150 psf. Figure letters correspond to events shown in Figure 60.

In contrast to prior runs, Run 144 shows a longer deployment sequence of about 472 ms. A unique characteristic to this deployment was the lack of a Kapton restraint, which had ripped prematurely as the tunnel was coming up to the freestream test condition. The lack

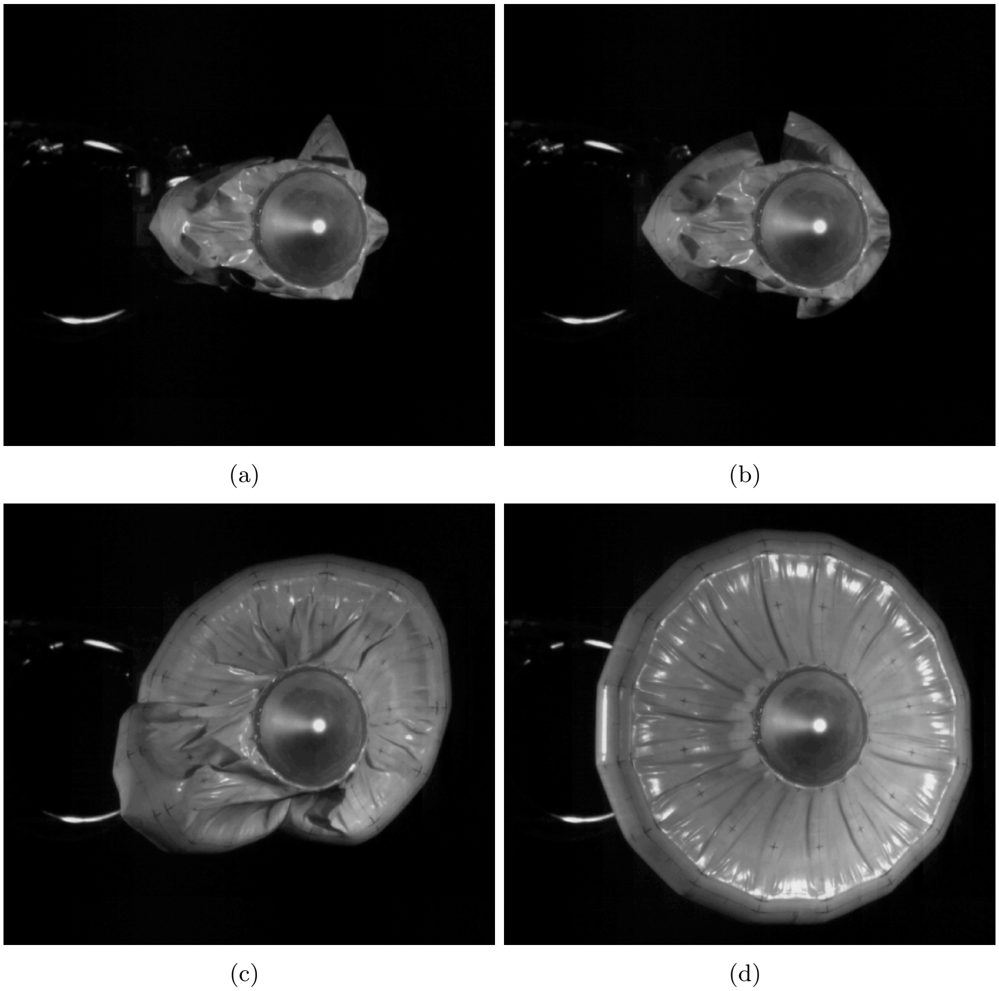
(a) (b)
(c) (d)

Figure 60: Deployment sequence images for an inflatable model at a Mach number of 2.5 and dynamic pressure of ∼150 psf. Figure letters correspond to events shown in Figure 59.

of a pre-pressurization of the torus along with the reduced inflation pressure resulted in a prolonged, and more gradual, deployment. Examination of the axial force history reveals virtually zero overshoot. Side and normal force histories also reveal relatively lower forces when compared against Run 25, especially considering that the deployment was conducted at three times the dynamic pressure. The momentary drop in torus pressure at time (c) caused by the rapid increase in volume can be seen to result in a very brief pause in the deployment sequence.

A summary of the target inflation pressures and resulting inflation durations for the six successful deployments is provided in Table 22. Table 22 shows two key trends. First, lower ratios of target inflation pressure to free-stream dynamic pressure result in longer deployment durations. Second, models without anti-torque panels consistently showed shorter deployments, though only slightly.

Table 22: Summary of target inflation pressures and inflation durations for six successful deployments.

Model Type	**Run Number**	**Target Torus Inflation Pressure (psia)**	**(Target Torus Inflation Pressure - $P_s)/q_\infty$**	**Deployment Duration (ms)**
w/ Anti-Torque	Run 25	32.2	88.23	116
	Run 77	60.9	91.75	131
	Run 144	33.3	31.61	472
w/o Anti-Torque	Run 36	32.4	89.55	72
	Run 50	61.0	91.63	91
	Run 151	52.4	49.86	218

3.3.5 Pressure Sweep Results

A total of 15 pressure sweeps were conducted at three discrete dynamic pressure conditions. During the pressure sweep sequence the models were observed to behave in a stable manner and exhibited no unsteady or oscillatory behavior, even when in a severely buckled state.

A key result from the pressure sweep sequence was the difference in collapse behavior between models with anti-torque panels and those without. These differences included the shape history that each exhibited during collapse, the pressures at which each began to collapse, and the axial forces produced by each model during the collapse sequence. Shown in Figure 61 are the axial forces produced by both model types as a function of inflation pressure for a dynamic pressure of ∼150 psf. Images corresponding to the events denoted in Figure 61 are provided in Figures 62 and 63 for the model with and without anti-torque panels, respectively.

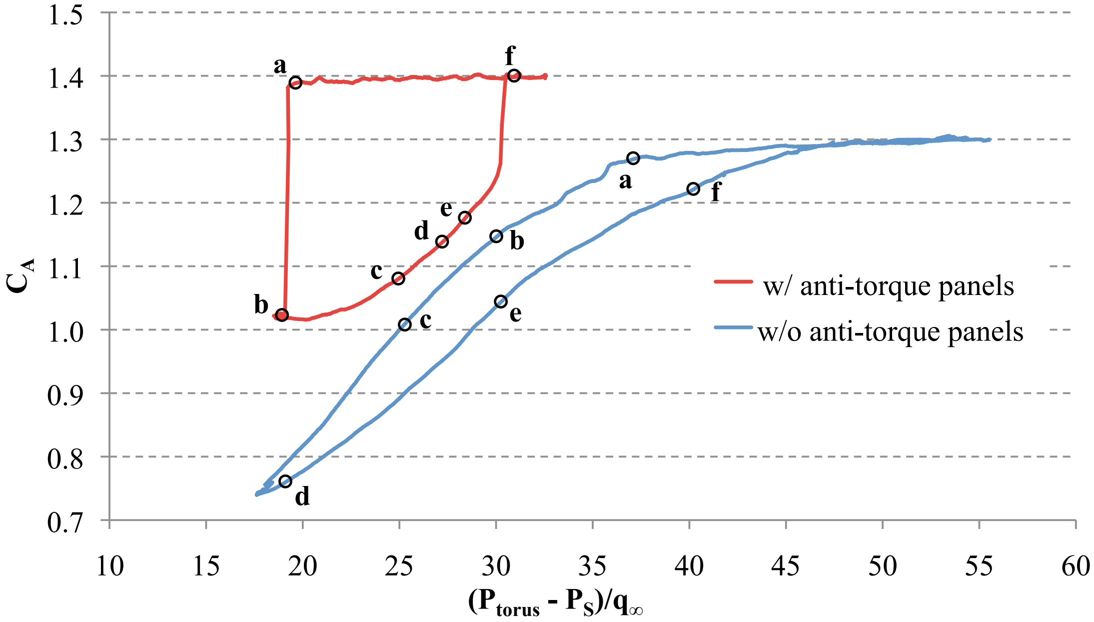

Figure 61: Axial force coefficient versus torus pressure for two inflatable model variants at a Mach number of 2.5 and dynamic pressure of ∼150 psf.

For models with anti-torque panels, moderate decreases in internal pressure had little impact on the production of drag. Further reductions in internal pressure eventually would

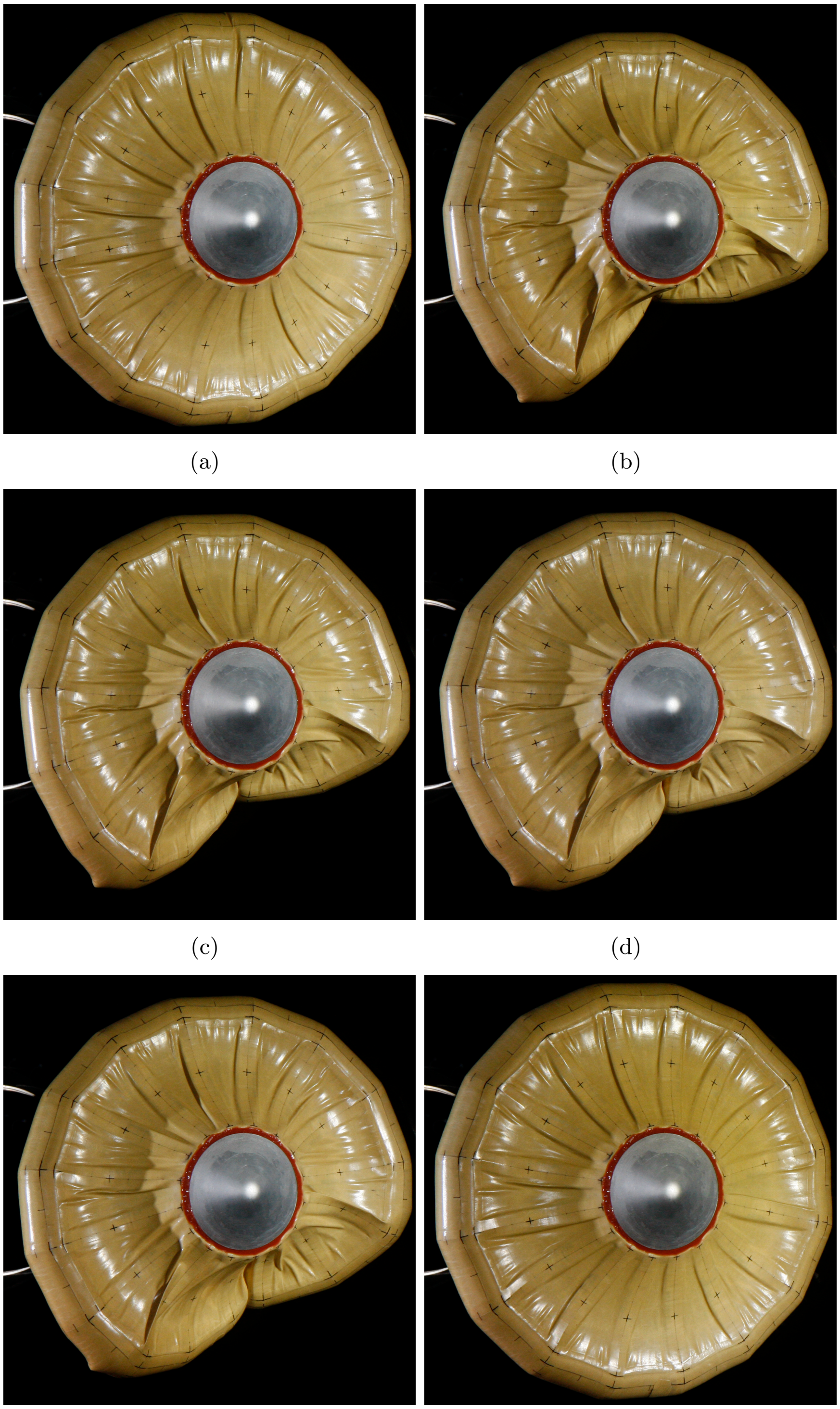
(a) (b)
(c) (d)
(e) (f)

Figure 62: Pressure sweep sequence for an inflatable model at a Mach number of 2.5 and dynamic pressure of ∼150 psf. Figure letters correspond to events shown in Figure 61 for a model incorporating anti-torque panels.

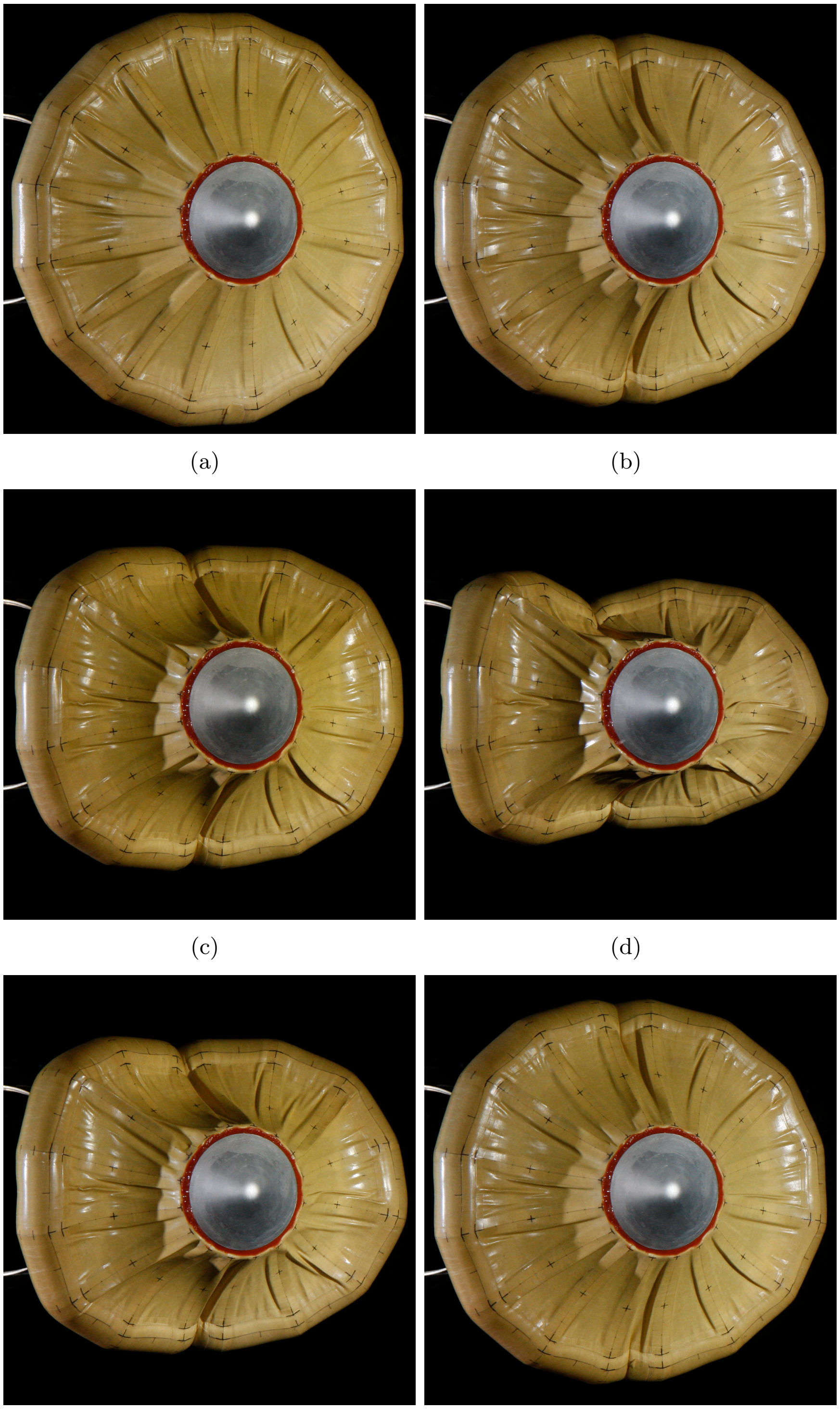

(a) (b)

(c) (d)

(e) (f)

Figure 63: Pressure sweep sequence for an inflatable model at a Mach number of 2.5 and dynamic pressure of ∼150 psf. Figure letters correspond to events shown in Figure 61 for a model without anti-torque panels.

lead to the formation of small creases on the torus, though still without any significant drag loss. However, at a given pressure, the torus would immediately go from an almost fully deployed state to a fully collapsed state (point a to point b on the red line in Figure 61). Re-pressurization of the torus took place on a somewhat different C_A versus torus pressure path with the torus requiring a much higher internal pressure before returning to fully inflated condition.

When compared to the anti-torque panel models, collapse of the models without anti-torque panels was much more gradual. Initial decreases in torus pressure resulted in large creases forming along the wall of the torus. When the pressure was lowered further the model began folding backwards over the sting. This behavior continued down to very low internal pressures. As with anti-torque models, a small hysteresis was evident as re-inflation of the torus produced lower values of C_A at a given torus pressure.

Figure 61 also reveals differences in the fully inflated values of axial force coefficient, a result discussed in more detail later.

Figure 64 is a plot of the internal pressures required for full deployment of both types of inflatable models. Of interest is that the required pressures are seen to vary linearly with loading, approximated as the product of dynamic pressure and axial force coefficient. This result indicates that the inflation pressure requirements may be easily predicted with a paucity of data points. Inflation pressures at torus collapse for models with anti-torque panels were nearly half those of the models without. Recovery pressures for anti-torque models were also less than those without panels, though not to the same degree. That is, the recovery pressure for models with anti-torque panels was nearly 50% higher than the initial collapse pressure while they were only 15% higher for models without panels. Both types of models exhibited required inflation pressures considerably lower than the values predicted using the conservative equations developed in Appendix A for models without anti-torque panels. Linear fits to the data are seen to result in intercept values very close to zero, as expected since a zero loading condition should require zero internal pressure.

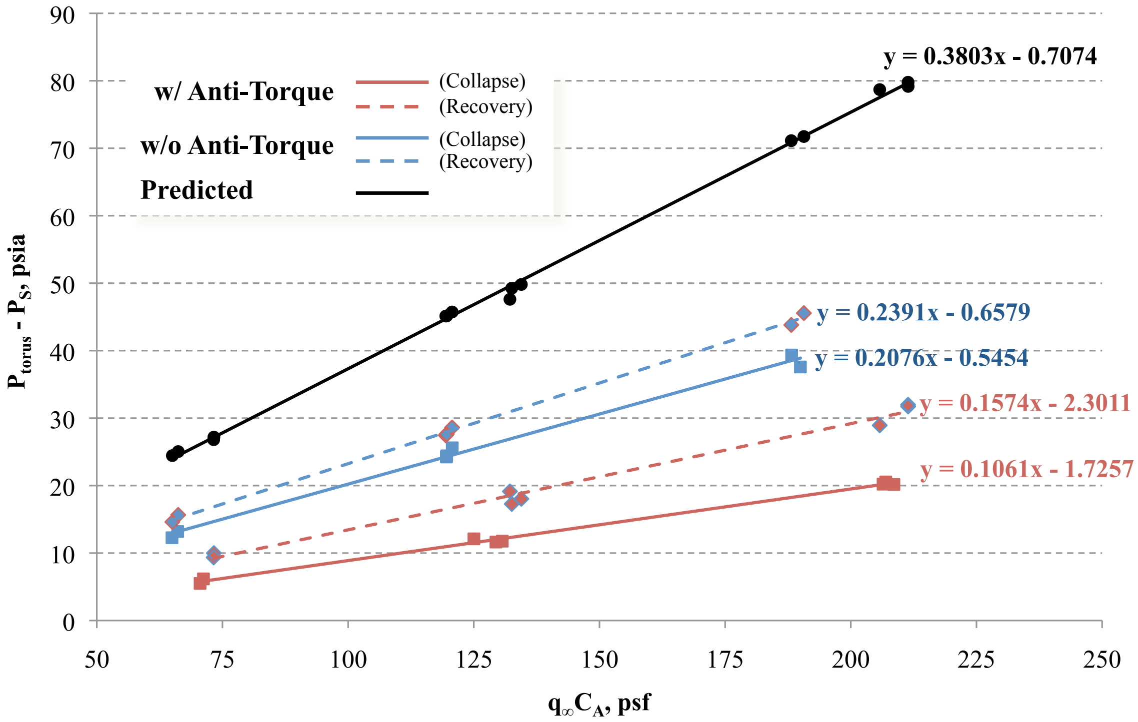

Figure 64: Tension cone collapse and recovery pressures versus axial loading.

3.3.6 Semi-Rigid Structural Behavior

Testing of the semi-rigid model revealed two key results regarding the structural behavior of the model. As with the inflatable models, models with and without anti-torque panels were tested. The primary differences between the two types are related to the shape the tension shell took under load. For the model with anti-torque panels, the axial location of the rigid torus was constrained which resulted in the tension shell acquiring more concavity near the torus/tension shell interface. This is visible in Figure 65, where the greater reflectivity seen on the periphery of the anti-torque model is due to the change in curvature at that location. This behavior was also evident on the inflatable models. The implication of this behavior to the drag performance of the model is discussed later in Section 3.3.7.

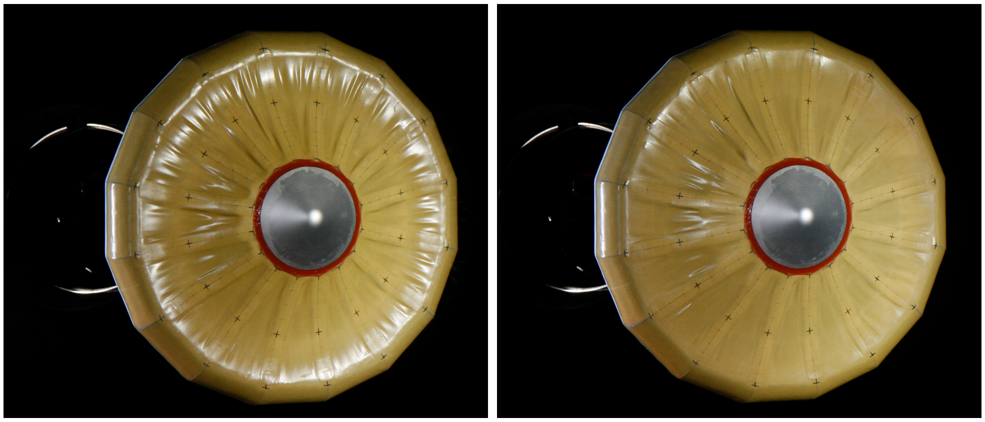
(a) (b)

Figure 65: Front view of the semi-rigid model a) with anti-torque panels and b) without anti-torque panels.

Angle of attack sweeps conducted with the semi-rigid model demonstrated that the flexible tension cone behaved more like a fully rigid article rather than one with more degrees of freedom. Prior tests conducted on flexible attached isotensoid models had shown that the model tended to align itself with the freestream direction during angle of attack sweeps [24]. However, the tension cone model in this investigation did not exhibit similar behavior. That is, at increasing angles of attack, the torus did not align itself with the freestream direction, but rather maintained a position nearly perpendicular to the sting, as shown in Figure 66. Though initially not expected, it is hypothesized that this behavior is due to two factors: the stiffness of the torus and the nature of the tension shell to maintain tension in the meridional direction. Since the tension shell is constrained at each end, in order for tension cone to align with the freestream, the tension shell would need to buckle or wrinkle at some location. However, the pressure on the surface of the shell produces sufficient tension to prevent this from occurring.

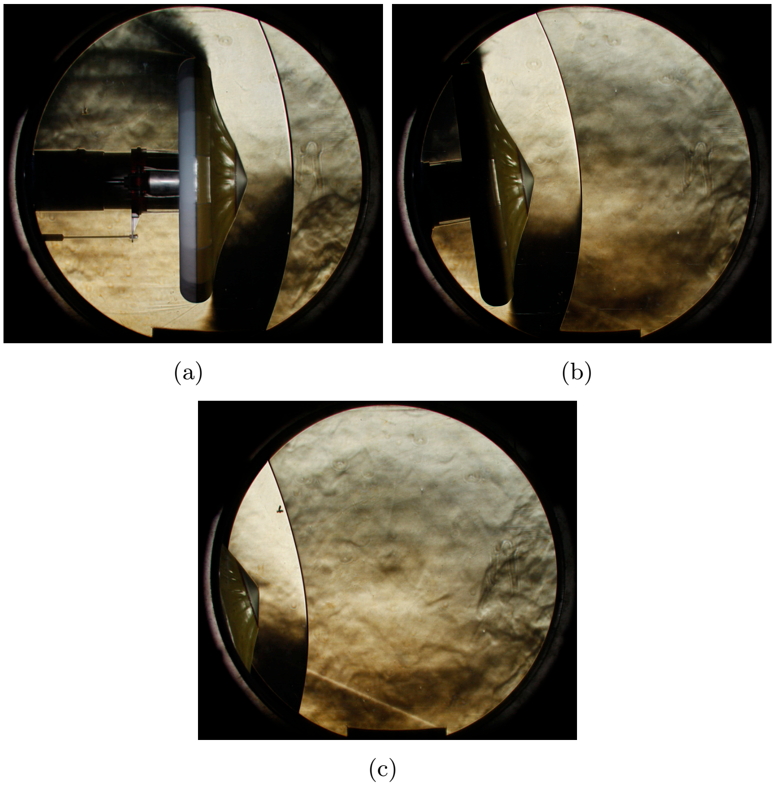
(a)
(b)
(c)

Figure 66: Schlieren images of the semi-rigid model at an angle of attack of a) 0° b) 9° c)18°.

Upon closer examination it was observed that the torus was not completely perpendicular, but rotation from a line normal to the axis of symmetry of the model was a few degrees or less. Using schlieren imagery, the degree of torus rotation was quantified for several angles of attack and test conditions. The results are shown in Figure 67. Models without anti-torque panels exhibited small torus rotation angles at a 0° angle of attack, though this angle decreased with increasing dynamic pressure. The rotation at a 0° angle of attack was likely due to the weight of the torus, which in the absence of flow would cause the torus to rest on the tunnel sting. As dynamic pressure increases, axial forces also increase and the weight of the torus is less of a factor. For the model with anti-torque panels, the torus appears more constrained and rotation is slightly less than for models without anti-torque panels. No major differences in torus rotation are apparent between the Mach 2.0 and Mach 2.5 conditions.

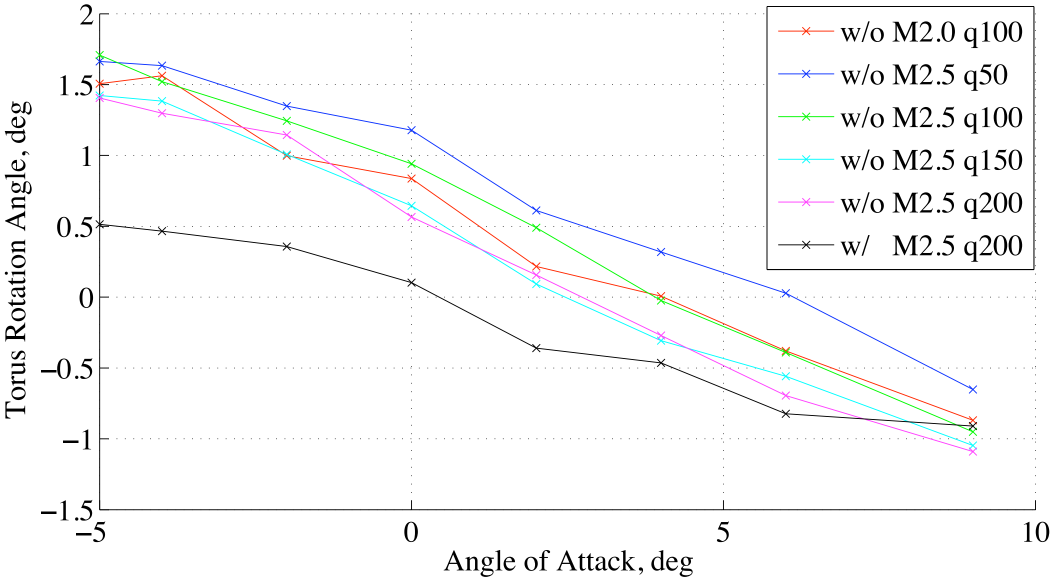

Figure 67: Torus rotation from a line normal to the model axis of symmetry versus angle of attack for several test conditions. With flow going from right to left, positive angles correspond to a counter-clockwise rotation of the torus. Data labels "w/" and "w/o" refer to the presence of anti-torque panels. Dynamic pressure (e.g. "q100") are approximate test conditions in units of psf.

3.3.7 Static Aerodynamics

Static force and moment data were acquired at several angles of attack using the semi-rigid model. Data tables of the results presented in this section are provided in Appendix F. Testing was predominantly conducted on a model without anti-torque panels at a Mach number of 2.5. Results on this type of model at four separate dynamic pressures are shown in Figure 68. From Figure 68, it can be seen that the aerodynamics of the semi-rigid are largely independent of dynamic pressure, and thus Reynolds number, for the range of conditions tested. A minor exception is seen for the lowest dynamic pressure, $\sim$50 psf, where the weight of the rigid torus likely influences the results. At this low of a dynamic pressure, the axial force is only about 225 lbs., while the torus weighs roughly 6 lbs. Since the torus weight is several percent of the total aerodynamic load, it is likely that the model would behave somewhat differently than if the torus had negligible weight. Figure 68 also illustrates that the axial force of the tension cone is nearly constant versus angle of attack and that the normal force and pitching moment are nearly linear. Furthermore, the slope of the pitching moment versus angle of attack indicates that the model is statically stable.

Two additional sets of tests were conducted on the semi-rigid model. These include testing at Mach 2.0 and testing of a model with anti-torque panels. The results from these tests are provided in Figure 69 along with a prior test for comparison. Differences in forces and moments between models with and without anti-torque panels are seen to be quite small and generally within the estimated uncertainty bounds. Testing at Mach 2.0 also produced similar results with the exception of the axial force coefficient at negative angles of attack. Rather than mirror the values at positive angles of attack, the axial force is seen to decrease at negative angles of attack. The difference is less than 3% of the value at positive angle of attack. It is theorized that this behavior is likely due to differences in the wake region directly behind the model that occur at Mach 2.0. For example, components of the retention system hardware (visible in Figure 66(a)) may interact with the wake region more prominently at Mach 2.0 than at Mach 2.5.

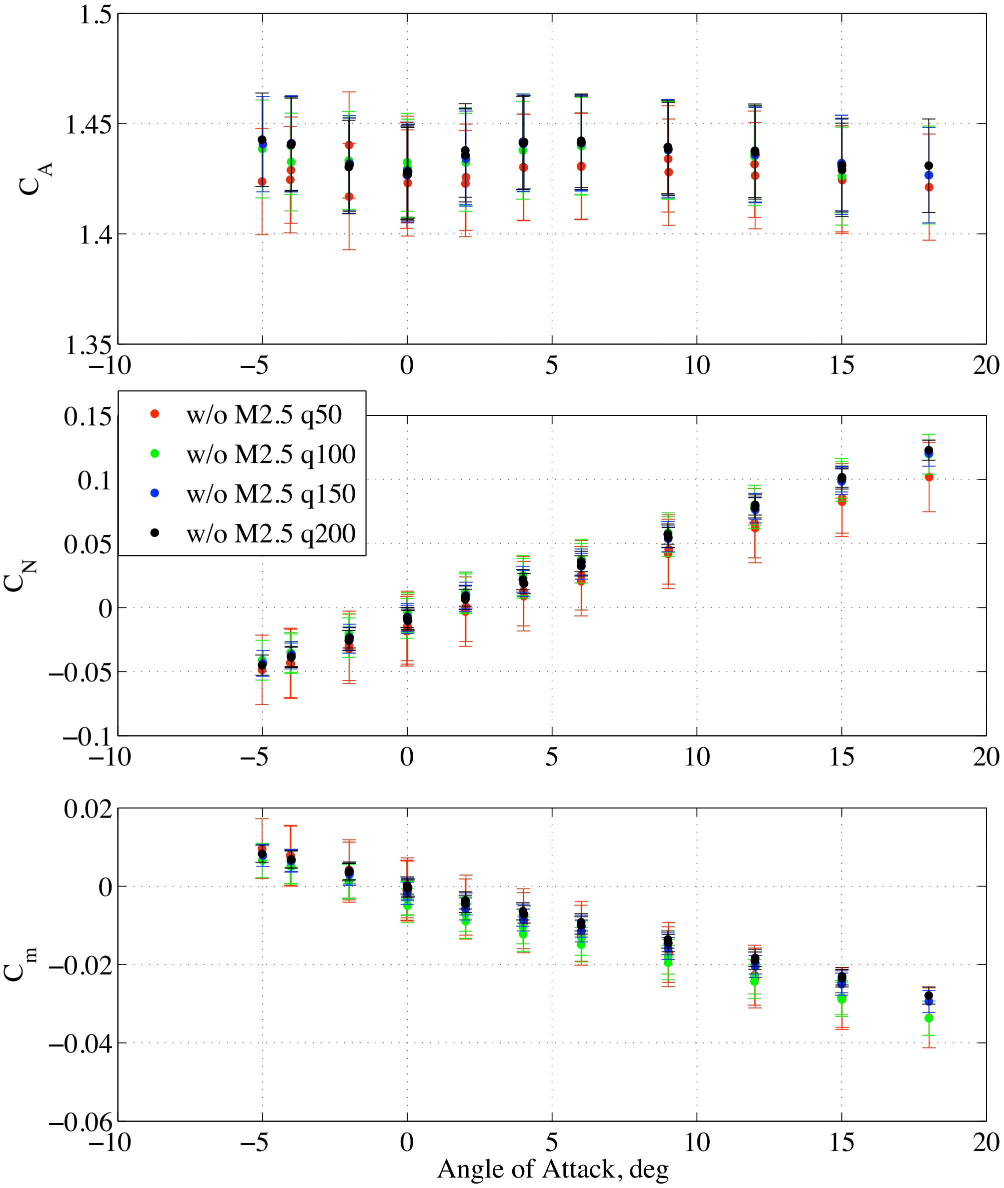

Figure 68: Static aerodynamic results for a semi-rigid model without anti-torque panels at Mach 2.5 and four separate dynamic pressures. Uncertainty bars correspond to 95% confidence intervals. Dynamic pressure (e.g. "q100") are approximate test conditions in units of psf.

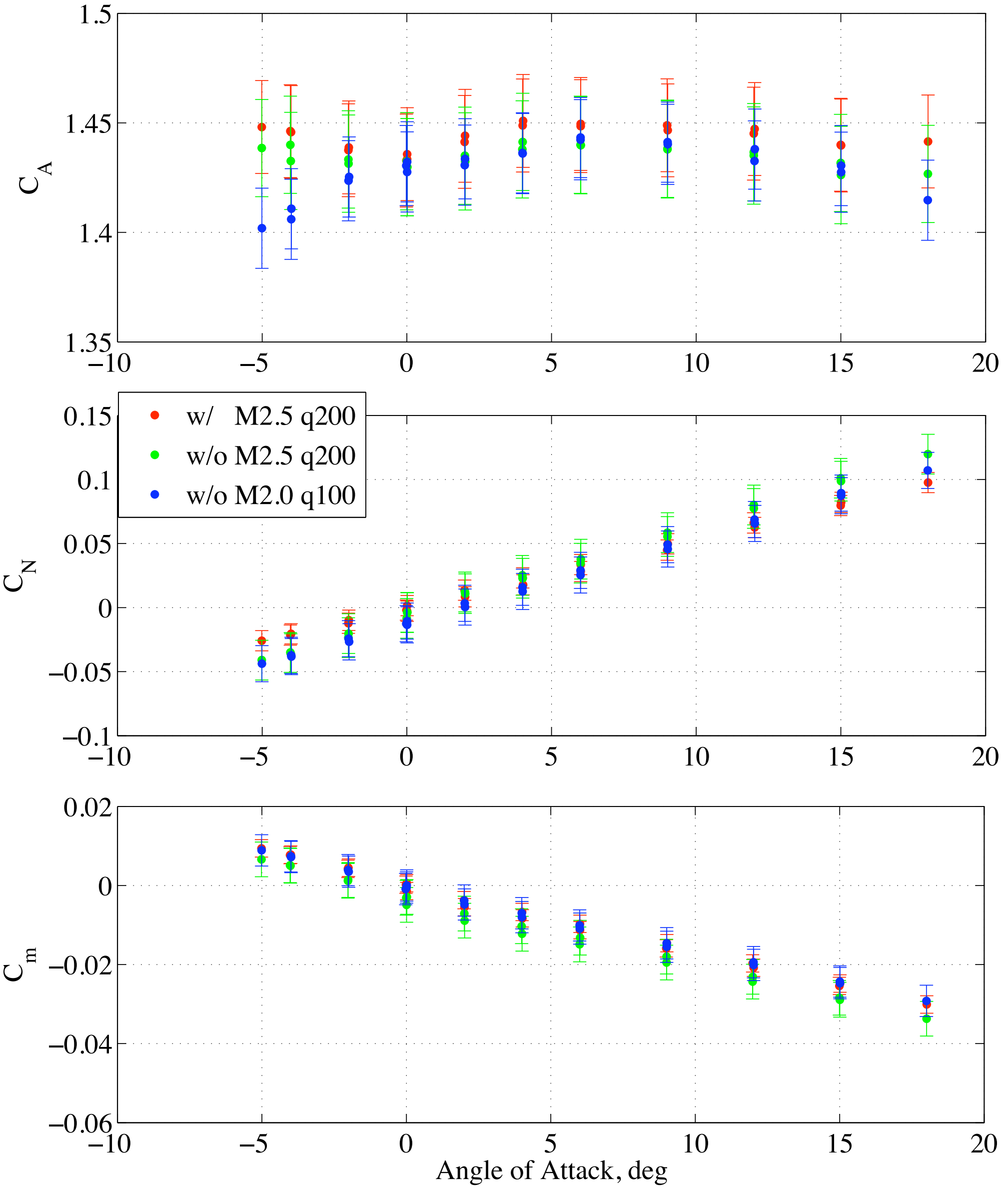

Figure 69: Static aerodynamic results for a semi-rigid models with and without anti-torque panels at Mach 2.5 and without anti-torque panels at Mach 2.0. Uncertainty bars correspond to 95% confidence intervals. Dynamic pressure (e.g. "q100") is shown in units of psf.

3.3.7.1 *Effects of Anti-Torque Panels*

Testing of models with and without anti-torque panels resulted in visible differences in the shape of the tension cone. Models with panels were observed to have a more forward torus and greater concavity in the tension shell. To examine the impact that this has on drag performance, the axial force coefficients of all model types at zero degree angle of attack are shown in Figure 70. It can be seen that although the presence of anti-torque panels appears to increase the drag of the inflatable model by almost 9%, the impact is negligible on the semi-rigid models. Though both the inflatable and semi-rigid models incurred greater concavity with anti-torque panels, it is likely that this did not produce any appreciable change in drag. Rather, it is more likely that in the case of the inflatable model the differences in measured axial force are due to the inflation tubes exerting a force on the model. For example, if the inflatable torus was constrained forward by the panels, this

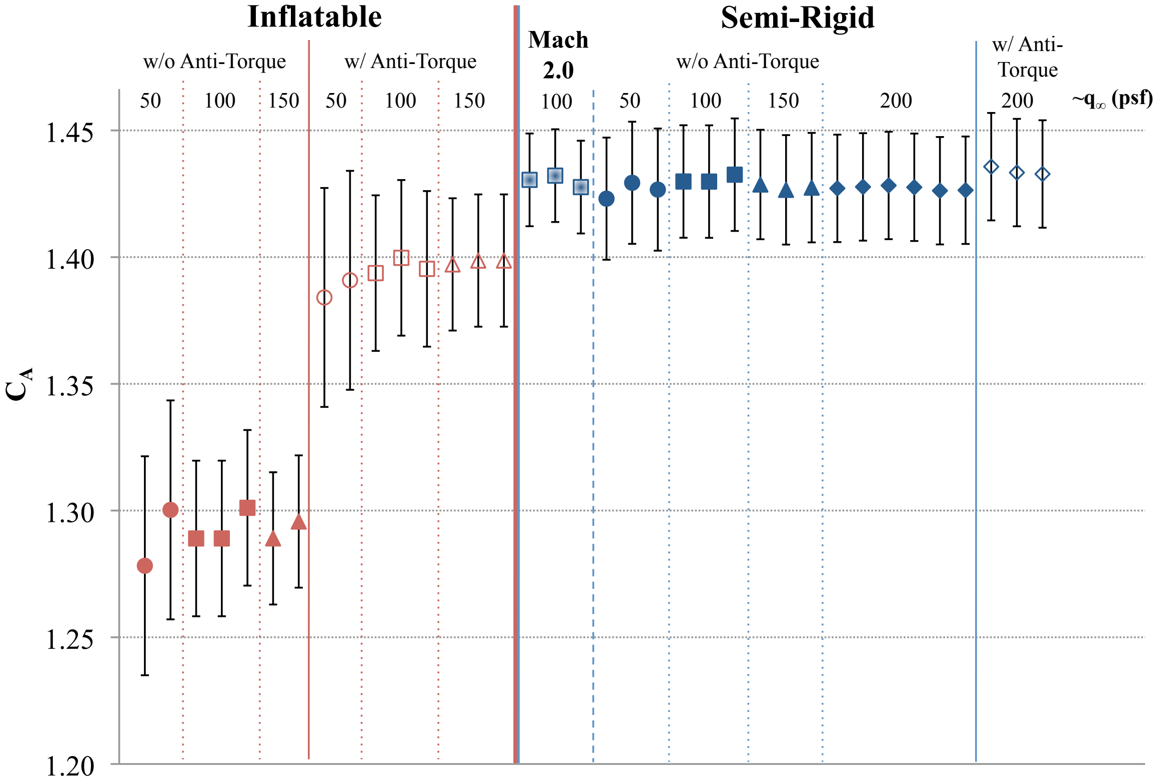

Figure 70: Axial force coefficient for models with and without anti-torque panels at zero degree angle of attack. All values are at Mach 2.5 unless otherwise indicated. Uncertainty bars correspond to 95% confidence intervals.

could cause the inflation tubes to also bend forward. This in turn would cause the inflation tubes to attempt to pull the torus further back, which would be measured as an increase in axial force. The inability to separate the inflation tubes from the metric portion of the balance may also contribute to the difference in axial force coefficients observed between the inflatable and semi-rigid models.

3.3.7.2 Comparison to Unitary Results

Provided in Figure 71 is a comparison of the static aerodynamics measured on the Unitary model with those measured on the semi-rigid model at Mach 2.5 and a Reynolds number of $\sim 1.0 \times 10^6$. Differences in measured axial force coefficients are less than 5% and decrease with increasing angle of attack. The largest differences occur in the measured normal force coefficients. Although the semi-rigid model was observed to remain mostly perpendicular to the sting at angle of attack, even a minor alignment to the freestream is sufficient to produce larger normal forces than would otherwise be seen. Since the total normal forces are already relatively small, this results in much larger normal force coefficient values. The larger normal forces also serve to shallow out the pitching moment slope when compared to the Unitary model.

Given the consistency of the measured axial force coefficients for both rigid and flexible models at several test conditions, it is useful to note that a 0° drag coefficient value of 1.40 - 1.45 would be appropriate for conceptual tension cone design purposes. Furthermore, static stability margin is sufficiently large so as to mitigate concerns about where axial location of the center of mass lies in the combined IAD/entry vehicle system.

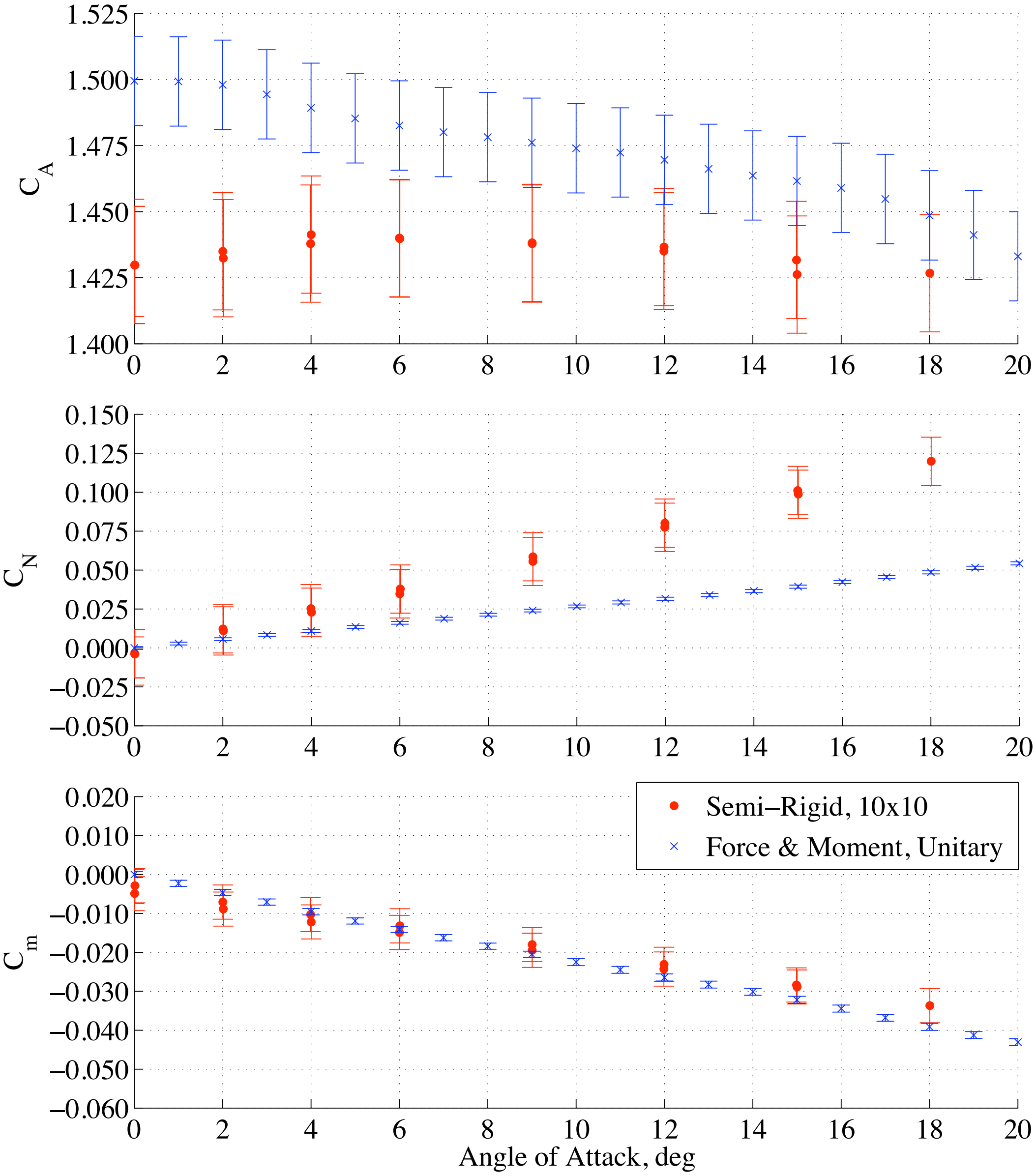

Figure 71: Comparison of static aerodynamics measured at Mach 2.5, $Re \sim 1.0 \times 10^6$ for the rigid Unitary model and semi-rigid 10x10 model. Uncertainty bars correspond to 95% confidence intervals.

3.3.8 Flow Field Observations

Schlieren imagery attained during testing was used to evaluate characteristics of the flow field. No flow instabilities were observed at any point during testing, including during model deployment and pressure sweeps. A stable, detached bow shock was observed at all times and no embedded shocks were seen. A caveat to the latter observation is that at large angles of attack the model was mostly out of the schlieren field of view.

The influence of the model type on the flow field is made evident by comparing schileren images of the different configurations. In particular, the outer mold lines of semi-rigid and inflatable models, both with and without anti-torque panels, were extracted from schlieren images along with the position of the bow shock. The results are shown superimposed in Figure 72.

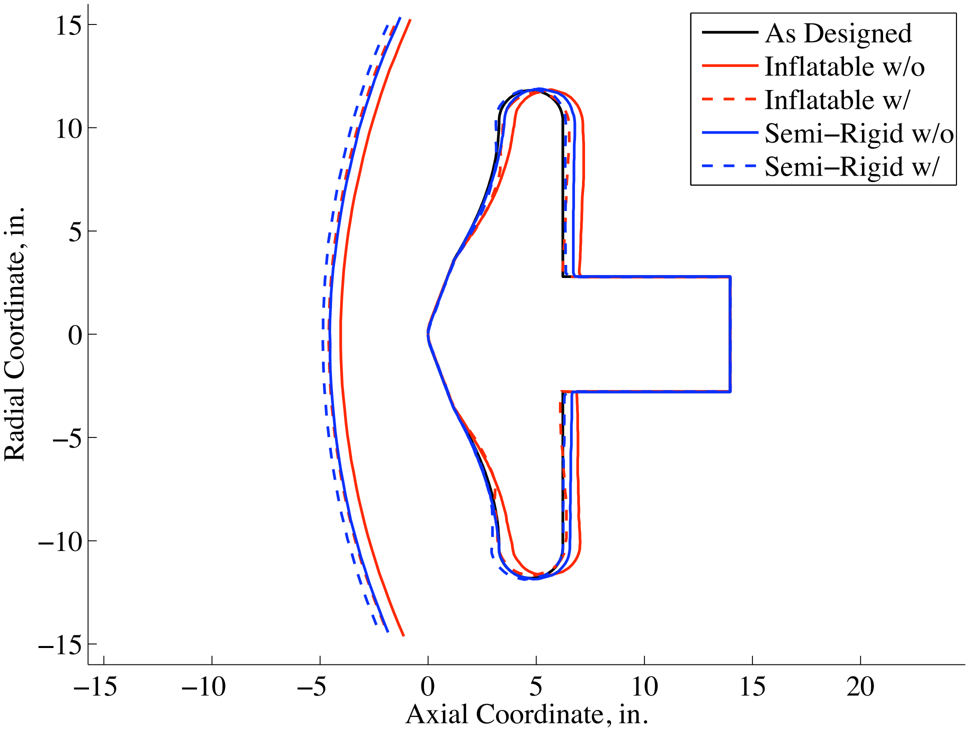

Figure 72: Comparison of outer mold lines and bow shock locations for each of the four different model configurations at Mach 2.5 and 0° angle of attack. Profiles are extracted from schlieren images taken at a free stream dynamic pressure of $\sim$200 psf for the semi-rigid models and $\sim$150 psf for the inflatable models. Note: “w/” and “w/o” designations refer to the inclusion of anti-torque panels.

As discussed previously, the presence of the anti-torque panels brought the torus forward and produced a slightly more concave tension shell. The location of the bow shock can be seen to be influenced primarily by the axial position of the torus and to a lesser degree by the concavity of the tension shell. The shape of the inflatable model without anti-torque panels is also seen to be the most swept-back.

3.4 Conclusions

This chapter presents the results of a successful wind tunnel test program that investigated the aerodynamic and structural performance of a tension cone supersonic inflatable aerodynamic decelerator. Testing of rigid force and moment models indicated favorable drag and stability performance throughout the supersonic flight regime with a zero degree angle of attack C_D of ~ 1.45 and a $C_{m_\alpha} \sim -0.00212$ deg^{-1}. Pressure distributions measured during rigid model testing provided insight into the influence of the geometry on the flow field. In particular, slope changes between the 70° sphere cone and the tension shell were seen to produce adverse pressure gradients on the leeward side of the model at high angles of attack. Despite this, there does not appear to be any evidence of flow separation in schlieren imagery or in measured pitching moments. Testing of textile inflatable and semi-rigid models provided consistent and favorable aerodynamic results. The addition of a set of anti-torque panels to the inflatable model was seen to dramatically reduce the inflation pressures required for complete deployment. Of particular significance in light of prior testing of tension cone models is that the flow field was observed to be stable at all test conditions for all models. This result underscores the successful design of a tension cone configuration that was free of large regions of separated flow or embedded shocks. The test program represents a significant advancement in the maturity of the tension cone configuration for use in planetary deceleration applications. The data from this test program serves as a valuable resource for the validation of tension cone aerodynamic, structural, and aeroelastic analyses.

CHAPTER IV

EVALUATION AND VALIDATION OF COMPUTATIONAL ANALYSES FOR SUPERSONIC TENSION CONE STATIC AERODYNAMIC PERFORMANCE

The future design and development efforts of supersonic IADs will rely heavily on computational analyses to accurately assess performance characteristics. Prior to their utilization, these computational tools must sufficiently demonstrate their suitability and accuracy in analyzing supersonic IADs. A key objective of the PAIDAE tension cone IAD wind tunnel test program was to acquire data useful for the validation of computational aerodynamic and structural analysis codes. This chapter presents the work performed in validating multiple CFD codes for supersonic tension cone analysis. The analysis is divided into two sections that address the capability of inviscid and viscous aerodynamic analyses to accurately predict force and moment coefficients, pressure distributions, and shock structure for a tension cone IAD. It should be noted that in the current context, validation is considered to be an assessment of the degree to which CFD can accurately reproduce the aerodynamic results of the wind tunnel tests discussed in Chapter 3. Although validation in this regard would be expected to provide insight into the ability to evaluate alternative IAD configurations and flight conditions, discretion is required in extrapolating the current results for that purpose.

4.1 Inviscid Computational Fluid Dynamics Comparison to Static Wind Tunnel Results

Prior studies on tension cone aerodynamics have definitively demonstrated that simple Newtonian impact methods are unsuitable for accurate prediction of surface pressures [23],[66]. A more advanced method, termed integral-relation theory or Belotserkovskii's method [8], that takes the governing non-linear partial differential equations and reduces them to a set of ordinary differential equations through several linear assumptions has also been used for analyzing tension cone aerodynamics. Pressure distributions derived using integral-relation theory [70] have shown reasonable accuracy for several variants of the tension cone [66]. However, this method appears to be limited in the types of geometries and conditions for which it is suitable [70]. One possible alternative for providing rapid analysis of tension cone geometries would be to use inviscid aerodynamics tools. An evaluation of this approach was performed using the Cartesian grid based code NASCART-GT. This effort focused on assessing the ability of axisymmetric inviscid aerodynamics to accurately predict the drag coefficients and pressures measured during the Unitary set of wind tunnel tests as well as the dominant flow features seen during Unitary and 10x10 testing.

4.1.1 Code Overview

Inviscid analysis of the tension cone was performed using the NASCART-GT code developed at the Georgia Institute of Technology [43],[44],[47],[48]. NASCART-GT is a solution-adaptive, Cartesian grid based analysis tool that provides automated generation of grids around axisymmetric, two-dimensional, or three-dimensional geometries. For this reason, it is particularly well-suited for providing rapid estimates of tension cone drag characteristics. Though capable of providing viscous analyses in the form of coupled Euler-integral boundary layer methods or full Navier-Stokes methods, for this research NASCART-GT was only utilized for inviscid analysis. Furthermore, execution of the code was limited to obtaining solutions for axisymmetric bodies at a 0° angle of attack.

4.1.2 Grid and Solution Development

Although NASCART-GT provides automated grid generation, several parameters are required for control of the grid resolution. A study of the grid resolution requirements for the present study was performed by varying the grid parameter *nbmin*, the minimum number of surface grid points placed along the longest body dimension. The analyzed configuration consisted of not only the basic tension shell outer mold line but also a sizable portion of the wind tunnel sting. For this reason, grid parameters were established for the tension cone and wind tunnel sting/wind shield independently and only those pertaining to the tension cone model were varied. As a result, the longest body dimension for the tension cone corresponded to the diameter of the wind tunnel model. A range of minimum surface grid points for the tension cone was evaluated from 64 to 2056, by powers of 2. The grids were evaluated using the freestream test conditions for the Mach 2.0, $Re = 1.0 \text{ x } 10^6$ test case from the Unitary portion of the wind tunnel test program.

Inviscid solutions were attained using a fixed time step and CFL number, meaning that finer resolution grids took successively smaller time steps for each iteration. Thus, rather than rely on iteration count, solution convergence requirements were assessed by evaluating the amount of solution time required to achieve a steady-state distribution of surface pressures across the forebody of the tension cone. The selection of surface pressure as a convergence criterion was based on the premise that a key source of validation data were the pressure distributions acquired from wind tunnel testing. Determination of the steady state pressure distribution was made through an examination of the maximum change in C_P for any single forebody grid point as well as the average change in C_P for the all forebody grid points. A plot of the results is provided in Figure 73. Based on the results in Figure 73 a solution time of 2 seconds was deemed sufficient for convergence. Examination of RMS residuals also indicated a decrease of at least 3 orders of magnitude for each grid resolution.

Final selection of the required grid resolution was made by examining the steady state pressure distribution for each grid at the converged solution time of 2 seconds. These distributions are shown in Figure 74. All examined grid resolutions are seen to converge to nearly the same steady state forebody pressure distribution, with only small deviations

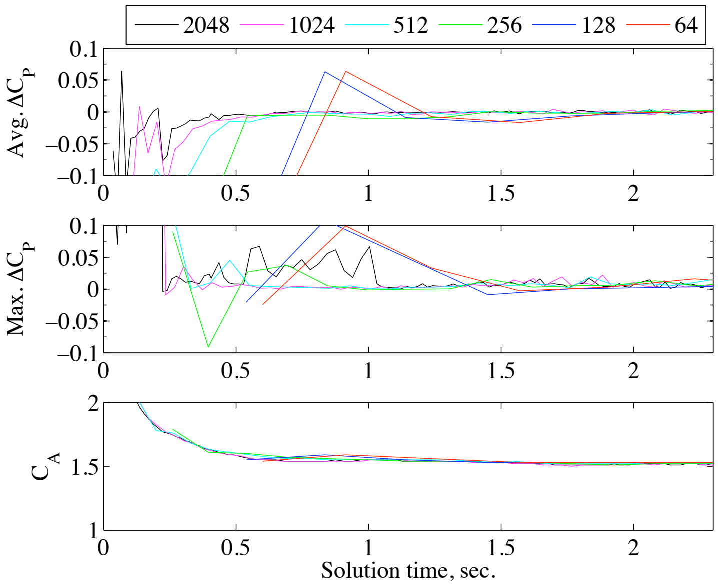

Figure 73: Variation in values of pressure coefficient of forebody grid cells and tension cone axial force coefficient as a function of solution time for multiple NASCART-GT grid resolutions. Grid resolution values correspond to the minimum number of grid points along the forebody of the tension cone. ΔC_P refers to the change in pressure coefficient at a grid cell between successive iterations.

being observed near the nose for coarser grids. Furthermore, all grids with forebody cell counts of 512 or greater have essentially identical pressure distributions. Based on these results all subsequent solutions were developed using grids with a minimum of 512 cells on the forebody of the tension cone geometry. A comparison of the initial Cartesian grid with the selected grid settings is shown in Figure 75 along with a final, adapted grid.

Solutions were advanced using a second-order accurate 2-stage, explicit time integration scheme. Flux reconstruction was performed using a second-order accurate, fully upwind, pressure weighted variation of the Advection Upstream Splitting (AUSM), AUSMPW+ [40].

It is worth noting that the final combination of grid resolution and convergence criteria was made with little consideration of the computational effort required to achieve a converged solution. Depending on the desired level of accuracy, coarse grids were observed to achieve values of axial force coefficient within a few percent of the converged, fine grid solutions. These coarse grid solutions required very modest computational effort; wall clock times of 20 minutes or less were typical on a single 3.0 GHz Intel E8400 processor.

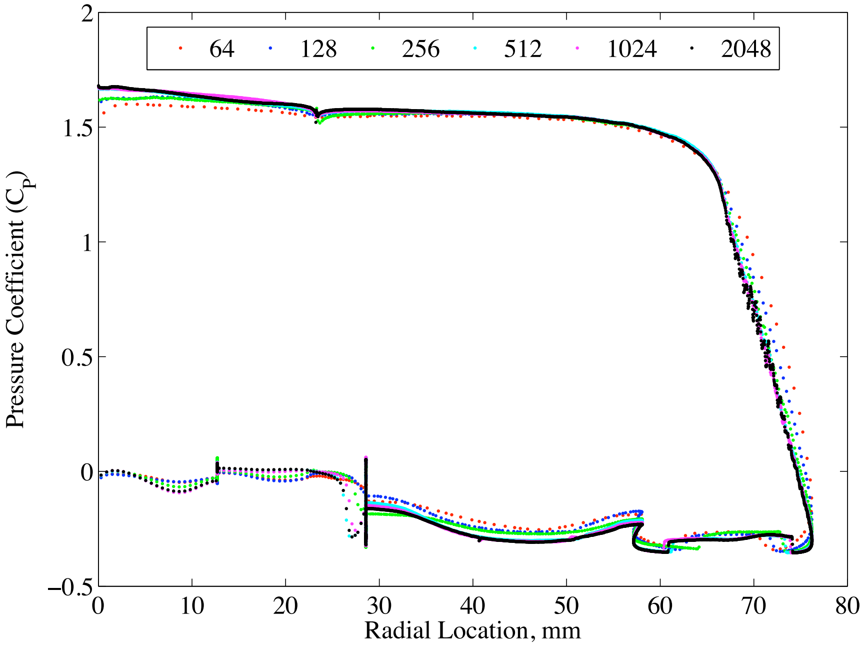

Figure 74: Steady state pressure distributions at a solution time of 2 seconds for several NASCART-GT grid resolutions.

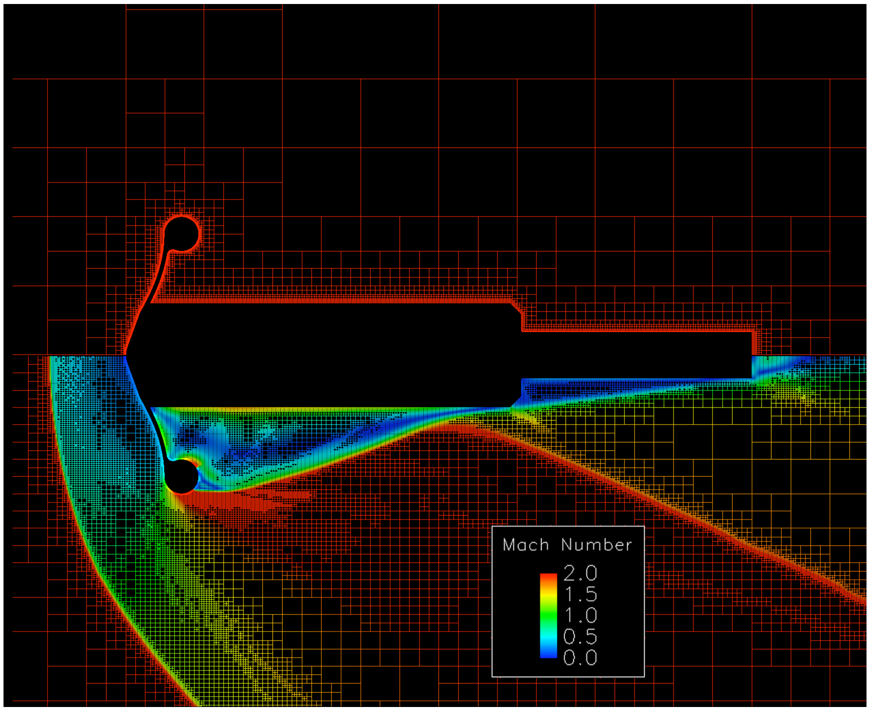

Figure 75: Computational mesh used for axisymmetric, inviscid analysis. Initial grid shown on top, adapted grid on bottom.

4.1.3 Computational Comparison to Unitary Results

Validation of the capability of inviscid aerodynamics for accurately predicting tension cone aerodynamics was performed in part by comparing pressure distributions and static aerodynamic coefficients calculated using NASCART with those values obtained during testing at the Unitary tunnel. The first of these comparisons is provided in Figure 76 in the form of a surface pressure comparison at each of the six Mach number test conditions. At lower Mach numbers (Figure 76(a)) predicted pressure coefficients are within the 95% uncertainty bounds across a majority of the forebody. Accuracy of the inviscid predictions on the shoulder region is seen to decrease slightly. Aft body pressures show considerably more variation than was evident during testing. However, the differences between computational and measured aftbody pressure coefficients are less than approximately 0.2 at all but the lowest Mach number. Pressure coefficient predictions at higher Mach numbers (Figure 76(b)) show even better agreement across the forebody and shoulder region. Aftbody pressure predictions are also improved but still show more variability than would otherwise be expected. The lack of agreement in aftbody pressures between the inviscid analysis and the measured values is attributed to the the flowfield in this region being heavily influenced by viscous phenomena. Though inviscid analysis is capable of predicting that recirculation occurs in the near aftbody region, the magnitude of the recirculation is generally over predicted by the lack of viscous damping. This results in lower, and more varied, pressures being predicted on the aftbody of the model.

The lower than actual aftbody pressures predicted by inviscid aerodynamics leads to an over prediction of the total drag provided, as seen in Figure 77. However, for the six cases analyzed, this difference is no more than 5% and in four of the cases is less than 1%. Noting that inviscid aerodynamics accurately predicted forebody pressures, an alternate comparison can be made of the forebody-only drag contribution. Estimates of the forebody-only drag coefficient are made by integrating the pressures measured on the Unitary pressure model and those predicted by CFD. These estimates are also shown in Figure 77. Differences in CFD-predicted and tunnel-measured values of this form of drag coefficient are seen to be less than 3% of the measured value and as close as 0.4%.

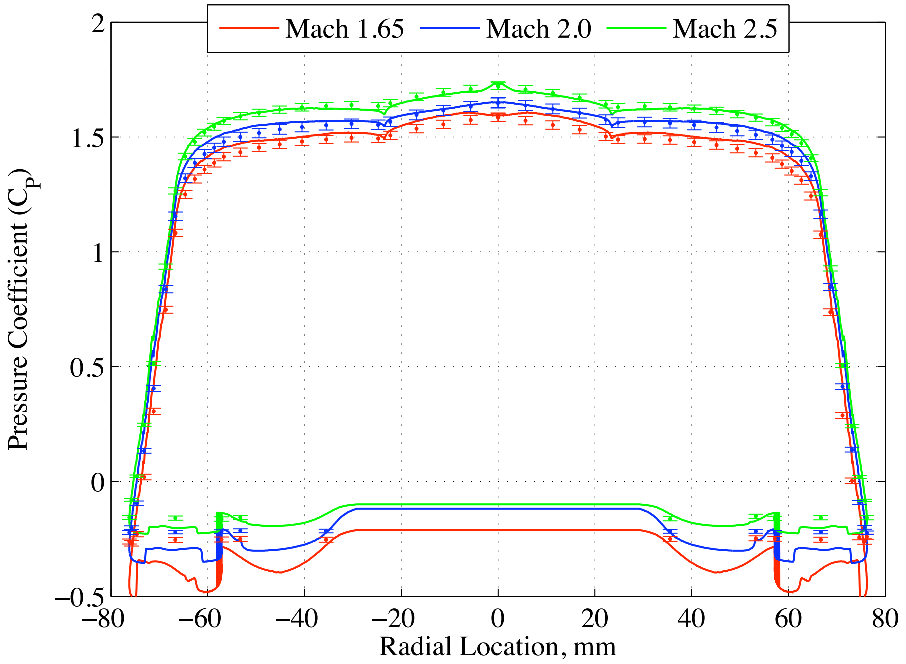

(a)

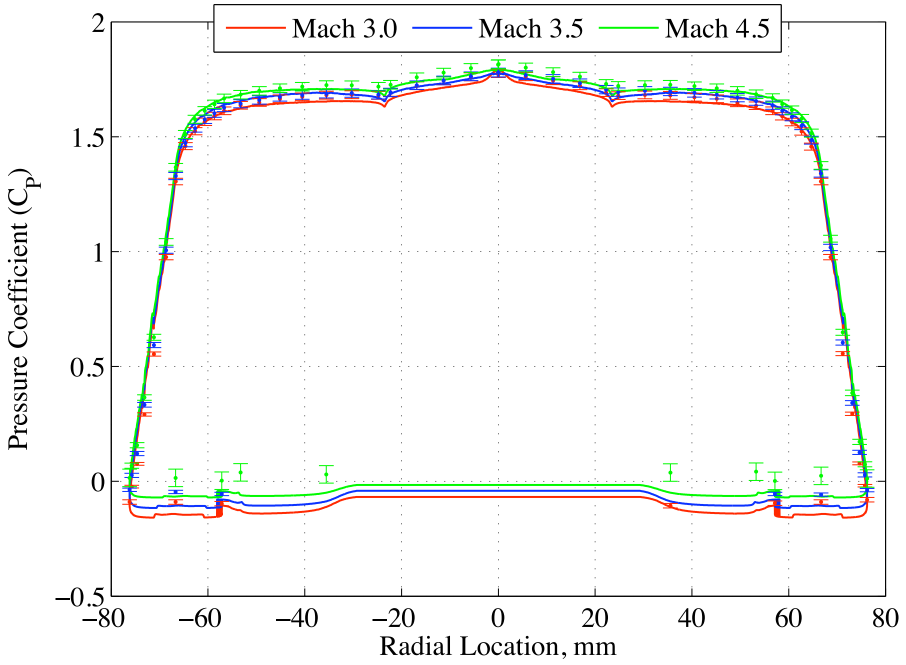

(b)

Figure 76: Comparison of surface pressure coefficients predicted by NASCART with those measured during wind tunnel testing at a 0° angle of attack and Reynolds number of 1.0 x 10^6. Solid lines correspond to CFD solutions.

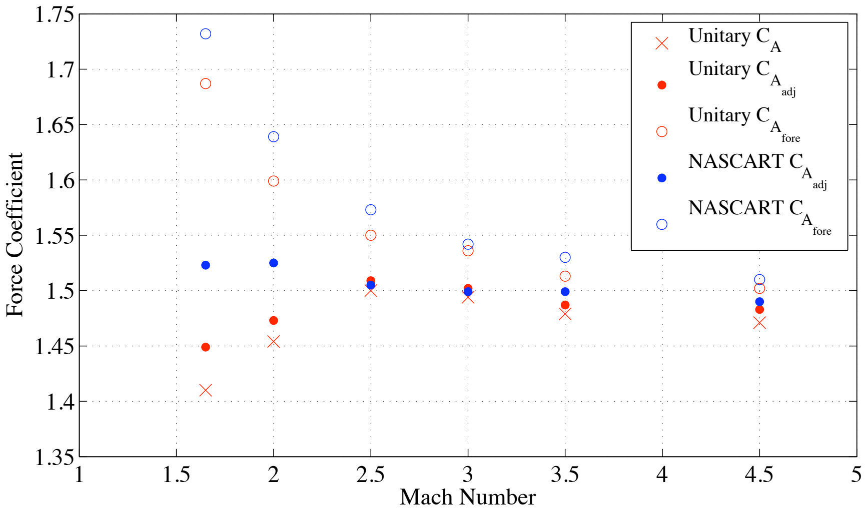

Figure 77: Measured and inviscid calculations of tension cone drag coefficient at a 0° angle of attack Reynolds number of 1.0 x 10^6.

The last comparison of inviscid CFD to results from testing at the Unitary wind tunnel entails an examination of the ability of CFD to capture dominant flow field features. Figure 78 is a comparison of the shock structure calculated by NASCART and that obtained from schlieren imagery. The computed solution provides excellent agreement in the location and curvature of the detached bow shock. However, other flow features such as the expansion and recompression details in the schlieren image are not resolved as well. This is not unexpected since these are features whose location and shape can be influenced by viscous interactions.

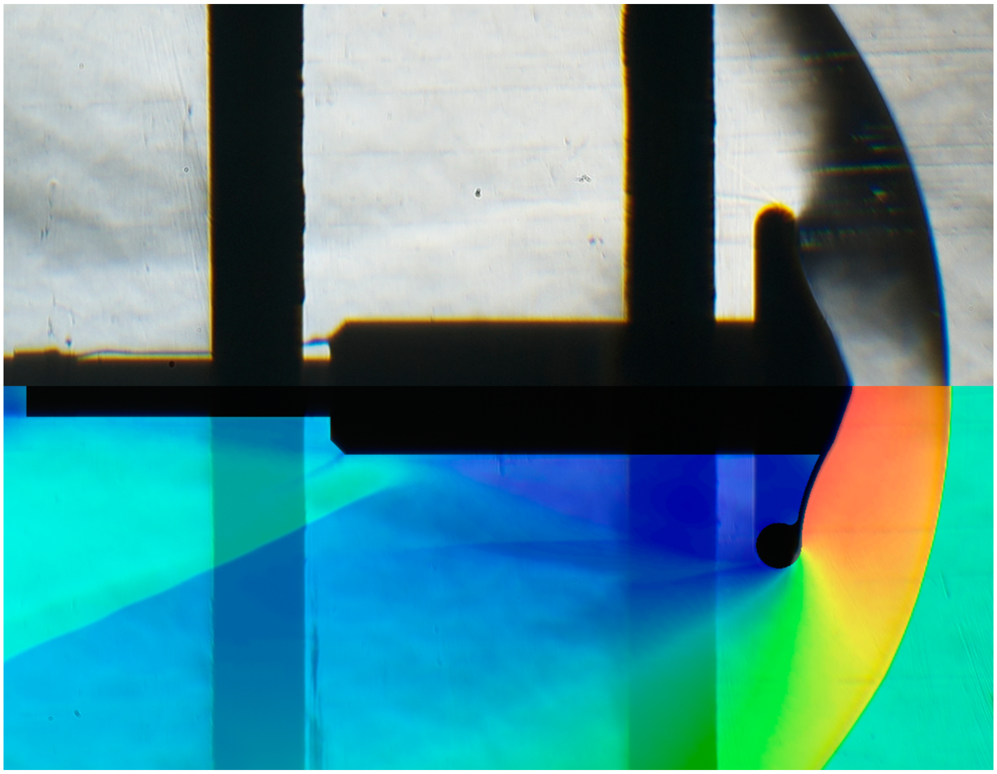

Figure 78: Comparison of shock structure from inviscid analysis to schlieren imagery at a 0° angle of attack for Mach 2.0 and Reynolds number of 1.0 x 10^6.

4.1.4 Computational Comparison to 10x10 Results

Inviscid CFD comparisons to results obtained during testing of the semi-rigid and inflatable tension cone models was predominantly limited to predicting principal flow field features and axial force coefficients. As noted in Chapter 3, during testing of the flexible tension cone models it was observed that the overall shape of the model under load varied with the model type (i.e. inflatable or semi-rigid, with or without anti-torque panels). Specifically, models with anti-torque panels were observed to have the torus positioned further upstream. The concavity of the tension shell was also seen to vary with model type. As a result of these variations four separate geometries were analyzed, an inflatable geometry and a semi-rigid geometry, both with and without anti-torque panels. Approximations of the overall shape of each model type were made by extracting an outer mold line (OML) from schlieren images taken during testing. Since the OML differed slightly between the bottom half and the top half, an axisymmetric shape was approximated as an average of the two. It should be noted that these derived OML's are a rough, axisymmetric approximation of the actual tension cone geometry. Features such as the scalloping of the tension shell and the segmented nature of the torus are not captured. However, this approach was chosen as it allowed for first-order insight into how well an inviscid analysis could capture the sensitivity of the bow shock shape and position as a function of model type and the pressures that resulted from the variations in OML.

A comparison of the schlieren derived bow shock position to that obtained from NASCART is shown in Figure 79 for the inflatable model and in Figure 80 for the semi-rigid model. Overall the agreement in bow shock shape and position is seen to be very good. The complexity of extracting the exact bow shock position and OML from schlieren imagery, and from CFD for that matter, likely means that the predicted bow shock positions would be well within the uncertainty of the extracted positions.

A comparison of the predicted and measured drag coefficients for the four model types is provided in Table 23. As with the Unitary cases, the total predicted drag coefficients are slightly higher than those measured, again likely a result of over expansion around the shoulder and lower than actual aftbody pressures. Since no surface pressure measurements

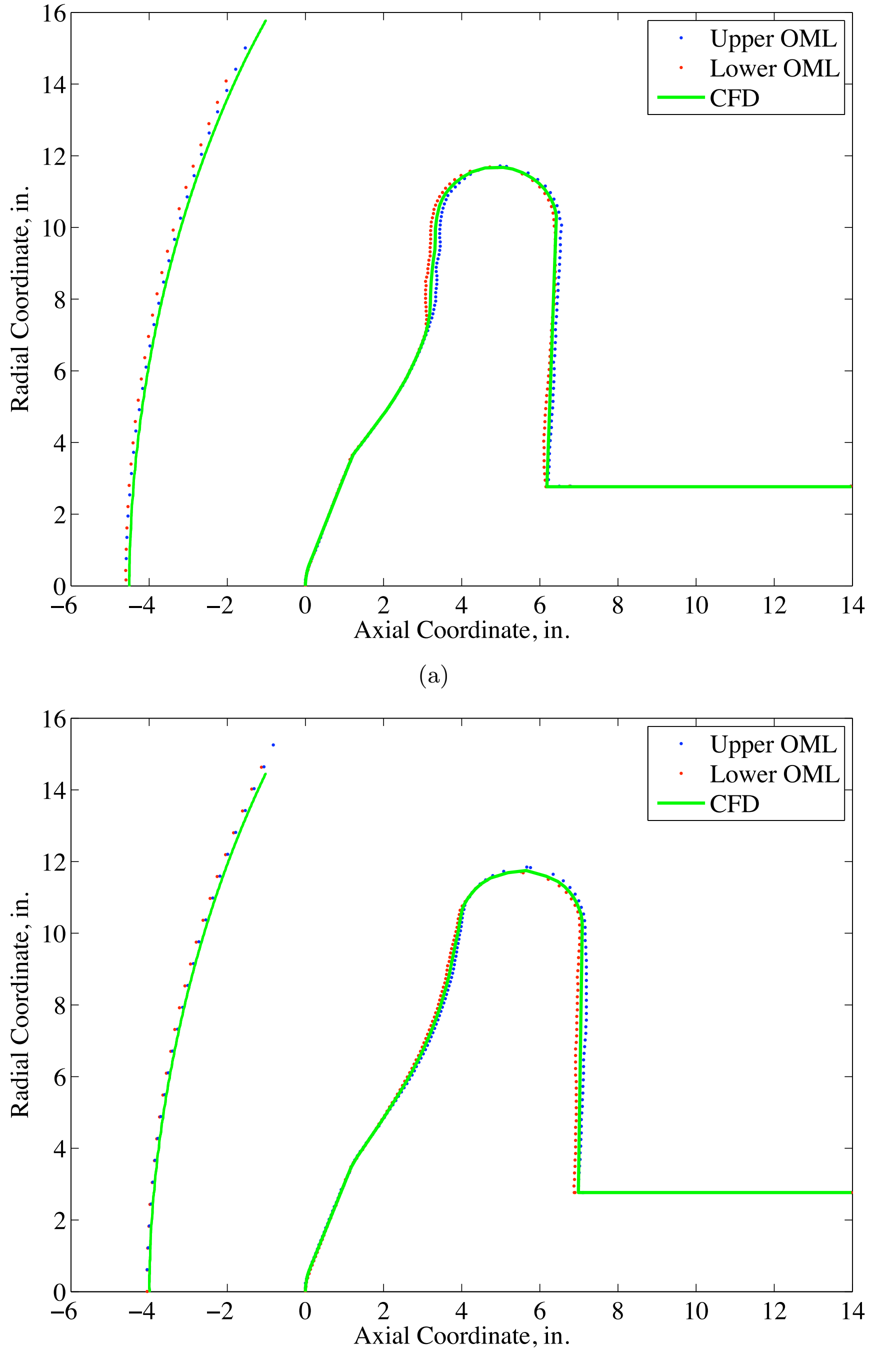

(a)

(b)

Figure 79: Comparison of inviscid CFD predicted and actual bow shock shape and position for the inflatable model with (a) and without (b) anti-torque panels. Freestream conditions are approximately Mach 2.47, 0° angle of attack, and Reynolds number of 1.6 x 10^6.

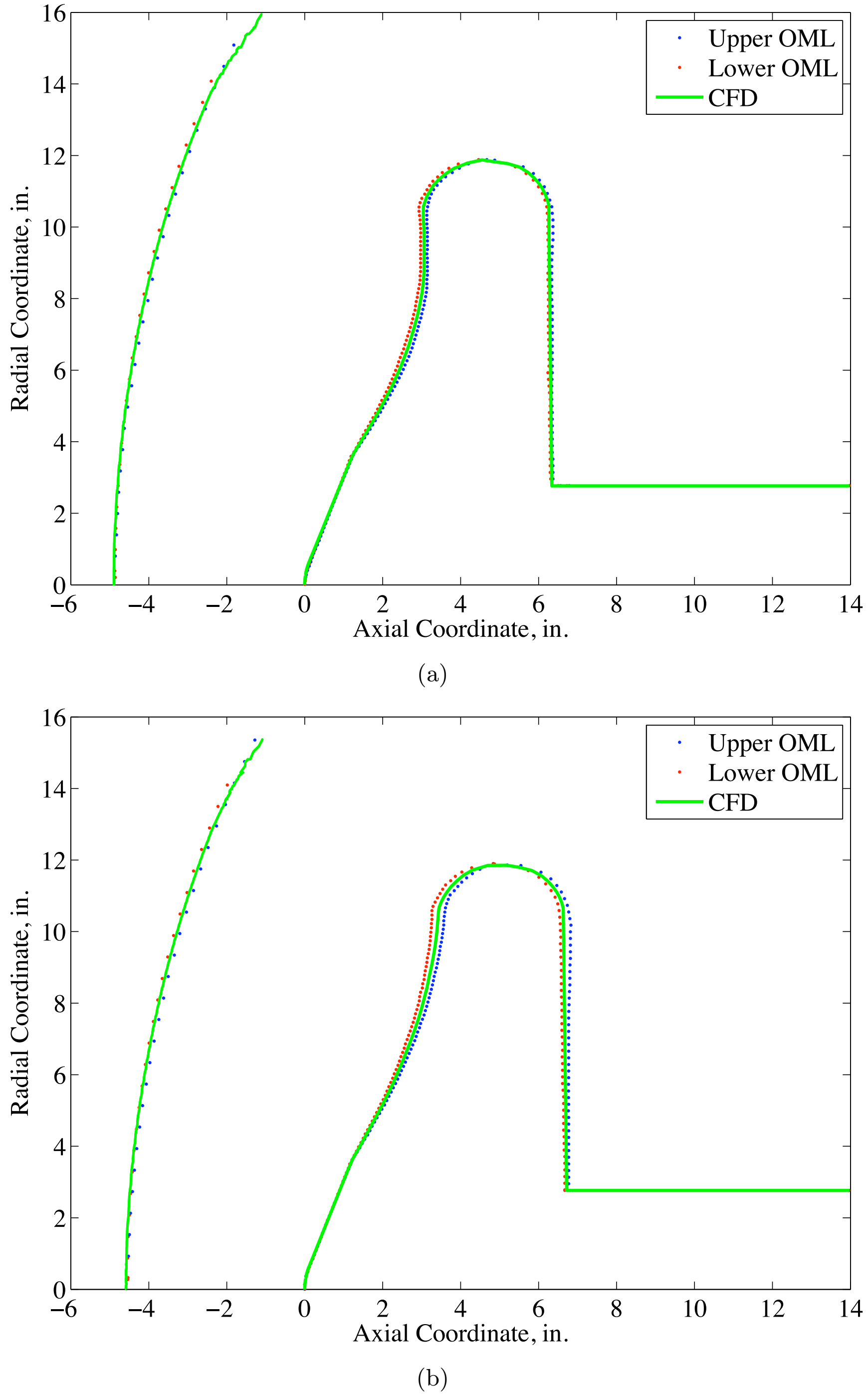

Figure 80: Comparison of inviscid CFD predicted and actual bow shock shape and position for the semi-rigid model with (a) and without (b) anti-torque panels. Freestream conditions are approximately Mach 2.47, 0° angle of attack, and Reynolds number of 2.1 x 10^6.

of the flexible models were taken during 10x10 testing, it is not possible to compare forebody-only drag predictions.

Table 23: Inviscid CFD predicted and measured drag coefficients for the inflatable and semi-rigid tension cone models.

	Inviscid CFD		10x10	
Model Type	$C_{A_{adj}}$	$C_{A_{fore}}$	C_D	Uncertainty
Inflatable w/	1.474	1.515	1.399	.0261
Inflatable w/o	1.487	1.521	1.289	.0261
Semi-Rigid w/	1.525	1.556	1.436	.0212
Semi-Rigid w/o	1.499	1.539	1.427	.0212

The implication of the variation in tension shell concavity and torus position to the surface pressure is examined in Figures 81 and 82. Although multiple smoothing algorithms were applied to the schlieren derived OML's, small pressure perturbations due to geometrical variations are still evident. In the case of the inflatable models (Figure 81) the presence of anti-torque panels moves the torus further upstream and results in higher pressures over the innermost regions of the tension shell. A small adverse pressure gradient is also evident, though no flow separation was visible in the schlieren imagery. Towards the periphery of the model the pressures are seen to decrease sooner for the anti-torque panel model. For the semi-rigid models (Figure 82) the differences in pressures are somewhat less. The greater concavity of the anti-torque model results in a small region over the center of the tension shell in which the pressures are approximately 5% higher.

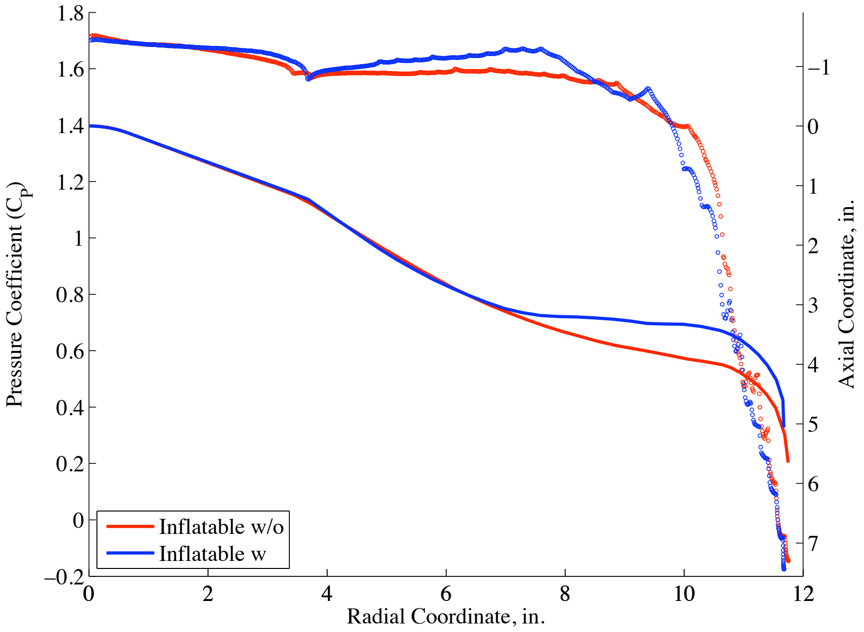

Figure 81: Inviscid CFD predicted forebody surface pressures for the inflatable tension cone model with and without anti-torque panels. Note: Lower curves represent forebody OML.

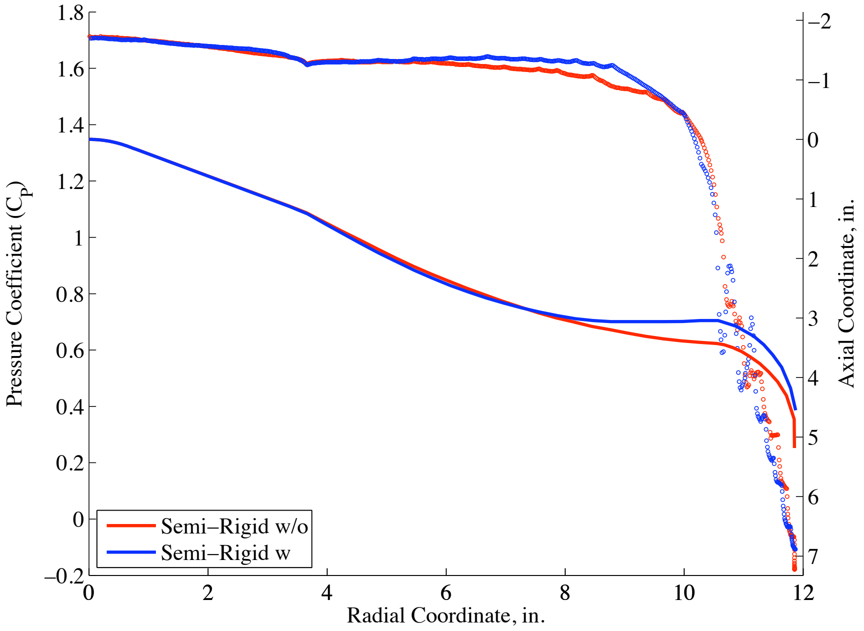

Figure 82: Inviscid CFD predicted forebody surface pressures for the semi-rigid tension cone model with and without anti-torque panels. Note: Lower curves represent forebody OML.

4.2 Viscous Computational Fluid Dynamics Comparison to Static Wind Tunnel Results

The preceding sections demonstrated that inviscid aerodynamic computations can provide good estimates of the zero degree angle of attack drag performance of supersonic tension cone decelerators. However, some deficiencies in predictive capability were evident, particularly in the areas of aftbody pressures and total drag. Whereas an inviscid analysis can be used for basic predictions of surface pressure, more complex flow phenomena such as boundary layer development and flow separation require that viscous terms be accounted for. Thus, viscous simulations of the rigid model Unitary testing were conducted. As with the inviscid analysis, these simulations focused on matching the static aerodynamic coefficients, surface pressures, and dominant flow field features. The complexity of the simulations was further increased by analyzing three dimensional models at multiple angles of attack.

4.2.1 Code Overview

Viscous CFD analysis was performed using the Reynolds Averaged Navier-Stokes code OVERFLOW [17],[59]. Originally developed as a rewrite of the F3D/Chimera code, OVERFLOW utilizes overset structured grids for near-body volumes and a Cartesian grid for off-body volumes. This overset approach has the advantage of simplifying the grid generation process since different grid blocks are not required to align with each other in any particular manner. This aspect allows for many of the grid generation processes to be scripted and performed in a more automated manner than typically possible, an approach initially taken in the current study. Overset grids are not required for OVERFLOW and in later simulations only a single structured grid was used. Solutions were generated using two separate versions of the code. A developmental release of version 2.1i was used for simulations that utilized the three-equation Lag turbulence model. In all other simulations, version 2.1t was used.

4.2.2 Grid Development and Setup

Due to difficulties discussed later, two separate sets of grids were incorporated into the CFD simulations. Initial simulations utilized 6 body-fitted structured grids and over 100 off-body Cartesian grids. Investigations into grid resolution requirements were focused on the initial surface-normal grid spacing and stretching ratios. Initial spacing values were chosen to provide three distinct values of the y^+ grid spacing parameter: 1, 10, and 100 with resulting cell counts of approximately 16 million, 10 million, and 8 million respectively. As a rule of thumb, a y^+ value of 1 is often chosen to place grid cells within the laminar sublayer of the boundary layer. Though this is important for capturing viscous shear forces, in the current context it is considered a conservative value as shear stresses are not expected to have measurable contributions to the static aerodynamic coefficients of the Unitary tension cone models. Solutions generated using the three grids at a Mach number of 2.0 produced no discernible differences in predicted surface pressures and identical C_D values of 1.42. Based on this outcome, and the availability of significant computational resources in the form of NASA's Columbia Supercomputer, subsequent simulations with an overset grid used the finest of the the grids evaluated. A visualization of this grid is provided in Figure 83.

Solutions were advanced using a local time step that varied with grid cell size. Thus, relying on a fixed solution time to determine convergence, as was done with the inviscid cases, was not feasible. Rather, solution convergence was determined through examination of the iteration histories of C_A, C_N, and C_m as well as examining individual grid residuals. For nearly all cases run with the overset grids, 3000 iterations was observed to be sufficient to converge the aerodynamic coefficients to at least 3 significant figures, as seen in Figure 84. A nominal value of 4000 iterations was used to allow for additional reduction in grid residuals, which varied from grid to grid but generally were seen to be four orders of magnitude lower than for the first iteration.

Complications in generating reliable solutions at the higher Mach numbers of 3.5 and 4.5 led to the development of a second set of grids provided by the NASA Langley Research Center. These grids consisted of a single-block, structured grid that was initially developed

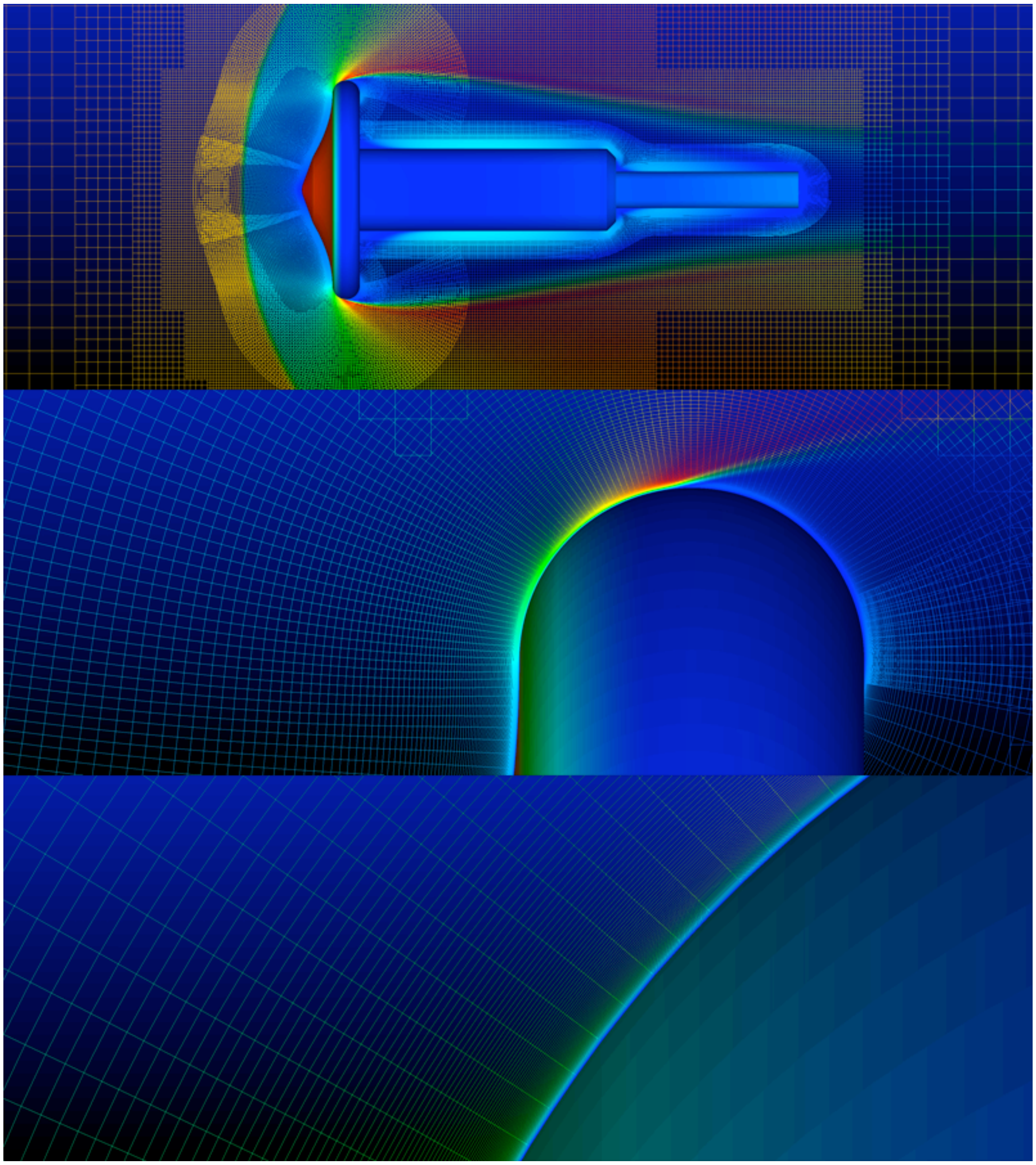

Figure 83: Three views of the baseline overset grids used in viscous OVERFLOW analyses.

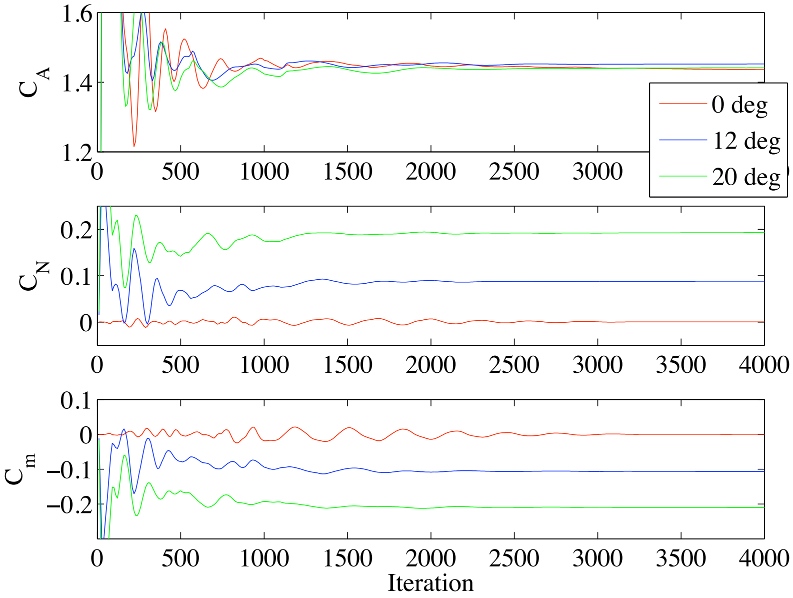

Figure 84: Static aerodynamic coefficient convergence histories for a Mach 2.0 overset grid case.

and subsequently adapted using the Langley Aerothermodynamic Upwind Relaxation Algorithm (LAURA) CFD code. Using LAURA, shock-aligned grids were developed for Mach numbers of 1.65, 2.50, 3.50, and 4.50 at angles of attack of 0°, 12°, and 20°. To simplify grid development, the grid was developed only for the forebody portion of the geometry. Although a detailed grid study was not performed on these grids, the grids were developed as if they would be used for estimates of heat transfer and subsequently placed a greater number of cells closer to the body than would otherwise be needed. The initial grid spacing yielded an estimated y^+ value of 0.15. Grid cell count was approximately 2.5 million. The reduced number of grid cells, versus the overset grids, is predominantly due to the large number of Cartesian off-body grid cells present in the overset grids. A example of this type of grid is shown in Figure 85.

Over the course of the study solutions were developed assuming both fully laminar and turbulent flow. For turbulent flow calculations, two separate turbulence models were utilized. The first was Menter's two-equation shear-stress transport (SST) model [53]. This model represents a hybrid version of the two-equation k-ω and k-ϵ models in that it utilizes the k-ω model near the wall and transitions to the k-ϵ model off the wall. The

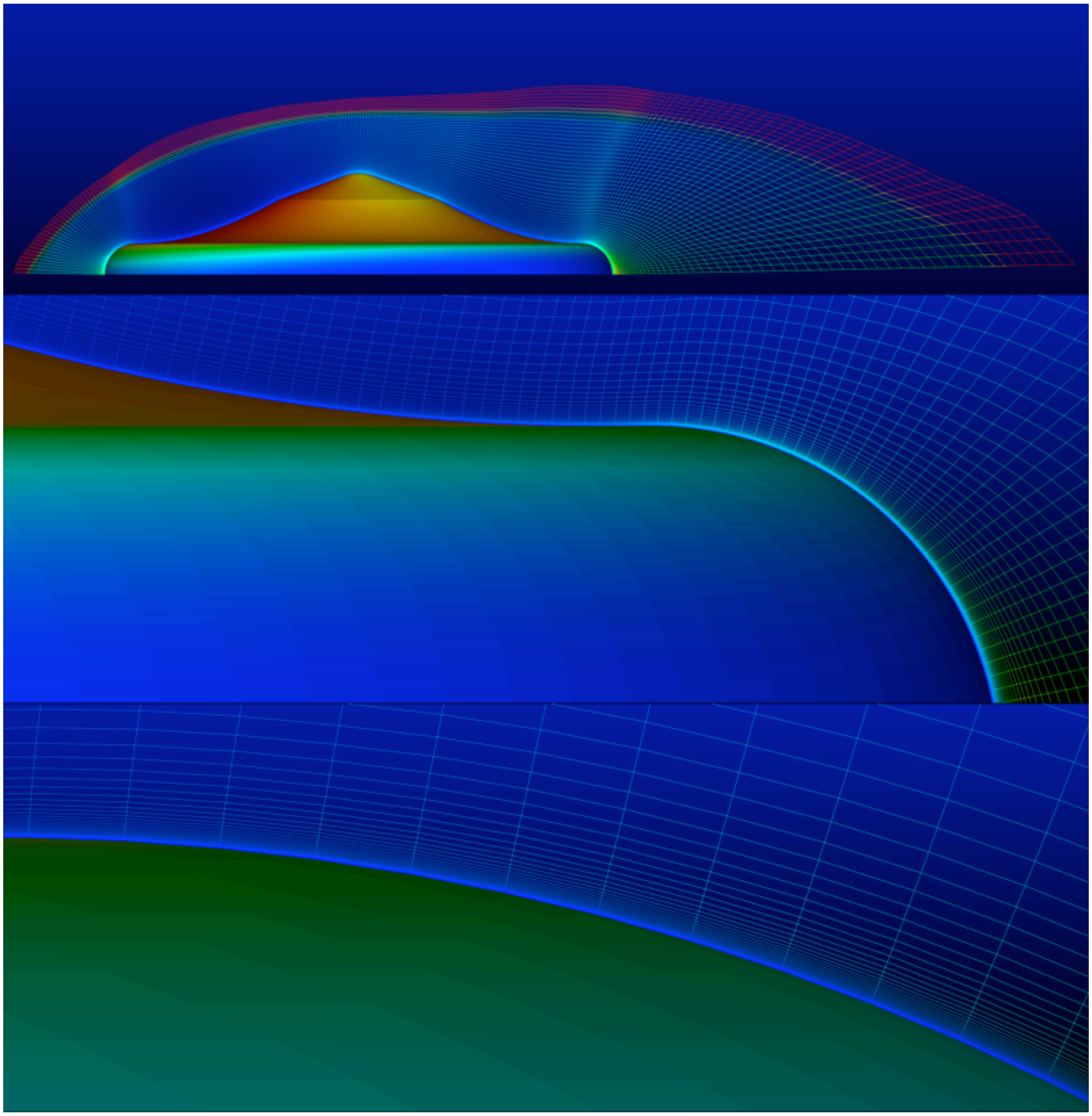

Figure 85: Three views of the LAURA generated, shock-aligned grid for Mach 4.5 and 20° angle of attack.

second turbulence model used for a majority of the simulations was the three-equation Lag turbulence model [60], [61]. The Lag model is a more recent modification of the basic two-equation k-ω turbulence model that adds a third equation to better model non-equilibrium effects for the eddy viscosity. The selection of this model was based on a prior study that noted its effectiveness at predicting supersonic aerodynamic performance of an Apollo-type blunt body [18].

All solutions were advanced using a Beam-Warming block tridiagonal implicit scheme. Flux terms were calculated using a 2nd order accurate central difference scheme. OVERFLOW solutions were computed in 16-processor parallel mode on NASA's Columbia Supercomputer. Typical wall-clock times for convergence of the initial overset grids were roughly 4-6 hours and 1-1.5 hours for the shock-aligned grids. The large difference in computation time is likely due to the greater number of cells used in the overset grids than in the single shock-aligned grid. Furthermore, the computation time for the shock-aligned grid does not include the initial time required to mature the solution sufficiently to allow for shock-alignment.

4.2.3 Computational Comparison to Unitary Results with Body-Fitted Overset Grids

The following pages present comparisons between the surface pressure coefficients obtained using the overset grids and Lag turbulence model with those measured during testing of the pressure model at the Unitary wind tunnel. At Mach numbers up to 3.0 (Figures 86 - 89) nearly perfect agreement is seen between the CFD and wind tunnel results at each of the three pressure port spoke locations. Relative to the inviscid results shown earlier, the viscous simulations are shown to accurately capture the drop in pressure that results from expansion around the shoulder as well as subtle variations in aft body pressure versus angle of attack. Leeward forebody pressures at angle of attack on the 0° spoke are shown to replicate the adverse pressure gradient seen in the vicinity of the sphere cone/tension shell interface (approximately the 23 mm radial location).

Beginning at the Mach 3.0, 20° angle of attack case the CFD predictions begin to deviate from the experimental results. Oscillations in surface pressure are initially observed on the windward pressure ports but as Mach number is increased the oscillations appear on leeward pressure ports as well. The oscillations in these steady-state solutions are indicative of large areas of flow separation. Since flow separation was not observed during testing via either schlieren imagery or real time display of the surface pressures, this result was not considered accurate. Attempts at resolving these differences initially focused on incorporating alternative turbulence models, utilizing different numerical schemes, refining the grid around the body, addition or adjustment of various dissipation parameters, alteration of boundary conditions, and adjustment of the freestream flow parameters, none of which produced appreciable improvements. In discussion with OVERFLOW code developers it was indicated that the similar behavior had been observed in prior, unpublished simulations of blunt bodies at Mach numbers between 3 and 5. In those cases, the difficulties arose because of stair-casing of the bow shock that occurred when the body-fitted structured grids were not well aligned with the bow shock. As a result, non-physical flow oscillations were generated through the bow shock that strongly influenced the surface pressures. Upon closer inspection, similar characteristics were observed in the tension cone solutions. Shown

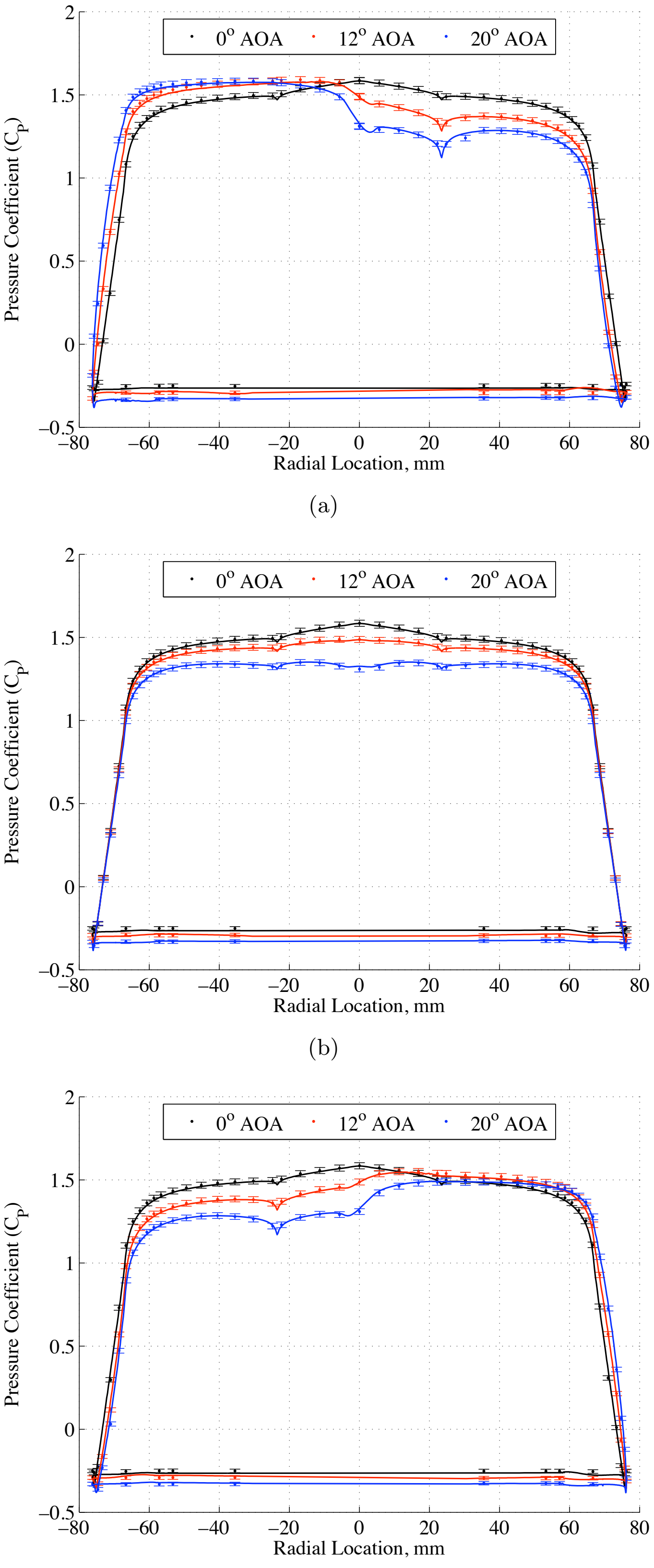

(a)

(b)

(c)

Figure 86: Comparison of OVERFLOW-predicted and measured pressure distributions at Mach 1.65 and a Reynolds number of 1.0 x 10^6 for the (a) 0°, (b) 90°, and (c) 225° spokes. Solid lines correspond to CFD solutions.

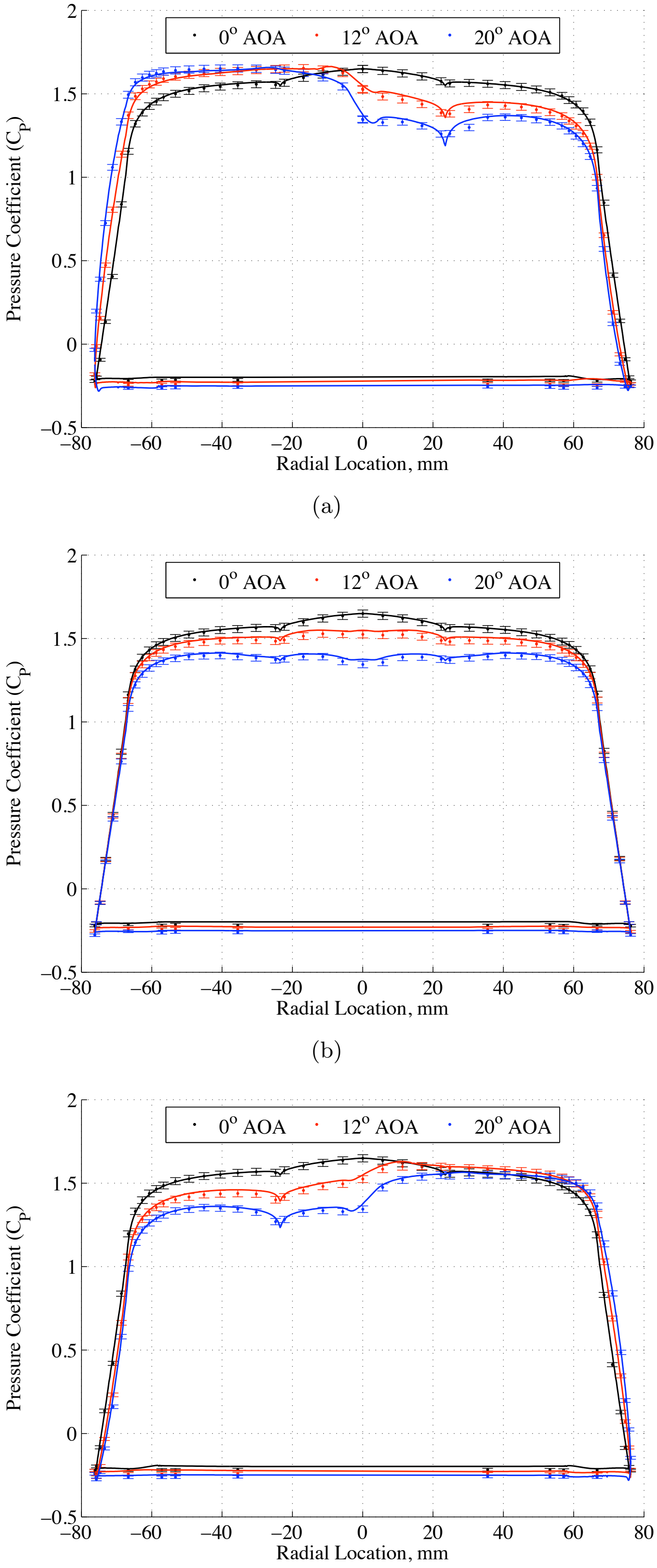

(a)

(b)

(c)

Figure 87: Comparison of OVERFLOW-predicted and measured pressure distributions at Mach 2.0 and a Reynolds number of 1.0 x 10^6 for the (a) 0°, (b) 90°, and (c) 225° spokes. Solid lines correspond to CFD solutions.

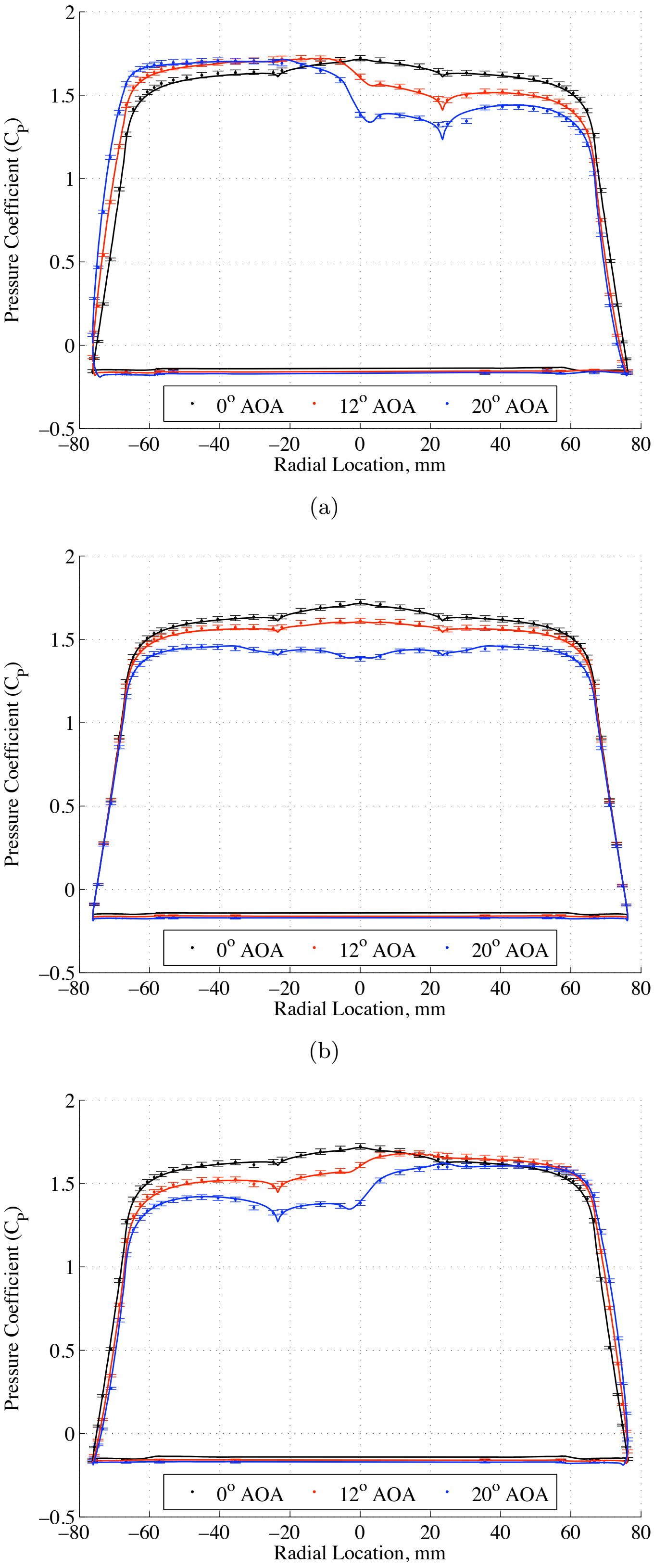

(a)

(b)

(c)

Figure 88: Comparison of OVERFLOW-predicted and measured pressure distributions at Mach 2.5 and a Reynolds number of 1.0 x 10^6 for the (a) 0°, (b) 90°, and (c) 225° spokes. Solid lines correspond to CFD solutions.

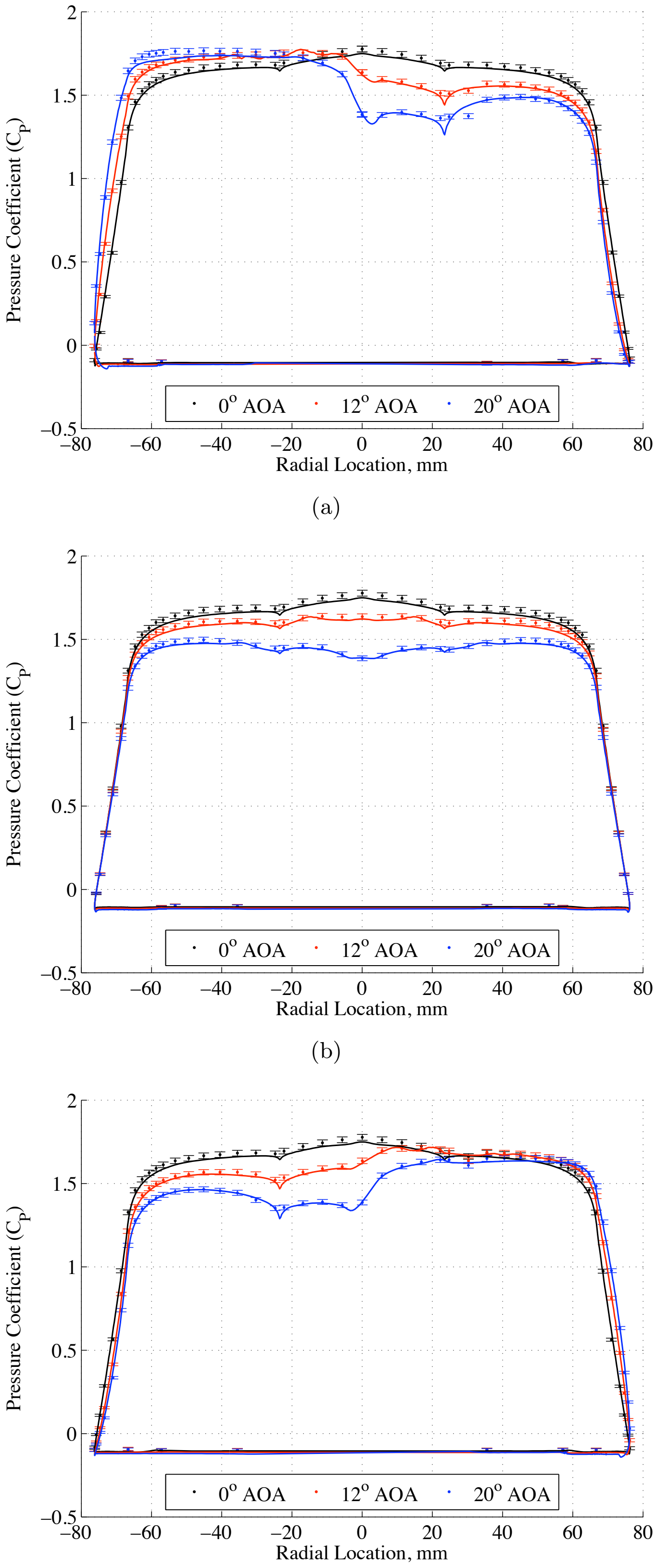

(a)

(b)

(c)

Figure 89: Comparison of OVERFLOW-predicted and measured pressure distributions at Mach 3.0 and a Reynolds number of 1.0 x 10^6 for the (a) 0°, (b) 90°, and (c) 225° spokes. Solid lines correspond to CFD solutions.

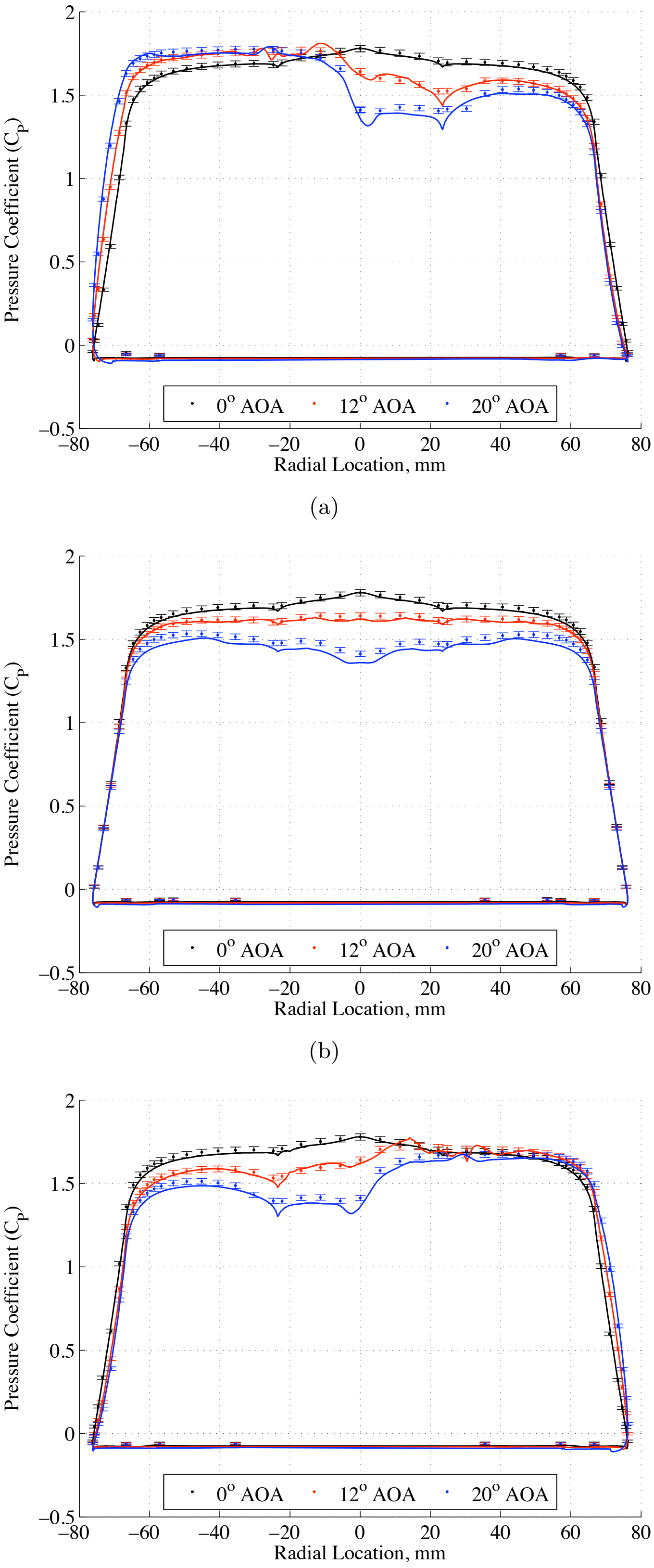

(a)

(b)

(c)

Figure 90: Comparison of OVERFLOW-predicted and measured pressure distributions at Mach 3.5 and a Reynolds number of 1.0 x 10^6 for the (a) 0°, (b) 90°, and (c) 225° spokes. Solid lines correspond to CFD solutions.

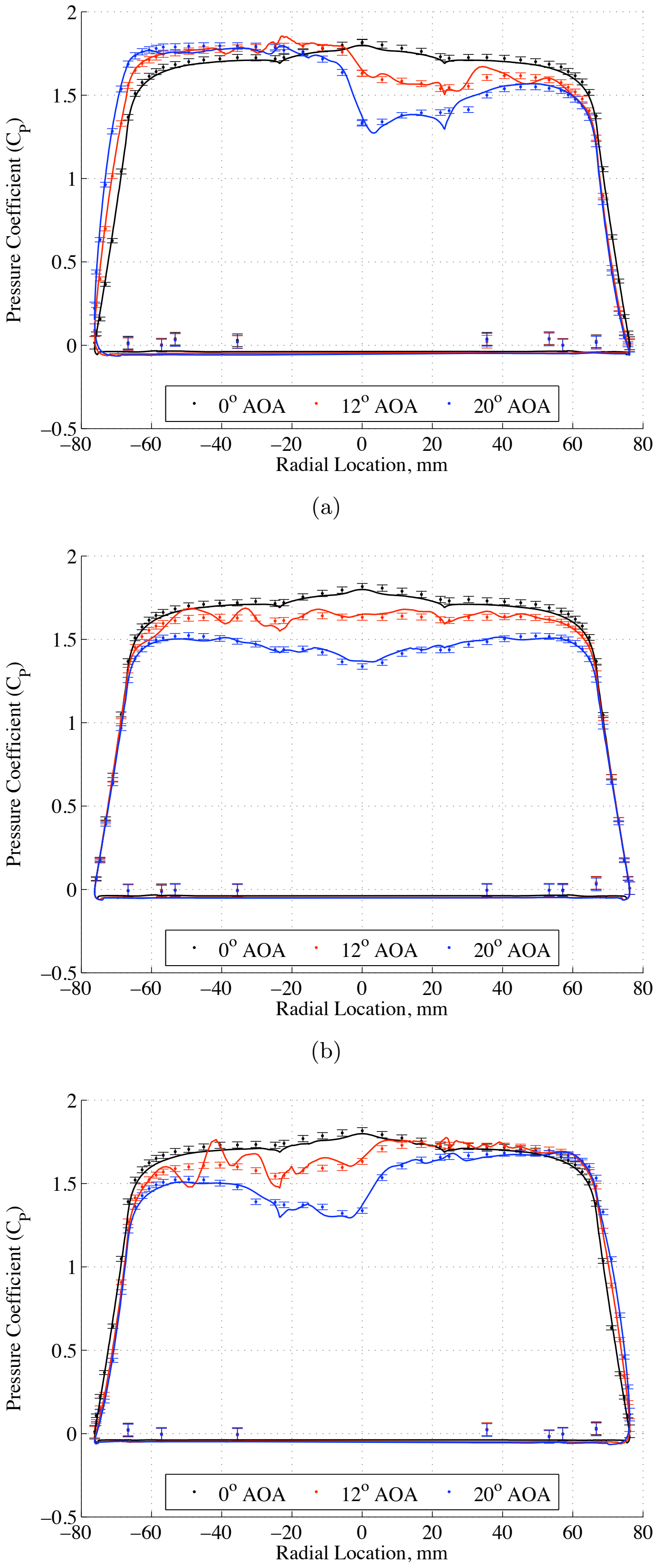

(a)

(b)

(c)

Figure 91: Comparison of OVERFLOW-predicted and measured pressure distributions at Mach 4.5 and a Reynolds number of 1.0 x 10^6 for the (a) 0°, (b) 90°, and (c) 225° spokes. Solid lines correspond to CFD solutions.

in Figure 92 are Mach contours for the Mach 3.5, 20° angle of attack solution. The color scale has been adjusted so as to accentuate the presence of oscillations emanating from the bow shock over the stagnation region of the model. Also evident in the figure is the degree to which non-alignment of the grid to the bow shock results in grid cells cutting through the shock at large angles and producing discrete jumps in the shock position. Although grid/shock misalignment is present at lower Mach number solutions as well, the strength of the shock is insufficient to cause discernible effects on the surface pressures.

The solution employed in the prior blunt body study, and explored in this study, was to align the grid to the bow shock. Because OVERFLOW does not presently contain shock alignment routines, an approach was utilized in which a separate CFD code, LAURA, would produce initial solutions and adapt a structured grid to those. The adapted grids were then used in later OVERFLOW computations to investigate the effectiveness of this approach and to address the issue of predictions of flow separation at high angles of attack. The results of this investigation are presented in a later subsection.

Calculations of static aerodynamic coefficients at Mach numbers up to 3.0 using the body-fitted overset grids produced close agreement with measured values, as shown in Figure 93. Calculated values of normal force and pitching moment versus angle of attack are generally within the 95% uncertainty bounds of the wind tunnel measurements. Calculated values of axial force coefficient show less agreement but differ by less than a few percent of the measured values. Additionally, the calculated $C_{A_{adj}}$ values exhibit the same trends versus angle of attack shown in the experimental data. Given the near-perfect agreement in surface pressures shown previously, differences in axial force are likely due to difficulties in reducing the wind tunnel data in a manner consistent with how the pressures are integrated in the CFD solutions to arrive at total force and moment coefficients. Specifically, pressure integration in the CFD solutions was limited to the forebody of the geometry, the aftbody up to the balance wind shield (the largest of the two cylinders comprising the sting shown in Figure 83), and a small portion of the windshield. During testing, a small gap between the wind shield and the back of the model existed and as a result the balance recorded forces over a larger portion of the aftbody than was modeled. A method of reducing the

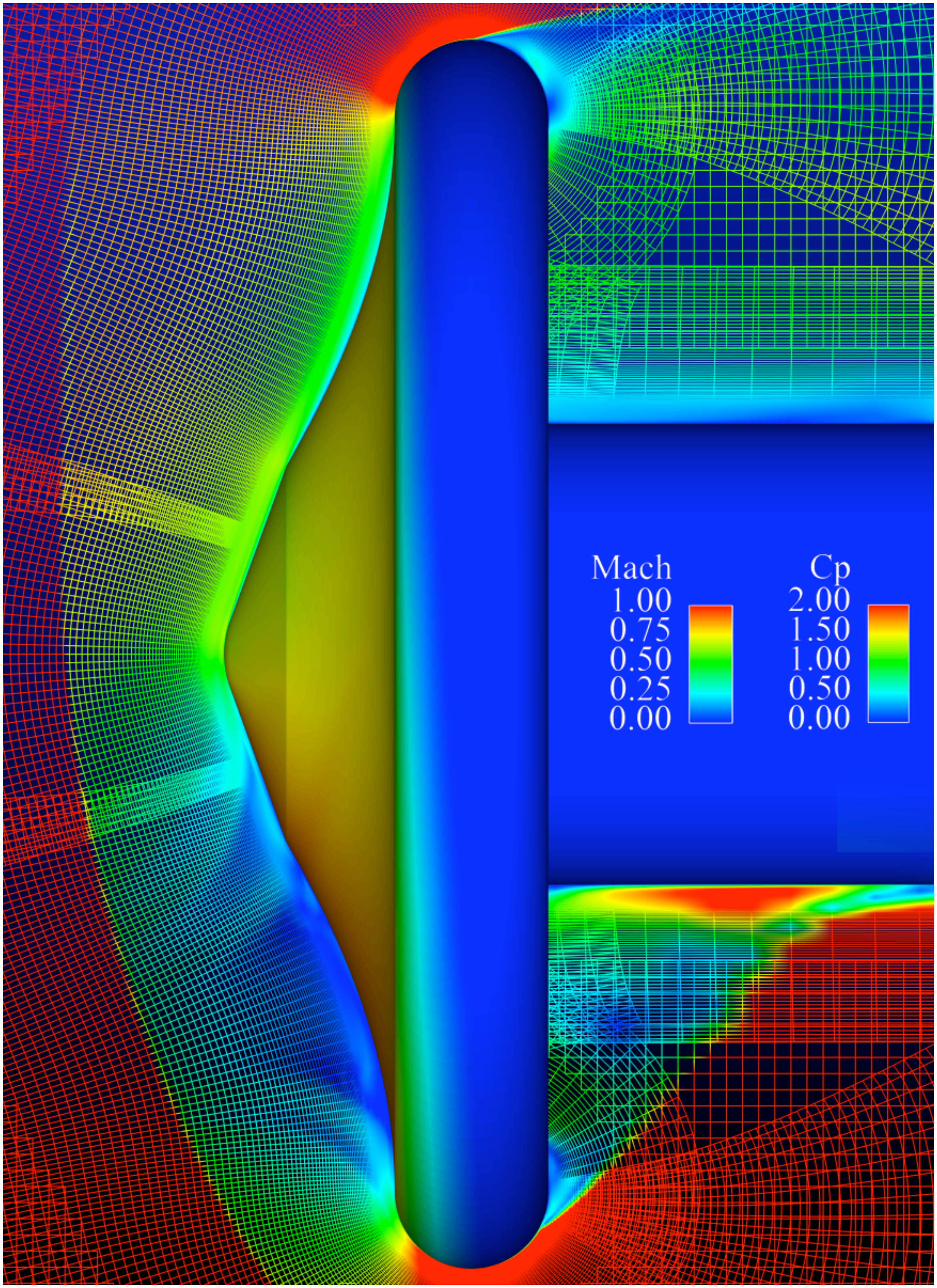

Figure 92: Contours of Mach number for the Mach 3.5, 20° angle of attack solution. Note: the color scale is adjusted to a maximum (red) at Mach 1.0. Surface colors correspond to pressure.

wind tunnel axial force data to a form more consistent with the CFD integration area was described in the previous chapter. However, no augmentation to the uncertainty estimate for the nominal C_A was made when calculating $C_{A_{adj}}$.

Flowfield characteristics were also matched well using the initial OVERFLOW grids. Shown in Figure 94 are comparisons between a schlieren image of a Mach 2.0, 20° angle of attack flowfield and the density contours calculated using OVERFLOW. The comparison reveals that OVERFLOW successfully resolved the location and curvature of the bow shock as well as the prominent expansion lines on the shoulders and the recompression shocks emanating from the wind tunnel sting.

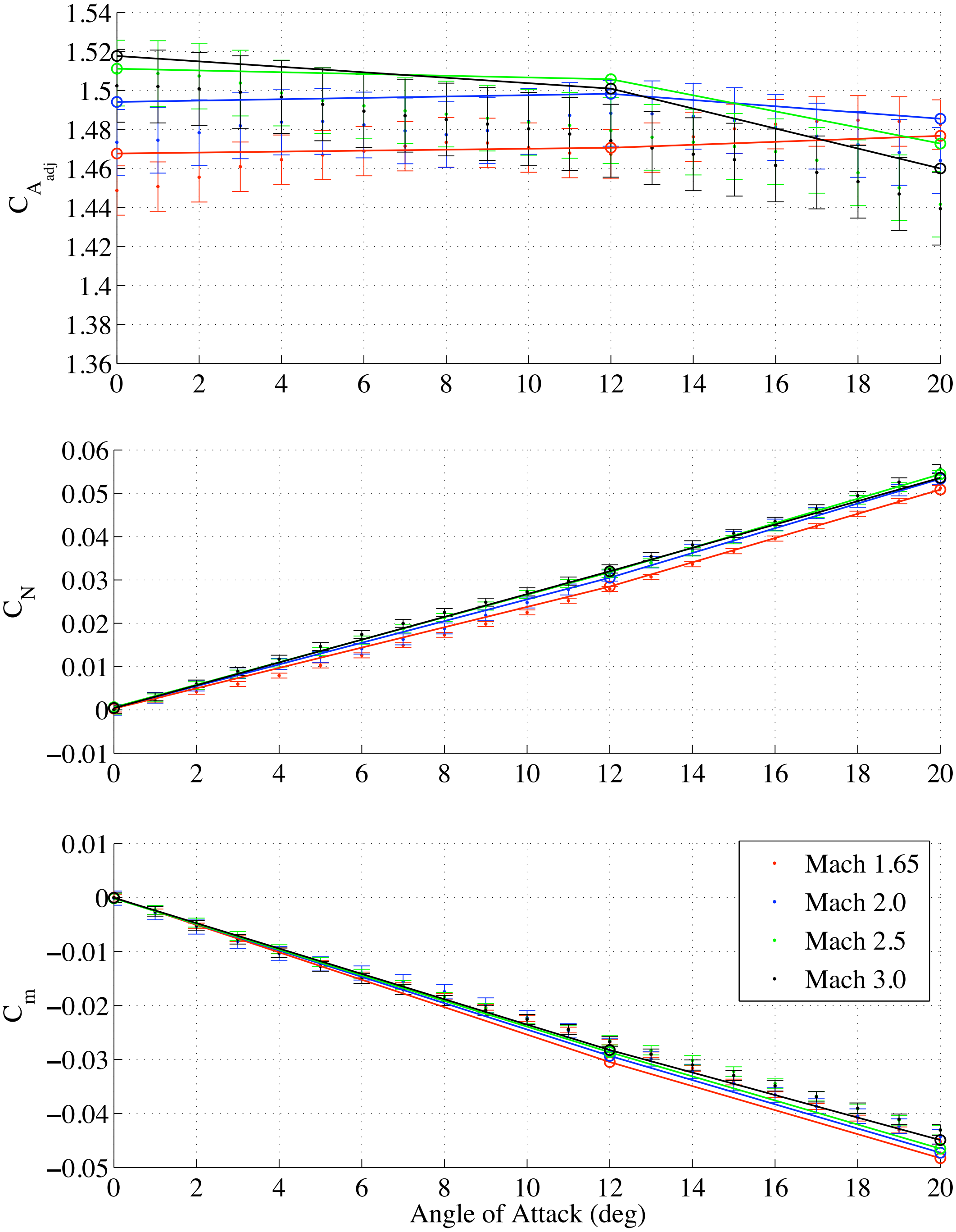

Figure 93: Comparison of $C_{A_{adj}}$, C_N, and C_m values calculated in OVERFLOW versus wind tunnel measurements up to Mach 3.0. CFD solutions denoted by solid lines and open circles.

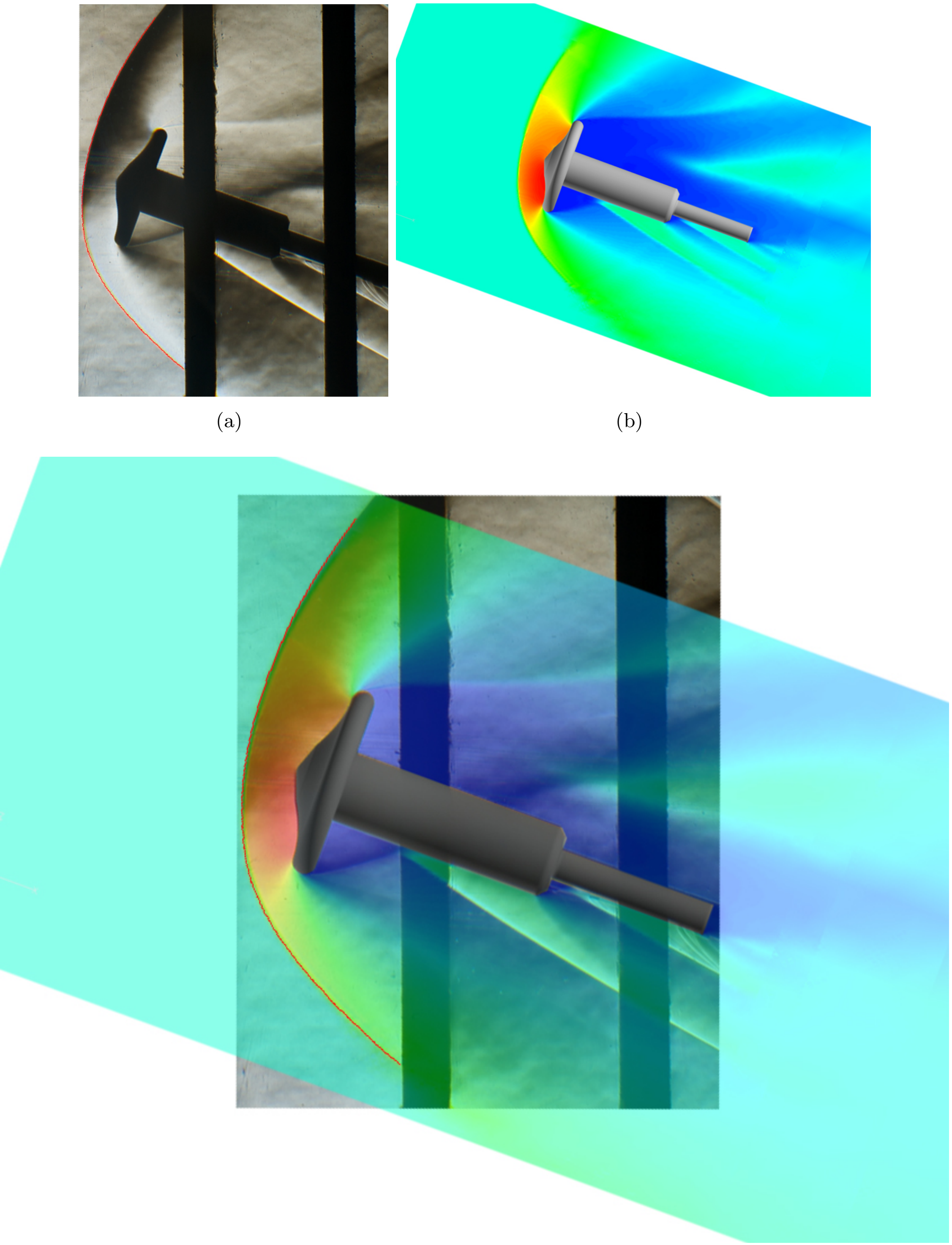

(a) (b)

(c)

Figure 94: Comparison of shock structure at a 20° angle of attack for Mach 2.0 and *Re* = 1.0 x 10^6. Note: red line is derived from shock position in schlieren image.

4.2.4 Computational Comparison to Unitary Results with Shock-Aligned Grids

As shown prior, attempts at matching higher Mach number wind tunnel results with CFD results using the original body-fitted grids were largely unsuccessful. As a result, a second set of solutions were computed using a shock-aligned grid. Early in the solution development process it was seen that an assumption of fully-laminar flow versus incorporation of a turbulence model produced considerable differences. Solutions computed in LAURA for the purposes of grid-development assumed fully-laminar flow and subsequently showed large regions of leeward-side flow separation for an angle of attack of 20° at even the lowest Mach number of 1.65. Laminar solutions computed in OVERFLOW also exhibited flow separation on the leeward portion, but only at Mach numbers of 3.5 and 4.5. Incorporating a turbulence model was seen to eliminate indications of flow separation for all conditions evaluated. An example of these results are shown in Figure 95 for the Mach 4.5, 20° angle of attack condition.

Figure 95 illustrates that predictions of windward surface pressures were consistent across all solutions while leeward pressures varied considerably. Although both the laminar LAURA and laminar OVERFLOW solutions predicted flow separation over the same general areas, the magnitude of the separation was substantially larger in the LAURA solution. Once a turbulence model is implemented, leeward pressures smooth out and match those measured during testing. Of note is that the two turbulence models tested produced identical solutions. The much improved predictions afforded by the turbulent solutions is indicative of a turbulent boundary layer being present on the leeward portion of the model. The wind tunnel data in Figure 95 exhibits an adverse pressure gradient across most of the leeward portion of the pitch plane. Because a laminar boundary layer can only support a relatively minor adverse pressure gradient, separation is predicted. However, due to increased mixing, a turbulent boundary layer can facilitate the flow remaining attached by entraining momentum from outside the boundary layer. Further evidence for the turbulent boundary layer hypothesis is shown in Figure 96. For example, the momentum vector fields of Figure 96(a) clearly illustrate the flow becoming separated at the sphere cone/tension shell interface. In the turbulent solution of Figure 96(b), beginning at the sphere cone interface the boundary layer is seen to thicken considerably, which again would be expected with a turbulent boundary layer.

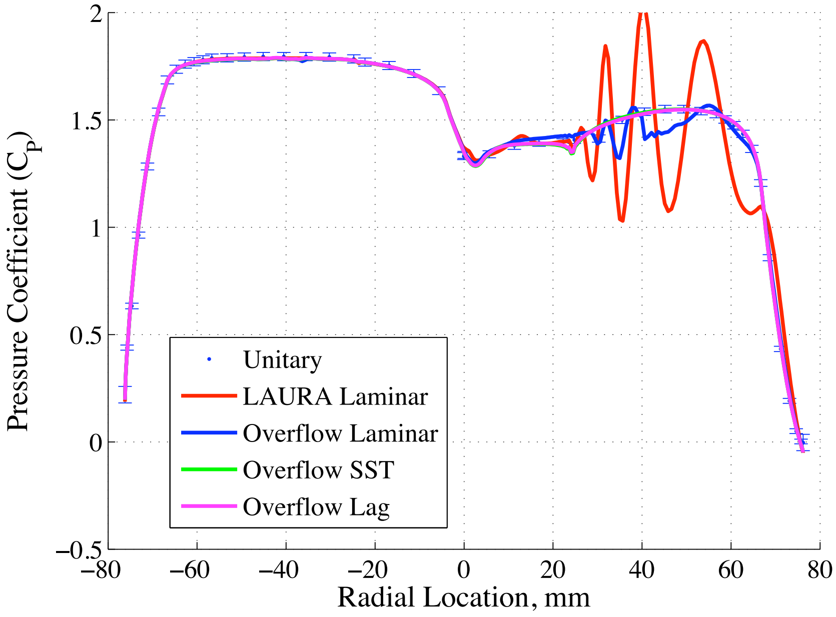

Figure 95: Pitch plane surface pressure distributions for a 20°, Mach 4.5 condition computed using shock-aligned grids, multiple codes, and turbulence assumptions.

A more complete visualization of the extent of flow separation for both laminar and turbulent solutions is shown in the simulated oil flows of Figure 97. For the laminar solution the region of separation encompasses the upper third of the tension cone forebody. However, the turbulent solution exhibits minimal, if any, separation across the forebody.

Given the relatively low Reynolds number of the wind tunnel tests, transition of the boundary layer was not expected. A recent survey on boundary layer transition on blunt bodies did not mention any prior wind tunnel experiments in which transition had occurred for a Reynolds number of 10^6 or lower [69]. The closest example to the current scenario provided was for a ballistic range test of the Mercury reentry capsule. During that test, a model with a roughened forebody was tested and resulted in the aftbody flow remaining attached well past the forebody shoulder for a Mach number of 3.28 and Reynolds number of 2.5 x 10^6. In this case, it was the turbulent boundary layer on the forebody that enabled the flow to remain attached. The tension cone model, however, was made from polished

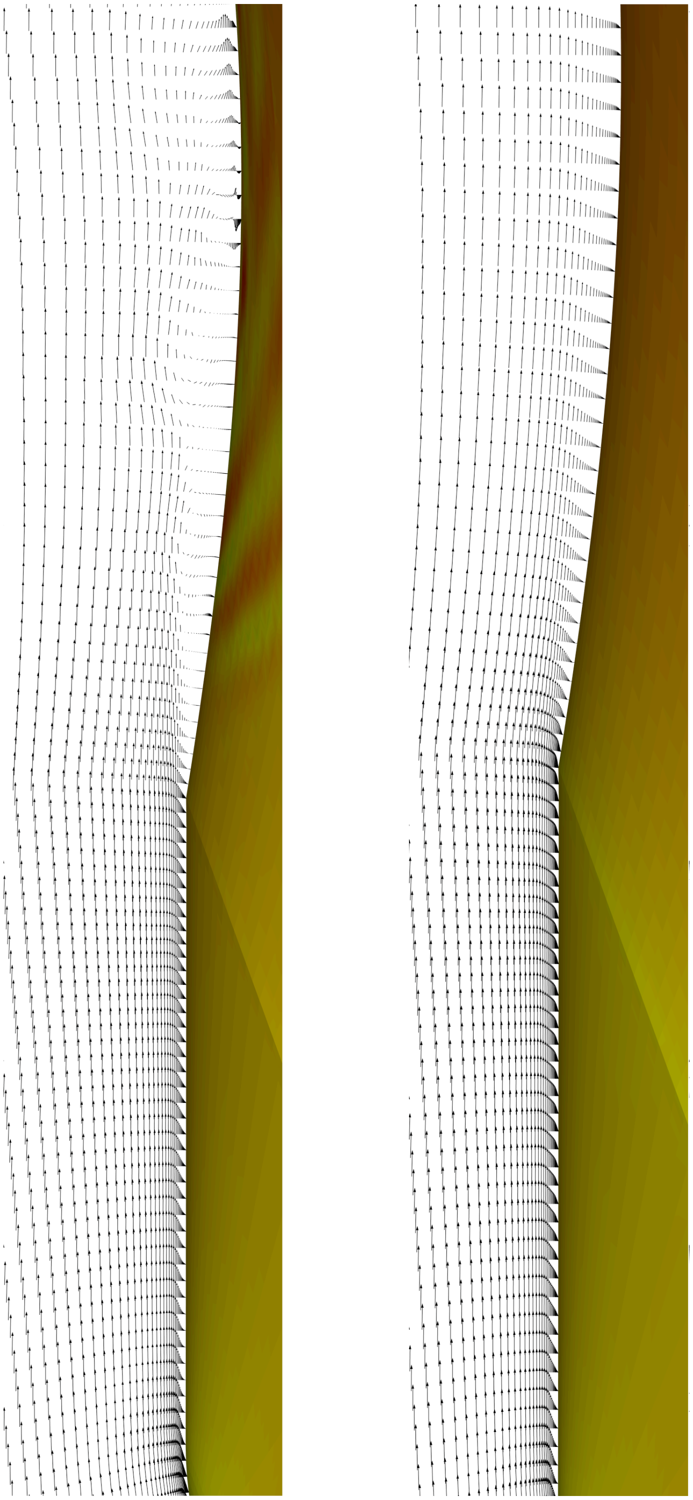

(a) (b)

Figure 96: Computed momentum vector fields for a (a) laminar solution and (b) turbulent solution for a 20° angle of attack, Mach 4.5 condition. Shown regions correspond to the leeward sphere cone/tension shell interface region on the pitch plane of the tension cone. Surface colors denote pressure.

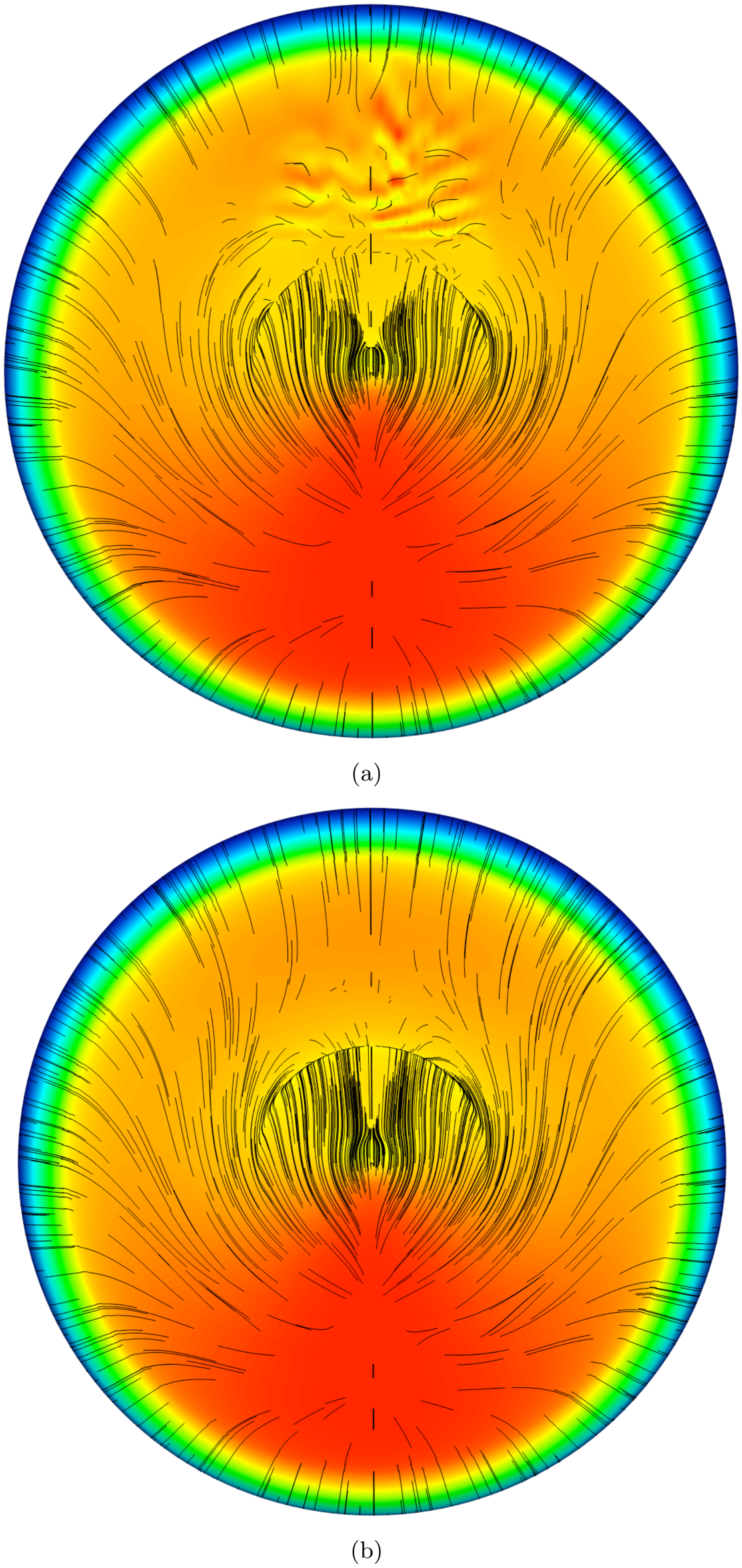

Figure 97: Simulated oil flows for a (a) laminar solution and (b) turbulent solution for a 20° angle of attack, Mach 4.5 condition. Surface colors denote pressure.

stainless steel and transition due to surface roughness would not be expected. An alternative mechanism for transition is hypothesized based on the concavity of the tension shell surface. Specifically, an instability is known to exist in boundary layer flow over a concave surface in which the radial direction opposes the velocity gradient [65]. This instability leads to the formation of Görtler vortices within the boundary layer. This phenomenon has been well-studied and in numerous experiments (e.g. [9] and [45]) has been shown to lead to boundary layer transition significantly sooner than would otherwise be expected for a convex surface. Although this is proffered as an explanation for the experimental results of attached leeward flow, it is unlikely that this type of phenomenon is capable of being captured by the turbulence models employed.

Complete results of the predicted pressure distributions for solutions computed using the shock-aligned grids are provided in Figures 98 - 101. As with prior solutions shown using the body-fitted overset grids, these distributions demonstrate nearly perfect agreement at Mach numbers of 1.65 and 2.5. This agreement continues for Mach numbers of 3.5 and 4.5 with only minor exceptions. For example, surface pressures at a 20° angle of attack are slightly under-predicted at Mach 3.5, although the trends are captured. Also, pressure distributions at a 0° angle of attack show a small disturbance at the nose which is attributed to there being a grid line on the axis of symmetry which introduces a pole singularity.

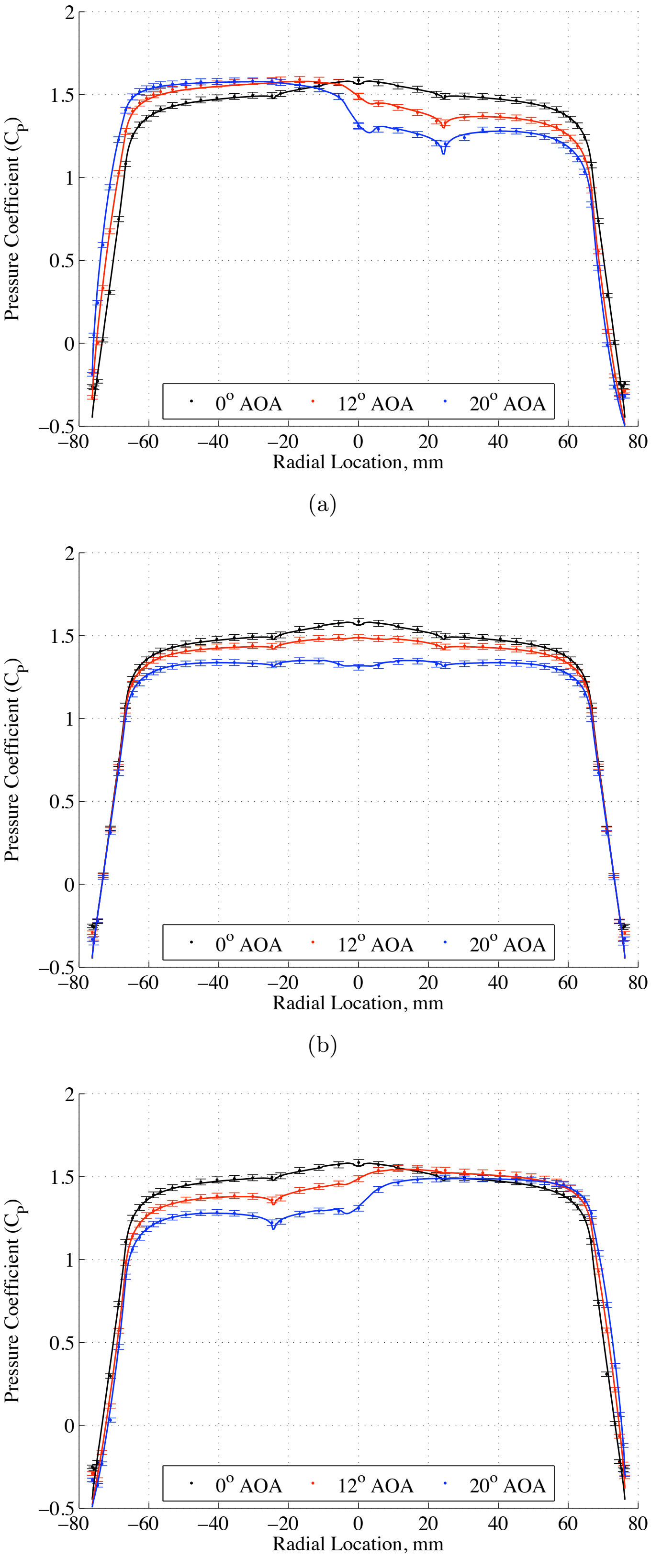

(a)

(b)

(c)

Figure 98: Comparison of pressure distributions predicted with a shock-aligned grid at Mach 1.65 and a Reynolds number of 1.0 x 10^6 for the (a) 0°, (b) 90°, and (c) 225° spokes.

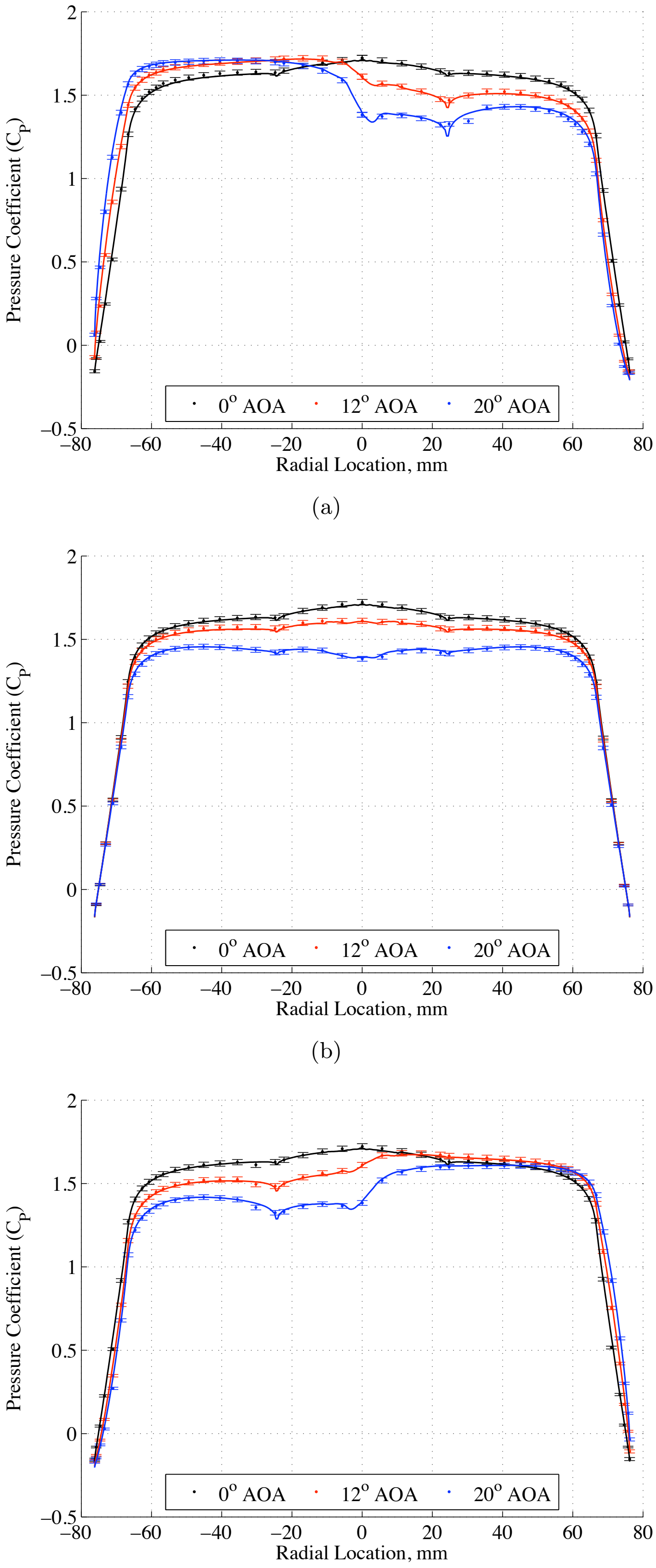

(a)

(b)

(c)

Figure 99: Comparison of pressure distributions predicted with a shock-aligned grid at Mach 2.5 and a Reynolds number of 1.0 x 10^6 for the (a) 0°, (b) 90°, and (c) 225° spokes.

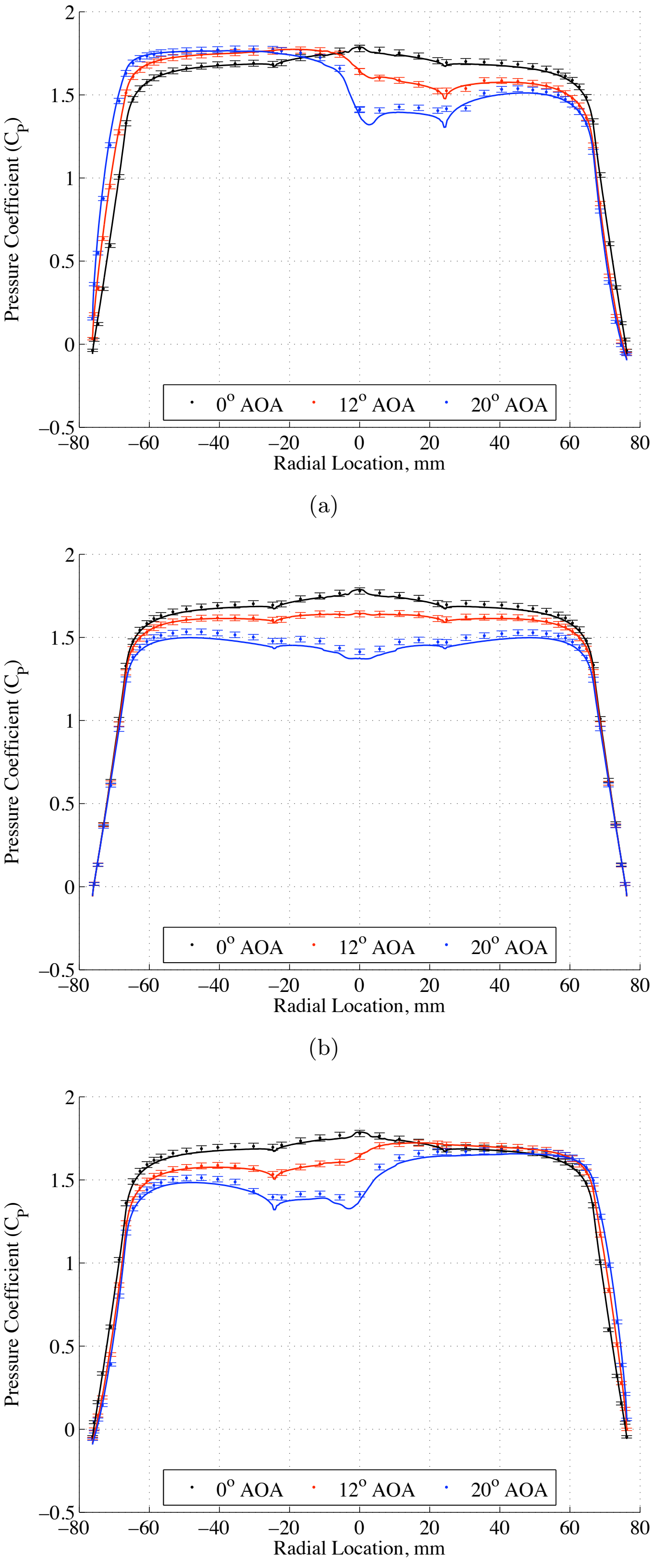

(a)

(b)

(c)

Figure 100: Comparison of pressure distributions predicted with a shock-aligned grid at Mach 3.5 and a Reynolds number of 1.0 x 10^6 for the (a) 0°, (b) 90°, and (c) 225° spokes.

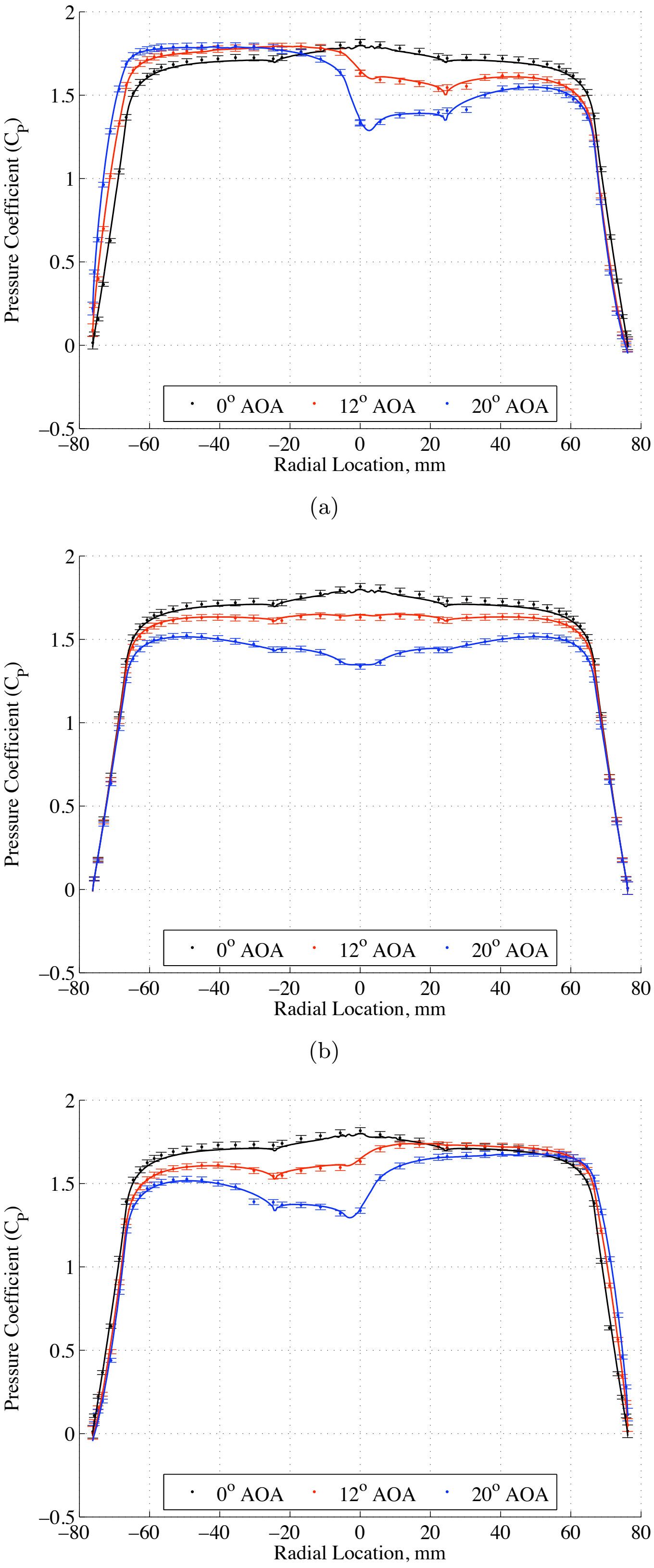

(a)

(b)

(c)

Figure 101: Comparison of pressure distributions predicted with a shock-aligned grid at Mach 4.5 and a Reynolds number of 1.0 x 10^6 for the (a) 0°, (b) 90°, and (c) 225° spokes.

4.3 Viscous Simulation of Supersonic Mars Entry Static Aerodynamics

The previous sections of this chapter focused on recreating the results of the wind tunnel test program conducted at ground based facilities. Having demonstrated the capability of CFD to accurately predict tension cone performance, the focus turns to extrapolating those capabilities to conditions typical of a Martian entry. This section presents the results of this effort.

4.3.1 Solution Approach

Computational solutions were generated with OVERFLOW and incorporated the shock-aligned grids used previously. Numerical schemes and convergence criteria consistent with the previous results were used. Modifications were made to the freestream conditions and the turbulence model. For the latter, difficulties in attaining convergence for different values of the ratio of specific heats were encountered and a newer version of the OVERFLOW code, which did not include the lag model, was required (version 2.1t). Early comparisons between the lag and SST models, such as those shown in Figure 95, revealed no discernible differences between the converged solutions and thus the SST model was used.

4.3.2 Freestream Conditions

Freestream conditions were developed from a nominal trajectory incorporating a full-size version of the tension cone configuration used during wind tunnel testing. The trajectory was identical to the 4200 kg entry mass, -16.7° entry flight path angle trajectories shown in Chapter 2 with the exception that the tension cone was 14.23 m in diameter so as to match the tension cone to aeroshell area ratio used for the wind tunnel model. Four discrete Mach numbers were analyzed and the corresponding conditions are provided in Table 24. The choice of Mach numbers was driven by the desire to reuse the previous shock-aligned grids and to mitigate errors due to misalignment of the grid and shock. Reynolds numbers shown in Table 24 are based on the total diameter of the tension cone (14.23 m). Estimates of viscosity were made using Sutherland's Law for CO_2.

Prior computational studies of the performance of blunt bodies in a Martian environment

Table 24: Freestream conditions used for Mars entry tension cone calculations.

Mach	Altitude (km)	Density (kg/m^3)	Temperature (K)	Pressure (Pa)	Reynolds Num.
4.50	22.33	2.064 x 10^{-3}	202.6	79.0	2.99 x 10^6
3.50	22.29	2.071 x 10^{-3}	202.7	79.3	2.33 x 10^6
2.50	22.13	2.101 x 10^{-3}	203.1	80.6	1.69 x 10^6
1.65	21.57	2.203 x 10^{-3}	204.6	85.2	1.12 x 10^6

indicated a noticeable difference between perfect gas and high-temperature gas simulations [32]. In particular, real gas simulations indicated a lack of static stability for multiple trajectory points that was in part due to the location of the sonic line. Although the instabilities were only observed in hypersonic solutions, some differences in computed lift and drag coefficients were also evident in supersonic cases. Examination of real gas effects for the present effort was achieved by computing solutions across three values of γ: 1.25, 1.33, and 1.40. The upper two values of γ are based on the values for ideal triatomic and diatomic gases respectively (i.e. CO_2 and N_2). The lower value of γ is based on matching the density ratio across a Mach 4.5 normal shock for equilibrium flow in a Martian atmosphere, as was done in [32].

4.3.3 Results

A summary of the computed forebody-only static aerodynamic coefficients for multiple values of γ is provided in Figure 102. Axial force coefficients are seen to exhibit the largest variations. At lower Mach numbers changes in γ have only small effects on axial force, with larger values occurring at lower γ's and a maximum difference in C_A of roughly 0.03. This sensitivity increases at higher Mach numbers to a maximum difference of 0.06 at Mach 4.5. However, these differences are still only 3-4% of the total forebody C_A. Variations in normal force and pitching moment slopes versus angle of attack are driven more by Mach number differences than by γ. Both the normal force and pitching moment slopes are seen to become slightly more positive with decreasing γ. In the case of C_m, this indicates a minor decrease in static stability, though considerable margin still exists.

The influence of γ on the sonic line location is explored for a Mach 4.5, 12° angle of attack solution in Figure 103. Clearly visible is the decrease in shock stand off distance that

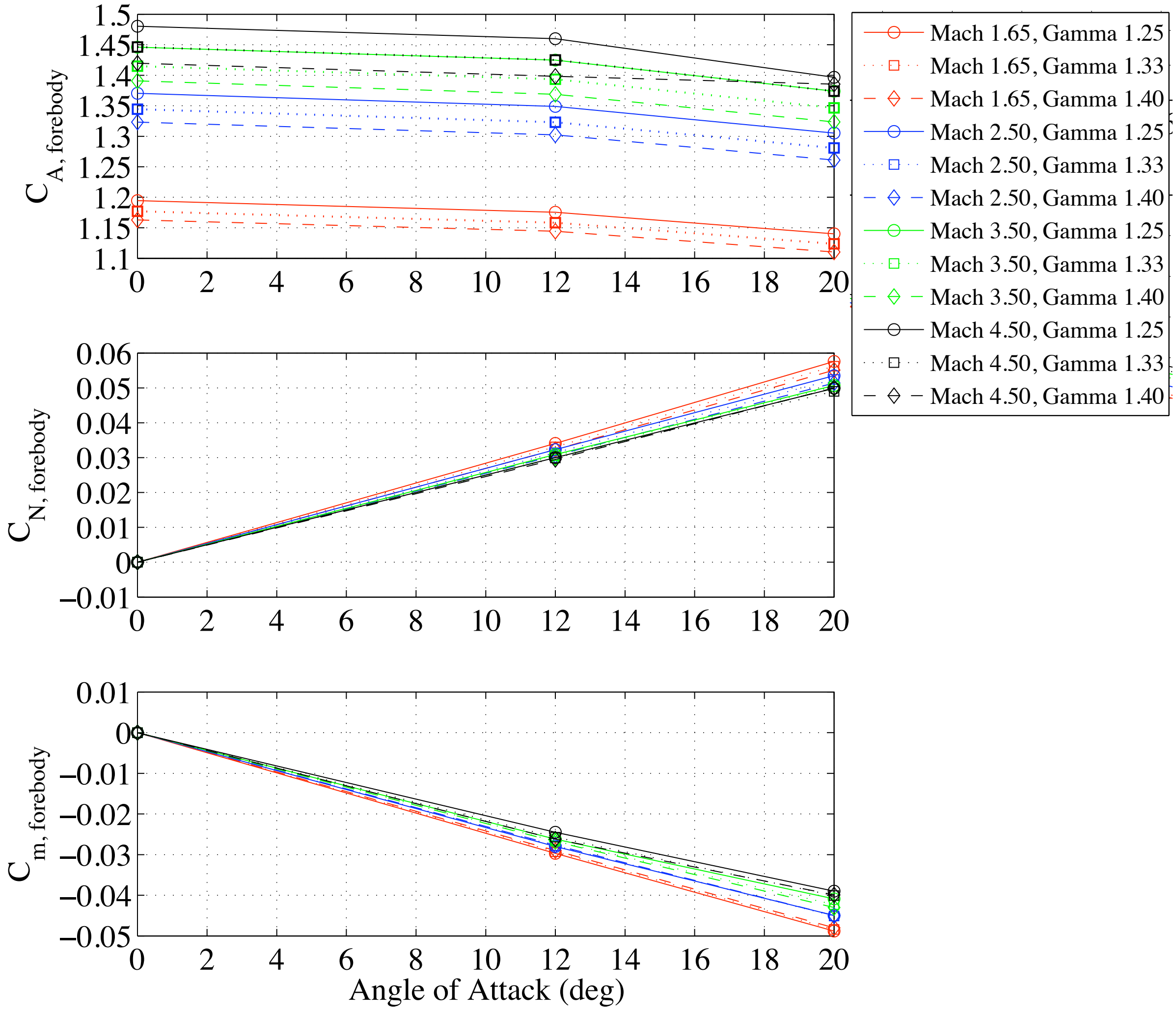

Figure 102: Forebody only values of static aerodynamic coefficients for multiple values of Mach number and γ.

occurs with decreasing γ. However, the progression of the bow shock does not influence the sonic line attachment point, which remains fixed on the frontal region of the shoulder. It is worth noting that flow separation was not observed in any of the computed solutions. Furthermore, a comparison of forebody aerodynamic coefficients between the $\gamma = 1.40$ cases computed early at a Reynolds number of 1.0 x 10^6 and those shown here revealed no discernible differences, indicating the lack of sensitivity to a tripling of Reynolds number.

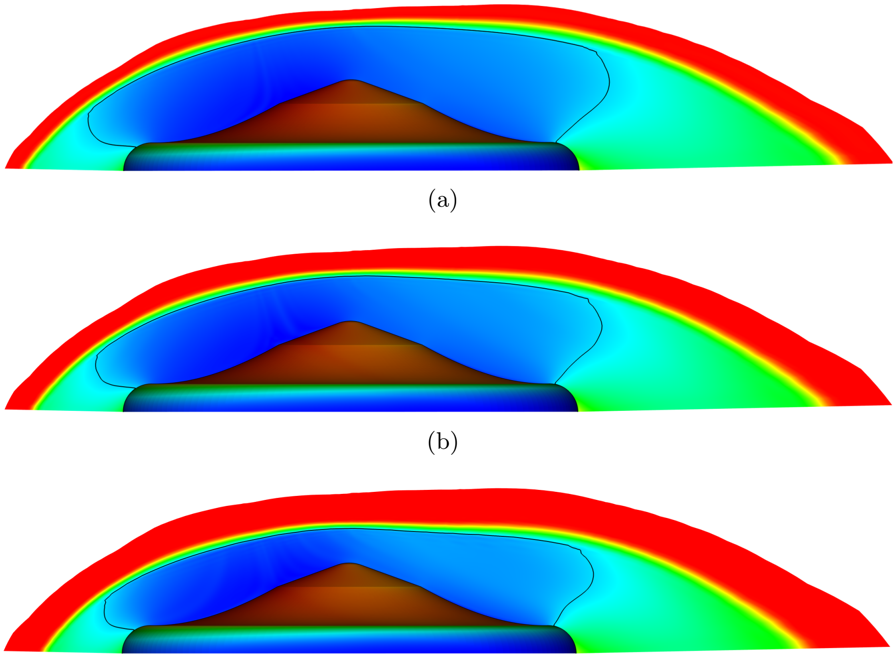

(a)

(b)

(c)

Figure 103: Mach number contours for a Mach 4.5, 12° angle of attack solution for γ values of (a) 1.40, (b) 1.33, and (c) 1.25. The sonic line is denoted by a solid black line and surface colors correspond to pressure.

4.4 Summary of Computational Results

This chapter presented the results of an effort aimed at demonstrating the ability of modern CFD to accurately predict the performance of a supersonic tension cone decelerator. The validation effort focused on matching static aerodynamic coefficients and surface pressure distributions obtained during wind tunnel testing. Using a Cartesian-grid based code, inviscid axisymmetric solutions were computed and were seen to match measured forebody pressure distributions. Predicted aftbody pressures exhibited more variability than would be expected, likely due to the aftbody region being more strongly influenced by viscous effects. Calculated drag coefficients were within 5% of the total drag coefficient and within 4% of a forebody-only drag coefficient. Inviscid analysis was also shown to accurately predict the shock curvature and location for several flexible tension cone models. Viscous analyses performed using an overset grid topology demonstrated near perfect agreement in calculated surface pressures, including aftbody pressures, at Mach numbers up to 3.0 and angles of attack up to 20°. Calculated normal force and pitching moment slopes versus angle of attack also matched the wind tunnel data. Differences in axial force coefficient values were evident and were attributed to complications in reducing the wind tunnel data in a manner consistent with the portion of the tension cone being modeled computationally. Attaining an accurate prediction of aerodynamic performance at Mach numbers above 3.5 proved more difficult and a shock-aligned grid was required to eliminate errors introduced as a result of shock-staircasing. Using the shock-aligned grids, it was determined that at higher Mach number and higher angle of attack conditions the leeward region of the tension cone likely transitions to a turbulent boundary layer, which in turn ensures that the flow remains attached through a strong adverse pressure gradient. Lastly, an investigation of aerodynamic performance in a Martian environment which approximated high temperature effects showed small increases in forebody-only axial force and minor decreases in static stability.

CHAPTER V

SUMMARY AND FUTURE WORK

5.1 Summary

This research effort has matured the state of the art of supersonic tension cone inflatable aerodynamic decelerators through conceptual studies, wind tunnel testing, and computational aerodynamic analyses. The results from each of these three research areas consistently demonstrate the tension cone to be a viable technology for future atmospheric entry systems.

A conceptual study was performed that investigated the capability of a supersonic IAD to enable higher altitude and higher mass landings on the surface of Mars. Two IAD configurations, the tension cone and the attached isotensoid, were evaluated in conjunction with traditional parachutes and hybrid IAD-parachute systems. Missions that incorporated supersonic IADs were able to significantly improve the altitudes at which subsonic velocities were achieved. Further improvements in subsonic staging altitude were possible when modifications to the reference trajectory were made that took greater advantage of the high Mach, high dynamic deployment conditions possible with an IAD. First order mass estimates developed for the two IAD configurations showed the isotensoid configuration to be lower mass system for larger drag areas and higher deployment dynamic pressures, a result attributable to the isotensoid not requiring a separate inflation system. Improvements to landed mass were possible with an IAD when the reference entry mass was increased by 25%. For example, increases in payload of over 600 kg (12% of the entry mass) were possible with IAD systems weighing less than 5% of the entry mass.

A series of wind tunnel tests were conducted on a tension configuration specifically designed to eliminate unfavorable aerodynamic characteristics observed in prior test programs, i.e. the presence of embedded shocks and flow separation along the forebody. Testing of rigid models of this configuration at Mach numbers from 1.65 to 4.5 indicated favorable drag and static stability performance. Axial force coefficients varied between 1.40 and 1.50

at all Mach numbers and angles of attack and a pitching moment slope (C_{m_α}) of -0.00212 deg^{-1} was measured. Surface pressures measured with the rigid models exhibited small regions of adverse pressure gradients in the vicinity of the aeroshell/tension shell interface. Although the adverse gradients steepened with increasing Mach number and angle of attack, schlieren images exhibited no evidence of flow separation and no changes in pitching moment slope were observed. Testing of textile models with both inflatable and rigid tori provided aerodynamic results consistent with those attained from rigid model tests. Deployments of the inflatable model conducted at supersonic conditions demonstrated rapid inflation and achievement of steady state axial forces. A structural modification in the form of anti-torque panels was seen to reduce the inflation pressures required for complete deployment by approximately 50%. During both rigid and flexible model testing the bow shock was observed to be fully detached and the forebody flow field was stable at all test conditions, thus demonstrating success in the design objectives of the configuration.

Computational fluid dynamic analyses of varying fidelity were conducted and the data set acquired during wind tunnel testing was used to validate these tools for predictions of tension cone aerodynamic performance. Inviscid axisymmetric solutions calculated on a Cartesian grid demonstrated the ability to accurately predict forebody surface pressures on the rigid wind tunnel models. Predictions of bow shock shape and location were in agreement for both rigid and flexible test articles. Calculated forebody-only drag coefficients did not differ appreciably between models with and without anti-torque panels despite the somewhat different profiles that each took. Viscous analyses using an overset grid topology provided improvements in aftbody surface pressure predictions and matched normal forces and pitching moments to within the uncertainty of the wind tunnel data at Mach numbers up to 3.0. Higher Mach number solutions exhibited large flow instabilities that were resolved when a shock-aligned grid topology was introduced. Comparisons between laminar solutions and solutions incorporating a turbulence model indicated that at high Mach number, high angle of attack test conditions the boundary layer on the leeward portion of the tension cone was likely turbulent. Lastly, a study of the effect of the ratio of specific heats on aerodynamic characteristics indicated increases in axial force of 3-4% with a γ of 1.25.

5.2 Suggestions for Future Work

Research conducted for the IAD overview has revealed a cyclic nature to the study of inflatable decelerators. A majority of the work performed on developing IADs, and supersonic IADs in particular, was performed during the 1960's and early 1970's, prior to the launch of the Viking Mars landers. During the late 1970's and 1980's supersonic IADs appear to have garnered little interest, as evidenced by the shortage of publications involving IADs during that time frame. The past decade has seen a resurgence in conceptual mission studies and designs of IADs. However, a majority of this research is strictly related to conceptual designs or computational work. Thus, although computational analysis tools have advanced considerably since the 1960's, the state of the art of IADs has not and for the most part is the same as it was during the Viking program.

An examination of the state of the art of inflatable decelerators performed by McShera and Bohon in 1967 [51] reveals that many of the technical challenges present then still remain. These were primarily divided into aerodynamic and structural uncertainties. The suite of wind tunnel tests conducted after 1967 addressed many of the issues regarding static aerodynamic performance, but dynamic issues are still unresolved.

IAD dynamic stability analysis is difficult to perform using ground based testing methods and the primary sources of data, ballistic range testing and forced-oscillation tests, often provide only partial answers. Recent ballistic range tests conducted as part of the PAIDAE program [75] have provided some of the only data pertaining to inflatable decelerator configurations but the configurations tested much more closely resemble a sphere cone rather than an isotensoid or tension cone shape. Maturation of computational tools for performing dynamic stability analyses is continuing and efforts aimed at recreating the PAIDAE ballistic range test data in a computational environment show promise [57].

Another area of uncertainty identified by McShera and Bohon regarded the structural design of IADs. Numerous IAD configurations and variations are possible but approaches for evaluating structural strength are generally restricted to complicated and time-consuming structural analysis codes. Validation of these codes for use on supersonic IADs requires test data of which there is presently little available. Analytic methods are available for examining basic isotensoid or tension cone shapes ([4],[3],[20],[42]), but it is difficult to expand these for more complicated configurations.

Some of the technical challenges remaining can only be addressed through the development and testing of flight-size models. These challenges include packaging and folding considerations, integration with an entry vehicle shape, and deployment and inflation at flight-like time scales. Scaling of test articles also introduces uncertainties in manufacturing. The largest test article fabricated to date was an 18 ft (5.5 m) diameter, trailing isotensoid shape that failed to achieve inflation during flight testing [49]. It is unclear if the manufacturing methods employed for this device are suitable for devices two or three times larger. The largest tension cone article tested to date are the 60 cm diameter models developed for the testing described in Chapter 4 of this dissertation. In 2009, a parallel IAD development effort by Vertigo Inc. succeeded in fabricating a tension cone of 5 m diameter. The Vertigo tension cone is designed to withstand over 10,000 pounds of axial load and is envisioned as a test article for a future series of subsonic wind tunnel tests. Methods suitable for even larger ($>$ 5 m diameter) tori, such as the fiber-reinforcement approach being explored for the hypercone [16], will need to be able to tolerate even greater loads without contributing significant mass to the system.

The computational portions of this thesis dealt predominantly with tension cone aerodynamics and further development efforts will require validated tools in other areas. Subsequent research will seek to perform a similar validation for structural dynamics codes. The validation of aerodynamic analysis capabilities performed in this thesis provides a foundation for the introduction of coupling with structural analysis capabilities. Follow on research will seek to perform a similar validation for structural dynamics codes. The end goal of these efforts is the development of a validated, coupled computational aerodynamic and structural analysis (fluid-structure interaction) capability that can be used in evaluation of supersonic IADs. In the absence of significant flight experience, such a capability is required to further advance this technology.The data acquired during testing of the flexible tension cone articles should be suitable for initial validation of statically coupled CFD and structural analysis codes. For example, the variability in tension shell concavity observed between models with and without anti-torque panels and the behavior of the tension cone at angle of attack are static phenomena that could be analyzed computationally and for which inviscid CFD would likely be sufficient.

APPENDIX A

TENSION CONE MASS ESTIMATION

This Appendix provides a derivation of the structural analysis and mass estimation equations developed for studying the tension cone decelerator configuration. The structural analysis equations are based on the work performed by Kyser [42]. Though the final stress relations are the same, this Appendix provides a more thorough derivation of those relations and extends them to use in mass estimation. The objective of the stress analysis is to develop relations for the meridional and circumferential stress resultants in the tension shell, $N_{\phi,ts}$ and $N_{\theta,ts}$, respectively, and in the torus, $N_{\phi,t}$ and $N_{\theta,t}$, respectively. The results are then used to form a first order estimate of the mass of a tension cone system.

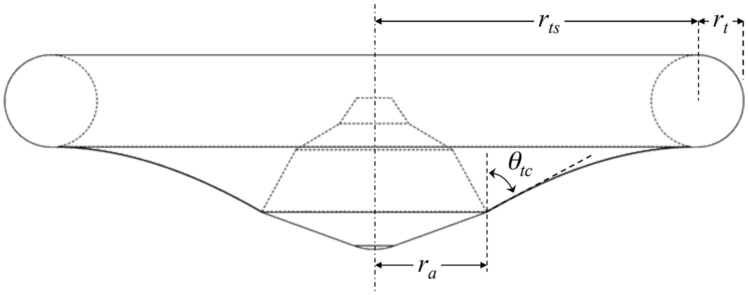

Figure 104: Tension Cone dimension reference.

Beginning with the dimensional references provided in Figure 104, a force balance can be drawn at the point of tension shell/aeroshell interface. This force balance is illustrated in Figure 105, where T corresponds to the tension load carried by the tension shell due to the drag of the IAD, D_{IAD}. Equilibrating the forces at the attachment location yields a relation for the tension load:

$$T = \frac{D_{IAD}}{\cos \theta_{tc}} \tag{4}$$

The meridional stress resultant for the tension shell is largest at the aeroshell interface and

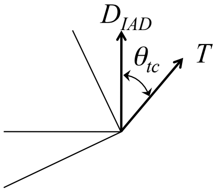

Figure 105: Tension shell/aeroshell interface forces.

can be equated as the tension load divided by the circumference of the aeroshell:

$$N_{\phi,ts}\left(r_a\right) = \frac{T}{2\pi r_a} = \frac{D_{IAD}}{2\pi r_a \cos\theta_{tc}} \tag{5}$$

From Anderson's original derivation of the tension shell theory [3], the ratio of circumferential to meridional stresses, α, is considered constant throughout the structure. Therefore, an equation for the circumferential stress resultant at the attachment location can be written as:

$$N_{\theta,ts} \; = \; \alpha N_{\phi,ts} \tag{6}$$

Anderson also notes that the meridional stress resultant at a radial location r in the tension shell can be calculated from a known location and value using the relation below

$$r_a^{(1-\alpha)} N_{\phi,ts}\left(r_a\right) = constant = r^{(1-\alpha)} N_{\phi,ts}\left(r\right) \tag{7}$$

It should be noted that a common assumption in tension shell derivations, and one that is used consistently in this dissertation, is that the tension shell carries no circumferential stresses, and therefore α is zero.

Attachment of the tension shell to the torus results in compressive meridional and circumferential stresses on the torus membrane. Calculation of the meridional stress begins by examining a top down view of the torus shown in Figure 106. The tension shell applies a uniform stress in the radial direction at the torus attachment location (shown with a dotted line). The compressive load is resisted at each end by a load P.

The compressive load can be calculated by integrating the stress resultant at the tension shell/torus interface, N_0. Performing this integration and subsequently equating the result

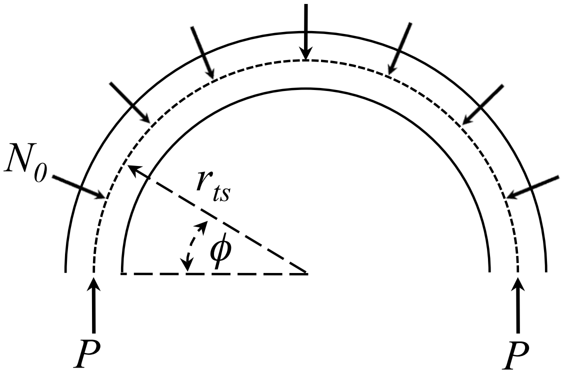

Figure 106: Inflated torus stress resultant distribution and counteracting loads.

to the two P loads yields the following results:

$$\int_0^\pi N_0 r_{ts} \sin\phi d\phi = 2N_0 r_{ts} = 2P \tag{8}$$

$$P = N_0 r_{ts} \tag{9}$$

The value of N_0 is dependent on the manner in which the tension shell is attached to the torus. In his original study, Kyser considered three such methods, shown in Figure 107. Kyser's preferred method, method (a), incorporated a second set of tethers that wrapped around the top of the torus and were attached to a central ring. Kyser noted that this method produced a radial loading on the torus that was twice that of method (b). Kyser discounted method (b) on the basis that it produced a compressive stress on the torus that was 50% larger than that for method (a), though no derivation of this result was provided. Attachment method (c) was also not seen as favorable, since the attachment of the second surface to the primary tension shell would introduce a distortion of the original tension shell curvature.

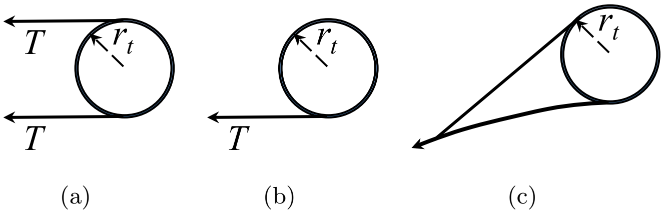

Figure 107: Torus/tension shell attachment methods originally considered by Kyser.

Using a subscript A to denote terms associated with attachment method (a) and a subscript B for terms associated with method (b), derivations of stress resultants for both configurations follow. The direction of the meridional and circumferential stresses, σ_ϕ and σ_θ respectively, are shown in Figure 108.

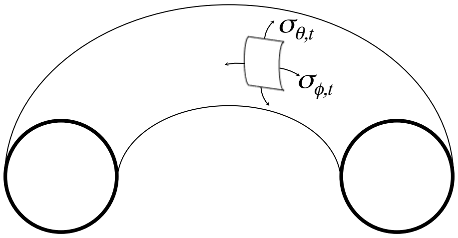

Figure 108: Orientation of meridional (subscript ϕ) and circumferential (subscript θ) torus stresses.

As Kyser originally noted, and from Figure 107(a), the second set of tethers are assumed sized in length such that they produce a radial load on the torus equal to that of the tension shell. Thus, the combined stress resultant at the torus/tension shell interface can be written as:

$$N_{0,A} = \frac{2T}{2\pi r_{ts}} \tag{10}$$

Alternatively, Equation 10 can be arrived at from combining Equations 5 and 7. Furthermore, it should be noted that this result assumes that that the torus contributes no drag, otherwise the value of the tension load T would be different than that attained from Equation 4. Though this is considered a conservative estimate, pressure data and CFD results presented in Chapters 3 and 4 show this to be a valid approximation. Substitution of Equation 10 into Equation 9 yields:

$$P_A = \frac{T}{\pi} \tag{11}$$

The meridional compressive stress in the torus is the load P divided by the cross sectional area of the torus $A_{t,cs}$, where t_t is the thickness of the torus membrane (written as negative since this is a compressive stress).

$$\sigma_{\phi_A,t} = \frac{-P_A}{A_{t,cs}} = \frac{-T}{2\pi^2 r_t t_t} = \frac{-D_{IAD}}{2\pi^2 r_t t_t \cos\theta_{tc}} \tag{12}$$

The relationship between a stress σ and a stress resultant N is simply

$$\sigma = \frac{N}{t} \tag{13}$$

where t is a thickness. Relating Equation 12 in terms of a stress resultant and substituting Equation 4 results in:

$$N_{\phi_A,t} = \frac{-D_{IAD}}{2\pi^2 r_t \cos\theta_{tc}} \tag{14}$$

The derivation for attachment method (b) follows a similar path. Because there is only one load applied on the torus, the stress resultant at the interface is written as:

$$N_{0,B} = \frac{T}{2\pi r_{ts}} \tag{15}$$

Again substituting into Equation 8, this yields:

$$P_B = \frac{T}{2\pi} \tag{16}$$

However, the compressive stress σ_B for this case includes an additional term due to a moment being generated by the unbalanced load. Thus, the stress is equated as:

$$\sigma_{\phi_B,t} = \frac{-P_B}{A_{t,cs}} + \frac{-Mr_t}{I} \tag{17}$$

where $\sigma_{\phi,B}$ is the maximum compressive stress on the torus due to the load. The moment M and cross-sectional moment of inertia I are:

$$M = P_B r_t = \frac{Tr_t}{2\pi} \tag{18}$$

$$I = \pi r_t^3 t_t \tag{19}$$

where I for a membrane torus is found in [31]. Combining Equations 17, 18, and 19 results in the following.

$$\sigma_{\phi_B,t} = \frac{-T}{4\pi^2 r_t t_t} + \frac{-Tr_t^2}{2\pi^2 r_t^3 t_t} = \frac{-3T}{4\pi^2 r_t t_t} = \frac{-3D_{IAD}}{4\pi^2 r_t t_t cos\theta_{tc}} \tag{20}$$

Comparing the result of Equation 20 with that of Equation 12, it is seen that attachment method (b) results in 50% greater stress on the torus, as Kyser originally stated. Lastly, though it is possible that a compressive circumferential stress on the torus may result from the tension shell, the mechanism for this stress is not immediately evident. Thus, for sizing purposes, the tensile stress due to pressurization is assumed to be the dominant circumferential stress resultant in the torus. This stress is maximum at the inner most location of the torus and is as follows [76]:

$$\sigma_{\theta_p,t} = \frac{pr_t}{2t_t}\left(\frac{2r_{ts} - r_t}{r_{ts} - r_t}\right) \tag{21}$$

Determination of the required torus inflation pressure is performed under the assumption that the tensile stresses induced by pressurization must meet or exceed the compressive stresses introduced by the tension shell in order to prevent localized wrinkling on the surface of the torus. That is:

$$\sigma_{\phi_p,t} + \sigma_{\phi,t} \geq 0 \tag{22}$$

The meridional stress due to pressurization is [76]:

$$\sigma_{\phi_p} = \frac{p_t r_t}{2t_t} \tag{23}$$

where p_t is the internal torus pressure. Since the two attachment methods considered yield different values of compressive stress, two separate inflation pressures can be calculated by equating Equation 23 with Equations 12 and 20 and solving for p.

$$p_{t_A} = \frac{D_{IAD}}{\pi^2 r_t^2 cos\theta_{tc}} \tag{24}$$

$$p_{t_B} = \frac{3D_{IAD}}{2\pi^2 r_t^2 cos\theta_{tc}} \tag{25}$$

The equations above demonstrate that attachment method (b) also results in a 50% higher required inflation pressure versus attachment method (a).

Often, a material strength is quoted as a stress resultant with an accompanying areal density, ρ_{areal} (mass/length^2), for that property. Thus, for sizing of the tension shell and torus the maximum stress resultants are required. In the case of the tension shell, $N_{\phi,ts,\max}$ and $N_{\theta,ts,\max}$ are found from Equations 5 and 6. For the torus, the maximum circumferential stress resultant is attained from Equations 13 and 21. The maximum meridional stress in the torus is again dependent on the manner in which the tension shell is attached. For attachment method (a), the tensile and compressive stress are equal throughout and thus

Table 25: Summary of largest stress resultants and required inflation pressures for attachment methods (a) and (b).

	Method (a)	Method (b)
$N_{\phi,ts}$	$\frac{D_{IAD}}{2\pi r_a \cos\theta_{tc}}$	$\frac{D_{IAD}}{2\pi r_a \cos\theta_{tc}}$
$N_{\theta,ts}$	0	0
$N_{\phi,t}$	$\frac{p_t r_t}{2}$	$\frac{p_t \pi^2 r_t^2 cos\theta_{tc} + D_{IAD}}{2\pi^2 r_t cos\theta_{tc}}$
$N_{\theta,t}$	$\frac{p_t r_t}{2}\left(\frac{2r_{ts}-r_t}{r_{ts}-r_t}\right)$	$\frac{p_t r_t}{2}\left(\frac{2r_{ts}-r_t}{r_{ts}-r_t}\right)$
p_t	$\frac{D_{IAD}}{\pi^2 r_t^2 cos\theta_{tc}}$	$\frac{3D_{IAD}}{2\pi^2 r_t^2 cos\theta_{tc}}$

the maximum stress resultant can be found from Equations 13 and 23. For attachment method (b), the moment that is generating a compressive stress at the attachment point is also producing a tensile stress at a point 180° opposite. Thus, the maximum meridional stress is that due to the combination of the tensile stress from pressurization and the tensile stress introduced by the asymmetrical loading.

$$\sigma_{\phi_{B,\max},t} = \frac{p_t r_t}{2t_t} + \frac{M r_t}{I} = \frac{p_t \pi^2 r_t^2 cos\theta_{tc} + D_{IAD}}{2\pi^2 r_t t_t cos\theta_{tc}} \tag{26}$$

A summary of the four maximum stress resultants and required inflation pressures for both attachment method (a) and method (b) is provided in Table 25. Though not provided here, a basic structural analysis of the torus should also include calculations of the in-plane and out-of-plane global buckling equations detailed in [31] and [42].

The simple tension cone mass model presented here is comprised of four components: the mass of the tension shell (m_{ts}), the mass of the torus (m_t), the mass of the inflation gas (m_{gas}), and the mass of the inflation system ($m_{gas,sys}$). Masses of the tension shell and torus are based upon the surface area of each (A_{ts}, A_t) and two material properties, the areal density (ρ_{areal}) and the allowable stress resultant ($N_{material}$). Using the larger of the two stress resultants calculated for the tension shell and torus, the masses are calculated as follows:

$$m_{ts} = A_{ts}\rho_{areal}\frac{N_{ts}}{N_{material}} \tag{27}$$

$$m_t = A_t\rho_{areal}\frac{N_t}{N_{material}} = 4\pi^2 r_{ts} r_t \rho_{areal}\frac{N_t}{N_{material}} \tag{28}$$

Note that due to its dependence on a given pressure distribution, an exact form of the general tension shell surface area is not possible and the value of A_{ts} must therefore be calculated using numerical integration. Furthermore, Equations 27 and 28 assume that the thickness of the material can scale linearly to achieve a required strength. In practice, some prudence should be used and consideration of a minimum gage thickness is advised.

Estimation of the inflation gas mass is achieved using the equation of state for a perfect gas and an assumption on the temperature of the inflation gas, T_{gas}:

$$m_{gas} = \frac{p_t V_t}{R_{gas}T_{gas}} = \frac{2\pi^2 p_t r_{ts} r_t^2}{R_{gas}T_{gas}} \tag{29}$$

Lastly, estimation of the mass of the system used to provide the inflation gas is left to the end user.

APPENDIX B

TENSION SHELL THEORY AND SHAPE TRADE SPACE

This Appendix provides a summary of the key equations used in tension shell theory based on the original derivation by Anderson [3]. This Appendix also provides an investigation of the tension cone shape trade space. In particular, several simplifying assumptions are made to allow for examination of the drag performance, surface area, and inflation pressure requirements for broad range of tension cone configurations.

B.1 Tension Shell Theory

A tension shell is a shell of revolution designed to exhibit only tensile stresses when an axisymmetric pressure distribution is applied. The theoretical formulation is derived on the basis of linear membrane theory and is published in [3]. Aside from an axisymmetric pressure distribution, three other assumptions are made. First, a pure membrane state of stress is assumed with a constant ratio of circumferential (N_θ) to meridional (N_ϕ) stress. Second, the tension in the shell is resisted at the aft end through the use of a compression ring. Third, the shell dimensions are large versus those of the payload/entry body at the forward end. From these considerations, the following relations (using the formulation of [66] and the coordinate system shown in Figure 109) can be used to define the shape of the tension shell:

$$\frac{d\phi}{dR} + \frac{\alpha}{R}\tan\phi - \frac{ZP}{\cos\phi}R^{1-\alpha} \;=\; 0 \tag{30}$$

$$\frac{dX}{dR} \;=\; -\tan\phi \tag{31}$$

where X denotes a non-dimensional axial coordinate, R is non-dimensional radial coordinate, ϕ is the meridional coordinate, P is the non-dimensional tension shell membrane

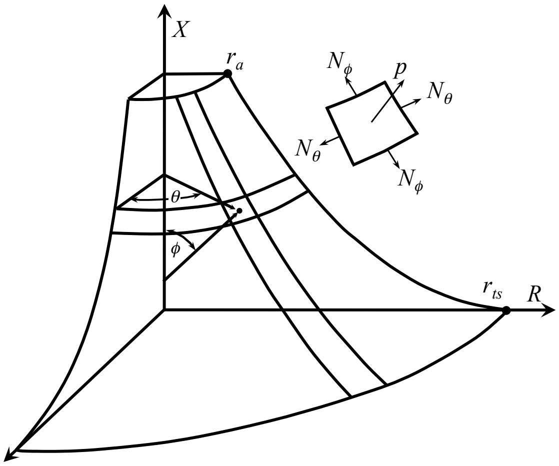

Figure 109: Tension shell coordinate system. Adapted from [3].

pressure differential defined in Equation 32, α is the ratio of circumferential to meridional stress, and Z is a shape parameter defined by Equation 33.

$$P = \frac{p - p_b}{q_\infty} \tag{32}$$

$$Z = \frac{q_\infty r_{ts}}{N_0} \tag{33}$$

In Equation 33, N_0 is the meridional stress resultant N_ϕ evaluated at the tension shell/compression ring interface ($R = 1$). Equation 30 is a first-order differential equation that may be solved for ϕ when the following boundary conditions are applied.

$$\tan\phi|_{R=1} = 0 \tag{34}$$

$$X|_{R=1} = 0 \tag{35}$$

Equation 34 is based on the assumption that there is no force in the X direction on the compression ring and thus the tension shell has a horizontal tangency. Equation 35 places the origin of the coordinate system at the aft of the tension shell. Although Equation 30 requires an input pressure distribution, a simplification can be made if a Newtonian pressure distribution is assumed such that the surface pressure, p, can be equated as:

$$p = 2q_\infty \cos^2\phi \tag{36}$$

Using Equation 36 and assuming zero back pressure ($p_b = 0$) on the tension shell membrane and zero circumferential stress ($\alpha = 0$) leads to the following expression for the slope of the tension shell at radial position R:

$$\frac{dX}{dR} = \sinh Z\left(1 - R^2\right) \tag{37}$$

Integration of Equation 37 can be performed to yield the following explicit relationship for the axial coordinate X as a function of R:

$$X\left(R\right) = \frac{-\sqrt{\pi}\left[\text{Erfi}\left(\sqrt{Z}R\right)\left[-\cosh\left(Z\right) + \sinh\left(Z\right)\right] + \text{Erf}\left(\sqrt{Z}R\right)\left[\cosh\left(Z\right) + \sinh\left(Z\right)\right]\right]}{4\sqrt{Z}} \tag{38}$$

Where Erfi is the imaginary error function defined as:

$$\text{Erfi}\ (z) = \frac{\text{Erf}\ (iz)}{i} = \frac{2}{i\sqrt{\pi}}\int_0^{iz} e^{-t^2}\,dt \tag{39}$$

Furthermore, the drag acting on the surface of a tension shell with Newtonian pressure loading can be analytically calculated and a corresponding drag coefficient based upon the base area of the tension shell can be equated as:

$$\text{C}_{D,ts} = \frac{R^{\alpha}\sin\phi}{Z}|_{r=r_a} \tag{40}$$

It should be noted that this drag coefficient corresponds only to the drag produced by the tension shell lying between the forebody and the aftbody compression rings. A complete tension cone drag coefficient must also account for the drag of the forebody shape and the compression ring (inflated torus). For the case where zero circumferential stress is assumed ($\alpha = 0$), Equation 40 simplifies to

$$\text{C}_{D,ts} = \frac{2}{Z}\tanh Z\left(1 - \left(\frac{r_a}{r_{ts}}\right)^2\right) \tag{41}$$

B.2 Tension Cone Shape Trade Space

Using the equations above, it is possible to gain insight into tension cone performance as a function of geometry. This section summarizes a study performed with that goal in mind. The study evaluated the effect of varying the dimensions of the tension shell itself, the dimensions of the inflated torus compression ring, and the angle at which the tension shell interfaced with the entry vehicle aeroshell. The trade study assumed a 4.5 m diameter 70° sphere cone aeroshell as the entry vehicle. For rapid evaluation, a Newtonian pressure distribution was assumed. Prior studies (e.g. [66]) have noted that this assumption yields surface pressure distributions that are quite different from those seen experimentally but that the overall drag coefficients are generally close.

To completely define the tension cone shape, four parameters are required: the radius of the tension shell (r_{ts}), the radius of the torus compression ring (r_t), the tension shell shape parameter (Z), and the ratio of circumferential to meridional stresses (α). In lieu of the first two, a ratio of tension cone reference area to aeroshell reference area, defined in Equation 42, and a ratio of tension shell radius to torus radius (r_{ts}/r_t) were used.

$$Area\ Ratio\ = \frac{(r_{ts} + r_t)^2}{r_a^2} \tag{42}$$

One difficulty with the standard formulation is that the tension shell shape parameter Z lacks an intuitive physical meaning. However, using Equation 37, one can solve for the value of Z that is required in order to achieve a given interface angle at the tension shell/aeroshell interface location ($R = r_a/r_{ts}$). Thus, the third parameter used in the parametric study was the tension shell interface angle. The last parameter, α, was observed to have only a small effect on the derived tension shell curvature. Furthermore, it was assumed that an axisymmetric shape would not exhibit any circumferential stress at a zero degree angle of attack and thus α was kept fixed at a value of zero.

A literature review of prior tension shell wind tunnel tests revealed that the tension shell angle could have a major impact on the stability of the flow field around the tension shell. That is, shallower tension shell angles exhibited the presence of an attached shock along the surface of the tension shell. As the cone angles are increased, this shock moves further towards the nose until it eventually detaches from the tension shell, as shown in Chapter 2, Figure 12. This effect was seen to be exacerbated at increasing angles of attack and increasing Mach numbers. The presence of the attached shock wave generally induced turbulent flow behind the shock wave, a behavior that would be detrimental on a flexible structure due to severe pressure oscillations on the surface. Based on the available literature, a lower bound of 50° was placed on the tension shell/aeroshell interface angle.

The parametric shape study focused on three primary performance metrics: the total drag coefficient of the tension cone, the surface area of the tension cone, and an estimate of the gas mass required for inflation of the torus. These three metrics were chosen since they provide insights into two primary measures of decelerator efficiency, drag and mass. In the absence of a detailed mass model, it was assumed that the total tension cone material acreage and inflation pressure could serve as indicators of the two major mass components of a tension cone, the mass of the materials used in fabrication and the mass of the required inflation system. Calculation of the total tension cone drag coefficient was achieved by accounting for the drag of the aeroshell, tension shell, and torus independently, as shown in Equation 43.

$$\mathrm{C}_{D,total} = \frac{\mathrm{C}_{D,a}\pi r_a^2 + \mathrm{C}_{D,ts}\pi r_{ts}^2 + \mathrm{C}_{D,t}\pi\left(r_t + r_{ts}\right)^2}{\pi\left(r_t + r_{ts}\right)^2} \tag{43}$$

For the aeroshell drag coefficient, a value of 1.6 was assumed. The tension shell drag coefficient was calculated from Equation 41 using the value of Z required for the desired tension shell/aeroshell interface angle. Assuming Newtonian flow, the torus drag coefficient can be calculated from Equation 44, shown normalized using the total tension cone radius.

$$\mathrm{C}_{D,t} = \frac{r_t\left(\frac{8}{3}r_{ts} + r_t\right)}{\left(r_{ts} + r_t\right)^2} \tag{44}$$

Calculations of the required torus pressure were based upon the requirement to eliminate wrinkling in the torus wall and used the equations derived in Appendix A for attachment method (b). Estimates of the tension shell surface area were made through numerical integration of the calculated tension shell shape. Torus surface area was calculated using Equation 45.

$$A_t = 4\pi^2 r_{ts} r_t \tag{45}$$

B.2.1 Results

Contours of the total drag coefficients calculated across a range of area and radius ratios and three interface angles are provided in Figure 110. For the range of shape parameters considered, it can be seen that the drag coefficient is reasonably insensitive to area ratio (above 6) and significantly more sensitive to the size of the torus relative to the entire tension cone, with larger tori providing lower drag coefficients. Furthermore, although steeper attachment angles produce higher drag coefficients, this is only marginally so. For much of the design space, reducing the attachment angle by 10° for a given value of area ratio and torus size reduces the calculated drag coefficient by less than 5%.

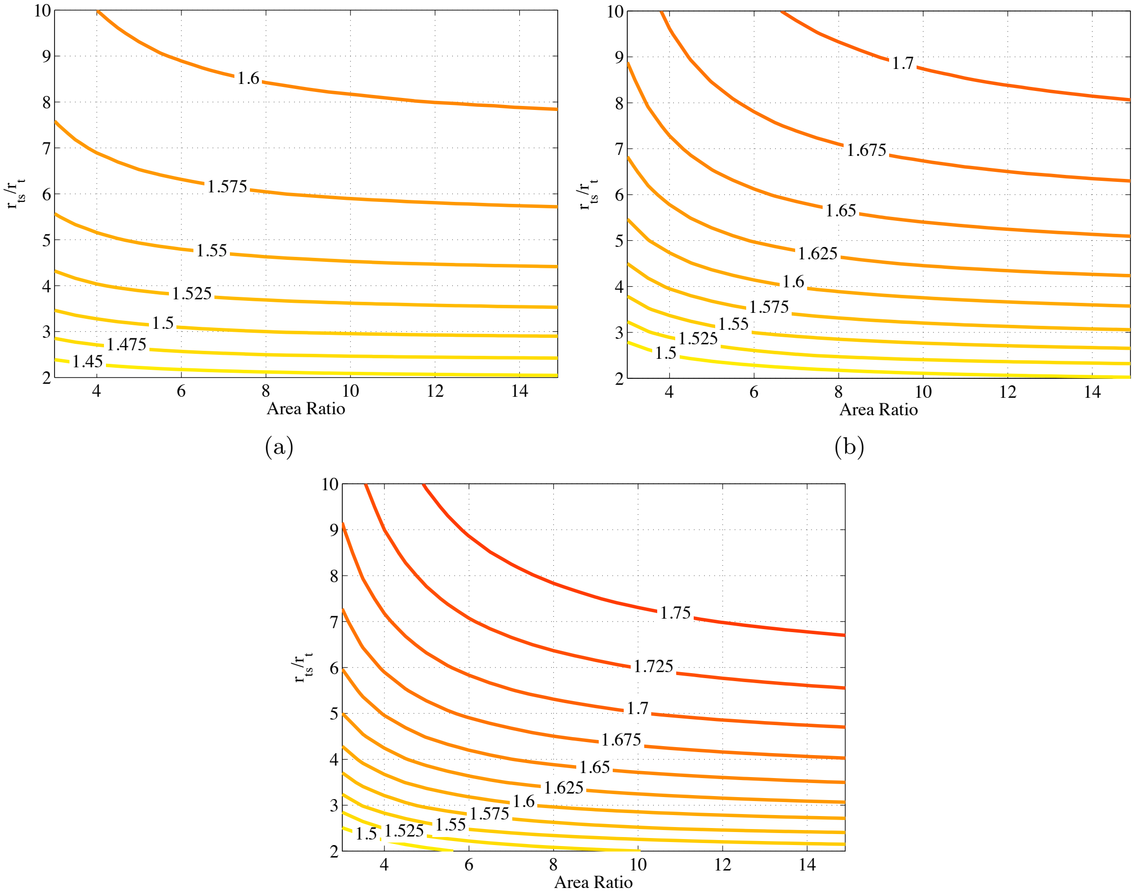

(a)

(b)

(c)

Figure 110: Total tension cone drag coefficient ($C_{D,t}$) sensitivity for tension shell attachment angles of (a) 50°, (b) 60°, and (c) 70°.

An examination of the tension shell and torus material acreage versus the discussed shape parameters is provided in Figure 111. The contours displayed correspond to a non-dimensional sum of the tension shell and torus surface areas normalized by reference area. Of note is that the acreage was observed to be mostly insensitive to tension shell interface angle and thus the results from only one interface angle (60°) are provided. It would be expected that the area ratio would have a large influence on total tension cone acreage; however, the size of the compression ring torus is seen to be equally influential. For a fixed area ratio, smaller values of the tension shell/torus radius ratio indicate larger tori and the surface area of the torus alone can approach that of the entire tension shell. This can be seen when examining the geometries produced by different combinations of tension cone shape parameters, as shown in Figure 112.

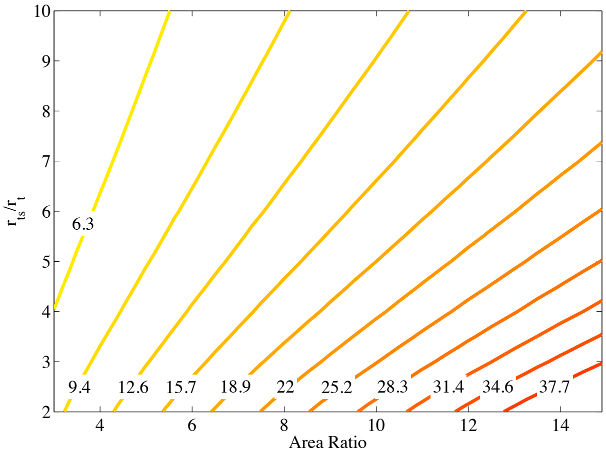

Figure 111: Normalized tension shell and torus surface area for a 60° attachment angle.

An estimate of the mass of gas required for inflation of the torus was made by calculating a non-dimensional torus inflation pressure (p_t/q_∞) and the volume of the torus. Inflation pressure estimates were based upon the formulas provided in Appendix A for attachment method (b). Since the mass of the inflation gas can be shown to scale linearly with gas temperature, molecular weight, and dynamic pressure, the product of the non-dimensional inflation pressure and the torus volume yields a value that is directly proportional to the mass of the gas and which can be used to illustrate sensitivities and trends. The results from these estimates are provided in Figure 113. The contours of Figure 113 reveal several interesting sensitivities. First, the inflation gas mass is seen to be more sensitive to the area

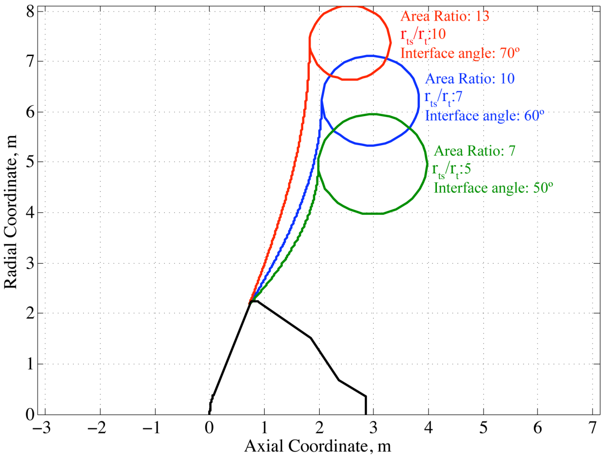

Figure 112: Three configurations of tension cones.

ratio than to the torus ratio, particularly at higher values of torus ratio. This is indicative of the total drag of the tension cone having a larger influence on the gas mass than the size of the torus. Second, the results of the parameter study show that larger attachment angles require higher inflation pressure, a result that is related to the increased drag produced by the tension shell. Steeper attachment angles generate flatter shapes which, when using Newtonian theory, provide more drag. This trend of increased drag with steeper attachment angles is expected even with higher fidelity aerodynamic methods. Lastly, increases in area ratio are seen to require disproportionate increases in inflation gas mass. For example, for a 60° attachment angle, doubling the area ratio yields a ∼3x increase in gas mass.

Combining the results of the drag coefficient sensitivities with the results of the inflation gas mass sensitivities provides a more complete picture of the performance of the tension cone. That is, assuming that the dominant contributor to the mass of the tension cone decelerator is the inflation gas (as was shown in Chapter 3), a measure of decelerator efficiency can be calculated as shown in Equation 46. Note that this does not represent a true decelerator ballistic coefficient but, as with the estimates of inflation gas above, is still able to provide insight into key sensitivities.

$$\beta_{TC} = \frac{p_t V_t}{q_\infty C_{D,total} \pi \left(r_t + r_{ts}\right)^2} \tag{46}$$

Contours of this efficiency measure are shown in Figure 114. As with a traditional

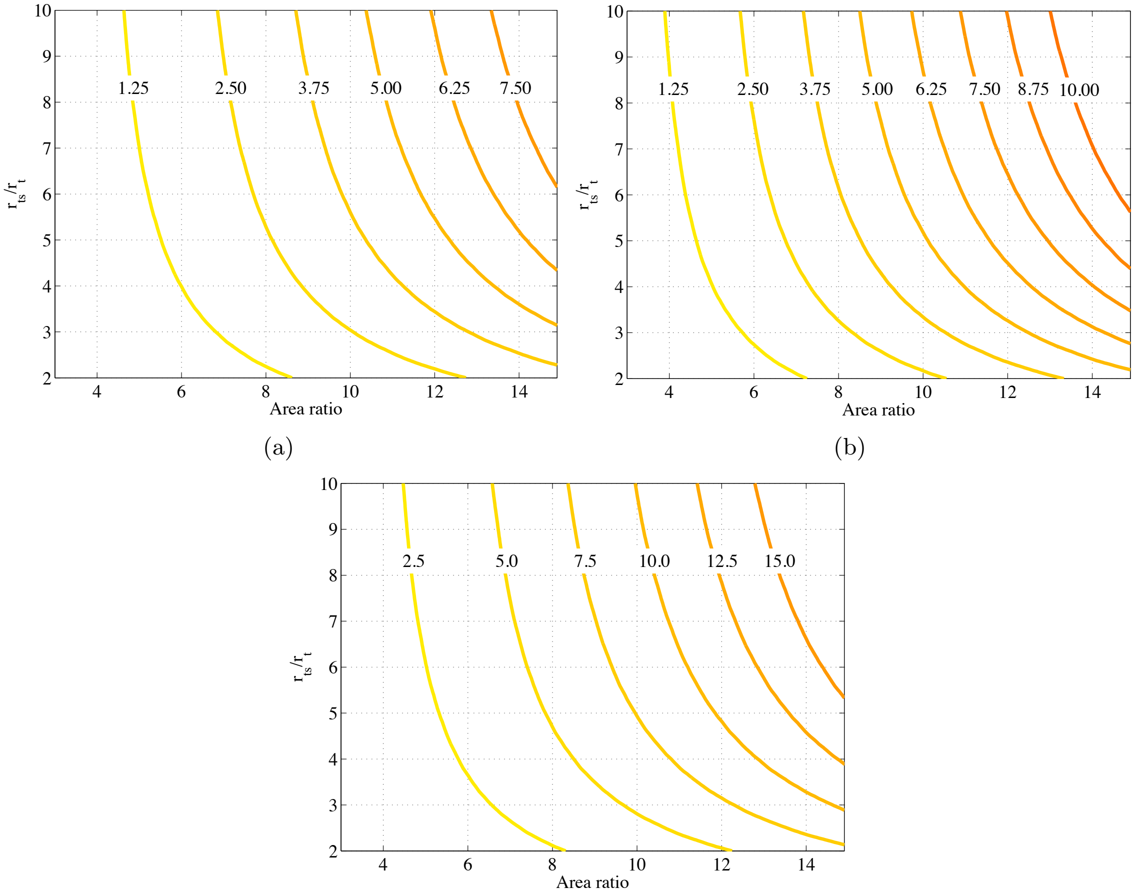

(a)

(b)

(c)

Figure 113: Scaled estimates of the inflation gas mass for tension shell attachment angles of (a) 50°, (b) 60°, and (c) 70°.

ballistic coefficient, smaller numbers indicate a more efficient system.

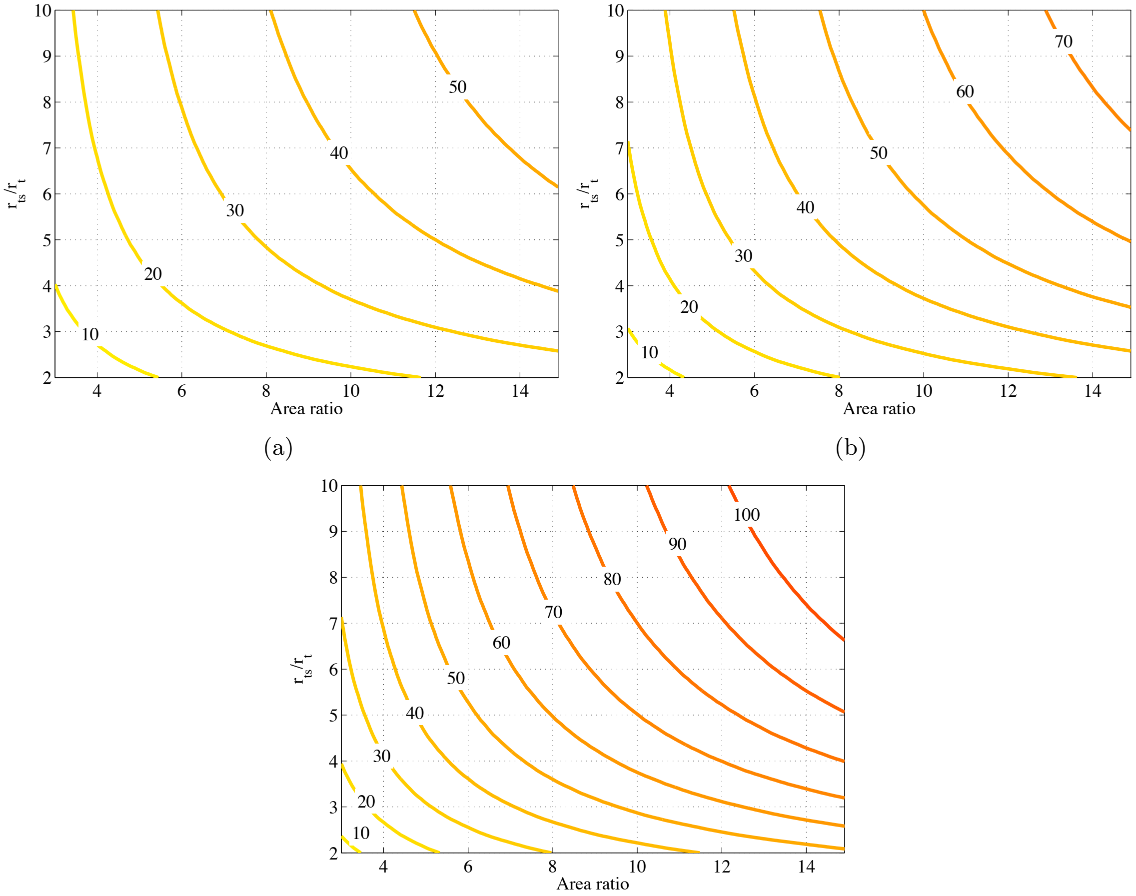

(a)

(b)

(c)

Figure 114: Contours of decelerator efficiency β_{TC} (m) for tension shell attachment angles of (a) 50°, (b) 60°, and (c) 70°.

From Figure 114, it can be seen that for a given combination of area ratio and torus size, smaller attachment angles yield lower values of β_{TC}. Additionally, the lowest values of β_{TC} are seen to occur for the smallest tension cones and largest tori. The favorability of larger tori is likely due to the reduced inflation pressures they afford and an over prediction of the drag contribution of they provide. Using Newtonian pressure assumptions, surface pressures at the periphery of the tension cone, along the flat portion of the tension shell and torus shoulder, are over predicted and likely skew the results shown in Figure 114 to some degree. Nonetheless, the general trends provided should still be valid.

APPENDIX C

TENSION CONE MODEL DIMENSIONS

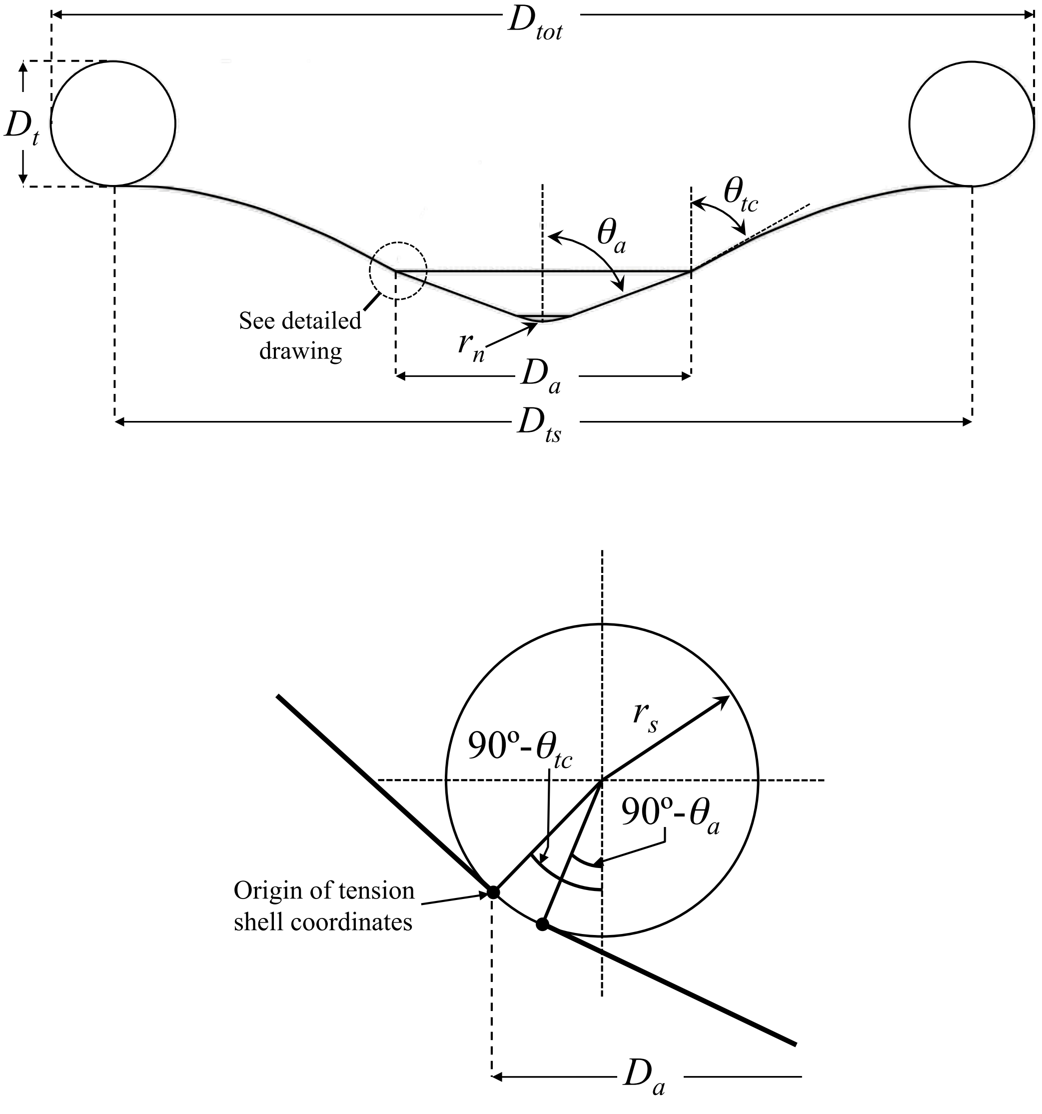

Figure 115: Geometry of the tension cone IAD wind tunnel test configuration.

Table 26: As-designed dimensions of the rigid LaRC Unitary models and the semi-rigid and inflatable GRC 10x10 models.

Quantity	**Symbol**	**Units**	**Unitary Models**	**10x10 Models**
Aeroshell Diameter	D_a	in	1.8447	7.2624
Tension Shell Diameter	D_{ts}	in	5.2500	20.6693
Torus Diameter	D_t	in	0.7500	2.9528
Total Diameter	D_{tot}	in	6.0000	23.6220
Aeroshell Nose Radius	r_a	in	0.4743	1.8675
Aeroshell Shoulder Radius	r_s	in	0.0527	0.2075
Aeroshell Cone Angle	θ_a	deg	70	70
Tension Cone Cone Angle	θ_{tc}	deg	60	60

Table 27: Tension shell coordinates. See Figure 115 for origin description.

LaRC Unitary Rigid Models		GRC 10x10 Models	
Axial Coord., in	Radial Coord., in	Axial Coord., in	Radial Coord., in
0.0000	0.0000	0.0000	0.0000
0.0717	0.1277	0.2822	0.5026
0.1409	0.2589	0.5547	1.0194
0.2052	0.3902	0.8078	1.5361
0.2643	0.5214	1.0404	2.0528
0.3179	0.6527	1.2515	2.5696
0.3658	0.7839	1.4401	3.0863
0.4078	0.9152	1.6056	3.6030
0.4437	1.0464	1.7470	4.1198
0.4734	1.1777	1.8638	4.6365
0.4967	1.3089	1.9553	5.1532
0.5133	1.4402	2.0210	5.6700
0.5233	1.5714	2.0604	6.1867
0.5266	1.7027	2.0733	6.7034

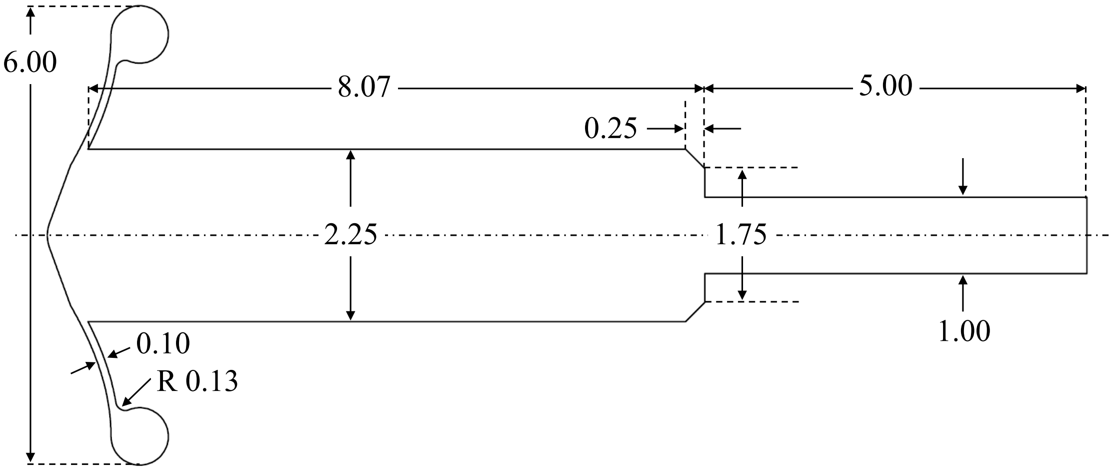

Figure 116: Dimensions of the tension cone configuration used during CFD analyses. All dimensions shown in inches. The tension cone forebody is identical to that described above for the LaRC UPWT rigid models.

APPENDIX D

LANGLEY RESEARCH CENTER UNITARY PLAN WIND TUNNEL RIGID FORCE AND MOMENT DATA TABLES

D.1 Description

The following presents tabulated values of the data presented in Chapter 3 for testing of the rigid force and moment model at the LaRC UPWT. Details of the data reduction and uncertainty analysis are provided in Subsection 3.2.3. The data tables are organized by Mach number. Test conditions pertaining to each Mach number are summarized in Table 28. The data column titled $C_{A_{adj}}$ refers to a value of axial force coefficient that subtracts an estimation of the pressure inside the balance wind shield. This value of axial force coefficient is more appropriate for comparisons to CFD models that only integrate pressures on the forebody and the aftbody region extending from the torus shoulder to the edge of the balance wind shield. Values of the uncertainty in coefficients C_x, listed as UC_x, are shown at the 95% confidence level for an individual observation.

Table 28: Run averaged test conditions for the LaRC Unitary Plan Wind Tunnel force and moment model tests.

Mach	$Re(10^6)$	P_0, **psf (kPa)**		P_S, **psf (kPa)**		T_0, **R (K)**		q_∞, **psf (kPa)**	
1.65	0.999	1095.00	(52.43)	238.89	(11.44)	584.82	(324.90)	455.65	(21.82)
2.00	0.997	1252.97	(59.99)	159.14	(7.62)	585.15	(325.08)	447.38	(21.42)
2.50	1.001	1600.30	(76.62)	93.18	(4.46)	583.81	(324.34)	408.75	(19.57)
3.00	1.003	2083.02	(99.74)	56.76	(2.72)	583.90	(324.39)	357.44	(17.11)
3.51	0.997	2702.85	(129.41)	34.92	(1.67)	583.93	(324.41)	301.23	(14.42)
4.51	0.997	4664.97	(223.36)	15.92	(0.76)	609.33	(338.52)	226.66	(10.85)

Table 29: Static aerodynamic coefficient data at a Mach number of 1.65.

Mach 1.65							
AoA (deg)	C_A	$C_{A_{adj}}$	C_N	C_m	UC_A	UC_N	UC_m
0.0	1.4102	1.4487	0.0001	0.0001	0.0127	0.0006	0.0005
1.0	1.4126	1.4507	0.0022	-0.0027	0.0127	0.0006	0.0005
2.0	1.4182	1.4555	0.0042	-0.0053	0.0127	0.0006	0.0005
3.0	1.4244	1.4609	0.0060	-0.0076	0.0127	0.0006	0.0005
4.0	1.4289	1.4645	0.0079	-0.0099	0.0127	0.0006	0.0005
5.0	1.4319	1.4669	0.0103	-0.0122	0.0127	0.0006	0.0005
6.0	1.4345	1.4689	0.0126	-0.0143	0.0127	0.0006	0.0005
7.0	1.4375	1.4714	0.0149	-0.0163	0.0127	0.0006	0.0005
8.0	1.4400	1.4734	0.0173	-0.0183	0.0127	0.0006	0.0005
9.0	1.4402	1.4731	0.0199	-0.0203	0.0127	0.0006	0.0005
10.0	1.4382	1.4707	0.0225	-0.0224	0.0127	0.0006	0.0005
11.0	1.4359	1.4679	0.0252	-0.0245	0.0127	0.0006	0.0005
12.0	1.4358	1.4673	0.0279	-0.0268	0.0127	0.0006	0.0005
13.0	1.4397	1.4707	0.0307	-0.0291	0.0127	0.0006	0.0005
14.0	1.4457	1.4762	0.0336	-0.0316	0.0127	0.0006	0.0005
15.0	1.4504	1.4803	0.0366	-0.0342	0.0127	0.0006	0.0005
16.0	1.4533	1.4827	0.0395	-0.0365	0.0127	0.0006	0.0005
17.0	1.4553	1.4841	0.0424	-0.0387	0.0127	0.0006	0.0005
18.0	1.4566	1.4847	0.0453	-0.0409	0.0127	0.0006	0.0006
19.0	1.4566	1.4841	0.0482	-0.0430	0.0127	0.0006	0.0006
20.0	1.4557	1.4825	0.0512	-0.0452	0.0127	0.0006	0.0006

Table 30: Static aerodynamic coefficient data at a Mach number of 2.0.

Mach 2.00							
AoA (deg)	C_A	$C_{A_{adj}}$	C_N	C_m	UC_A	UC_N	UC_m
0.0	1.4540	1.4734	0.0000	-0.0001	0.0169	0.0012	0.0013
1.0	1.4551	1.4745	0.0028	-0.0028	0.0169	0.0012	0.0013
2.0	1.4590	1.4783	0.0056	-0.0055	0.0169	0.0012	0.0013
3.0	1.4627	1.4819	0.0085	-0.0081	0.0169	0.0012	0.0013
4.0	1.4647	1.4838	0.0106	-0.0104	0.0169	0.0012	0.0013
5.0	1.4653	1.4841	0.0123	-0.0123	0.0169	0.0013	0.0013
6.0	1.4637	1.4823	0.0141	-0.0140	0.0169	0.0013	0.0013
7.0	1.4610	1.4793	0.0163	-0.0156	0.0169	0.0013	0.0013
8.0	1.4592	1.4773	0.0188	-0.0174	0.0169	0.0013	0.0013
9.0	1.4617	1.4794	0.0218	-0.0199	0.0169	0.0013	0.0013
10.0	1.4668	1.4841	0.0248	-0.0223	0.0169	0.0013	0.0013
11.0	1.4703	1.4872	0.0278	-0.0247	0.0169	0.0013	0.0013
12.0	1.4718	1.4883	0.0310	-0.0274	0.0169	0.0013	0.0013
13.0	1.4719	1.4880	0.0341	-0.0299	0.0169	0.0013	0.0013
14.0	1.4712	1.4868	0.0370	-0.0322	0.0169	0.0013	0.0013
15.0	1.4693	1.4846	0.0399	-0.0344	0.0169	0.0013	0.0013
16.0	1.4661	1.4810	0.0427	-0.0366	0.0169	0.0013	0.0013
17.0	1.4619	1.4766	0.0455	-0.0386	0.0169	0.0013	0.0013
18.0	1.4580	1.4723	0.0481	-0.0405	0.0169	0.0013	0.0014
19.0	1.4542	1.4682	0.0507	-0.0423	0.0169	0.0013	0.0014
20.0	1.4504	1.4641	0.0534	-0.0443	0.0169	0.0013	0.0014

Table 31: Static aerodynamic coefficient data at a Mach number of 2.5.

Mach 2.50							
AoA (deg)	C_A	$C_{A_{adj}}$	C_N	C_m	UC_A	UC_N	UC_m
0.0	1.4995	1.5089	-0.0001	0.0000	0.0169	0.0009	0.0008
1.0	1.4993	1.5087	0.0028	-0.0023	0.0169	0.0009	0.0008
2.0	1.4980	1.5074	0.0056	-0.0047	0.0169	0.0009	0.0008
3.0	1.4944	1.5038	0.0083	-0.0071	0.0169	0.0009	0.0008
4.0	1.4893	1.4987	0.0108	-0.0096	0.0169	0.0009	0.0008
5.0	1.4853	1.4948	0.0135	-0.0119	0.0169	0.0009	0.0008
6.0	1.4826	1.4921	0.0161	-0.0141	0.0169	0.0009	0.0008
7.0	1.4801	1.4896	0.0187	-0.0162	0.0169	0.0009	0.0008
8.0	1.4782	1.4879	0.0213	-0.0184	0.0169	0.0009	0.0008
9.0	1.4761	1.4858	0.0240	-0.0205	0.0169	0.0009	0.0008
10.0	1.4740	1.4837	0.0266	-0.0225	0.0169	0.0009	0.0009
11.0	1.4724	1.4821	0.0292	-0.0245	0.0169	0.0010	0.0009
12.0	1.4696	1.4794	0.0315	-0.0264	0.0169	0.0010	0.0009
13.0	1.4662	1.4760	0.0339	-0.0283	0.0169	0.0010	0.0009
14.0	1.4637	1.4735	0.0365	-0.0302	0.0169	0.0010	0.0009
15.0	1.4616	1.4713	0.0393	-0.0322	0.0169	0.0010	0.0009
16.0	1.4590	1.4686	0.0423	-0.0345	0.0169	0.0010	0.0009
17.0	1.4548	1.4642	0.0454	-0.0368	0.0169	0.0010	0.0009
18.0	1.4486	1.4578	0.0485	-0.0391	0.0169	0.0010	0.0009
19.0	1.4412	1.4501	0.0514	-0.0413	0.0169	0.0010	0.0009
20.0	1.4331	1.4417	0.0542	-0.0431	0.0169	0.0010	0.0009

Table 32: Static aerodynamic coefficient data at a Mach number of 3.0.

Mach 3.00							
AoA (deg)	C_A	$C_{A_{adj}}$	C_N	C_m	UC_A	UC_N	UC_m
0.0	1.4938	1.5024	0.0000	0.0000	0.0187	0.0009	0.0009
1.0	1.4933	1.5020	0.0030	-0.0026	0.0187	0.0009	0.0009
2.0	1.4922	1.5008	0.0060	-0.0051	0.0187	0.0009	0.0009
3.0	1.4905	1.4991	0.0089	-0.0077	0.0187	0.0009	0.0009
4.0	1.4880	1.4966	0.0117	-0.0102	0.0187	0.0009	0.0009
5.0	1.4843	1.4929	0.0146	-0.0127	0.0187	0.0009	0.0009
6.0	1.4807	1.4894	0.0174	-0.0150	0.0187	0.0009	0.0009
7.0	1.4784	1.4871	0.0200	-0.0171	0.0187	0.0009	0.0009
8.0	1.4764	1.4851	0.0225	-0.0191	0.0187	0.0009	0.0009
9.0	1.4742	1.4828	0.0249	-0.0209	0.0187	0.0009	0.0009
10.0	1.4717	1.4803	0.0272	-0.0226	0.0187	0.0009	0.0009
11.0	1.4691	1.4777	0.0298	-0.0244	0.0187	0.0009	0.0009
12.0	1.4656	1.4742	0.0325	-0.0267	0.0187	0.0009	0.0009
13.0	1.4619	1.4705	0.0354	-0.0290	0.0187	0.0010	0.0009
14.0	1.4587	1.4673	0.0381	-0.0310	0.0187	0.0010	0.0009
15.0	1.4560	1.4645	0.0408	-0.0330	0.0187	0.0010	0.0009
16.0	1.4531	1.4616	0.0435	-0.0349	0.0187	0.0010	0.0010
17.0	1.4496	1.4580	0.0464	-0.0369	0.0187	0.0010	0.0010
18.0	1.4448	1.4532	0.0494	-0.0390	0.0187	0.0010	0.0010
19.0	1.4387	1.4469	0.0526	-0.0411	0.0187	0.0010	0.0010
20.0	1.4313	1.4394	0.0556	-0.0431	0.0187	0.0010	0.0010

Table 33: Static aerodynamic coefficient data at a Mach number of 3.5.

Mach 3.51							
AoA (deg)	C_A	$C_{A_{adj}}$	C_N	C_m	UC_A	UC_N	UC_m
0.0	1.4790	1.4872	0.0001	-0.0002	0.0209	0.0009	0.0009
1.0	1.4786	1.4868	0.0026	-0.0021	0.0209	0.0009	0.0009
2.0	1.4781	1.4863	0.0053	-0.0042	0.0209	0.0009	0.0009
3.0	1.4773	1.4854	0.0080	-0.0065	0.0209	0.0009	0.0009
4.0	1.4757	1.4838	0.0107	-0.0090	0.0209	0.0009	0.0009
5.0	1.4736	1.4817	0.0133	-0.0110	0.0209	0.0009	0.0009
6.0	1.4714	1.4795	0.0159	-0.0129	0.0209	0.0009	0.0009
7.0	1.4692	1.4773	0.0185	-0.0151	0.0209	0.0009	0.0009
8.0	1.4673	1.4753	0.0212	-0.0173	0.0209	0.0009	0.0009
9.0	1.4654	1.4734	0.0239	-0.0194	0.0209	0.0009	0.0009
10.0	1.4633	1.4713	0.0265	-0.0215	0.0209	0.0009	0.0009
11.0	1.4606	1.4686	0.0292	-0.0235	0.0209	0.0009	0.0009
12.0	1.4563	1.4642	0.0319	-0.0256	0.0209	0.0009	0.0009
13.0	1.4514	1.4593	0.0344	-0.0276	0.0209	0.0009	0.0009
14.0	1.4476	1.4555	0.0370	-0.0294	0.0209	0.0009	0.0009
15.0	1.4442	1.4520	0.0398	-0.0314	0.0209	0.0009	0.0010
16.0	1.4393	1.4471	0.0428	-0.0336	0.0209	0.0009	0.0010
17.0	1.4328	1.4405	0.0461	-0.0363	0.0209	0.0010	0.0010
18.0	1.4251	1.4327	0.0495	-0.0388	0.0209	0.0010	0.0010
19.0	1.4166	1.4241	0.0523	-0.0408	0.0209	0.0010	0.0010
20.0	1.4084	1.4158	0.0547	-0.0423	0.0209	0.0010	0.0010

Table 34: Static aerodynamic coefficient data at a Mach number of 4.5.

Mach 4.51							
AoA (deg)	C_A	$C_{A_{adj}}$	C_N	C_m	UC_A	UC_N	UC_m
0.0	1.4712	1.4826	0.0000	-0.0002	0.0246	0.0010	0.0011
1.0	1.4709	1.4822	0.0028	-0.0023	0.0246	0.0010	0.0011
2.0	1.4701	1.4814	0.0054	-0.0043	0.0246	0.0010	0.0011
3.0	1.4690	1.4803	0.0081	-0.0065	0.0246	0.0010	0.0011
4.0	1.4679	1.4793	0.0109	-0.0088	0.0246	0.0010	0.0011
5.0	1.4662	1.4775	0.0136	-0.0110	0.0246	0.0010	0.0011
6.0	1.4642	1.4756	0.0160	-0.0129	0.0246	0.0010	0.0011
7.0	1.4624	1.4737	0.0186	-0.0148	0.0246	0.0010	0.0011
8.0	1.4601	1.4713	0.0211	-0.0166	0.0246	0.0010	0.0011
9.0	1.4570	1.4683	0.0236	-0.0185	0.0246	0.0010	0.0011
10.0	1.4550	1.4662	0.0262	-0.0205	0.0246	0.0011	0.0011
11.0	1.4521	1.4633	0.0289	-0.0225	0.0246	0.0011	0.0011
12.0	1.4463	1.4575	0.0315	-0.0245	0.0246	0.0011	0.0011
13.0	1.4406	1.4517	0.0340	-0.0263	0.0246	0.0011	0.0011
14.0	1.4353	1.4464	0.0365	-0.0281	0.0246	0.0011	0.0011
15.0	1.4304	1.4414	0.0390	-0.0298	0.0246	0.0011	0.0011
16.0	1.4258	1.4367	0.0418	-0.0317	0.0246	0.0011	0.0011
17.0	1.4209	1.4318	0.0446	-0.0336	0.0246	0.0011	0.0012
18.0	1.4151	1.4259	0.0473	-0.0354	0.0246	0.0011	0.0012
19.0	1.4087	1.4196	0.0500	-0.0372	0.0246	0.0011	0.0012
20.0	1.4019	1.4126	0.0528	-0.0388	0.0246	0.0011	0.0012

APPENDIX E

LANGLEY RESEARCH CENTER UNITARY PLAN WIND TUNNEL PRESSURE MODEL RESULTS

E.1 Description

The following presents tabulated values of the data presented in Chapter 3 for testing of the rigid pressure model at the LaRC UPWT. Details of the data reduction and uncertainty analysis are provided in Subsection 3.2.3. The data tables are organized by Mach number, approximate angle of attack, and roll angle. Run averaged test conditions pertaining to each Mach number are summarized in Table 35. The specific Mach number and angle of attack at which the pressure data was recorded is also provided in each data table. Radial coordinates for each pressure port are provided in Table 36. During testing, some of the pressure ports were observed to fail and for those ports and test conditions the C_P value is left blank. Values of the uncertainty in C_P, listed as UC_P, are shown at the 95% confidence level for an individual observation.

Table 35: Run averaged test conditions for the LaRC Unitary Plan Wind Tunnel pressure model tests.

Mach	$Re(10^6)$	P_0, **psf (kPa)**		P_S, **psf (kPa)**		T_0, **R (K)**		q_∞, **psf (kPa)**	
1.65	0.998	1094.60	(52.41)	239.00	(11.44)	585.31	(325.17)	455.56	(21.81)
2.00	1.000	1252.98	(59.99)	159.82	(7.65)	584.23	(324.57)	448.06	(21.45)
2.50	0.998	1599.98	(76.61)	93.18	(4.46)	584.11	(324.51)	408.70	(19.57)
3.00	1.002	2083.06	(99.74)	56.69	(2.71)	583.84	(324.36)	357.18	(17.10)
3.51	0.992	2703.00	(129.42)	34.98	(1.67)	583.89	(324.38)	301.52	(14.44)
4.51	0.991	4665.88	(223.40)	15.98	(0.77)	610.28	(339.05)	227.21	(10.88)

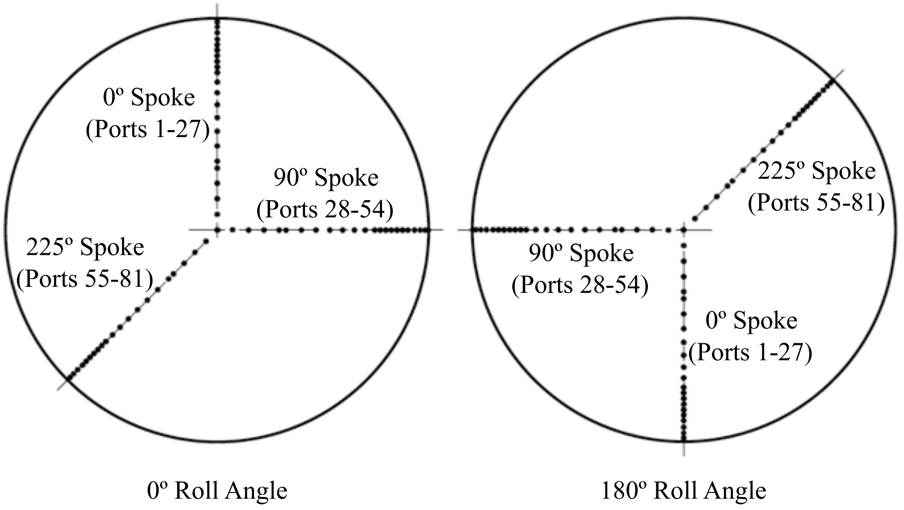

Figure 117: Pressure port location for the UPWT pressure model (front view). Port radial locations are provided in Table 36.

Table 36: Radial location of each of the pressure ports on the UPWT pressure model. Note that ports 24-27, 51-54, and 78-81 are on the backside of the model.

0° Spoke		**45° Spoke**		**225° Spoke**	
ID	**Coord., in. (mm)**	**ID**	**Coord., in. (mm)**	**ID**	**Coord., in. (mm)**
0	0.0016 (0.0407)				
1	0.2232 (5.6693)	28	0.2249 (5.7125)	55	0.2233 (5.6721)
2	0.4449 (11.3005)	29	0.4466 (11.3436)	56	0.4451 (11.3044)
3	0.6633 (16.8478)	30	0.6648 (16.8859)	57	0.6633 (16.8470)
4	0.8771 (22.2783)	31	0.8786 (22.3164)	58	0.8767 (22.2693)
5	0.9752 (24.7701)	32	0.9770 (24.8158)	59	0.9754 (24.7748)
6	1.1919 (30.2743)	33	1.1939 (30.3251)	60	1.1921 (30.2797)
7	1.3990 (35.5346)	34	1.4008 (35.5803)	61	1.3993 (35.5421)
8	1.5949 (40.5105)	35	1.5963 (40.5460)	62	1.5946 (40.5028)
9	1.7768 (45.1307)	36	1.7788 (45.1815)	63	1.7772 (45.1402)
10	1.9445 (49.3903)	37	1.9463 (49.4360)	64	1.9450 (49.4022)
11	2.0967 (53.2562)	38	2.0981 (53.2917)	65	2.0968 (53.2583)
12	2.2311 (56.6699)	39	2.2326 (56.7080)	66	2.2311 (56.6708)
13	2.3099 (58.6715)	40	2.3114 (58.7096)	67	2.3099 (58.6716)
14	2.3885 (60.6679)	41	2.3900 (60.7060)	68	2.3887 (60.6724)
15	2.4673 (62.6694)	42	2.4686 (62.7024)	69	2.4673 (62.6696)
16	2.5460 (64.6684)	43	2.5476 (64.7090)	70	2.5463 (64.6758)
17	2.6246 (66.6648)	44	2.6263 (66.7080)	71	2.6246 (66.6658)
18	2.7024 (68.6410)	45	2.7032 (68.6613)	72	2.7020 (68.6307)
19	2.8017 (71.1632)	46	2.7960 (71.0184)	73	2.7950 (70.9925)
20	2.8792 (73.1317)	47	2.8771 (73.0783)	74	2.8907 (73.4250)
21	2.9391 (74.6524)	48	2.9396 (74.6656)	75	2.9397 (74.6673)
22	2.9821 (75.7443)	49	2.9822 (75.7468)	76	2.9821 (75.7460)
23	2.9996 (76.1897)	50	2.9996 (76.1894)	77	2.9996 (76.1903)
24	2.6250 (66.6750)	51	2.6250 (66.6750)	78	2.6250 (66.6750)
25	2.2503 (57.1576)	52	2.2503 (57.1576)	79	2.2503 (57.1576)
26	2.0968 (53.2587)	53	2.0968 (53.2587)	80	2.0968 (53.2587)
27	1.3993 (35.5422)	54	1.3993 (35.5422)	81	1.3993 (35.5422)

Table 37: Pressure coefficient data at a Mach number of 1.65, ∼0° angle of attack, and 0° roll angle.

Mach Number	1.651	**AoA (deg)**	0.644	**Roll (deg)**	0.0

ID	C_P	UC_P	**ID**	C_P	UC_P	**ID**	C_P	UC_P
0	1.585	0.018						
1	1.571	0.018	28	1.574	0.018	55	1.572	0.018
2	1.552	0.018	29	1.556	0.018	56	1.557	0.018
3	1.532	0.018	30	1.537	0.018	57	1.539	0.018
4	1.502	0.018	31	1.505	0.018	58	1.507	0.018
5	1.489	0.018	32	1.496	0.018	59	1.498	0.018
6	1.491	0.018	33	1.495	0.018	60	1.496	0.018
7	1.487	0.018	34	1.489	0.018	61	1.489	0.018
8	1.477	0.018	35	1.480	0.018	62	1.482	0.018
9	1.465	0.018	36	1.465	0.018	63	1.469	0.018
10	1.449	0.018	37	1.450	0.018	64	1.454	0.018
11	1.431	0.018	38	1.429	0.018	65	1.435	0.018
12	1.409	0.018	39	1.406	0.018	66	1.412	0.018
13	1.382	0.018	40	1.385	0.018	67	1.392	0.018
14	1.352	0.018	41	1.354	0.018	68	1.363	0.018
15	1.312	0.017	42	1.310	0.017	69	1.316	0.017
16	1.243	0.017	43	1.236	0.017	70	1.253	0.017
17	1.074	0.016	44	1.077	0.016	71	1.109	0.017
18	0.737	0.015	45	0.725	0.015	72	0.738	0.015
19	0.288	0.013	46	0.336	0.014	73	0.308	0.013
20	0.003	0.012	47	0.053	0.013	74	0.010	0.012
21	-0.242	0.012	48	-0.225	0.012	75	-0.219	0.012
22	-0.261	0.011	49	-0.261	0.011	76	-0.268	0.011
23	-0.240	0.011	50	-0.252	0.011	77	-0.252	0.011
24	-0.253	0.011	51	-0.253	0.011	78	-0.255	0.011
25	-0.249	0.011	52	-0.251	0.011	79	-0.252	0.011
26	-0.247	0.011	53	-0.251	0.011	80	-0.252	0.011
27	-0.250	0.011	54	-0.252	0.011	81	-0.252	0.011

Table 38: Pressure coefficient data at a Mach number of 1.65, ∼0° angle of attack, and 180° roll angle.

Mach Number		1.651	**AoA (deg)**		0.354	**Roll (deg)**		180.0
ID	C_P	UC_P	**ID**	C_P	UC_P	**ID**	C_P	UC_P
0	1.586	0.018						
1	1.574	0.018	28	1.574	0.018	55	1.571	0.018
2	1.555	0.018	29	1.555	0.018	56	1.556	0.018
3	1.536	0.018	30	1.537	0.018	57	1.537	0.018
4	1.507	0.018	31	1.504	0.018	58	1.505	0.018
5	1.493	0.018	32	1.494	0.018	59	1.496	0.018
6	1.496	0.018	33	1.495	0.018	60	1.493	0.018
7	1.489	0.018	34	1.488	0.018	61	1.488	0.018
8	1.480	0.018	35	1.478	0.018	62	1.481	0.018
9	1.468	0.018	36	1.465	0.018	63	1.468	0.018
10	1.454	0.018	37	1.450	0.018	64	1.452	0.018
11	1.434	0.018	38	1.430	0.018	65	1.433	0.018
12	1.414	0.018	39	1.407	0.018	66	1.410	0.018
13	1.387	0.018	40	1.385	0.018	67	1.390	0.018
14	1.358	0.018	41	1.354	0.018	68	1.361	0.018
15	1.317	0.017	42	1.309	0.017	69	1.314	0.017
16	1.250	0.017	43	1.236	0.017	70	1.250	0.017
17	1.082	0.016	44	1.076	0.016	71	1.105	0.017
18	0.748	0.015	45	0.725	0.015	72	0.731	0.015
19	0.306	0.013	46	0.337	0.014	73	0.297	0.013
20	0.020	0.012	47	0.055	0.013	74	0.000	0.012
21	-0.229	0.012	48	-0.224	0.012	75	-0.224	0.012
22	-0.269	0.011	49	-0.260	0.011	76	-0.263	0.011
23	-0.261	0.011	50	-0.251	0.011	77	-0.251	0.011
24	-0.254	0.011	51	-0.252	0.011	78	-0.254	0.011
25	-0.252	0.011	52	-0.251	0.011	79	-0.251	0.011
26	-0.250	0.011	53	-0.251	0.011	80	-0.250	0.011
27	-0.253	0.011	54	-0.251	0.011	81	-0.251	0.011

Table 39: Pressure coefficient data at a Mach number of 1.65, ~12° angle of attack, and 0° roll angle.

Mach Number		1.651	**AoA (deg)**		12.621	**Roll (deg)**		0.0
ID	C_P	UC_P	**ID**	C_P	UC_P	**ID**	C_P	UC_P
0	1.487	0.018						
1	1.445	0.018	28	1.482	0.018	55	1.537	0.018
2	1.423	0.018	29	1.478	0.018	56	1.549	0.018
3	1.392	0.018	30	1.468	0.018	57	1.550	0.018
4	1.340	0.018	31	1.441	0.018	58	1.539	0.018
5	1.330	0.017	32	1.431	0.018	59	1.538	0.018
6	1.362	0.018	33	1.437	0.018	60	1.527	0.018
7	1.373	0.018	34	1.435	0.018	61	1.523	0.018
8	1.369	0.018	35	1.430	0.018	62	1.520	0.018
9	1.360	0.018	36	1.419	0.018	63	1.510	0.018
10	1.345	0.018	37	1.408	0.018	64	1.499	0.018
11	1.326	0.017	38	1.392	0.018	65	1.485	0.018
12	1.302	0.017	39	1.370	0.018	66	1.467	0.018
13	1.271	0.017	40	1.350	0.018	67	1.454	0.018
14	1.238	0.017	41	1.321	0.017	68	1.430	0.018
15	1.190	0.017	42	1.278	0.017	69	1.392	0.018
16	1.114	0.017	43	1.207	0.017	70	1.343	0.018
17	0.922	0.016	44	1.051	0.016	71	1.230	0.017
18	0.554	0.014	45	0.709	0.015	72	0.928	0.016
19	0.071	0.013	46	0.332	0.014	73	0.572	0.015
20	-0.197	0.012	47	0.053	0.013	74	0.214	0.013
21	-0.311	0.011	48	-0.222	0.012	75	-0.066	0.012
22	-0.290	0.011	49	-0.330	0.011	76	-0.234	0.012
23	-0.289	0.011	50	-0.294	0.011	77	-0.312	0.011
24	-0.293	0.011	51	-0.293	0.011	78	-0.295	0.011
25	-0.294	0.011	52	-0.294	0.011	79	-0.294	0.011
26	-0.292	0.011	53	-0.295	0.011	80	-0.294	0.011
27	-0.293	0.011	54	-0.293	0.011	81	-0.294	0.011

Table 40: Pressure coefficient data at a Mach number of 1.65, ~12° angle of attack, and 180° roll angle.

Mach Number		1.651	**AoA (deg)**		12.361	**Roll (deg)**		180.0
ID	C_P	UC_P	**ID**	C_P	UC_P	**ID**	C_P	UC_P
0	1.491	0.018						
1	1.572	0.018	28	1.488	0.018	55	1.456	0.018
2	1.586	0.019	29	1.483	0.018	56	1.441	0.018
3	1.591	0.019	30	1.473	0.018	57	1.416	0.018
4	1.588	0.019	31	1.445	0.018	58	1.371	0.018
5	1.583	0.019	32	1.436	0.018	59	1.360	0.018
6	1.578	0.018	33	1.440	0.018	60	1.381	0.018
7	1.572	0.018	34	1.437	0.018	61	1.385	0.018
8	1.564	0.018	35	1.432	0.018	62	1.383	0.018
9	1.556	0.018	36	1.421	0.018	63	1.374	0.018
10	1.546	0.018	37	1.410	0.018	64	1.359	0.018
11	1.531	0.018	38	1.392	0.018	65	1.339	0.018
12	1.518	0.018	39	1.371	0.018	66	1.315	0.017
13	1.499	0.018	40	1.351	0.018	67	1.295	0.017
14	1.477	0.018	41	1.320	0.017	68	1.265	0.017
15	1.449	0.018	42	1.278	0.017	69	1.212	0.017
16	1.400	0.018	43	1.207	0.017	70	1.141	0.017
17	1.278	0.017	44	1.049	0.016	71	0.981	0.016
18	1.025	0.016	45	0.706	0.015	72	0.570	0.015
19	0.675	0.015	46	0.329	0.014	73	0.116	0.013
20	0.333	0.014	47	0.051	0.013	74	-0.164	0.012
21	0.002	0.012	48	-0.220	0.012	75	-0.328	0.011
22	-0.169	0.012	49	-0.326	0.011	76	-0.292	0.011
23	-0.327	0.011	50	-0.292	0.011	77	-0.291	0.011
24	-0.292	0.011	51	-0.290	0.011	78	-0.292	0.011
25	-0.292	0.011	52	-0.292	0.011	79	-0.292	0.011
26	-0.291	0.011	53	-0.292	0.011	80	-0.291	0.011
27	-0.293	0.011	54	-0.291	0.011	81	-0.290	0.011

Table 41: Pressure coefficient data at a Mach number of 1.65, ~20° angle of attack, and 0° roll angle.

Mach Number		1.643	**AoA (deg)**		20.401	**Roll (deg)**		0.0
ID	C_P	UC_P	**ID**	C_P	UC_P	**ID**	C_P	UC_P
0	1.309	0.017						
1	1.291	0.017	28	1.320	0.017	55	1.422	0.018
2	1.285	0.017	29	1.344	0.018	56	1.462	0.018
3	1.259	0.017	30	1.346	0.018	57	1.481	0.018
4	1.207	0.017	31	1.327	0.017	58	1.486	0.018
5	1.203	0.017	32	1.320	0.017	59	1.490	0.018
6	1.240	0.017	33	1.330	0.017	60	1.485	0.018
7	1.287	0.017	34	1.336	0.017	61	1.487	0.018
8	1.284	0.017	35	1.338	0.018	62	1.488	0.018
9	1.279	0.017	36	1.333	0.017	63	1.484	0.018
10	1.265	0.017	37	1.327	0.017	64	1.479	0.018
11	1.247	0.017	38	1.314	0.017	65	1.470	0.018
12	1.224	0.017	39	1.297	0.017	66	1.459	0.018
13	1.195	0.017	40	1.279	0.017	67	1.450	0.018
14	1.160	0.017	41	1.253	0.017	68	1.432	0.018
15	1.111	0.017	42	1.214	0.017	69	1.402	0.018
16	1.034	0.016	43	1.146	0.017	70	1.366	0.018
17	0.837	0.016	44	0.997	0.016	71	1.278	0.017
18	0.455	0.014	45	0.672	0.015	72	1.037	0.016
19	-0.010	0.012	46	0.310	0.014	73	0.726	0.015
20	-0.265	0.011	47	0.039	0.013	74	0.359	0.014
21	-0.327	0.011	48	-0.227	0.012	75	0.065	0.013
22	-0.320	0.011	49	-0.356	0.011	76	-0.121	0.012
23	-0.320	0.011	50	-0.328	0.011	77	-0.298	0.011
24	-0.324	0.011	51	-0.327	0.011	78	-0.331	0.011
25	-0.326	0.011	52	-0.326	0.011	79	-0.326	0.011
26	-0.322	0.011	53	-0.326	0.011	80	-0.326	0.011
27	-0.326	0.011	54	-0.326	0.011	81	-0.325	0.011

Table 42: Pressure coefficient data at a Mach number of 1.65, ∼20° angle of attack, and 180° roll angle.

Mach Number	1.643	**AoA (deg)**	20.175	**Roll (deg)**	180.0

ID	C_P	UC_P	**ID**	C_P	UC_P	**ID**	C_P	UC_P
0	1.313	0.017						
1	1.488	0.018	28	1.327	0.017	55	1.291	0.017
2	1.535	0.018	29	1.347	0.018	56	1.293	0.017
3	1.560	0.018	30	1.349	0.018	57	1.274	0.017
4	1.573	0.018	31	1.329	0.017	58	1.230	0.017
5	1.578	0.018	32	1.323	0.017	59	1.222	0.017
6	1.582	0.018	33	1.331	0.017	60	1.264	0.017
7	1.582	0.018	34	1.337	0.018	61	1.279	0.017
8	1.579	0.018	35	1.338	0.018	62	1.285	0.017
9	1.577	0.018	36	1.335	0.017	63	1.282	0.017
10	1.573	0.018	37	1.329	0.017	64	1.271	0.017
11	1.564	0.018	38	1.315	0.017	65	1.255	0.017
12	1.559	0.018	39	1.297	0.017	66	1.233	0.017
13	1.547	0.018	40	1.280	0.017	67	1.214	0.017
14	1.534	0.018	41	1.254	0.017	68	1.185	0.017
15	1.518	0.018	42	1.214	0.017	69	1.133	0.017
16	1.486	0.018	43	1.147	0.017	70	1.061	0.016
17	1.406	0.018	44	0.997	0.016	71	0.896	0.016
18	1.228	0.017	45	0.670	0.015	72	0.472	0.014
19	0.940	0.016	46	0.312	0.014	73	0.031	0.013
20	0.593	0.015	47	0.040	0.013	74	-0.232	0.012
21	0.244	0.013	48	-0.221	0.012	75	-0.362	0.011
22	0.048	0.013	49	-0.355	0.011	76	-0.331	0.011
23	-0.188	0.011	50	-0.333	0.011	77	-0.330	0.011
24	-0.335	0.011	51	-0.331	0.011	78	-0.332	0.011
25	-0.332	0.011	52	-0.331	0.011	79	-0.331	0.011
26	-0.330	0.011	53	-0.331	0.011	80	-0.330	0.011
27	-0.330	0.011	54	-0.330	0.011	81	-0.330	0.011

Table 43: Pressure coefficient data at a Mach number of 2.0, ∼0° angle of attack, and 0° roll angle.

Mach Number		2.002	**AoA (deg)**		0.237	**Roll (deg)**		0.0
ID	C_P	UC_P	**ID**	C_P	UC_P	**ID**	C_P	UC_P
0	1.649	0.022						
1	1.637	0.022	28	1.635	0.022	55	1.635	0.022
2	1.622	0.022	29	1.620	0.022	56	1.619	0.022
3	1.604	0.021	30	1.598	0.021	57	1.598	0.021
4	1.575	0.021	31	1.570	0.021	58	1.572	0.021
5	1.562	0.021	32	1.562	0.021	59	1.556	0.021
6	1.565	0.021	33	1.564	0.021	60	1.564	0.021
7	1.560	0.021	34	1.556	0.021	61	1.556	0.021
8	1.552	0.021	35	1.551	0.021	62	1.546	0.021
9	1.541	0.021	36	1.537	0.021	63	1.537	0.021
10	1.526	0.021	37	1.524	0.021	64	1.521	0.021
11	1.509	0.021	38	1.504	0.021	65	1.506	0.021
12	1.488	0.021	39	1.481	0.021	66	1.480	0.021
13	1.462	0.020	40	1.461	0.020	67	1.460	0.020
14	1.435	0.020	41	1.432	0.020	68	1.432	0.020
15	1.396	0.020	42	1.388	0.020	69	1.392	0.020
16	1.329	0.019	43	1.317	0.019	70	1.325	0.019
17	1.164	0.018	44	1.166	0.018	71	1.190	0.018
18	0.847	0.016	45	0.826	0.016	72	0.830	0.016
19	0.413	0.013	46	0.451	0.013	73	0.412	0.013
20	0.139	0.011	47	0.183	0.011	74	0.128	0.011
21	-0.091	0.009	48	-0.082	0.009	75	-0.087	0.009
22	-0.199	0.009	49	-0.206	0.009	76	-0.200	0.009
23	-0.223	0.008	50	-0.221	0.008	77	-0.223	0.008
24	-0.220	0.008	51	-0.215	0.008	78	-0.220	0.008
25	-0.220	0.008	52	-0.221	0.008	79	-0.220	0.008
26	-0.217	0.008	53	-0.216	0.008	80	-0.218	0.008
27	-0.217	0.008	54	-0.220	0.008	81	-0.217	0.008

Table 44: Pressure coefficient data at a Mach number of 2.0, ∼0° angle of attack, and 180° roll angle.

Mach Number		2.002	**AoA (deg)**		-0.001	**Roll (deg)**		180.0
ID	C_P	UC_P	**ID**	C_P	UC_P	**ID**	C_P	UC_P
0	1.648	0.022						
1	1.632	0.022	28	1.635	0.022	55	1.636	0.022
2	1.615	0.022	29	1.620	0.022	56	1.621	0.022
3	1.596	0.021	30	1.597	0.021	57	1.602	0.021
4	1.566	0.021	31	1.570	0.021	58	1.577	0.021
5	1.553	0.021	32	1.562	0.021	59	1.562	0.021
6	1.557	0.021	33	1.563	0.021	60	1.568	0.021
7	1.551	0.021	34	1.556	0.021	61	1.561	0.021
8	1.543	0.021	35	1.550	0.021	62	1.551	0.021
9	1.533	0.021	36	1.536	0.021	63	1.542	0.021
10	1.517	0.021	37	1.523	0.021	64	1.526	0.021
11	1.500	0.021	38	1.503	0.021	65	1.512	0.021
12	1.479	0.021	39	1.479	0.020	66	1.486	0.021
13	1.453	0.020	40	1.460	0.020	67	1.465	0.020
14	1.426	0.020	41	1.429	0.020	68	1.438	0.020
15	1.387	0.020	42	1.386	0.020	69	1.398	0.020
16	1.320	0.019	43	1.315	0.019	70	1.331	0.019
17	1.155	0.018	44	1.162	0.018	71	1.196	0.018
18	0.837	0.016	45	0.821	0.016	72	0.838	0.016
19	0.405	0.013	46	0.445	0.013	73	0.420	0.013
20	0.134	0.011	47	0.177	0.011	74	0.135	0.011
21	-0.094	0.009	48	-0.085	0.009	75	-0.083	0.009
22	-0.201	0.009	49	-0.208	0.008	76	-0.198	0.009
23	-0.222	0.008	50	-0.220	0.008	77	-0.222	0.008
24	-0.220	0.008	51	-0.213	0.008	78	-0.220	0.008
25	-0.218	0.008	52	-0.220	0.008	79	-0.219	0.008
26	-0.214	0.008	53	-0.215	0.008	80	-0.219	0.008
27	-0.215	0.008	54	-0.219	0.008	81	-0.217	0.008

Table 45: Pressure coefficient data at a Mach number of 2.0, ∼12° angle of attack, and 0° roll angle.

Mach Number		1.999	**AoA (deg)**		13.325	**Roll (deg)**		0.0
ID	C_P	UC_P	**ID**	C_P	UC_P	**ID**	C_P	UC_P
0	1.524	0.021						
1	1.483	0.021	28	1.520	0.021	55	1.584	0.021
2	1.465	0.020	29	1.523	0.021	56	1.599	0.021
3	1.437	0.020	30	1.510	0.021	57	1.602	0.021
4	1.386	0.020	31	1.488	0.021	58	1.598	0.021
5	1.380	0.020	32	1.481	0.021	59	1.590	0.021
6	1.407	0.020	33	1.488	0.021	60	1.589	0.021
7	1.433	0.020	34	1.486	0.021	61	1.583	0.021
8	1.428	0.020	35	1.486	0.021	62	1.577	0.021
9	1.421	0.020	36	1.476	0.020	63	1.572	0.021
10	1.405	0.020	37	1.467	0.020	64	1.562	0.021
11	1.389	0.020	38	1.452	0.020	65	1.551	0.021
12	1.366	0.020	39	1.432	0.020	66	1.533	0.021
13	1.337	0.019	40	1.414	0.020	67	1.517	0.021
14	1.307	0.019	41	1.386	0.020	68	1.497	0.021
15	1.261	0.019	42	1.346	0.019	69	1.467	0.020
16	1.186	0.018	43	1.277	0.019	70	1.416	0.020
17	1.000	0.017	44	1.131	0.018	71	1.312	0.019
18	0.652	0.014	45	0.803	0.015	72	1.028	0.017
19	0.190	0.011	46	0.441	0.013	73	0.689	0.015
20	-0.061	0.009	47	0.178	0.011	74	0.345	0.012
21	-0.221	0.008	48	-0.082	0.009	75	0.071	0.010
22	-0.249	0.008	49	-0.205	0.009	76	-0.084	0.009
23	-0.239	0.008	50	-0.257	0.008	77	-0.217	0.008
24	-0.245	0.008	51	-0.240	0.008	78	-0.245	0.008
25	-0.245	0.008	52	-0.246	0.008	79	-0.245	0.008
26	-0.241	0.008	53	-0.242	0.008	80	-0.244	0.008
27	-0.240	0.008	54	-0.245	0.008	81	-0.242	0.008

Table 46: Pressure coefficient data at a Mach number of 2.0, ∼12° angle of attack, and 180° roll angle.

Mach Number	1.999	**AoA (deg)**	13.079	**Roll (deg)**	180.0

ID	C_P	UC_P	**ID**	C_P	UC_P	**ID**	C_P	UC_P
0	1.529	0.021						
1	1.624	0.022	28	1.526	0.021	55	1.495	0.021
2	1.645	0.022	29	1.528	0.021	56	1.481	0.021
3	1.653	0.022	30	1.514	0.021	57	1.456	0.020
4	1.651	0.022	31	1.491	0.021	58	1.417	0.020
5	1.648	0.022	32	1.484	0.021	59	1.400	0.020
6	1.642	0.022	33	1.490	0.021	60	1.435	0.020
7	1.636	0.022	34	1.488	0.021	61	1.438	0.020
8	1.631	0.022	35	1.487	0.021	62	1.436	0.020
9	1.624	0.022	36	1.478	0.020	63	1.431	0.020
10	1.614	0.022	37	1.468	0.020	64	1.417	0.020
11	1.603	0.021	38	1.452	0.020	65	1.402	0.020
12	1.590	0.021	39	1.432	0.020	66	1.377	0.020
13	1.572	0.021	40	1.413	0.020	67	1.355	0.020
14	1.556	0.021	41	1.386	0.020	68	1.326	0.019
15	1.529	0.021	42	1.344	0.019	69	1.283	0.019
16	1.485	0.021	43	1.276	0.019	70	1.209	0.018
17	1.371	0.020	44	1.128	0.018	71	1.057	0.017
18	1.138	0.018	45	0.797	0.015	72	0.663	0.014
19	0.805	0.015	46	0.436	0.013	73	0.231	0.011
20	0.473	0.013	47	0.173	0.011	74	-0.033	0.010
21	0.155	0.011	48	-0.082	0.009	75	-0.195	0.009
22	-0.013	0.010	49	-0.205	0.009	76	-0.262	0.008
23	-0.180	0.008	50	-0.253	0.008	77	-0.222	0.008
24	-0.244	0.008	51	-0.238	0.008	78	-0.243	0.008
25	-0.244	0.008	52	-0.244	0.008	79	-0.244	0.008
26	-0.240	0.008	53	-0.240	0.008	80	-0.243	0.008
27	-0.241	0.008	54	-0.244	0.008	81	-0.241	0.008

Table 47: Pressure coefficient data at a Mach number of 2.0, ∼20° angle of attack, and 0° roll angle.

Mach Number		1.990	**AoA (deg)**		20.940	**Roll (deg)**		0.0
ID	C_P	UC_P	**ID**	C_P	UC_P	**ID**	C_P	UC_P
0	1.344	0.019						
1	1.328	0.019	28	1.356	0.020	55	1.474	0.020
2	1.331	0.019	29	1.387	0.020	56	1.519	0.021
3	1.308	0.019	30	1.388	0.020	57	1.539	0.021
4	1.259	0.019	31	1.376	0.020	58	1.548	0.021
5	1.261	0.019	32	1.370	0.020	59	1.545	0.021
6	1.298	0.019	33	1.384	0.020	60	1.549	0.021
7	1.358	0.020	34	1.392	0.020	61	1.549	0.021
8	1.360	0.020	35	1.399	0.020	62	1.548	0.021
9	1.356	0.020	36	1.396	0.020	63	1.548	0.021
10	1.345	0.019	37	1.393	0.020	64	1.544	0.021
11	1.330	0.019	38	1.383	0.020	65	1.539	0.021
12	1.308	0.019	39	1.367	0.020	66	1.526	0.021
13	1.278	0.019	40	1.352	0.020	67	1.515	0.021
14	1.247	0.019	41	1.326	0.019	68	1.500	0.021
15	1.201	0.018	42	1.289	0.019	69	1.479	0.021
16	1.124	0.018	43	1.224	0.019	70	1.440	0.020
17	0.934	0.016	44	1.085	0.017	71	1.362	0.020
18	0.570	0.014	45	0.771	0.015	72	1.136	0.018
19	0.121	0.011	46	0.424	0.013	73	0.839	0.016
20	-0.118	0.009	47	0.166	0.011	74	0.486	0.013
21	-0.256	0.008	48	-0.085	0.009	75	0.197	0.011
22	-0.253	0.008	49	-0.205	0.009	76	0.024	0.010
23	-0.252	0.008	50	-0.277	0.008	77	-0.146	0.008
24	-0.262	0.008	51	-0.254	0.008	78	-0.262	0.008
25	-0.263	0.008	52	-0.262	0.008	79	-0.261	0.008
26	-0.258	0.008	53	-0.257	0.008	80	-0.260	0.008
27	-0.256	0.008	54	-0.261	0.008	81	-0.258	0.008

Table 48: Pressure coefficient data at a Mach number of 2.0, ~20° angle of attack, and 180° roll angle.

Mach Number		1.991	**AoA (deg)**		20.726	**Roll (deg)**		180.0
ID	C_P	UC_P	**ID**	C_P	UC_P	**ID**	C_P	UC_P
0	1.348	0.019						
1	1.544	0.021	28	1.362	0.020	55	1.329	0.019
2	1.598	0.021	29	1.391	0.020	56	1.336	0.019
3	1.625	0.022	30	1.391	0.020	57	1.320	0.019
4	1.638	0.022	31	1.378	0.020	58	1.282	0.019
5	1.644	0.022	32	1.372	0.020	59	1.269	0.019
6	1.650	0.022	33	1.384	0.020	60	1.326	0.019
7	1.652	0.022	34	1.392	0.020	61	1.345	0.019
8	1.651	0.022	35	1.398	0.020	62	1.350	0.020
9	1.649	0.022	36	1.396	0.020	63	1.353	0.020
10	1.645	0.022	37	1.392	0.020	64	1.344	0.019
11	1.640	0.022	38	1.381	0.020	65	1.333	0.019
12	1.633	0.022	39	1.364	0.020	66	1.309	0.019
13	1.623	0.022	40	1.350	0.019	67	1.289	0.019
14	1.614	0.022	41	1.323	0.019	68	1.262	0.019
15	1.597	0.021	42	1.286	0.019	69	1.219	0.018
16	1.569	0.021	43	1.222	0.019	70	1.144	0.018
17	1.494	0.021	44	1.081	0.017	71	0.989	0.017
18	1.332	0.019	45	0.763	0.015	72	0.580	0.014
19	1.059	0.017	46	0.418	0.013	73	0.160	0.011
20	0.725	0.015	47	0.162	0.011	74	-0.090	0.009
21	0.389	0.012	48	-0.084	0.009	75	-0.233	0.008
22	0.198	0.011	49	-0.205	0.009	76	-0.276	0.008
23	-0.035	0.009	50	-0.278	0.008	77	-0.242	0.008
24	-0.264	0.008	51	-0.255	0.008	78	-0.263	0.008
25	-0.264	0.008	52	-0.264	0.008	79	-0.263	0.008
26	-0.261	0.008	53	-0.259	0.008	80	-0.262	0.008
27	-0.258	0.008	54	-0.262	0.008	81	-0.260	0.008

Table 49: Pressure coefficient data at a Mach number of 2.5, ∼0° angle of attack, and 0° roll angle.

Mach Number		2.505	**AoA (deg)**		0.348	**Roll (deg)**		0.0
ID	C_P	UC_P	**ID**	C_P	UC_P	**ID**	C_P	UC_P
0	1.722	0.017						
1	1.707	0.016	28	1.708	0.017	55	1.709	0.017
2	1.691	0.016	29	1.690	0.016	56	1.693	0.016
3	1.671	0.016	30	1.669	0.016	57	1.672	0.016
4	1.642	0.016	31	1.637	0.016	58	1.645	0.016
5	1.630	0.016	32	1.628	0.016	59	1.631	0.016
6	1.634	0.016	33	1.633	0.016	60	1.637	0.016
7	1.629	0.016	34	1.626	0.016	61	1.630	0.016
8	1.623	0.016	35	1.619	0.016	62	1.622	0.016
9	1.614	0.016	36	1.609	0.016	63	1.614	0.016
10	1.599	0.016	37	1.595	0.016	64	1.599	0.016
11	1.584	0.016	38	1.577	0.016	65	1.584	0.016
12	1.564	0.015	39	1.552	0.015	66	1.560	0.015
13	1.540	0.015	40	1.534	0.015	67	1.540	0.015
14	1.512	0.015	41	1.504	0.015	68	1.514	0.015
15	1.473	0.015	42	1.461	0.015	69	1.474	0.015
16	1.408	0.014	43	1.391	0.014	70	1.408	0.014
17	1.257	0.013	44	1.242	0.013	71	1.277	0.014
18	0.928	0.011	45	0.908	0.011	72	0.926	0.011
19	0.506	0.009	46	0.535	0.009	73	0.516	0.009
20	0.241	0.007	47	0.276	0.007	74	0.234	0.007
21	0.020	0.006	48	0.025	0.006	75	0.051	0.006
22	-0.082	0.005	49	-0.093	0.005	76	-0.081	0.005
23	-0.157	0.009	50			77	-0.153	0.009
24	-0.157	0.009	51	-0.165	0.009	78	-0.164	0.009
25	-0.160	0.009	52	-0.163	0.009	79	-0.163	0.009
26	-0.151	0.009	53	-0.163	0.009	80	0.000	0.010
27	-0.162	0.009	54	-0.164	0.009	81	-0.164	0.009

Table 50: Pressure coefficient data at a Mach number of 2.5, ~0° angle of attack, and 180° roll angle.

Mach Number		2.505	**AoA (deg)**		0.339	**Roll (deg)**		180.0
ID	C_P	UC_P	**ID**	C_P	UC_P	**ID**	C_P	UC_P
0	1.723	0.017						
1	1.709	0.017	28	1.709	0.017	55	1.708	0.016
2	1.694	0.016	29	1.690	0.016	56	1.691	0.016
3	1.675	0.016	30	1.670	0.016	57	1.670	0.016
4	1.647	0.016	31	1.638	0.016	58	1.642	0.016
5	1.635	0.016	32	1.629	0.016	59	1.628	0.016
6	1.639	0.016	33	1.634	0.016	60	1.612	0.016
7	1.635	0.016	34	1.627	0.016	61	1.628	0.016
8	1.629	0.016	35	1.620	0.016	62	1.620	0.016
9	1.619	0.016	36	1.611	0.016	63	1.612	0.016
10	1.605	0.016	37	1.596	0.016	64	1.596	0.016
11	1.590	0.016	38	1.578	0.016	65	1.581	0.016
12	1.570	0.016	39	1.553	0.015	66	1.556	0.015
13	1.545	0.015	40	1.535	0.015	67	1.537	0.015
14	1.519	0.015	41	1.506	0.015	68	1.510	0.015
15	1.479	0.015	42	1.463	0.015	69	1.470	0.015
16	1.415	0.014	43	1.393	0.014	70	1.404	0.014
17	1.265	0.013	44	1.245	0.013	71	1.271	0.013
18	0.936	0.011	45	0.912	0.011	72	0.918	0.011
19	0.514	0.009	46	0.539	0.009	73	0.506	0.009
20	0.247	0.007	47	0.278	0.007	74	0.226	0.007
21	0.023	0.006	48	0.027	0.006	75	0.045	0.006
22	-0.080	0.005	49	-0.092	0.005	76	-0.081	0.005
23	-0.156	0.009	50			77	-0.157	0.009
24	-0.159	0.009	51			78	-0.165	0.009
25	-0.163	0.009	52	-0.165	0.009	79	-0.164	0.009
26	-0.156	0.009	53	-0.165	0.009	80		
27			54	-0.166	0.009	81	-0.165	0.009

Table 51: Pressure coefficient data at a Mach number of 2.5, ∼12° angle of attack, and 0° roll angle.

Mach Number		2.498	**AoA (deg)**		12.210	**Roll (deg)**		0.0
ID	C_P	UC_P	**ID**	C_P	UC_P	**ID**	C_P	UC_P
0	1.611	0.016						
1	1.569	0.016	28	1.604	0.016	55	1.668	0.016
2	1.551	0.015	29	1.604	0.016	56	1.681	0.016
3	1.522	0.015	30	1.592	0.016	57	1.680	0.016
4	1.476	0.015	31	1.566	0.016	58	1.672	0.016
5	1.469	0.015	32	1.559	0.015	59	1.665	0.016
6	1.498	0.015	33	1.570	0.016	60	1.660	0.016
7	1.522	0.015	34	1.568	0.016	61	1.654	0.016
8	1.521	0.015	35	1.567	0.016	62	1.648	0.016
9	1.514	0.015	36	1.562	0.015	63	1.641	0.016
10	1.499	0.015	37	1.552	0.015	64	1.631	0.016
11	1.484	0.015	38	1.537	0.015	65	1.620	0.016
12	1.462	0.015	39	1.515	0.015	66	1.601	0.016
13	1.434	0.015	40	1.499	0.015	67	1.586	0.016
14	1.403	0.014	41	1.471	0.015	68	1.566	0.016
15	1.358	0.014	42	1.430	0.015	69	1.534	0.015
16	1.283	0.014	43	1.362	0.014	70	1.482	0.015
17	1.109	0.012	44	1.218	0.013	71	1.378	0.014
18	0.750	0.010	45	0.895	0.011	72	1.092	0.012
19	0.305	0.007	46	0.530	0.009	73	0.753	0.010
20	0.060	0.006	47	0.273	0.007	74	0.420	0.008
21	-0.096	0.005	48	0.024	0.006	75	0.175	0.007
22	-0.153	0.005	49	-0.093	0.005	76	0.014	0.006
23	-0.159	0.009	50			77	-0.107	0.009
24	-0.153	0.009	51	-0.162	0.009	78	-0.161	0.009
25	-0.160	0.009	52	-0.161	0.009	79	-0.161	0.009
26	-0.147	0.009	53	-0.161	0.009	80		
27	-0.159	0.009	54	-0.162	0.009	81	-0.161	0.009

Table 52: Pressure coefficient data at a Mach number of 2.5, ∼12° angle of attack, and 180° roll angle.

Mach Number		2.498	**AoA (deg)**		12.206	**Roll (deg)**		180.0
ID	C_P	UC_P	**ID**	C_P	UC_P	**ID**	C_P	UC_P
0	1.611	0.016						
1	1.700	0.016	28	1.609	0.016	55	1.575	0.016
2	1.719	0.017	29	1.609	0.016	56	1.561	0.015
3	1.721	0.017	30	1.598	0.016	57	1.537	0.015
4	1.718	0.017	31	1.572	0.016	58	1.498	0.015
5	1.713	0.017	32	1.565	0.016	59	1.484	0.015
6	1.707	0.016	33	1.573	0.016	60	1.495	0.015
7	1.701	0.016	34	1.572	0.016	61	1.524	0.015
8	1.696	0.016	35	1.570	0.016	62	1.523	0.015
9	1.688	0.016	36	1.565	0.015	63	1.520	0.015
10	1.678	0.016	37	1.554	0.015	64	1.507	0.015
11	1.667	0.016	38	1.538	0.015	65	1.492	0.015
12	1.654	0.016	39	1.516	0.015	66	1.468	0.015
13	1.636	0.016	40	1.500	0.015	67	1.448	0.015
14	1.620	0.016	41	1.472	0.015	68	1.420	0.014
15	1.592	0.016	42	1.431	0.015	69	1.376	0.014
16	1.545	0.015	43	1.363	0.014	70	1.304	0.014
17	1.441	0.015	44	1.219	0.013	71	1.157	0.013
18	1.191	0.013	45	0.895	0.011	72	0.772	0.010
19	0.859	0.011	46	0.534	0.009	73	0.347	0.008
20	0.541	0.009	47	0.276	0.007	74	0.085	0.006
21	0.235	0.007	48	0.030	0.006	75	-0.039	0.005
22	0.078	0.006	49	-0.089	0.005	76	-0.130	0.005
23	-0.072	0.009	50			77	-0.165	0.009
24	-0.156	0.009	51			78	-0.162	0.009
25	-0.161	0.009	52	-0.162	0.009	79	-0.162	0.009
26	-0.153	0.009	53	-0.162	0.009	80		
27			54	-0.162	0.009	81	-0.162	0.009

Table 53: Pressure coefficient data at a Mach number of 2.5, ∼20° angle of attack, and 0° roll angle.

Mach Number		2.490	**AoA (deg)**		20.135	**Roll (deg)**		0.0
ID	C_P	UC_P	**ID**	C_P	UC_P	**ID**	C_P	UC_P
0	1.383	0.014						
1	1.372	0.014	28	1.395	0.014	55	1.518	0.015
2	1.378	0.014	29	1.427	0.015	56	1.567	0.016
3	1.361	0.014	30	1.433	0.015	57	1.588	0.016
4	1.323	0.014	31	1.419	0.014	58	1.598	0.016
5	1.327	0.014	32	1.415	0.014	59	1.599	0.016
6	1.344	0.014	33	1.434	0.015	60	1.606	0.016
7	1.426	0.015	34	1.443	0.015	61	1.605	0.016
8	1.430	0.015	35	1.451	0.015	62	1.606	0.016
9	1.429	0.015	36	1.453	0.015	63	1.607	0.016
10	1.417	0.014	37	1.449	0.015	64	1.603	0.016
11	1.404	0.014	38	1.441	0.015	65	1.598	0.016
12	1.384	0.014	39	1.425	0.015	66	1.588	0.016
13	1.356	0.014	40	1.411	0.014	67	1.579	0.016
14	1.326	0.014	41	1.386	0.014	68	1.565	0.015
15	1.279	0.014	42	1.350	0.014	69	1.543	0.015
16	1.205	0.013	43	1.287	0.014	70	1.506	0.015
17	1.028	0.012	44	1.152	0.013	71	1.430	0.015
18	0.663	0.010	45	0.848	0.011	72	1.210	0.013
19	0.238	0.007	46	0.506	0.009	73	0.917	0.011
20	0.006	0.006	47	0.258	0.007	74	0.571	0.009
21	-0.128	0.005	48	0.020	0.006	75	0.301	0.007
22	-0.171	0.005	49	-0.093	0.005	76	0.122	0.006
23	-0.165	0.009	50			77	-0.035	0.010
24	-0.163	0.009	51	-0.169	0.009	78	-0.169	0.009
25	-0.165	0.009	52	-0.167	0.009	79	-0.167	0.009
26	-0.158	0.009	53	-0.167	0.009	80		
27	-0.166	0.009	54	-0.168	0.009	81	-0.167	0.009

Table 54: Pressure coefficient data at a Mach number of 2.5, ~20° angle of attack, and 180° roll angle.

Mach Number		2.490	**AoA (deg)**		20.130	**Roll (deg)**		180.0
ID	C_P	UC_P	**ID**	C_P	UC_P	**ID**	C_P	UC_P
0	1.381	0.014						
1	1.589	0.016	28	1.401	0.014	55	1.365	0.014
2	1.647	0.016	29	1.433	0.015	56	1.376	0.014
3	1.675	0.016	30	1.439	0.015	57	1.363	0.014
4	1.691	0.016	31	1.425	0.015	58	1.330	0.014
5	1.698	0.016	32	1.421	0.015	59	1.324	0.014
6	1.704	0.016	33	1.437	0.015	60	1.356	0.014
7	1.706	0.016	34	1.446	0.015	61	1.404	0.014
8	1.707	0.016	35	1.453	0.015	62	1.413	0.014
9	1.704	0.016	36	1.456	0.015	63	1.418	0.014
10	1.700	0.016	37	1.452	0.015	64	1.411	0.014
11	1.696	0.016	38	1.443	0.015	65	1.400	0.014
12	1.691	0.016	39	1.426	0.015	66	1.380	0.014
13	1.682	0.016	40	1.412	0.014	67	1.362	0.014
14	1.672	0.016	41	1.389	0.014	68	1.335	0.014
15	1.656	0.016	42	1.352	0.014	69	1.293	0.014
16	1.629	0.016	43	1.290	0.014	70	1.221	0.013
17	1.565	0.015	44	1.156	0.013	71	1.072	0.012
18	1.395	0.014	45	0.854	0.011	72	0.679	0.010
19	1.127	0.013	46	0.516	0.009	73	0.271	0.007
20	0.800	0.010	47	0.267	0.007	74	0.027	0.006
21	0.467	0.008	48	0.030	0.006	75	-0.068	0.005
22	0.280	0.007	49	-0.087	0.005	76	-0.146	0.005
23	0.062	0.010	50			77	-0.168	0.009
24	-0.169	0.009	51			78	-0.169	0.009
25	-0.167	0.009	52	-0.168	0.009	79	-0.168	0.009
26	-0.161	0.009	53	-0.168	0.009	80		
27			54	-0.169	0.009	81	-0.168	0.009

Table 55: Pressure coefficient data at a Mach number of 3.0, ∼0° angle of attack, and 0° roll angle.

Mach Number	3.000	**AoA (deg)**	0.259	**Roll (deg)**	0.0

ID	C_P	UC_P	**ID**	C_P	UC_P	**ID**	C_P	UC_P
0	1.777	0.018						
1	1.762	0.018	28	1.761	0.018	55	1.762	0.018
2	1.744	0.017	29	1.746	0.017	56	1.745	0.017
3	1.722	0.017	30	1.724	0.017	57	1.724	0.017
4	1.692	0.017	31	1.692	0.017	58	1.695	0.017
5	1.679	0.017	32	1.683	0.017	59	1.680	0.017
6	1.682	0.017	33	1.688	0.017	60	1.662	0.017
7	1.680	0.017	34	1.686	0.017	61	1.683	0.017
8	1.672	0.017	35	1.680	0.017	62	1.674	0.017
9	1.665	0.017	36	1.674	0.017	63	1.667	0.017
10	1.648	0.017	37	1.657	0.017	64	1.651	0.017
11	1.635	0.017	38	1.640	0.017	65	1.636	0.017
12	1.613	0.016	39	1.616	0.016	66	1.613	0.016
13	1.589	0.016	40	1.599	0.016	67	1.592	0.016
14	1.564	0.016	41	1.567	0.016	68	1.566	0.016
15	1.523	0.016	42	1.527	0.016	69	1.525	0.016
16	1.457	0.015	43	1.457	0.015	70	1.460	0.015
17	1.305	0.014	44	1.312	0.014	71	1.326	0.014
18	0.976	0.012	45	0.979	0.012	72	0.974	0.012
19	0.556	0.009	46	0.606	0.009	73	0.563	0.009
20	0.294	0.007	47	0.343	0.008	74	0.284	0.007
21	0.078	0.006	48	0.092	0.006	75	0.111	0.006
22	-0.019	0.006	49	-0.025	0.006	76	-0.009	0.006
23	-0.080	0.010	50			77	-0.088	0.010
24	-0.090	0.010	51			78	-0.097	0.010
25	-0.095	0.010	52	-0.105	0.010	79	-0.096	0.010
26			53	-0.096	0.010	80		
27	-0.106	0.010	54	-0.099	0.010	81	-0.097	0.010

Table 56: Pressure coefficient data at a Mach number of 3.0, ∼0° angle of attack, and 180° roll angle.

Mach Number	3.000	**AoA (deg)**	0.251	**Roll (deg)**	180.0

ID	C_P	UC_P	**ID**	C_P	UC_P	**ID**	C_P	UC_P
0	1.776	0.018						
1	1.761	0.018	28	1.762	0.018	55	1.762	0.018
2	1.744	0.017	29	1.747	0.017	56	1.744	0.017
3	1.722	0.017	30	1.725	0.017	57	1.722	0.017
4	1.693	0.017	31	1.693	0.017	58	1.694	0.017
5	1.680	0.017	32	1.684	0.017	59	1.678	0.017
6	1.683	0.017	33	1.689	0.017	60	1.683	0.017
7	1.681	0.017	34	1.687	0.017	61	1.682	0.017
8	1.674	0.017	35	1.681	0.017	62	1.673	0.017
9	1.665	0.017	36	1.675	0.017	63	1.666	0.017
10	1.649	0.017	37	1.658	0.017	64	1.651	0.017
11	1.637	0.017	38	1.641	0.017	65	1.636	0.017
12	1.613	0.016	39	1.616	0.016	66	1.612	0.016
13	1.590	0.016	40	1.601	0.016	67	1.591	0.016
14	1.565	0.016	41	1.567	0.016	68	1.564	0.016
15	1.524	0.016	42	1.528	0.016	69	1.525	0.016
16	1.459	0.015	43	1.457	0.015	70	1.459	0.015
17	1.305	0.014	44	1.312	0.014	71	1.327	0.014
18	0.976	0.012	45	0.979	0.012	72	0.976	0.012
19	0.554	0.009	46	0.605	0.009	73	0.565	0.009
20	0.291	0.007	47	0.342	0.008	74	0.286	0.007
21	0.076	0.006	48	0.090	0.006	75	0.110	0.006
22	-0.023	0.006	49	-0.026	0.006	76	-0.006	0.006
23	-0.090	0.010	50			77	-0.085	0.010
24	-0.090	0.010	51			78	-0.095	0.010
25	-0.097	0.010	52	-0.106	0.010	79	-0.099	0.010
26			53	-0.098	0.010	80		
27			54	-0.101	0.010	81	-0.099	0.010

Table 57: Pressure coefficient data at a Mach number of 3.0, ∼12° angle of attack, and 0° roll angle.

Mach Number		2.995	**AoA (deg)**		12.091	**Roll (deg)**		0.0
ID	C_P	UC_P	**ID**	C_P	UC_P	**ID**	C_P	UC_P
0	1.636	0.017						
1	1.595	0.016	28	1.632	0.017	55	1.697	0.017
2	1.580	0.016	29	1.637	0.017	56	1.710	0.017
3	1.553	0.016	30	1.626	0.017	57	1.710	0.017
4	1.512	0.016	31	1.603	0.016	58	1.703	0.017
5	1.509	0.016	32	1.597	0.016	59	1.695	0.017
6	1.527	0.016	33	1.607	0.016	60	1.636	0.017
7	1.568	0.016	34	1.611	0.016	61	1.688	0.017
8	1.564	0.016	35	1.611	0.016	62	1.682	0.017
9	1.562	0.016	36	1.610	0.016	63	1.677	0.017
10	1.545	0.016	37	1.598	0.016	64	1.667	0.017
11	1.533	0.016	38	1.585	0.016	65	1.656	0.017
12	1.510	0.016	39	1.564	0.016	66	1.640	0.017
13	1.483	0.015	40	1.549	0.016	67	1.624	0.017
14	1.455	0.015	41	1.520	0.016	68	1.604	0.016
15	1.409	0.015	42	1.483	0.015	69	1.573	0.016
16	1.336	0.014	43	1.415	0.015	70	1.524	0.016
17	1.163	0.013	44	1.279	0.014	71	1.424	0.015
18	0.810	0.011	45	0.960	0.012	72	1.145	0.013
19	0.371	0.008	46	0.601	0.009	73	0.812	0.011
20	0.127	0.007	47	0.340	0.008	74	0.483	0.009
21	-0.027	0.006	48	0.091	0.006	75	0.243	0.007
22	-0.084	0.005	49	-0.025	0.006	76	0.084	0.006
23	-0.098	0.010	50			77	-0.040	0.010
24	-0.090	0.010	51			78	-0.098	0.010
25	-0.096	0.010	52	-0.106	0.010	79	-0.097	0.010
26			53	-0.097	0.010	80		
27	-0.106	0.010	54	-0.100	0.010	81	-0.098	0.010

Table 58: Pressure coefficient data at a Mach number of 3.0, ∼12° angle of attack, and 180° roll angle.

Mach Number		2.995	**AoA (deg)**		12.091	**Roll (deg)**		180.0
ID	C_P	UC_P	**ID**	C_P	UC_P	**ID**	C_P	UC_P
0	1.635	0.017						
1	1.733	0.017	28	1.634	0.017	55	1.601	0.016
2	1.751	0.017	29	1.638	0.017	56	1.589	0.016
3	1.754	0.018	30	1.627	0.017	57	1.568	0.016
4	1.753	0.018	31	1.601	0.016	58	1.535	0.016
5	1.748	0.017	32	1.595	0.016	59	1.521	0.016
6	1.742	0.017	33	1.604	0.016	60	1.554	0.016
7	1.738	0.017	34	1.608	0.016	61	1.568	0.016
8	1.732	0.017	35	1.607	0.016	62	1.568	0.016
9	1.728	0.017	36	1.605	0.016	63	1.567	0.016
10	1.716	0.017	37	1.592	0.016	64	1.555	0.016
11	1.710	0.017	38	1.578	0.016	65	1.543	0.016
12	1.695	0.017	39	1.558	0.016	66	1.519	0.016
13	1.681	0.017	40	1.543	0.016	67	1.498	0.016
14	1.666	0.017	41	1.512	0.016	68	1.472	0.015
15	1.638	0.017	42	1.476	0.015	69	1.429	0.015
16	1.595	0.016	43	1.408	0.015	70	1.358	0.015
17	1.493	0.016	44	1.269	0.014	71	1.214	0.013
18	1.252	0.014	45	0.949	0.012	72	0.837	0.011
19	0.926	0.011	46	0.592	0.009	73	0.415	0.008
20	0.608	0.009	47	0.336	0.008	74	0.155	0.007
21	0.304	0.008	48	0.093	0.006	75	0.035	0.006
22	0.147	0.007	49	-0.023	0.006	76	-0.050	0.006
23	-0.004	0.010	50			77	-0.096	0.010
24	-0.092	0.010	51			78	-0.092	0.010
25	-0.097	0.010	52	-0.106	0.010	79	-0.099	0.010
26			53	-0.098	0.010	80		
27			54	-0.101	0.010	81	-0.099	0.010

Table 59: Pressure coefficient data at a Mach number of 3.0, ∼20° angle of attack, and 0° roll angle.

Mach Number		2.992	**AoA (deg)**		19.918	**Roll (deg)**		0.0
ID	C_P	UC_P	**ID**	C_P	UC_P	**ID**	C_P	UC_P
0	1.386	0.015						
1	1.381	0.015	28	1.401	0.015	55	1.547	0.016
2	1.397	0.015	29	1.443	0.015	56	1.604	0.016
3	1.386	0.015	30	1.452	0.015	57	1.629	0.017
4	1.362	0.015	31	1.442	0.015	58	1.642	0.017
5	1.371	0.015	32	1.438	0.015	59	1.642	0.017
6	1.374	0.015	33	1.460	0.015	60	1.609	0.016
7	1.472	0.015	34	1.477	0.015	61	1.650	0.017
8	1.486	0.015	35	1.487	0.015	62	1.651	0.017
9	1.489	0.016	36	1.495	0.016	63	1.653	0.017
10	1.477	0.015	37	1.492	0.016	64	1.650	0.017
11	1.467	0.015	38	1.487	0.015	65	1.646	0.017
12	1.446	0.015	39	1.471	0.015	66	1.638	0.017
13	1.421	0.015	40	1.460	0.015	67	1.627	0.017
14	1.392	0.015	41	1.434	0.015	68	1.614	0.016
15	1.346	0.014	42	1.402	0.015	69	1.590	0.016
16	1.272	0.014	43	1.339	0.014	70	1.557	0.016
17	1.098	0.013	44	1.211	0.013	71	1.483	0.015
18	0.738	0.010	45	0.911	0.011	72	1.268	0.014
19	0.313	0.008	46	0.574	0.009	73	0.977	0.012
20	0.080	0.006	47	0.325	0.008	74	0.633	0.010
21	-0.055	0.006	48	0.088	0.006	75	0.366	0.008
22	-0.098	0.005	49	-0.024	0.006	76	0.189	0.007
23	-0.099	0.010	50			77	0.030	0.010
24	-0.093	0.010	51			78	-0.101	0.010
25	-0.097	0.010	52	-0.109	0.010	79	-0.099	0.010
26			53	-0.099	0.010	80		
27	-0.110	0.010	54	-0.102	0.010	81	-0.100	0.010

Table 60: Pressure coefficient data at a Mach number of 3.0, ∼20° angle of attack, and 180° roll angle.

Mach Number	2.992	**AoA (deg)**	19.919	**Roll (deg)**	180.0

ID	C_P	UC_P	**ID**	C_P	UC_P	**ID**	C_P	UC_P
0	1.382	0.015						
1	1.626	0.017	28	1.410	0.015	55	1.370	0.015
2	1.693	0.017	29	1.452	0.015	56	1.389	0.015
3	1.724	0.017	30	1.460	0.015	57	1.381	0.015
4	1.742	0.017	31	1.448	0.015	58	1.356	0.015
5	1.751	0.018	32	1.445	0.015	59	1.352	0.014
6	1.758	0.018	33	1.462	0.015	60	1.401	0.015
7	1.763	0.018	34	1.479	0.015	61	1.444	0.015
8	1.763	0.018	35	1.489	0.016	62	1.456	0.015
9	1.766	0.018	36	1.497	0.016	63	1.465	0.015
10	1.762	0.018	37	1.492	0.016	64	1.461	0.015
11	1.763	0.018	38	1.486	0.015	65	1.452	0.015
12	1.756	0.018	39	1.471	0.015	66	1.432	0.015
13	1.751	0.017	40	1.460	0.015	67	1.413	0.015
14	1.745	0.017	41	1.433	0.015	68	1.389	0.015
15	1.730	0.017	42	1.401	0.015	69	1.348	0.014
16	1.706	0.017	43	1.338	0.014	70	1.275	0.014
17	1.645	0.017	44	1.208	0.013	71	1.129	0.013
18	1.484	0.015	45	0.905	0.011	72	0.740	0.010
19	1.218	0.014	46	0.570	0.009	73	0.335	0.008
20	0.886	0.011	47	0.323	0.008	74	0.094	0.006
21	0.547	0.009	48	0.090	0.006	75	0.007	0.006
22	0.355	0.008	49	-0.022	0.006	76	-0.063	0.006
23	0.132	0.010	50			77	-0.098	0.010
24	-0.095	0.010	51			78	-0.096	0.010
25	-0.099	0.010	52	-0.110	0.010	79	-0.101	0.010
26			53	-0.100	0.010	80		
27			54	-0.103	0.010	81	-0.102	0.010

Table 61: Pressure coefficient data at a Mach number of 3.5, ∼0° angle of attack, and 0° roll angle.

Mach Number		3.515	**AoA (deg)**		0.209	**Roll (deg)**		0.0
ID	C_P	UC_P	**ID**	C_P	UC_P	**ID**	C_P	UC_P
0	1.779	0.019						
1	1.768	0.019	28	1.767	0.019	55	1.764	0.019
2	1.752	0.019	29	1.751	0.019	56	1.745	0.019
3	1.733	0.019	30	1.734	0.019	57	1.726	0.019
4	1.705	0.018	31	1.703	0.018	58	1.700	0.018
5	1.694	0.018	32	1.696	0.018	59	1.686	0.018
6	1.700	0.018	33	1.704	0.018	60	1.694	0.018
7	1.697	0.018	34	1.698	0.018	61	1.691	0.018
8	1.691	0.018	35	1.694	0.018	62	1.685	0.018
9	1.683	0.018	36	1.686	0.018	63	1.677	0.018
10	1.670	0.018	37	1.673	0.018	64	1.663	0.018
11	1.655	0.018	38	1.656	0.018	65	1.650	0.018
12	1.637	0.018	39	1.634	0.018	66	1.626	0.018
13	1.613	0.018	40	1.616	0.018	67	1.607	0.018
14	1.587	0.018	41	1.586	0.018	68	1.581	0.017
15	1.548	0.017	42	1.546	0.017	69	1.541	0.017
16	1.485	0.017	43	1.478	0.017	70	1.478	0.017
17	1.340	0.016	44	1.333	0.016	71	1.347	0.016
18	1.018	0.014	45	1.010	0.014	72	1.004	0.014
19	0.604	0.011	46	0.640	0.012	73	0.598	0.011
20	0.341	0.010	47	0.380	0.010	74	0.320	0.010
21	0.126	0.009	48	0.133	0.009	75	0.155	0.009
22	0.028	0.009	49	0.017	0.009	76	0.039	0.009
23	-0.038	0.007	50			77	-0.046	0.007
24	-0.058	0.007	51	-0.060	0.007	78	-0.058	0.007
25	-0.055	0.007	52	-0.060	0.007	79	-0.058	0.007
26			53	-0.057	0.007	80		
27			54	-0.059	0.007	81	-0.058	0.007

Table 62: Pressure coefficient data at a Mach number of 3.5, ∼0° angle of attack, and 180° roll angle.

Mach Number		3.515	**AoA (deg)**		0.214	**Roll (deg)**		180.0
ID	C_P	UC_P	**ID**	C_P	UC_P	**ID**	C_P	UC_P
0	1.779	0.019						
1	1.763	0.019	28	1.765	0.019	55	1.768	0.019
2	1.745	0.019	29	1.749	0.019	56	1.752	0.019
3	1.724	0.019	30	1.731	0.019	57	1.734	0.019
4	1.693	0.018	31	1.701	0.018	58	1.709	0.018
5	1.683	0.018	32	1.694	0.018	59	1.696	0.018
6	1.690	0.018	33	1.702	0.018	60	1.702	0.018
7	1.687	0.018	34	1.695	0.018	61	1.700	0.018
8	1.681	0.018	35	1.691	0.018	62	1.695	0.018
9	1.673	0.018	36	1.682	0.018	63	1.687	0.018
10	1.660	0.018	37	1.671	0.018	64	1.673	0.018
11	1.644	0.018	38	1.653	0.018	65	1.660	0.018
12	1.627	0.018	39	1.631	0.018	66	1.637	0.018
13	1.602	0.018	40	1.613	0.018	67	1.618	0.018
14	1.575	0.017	41	1.583	0.017	68	1.592	0.018
15	1.537	0.017	42	1.543	0.017	69	1.552	0.017
16	1.473	0.017	43	1.474	0.017	70	1.490	0.017
17	1.329	0.016	44	1.328	0.016	71	1.360	0.016
18	1.006	0.014	45	1.005	0.014	72	1.019	0.014
19	0.593	0.011	46	0.634	0.012	73	0.615	0.011
20	0.333	0.010	47	0.375	0.010	74	0.335	0.010
21	0.121	0.009	48	0.131	0.009	75	0.163	0.009
22	0.026	0.009	49	0.016	0.009	76	0.042	0.009
23	-0.037	0.007	50			77	-0.046	0.007
24	-0.046	0.007	51	-0.061	0.007	78	-0.059	0.007
25	-0.055	0.007	52	-0.059	0.007	79	-0.058	0.007
26			53	-0.058	0.007	80		
27			54	-0.059	0.007	81	-0.059	0.007

Table 63: Pressure coefficient data at a Mach number of 3.5, ∼12° angle of attack, and 0° roll angle.

Mach Number		3.498	**AoA (deg)**		12.222	**Roll (deg)**		0.0
ID	C_P	UC_P	**ID**	C_P	UC_P	**ID**	C_P	UC_P
0	1.641	0.018						
1	1.601	0.018	28	1.639	0.018	55	1.705	0.018
2	1.587	0.018	29	1.643	0.018	56	1.719	0.018
3	1.563	0.017	30	1.636	0.018	57	1.721	0.018
4	1.523	0.017	31	1.613	0.018	58	1.715	0.018
5	1.524	0.017	32	1.606	0.018	59	1.709	0.018
6	1.538	0.017	33	1.622	0.018	60	1.706	0.018
7	1.586	0.018	34	1.621	0.018	61	1.704	0.018
8	1.585	0.018	35	1.622	0.018	62	1.701	0.018
9	1.581	0.017	36	1.618	0.018	63	1.695	0.018
10	1.570	0.017	37	1.611	0.018	64	1.686	0.018
11	1.555	0.017	38	1.597	0.018	65	1.677	0.018
12	1.536	0.017	39	1.578	0.017	66	1.660	0.018
13	1.508	0.017	40	1.562	0.017	67	1.646	0.018
14	1.479	0.017	41	1.535	0.017	68	1.627	0.018
15	1.435	0.016	42	1.496	0.017	69	1.595	0.018
16	1.363	0.016	43	1.430	0.016	70	1.548	0.017
17	1.196	0.015	44	1.291	0.016	71	1.447	0.017
18	0.846	0.013	45	0.979	0.014	72	1.170	0.015
19	0.411	0.010	46	0.622	0.012	73	0.835	0.013
20	0.169	0.009	47	0.368	0.010	74	0.508	0.011
21	0.016	0.009	48	0.128	0.009	75	0.277	0.010
22	-0.039	0.009	49	0.015	0.009	76	0.122	0.009
23	-0.058	0.007	50			77	-0.001	0.007
24	-0.060	0.007	51	-0.061	0.007	78	-0.060	0.007
25	-0.057	0.007	52	-0.067	0.007	79	-0.060	0.007
26			53	-0.059	0.007	80		
27			54	-0.061	0.007	81	-0.060	0.007

Table 64: Pressure coefficient data at a Mach number of 3.5, ∼12° angle of attack, and 180° roll angle.

Mach Number		3.498	**AoA (deg)**		12.237	**Roll (deg)**		180.0
ID	C_P	UC_P	**ID**	C_P	UC_P	**ID**	C_P	UC_P
0	1.640	0.018						
1	1.744	0.019	28	1.637	0.018	55	1.606	0.018
2	1.765	0.019	29	1.641	0.018	56	1.596	0.018
3	1.769	0.019	30	1.632	0.018	57	1.577	0.017
4	1.766	0.019	31	1.608	0.018	58	1.544	0.017
5	1.763	0.019	32	1.603	0.018	59	1.533	0.017
6	1.757	0.019	33	1.616	0.018	60	1.568	0.017
7	1.754	0.019	34	1.617	0.018	61	1.583	0.017
8	1.748	0.019	35	1.617	0.018	62	1.587	0.018
9	1.741	0.019	36	1.615	0.018	63	1.584	0.018
10	1.734	0.019	37	1.607	0.018	64	1.575	0.017
11	1.724	0.019	38	1.593	0.018	65	1.562	0.017
12	1.712	0.018	39	1.575	0.017	66	1.540	0.017
13	1.697	0.018	40	1.558	0.017	67	1.522	0.017
14	1.679	0.018	41	1.531	0.017	68	1.494	0.017
15	1.653	0.018	42	1.494	0.017	69	1.451	0.017
16	1.610	0.018	43	1.428	0.016	70	1.382	0.016
17	1.512	0.017	44	1.289	0.015	71	1.239	0.015
18	1.274	0.015	45	0.978	0.014	72	0.867	0.013
19	0.948	0.013	46	0.625	0.012	73	0.449	0.011
20	0.635	0.012	47	0.371	0.010	74	0.191	0.010
21	0.335	0.010	48	0.133	0.009	75	0.082	0.009
22	0.180	0.010	49	0.018	0.009	76	-0.001	0.009
23	0.033	0.007	50			77	-0.056	0.007
24	-0.053	0.007	51	-0.063	0.007	78	-0.061	0.007
25	-0.058	0.007	52	-0.064	0.007	79	-0.060	0.007
26			53	-0.060	0.007	80		
27			54	-0.062	0.007	81	-0.061	0.007

Table 65: Pressure coefficient data at a Mach number of 3.5, ∼20° angle of attack, and 0° roll angle.

Mach Number		3.476	**AoA (deg)**		20.076	**Roll (deg)**		0.0
ID	C_P	UC_P	**ID**	C_P	UC_P	**ID**	C_P	UC_P
0	1.413	0.016						
1	1.406	0.016	28	1.430	0.016	55	1.577	0.017
2	1.427	0.016	29	1.472	0.017	56	1.633	0.018
3	1.422	0.016	30	1.484	0.017	57	1.659	0.018
4	1.405	0.016	31	1.472	0.017	58	1.669	0.018
5	1.416	0.016	32	1.470	0.017	59	1.669	0.018
6	1.419	0.016	33	1.498	0.017	60	1.671	0.018
7	1.510	0.017	34	1.510	0.017	61	1.674	0.018
8	1.533	0.017	35	1.522	0.017	62	1.676	0.018
9	1.537	0.017	36	1.528	0.017	63	1.675	0.018
10	1.529	0.017	37	1.528	0.017	64	1.671	0.018
11	1.517	0.017	38	1.522	0.017	65	1.666	0.018
12	1.499	0.017	39	1.508	0.017	66	1.657	0.018
13	1.473	0.017	40	1.495	0.017	67	1.647	0.018
14	1.443	0.017	41	1.472	0.017	68	1.632	0.018
15	1.398	0.016	42	1.438	0.016	69	1.610	0.018
16	1.326	0.016	43	1.376	0.016	70	1.574	0.017
17	1.157	0.015	44	1.245	0.015	71	1.497	0.017
18	0.801	0.012	45	0.951	0.013	72	1.278	0.015
19	0.371	0.010	46	0.612	0.011	73	0.986	0.014
20	0.134	0.009	47	0.365	0.010	74	0.645	0.012
21	-0.006	0.009	48	0.130	0.009	75	0.386	0.010
22	-0.054	0.009	49	0.017	0.009	76	0.212	0.010
23	-0.062	0.007	50			77	0.059	0.007
24	-0.064	0.007	51	-0.066	0.007	78	-0.064	0.007
25	-0.060	0.007	52	-0.071	0.007	79	-0.063	0.007
26			53	-0.063	0.007	80		
27			54	-0.065	0.007	81	-0.064	0.007

Table 66: Pressure coefficient data at a Mach number of 3.5, ∼20° angle of attack, and 180° roll angle.

Mach Number		3.476	**AoA (deg)**		20.077	**Roll (deg)**		180.0
ID	C_P	UC_P	**ID**	C_P	UC_P	**ID**	C_P	UC_P
0	1.409	0.016						
1	1.659	0.018	28	1.435	0.016	55	1.395	0.016
2	1.724	0.019	29	1.477	0.017	56	1.416	0.016
3	1.752	0.019	30	1.489	0.017	57	1.414	0.016
4	1.765	0.019	31	1.478	0.017	58	1.394	0.016
5	1.773	0.019	32	1.477	0.017	59	1.396	0.016
6	1.775	0.019	33	1.501	0.017	60	1.432	0.016
7	1.775	0.019	34	1.515	0.017	61	1.487	0.017
8	1.771	0.019	35	1.526	0.017	62	1.504	0.017
9	1.768	0.019	36	1.533	0.017	63	1.513	0.017
10	1.764	0.019	37	1.533	0.017	64	1.511	0.017
11	1.758	0.019	38	1.525	0.017	65	1.503	0.017
12	1.753	0.019	39	1.512	0.017	66	1.484	0.017
13	1.743	0.019	40	1.499	0.017	67	1.467	0.017
14	1.734	0.019	41	1.475	0.017	68	1.441	0.017
15	1.718	0.018	42	1.441	0.017	69	1.399	0.016
16	1.691	0.018	43	1.380	0.016	70	1.329	0.016
17	1.629	0.018	44	1.247	0.015	71	1.183	0.015
18	1.463	0.017	45	0.948	0.013	72	0.801	0.012
19	1.197	0.015	46	0.610	0.011	73	0.390	0.010
20	0.876	0.013	47	0.362	0.010	74	0.145	0.009
21	0.548	0.011	48	0.132	0.009	75	0.058	0.009
22	0.361	0.010	49	0.017	0.009	76	-0.014	0.009
23	0.153	0.008	50			77	-0.061	0.007
24	-0.056	0.007	51	-0.066	0.007	78	-0.065	0.007
25	-0.061	0.007	52	-0.068	0.007	79	-0.064	0.007
26			53	-0.064	0.007	80		
27			54	-0.065	0.007	81	-0.065	0.007

Table 67: Pressure coefficient data at a Mach number of 4.5, ∼0° angle of attack, and 0° roll angle.

Mach Number		4.513	**AoA (deg)**		-0.043	**Roll (deg)**		0.0
ID	C_P	UC_P	**ID**	C_P	UC_P	**ID**	C_P	UC_P
0	1.816	0.019						
1	1.801	0.019	28	1.807	0.019	55	1.793	0.019
2	1.781	0.019	29	1.788	0.019	56	1.773	0.019
3	1.762	0.019	30	1.769	0.019	57	1.753	0.019
4	1.730	0.019	31	1.739	0.019	58	1.723	0.019
5	1.721	0.019	32	1.730	0.019	59	1.713	0.019
6	1.725	0.019	33	1.739	0.019	60	1.722	0.019
7	1.726	0.019	34	1.730	0.019	61	1.718	0.019
8	1.720	0.019	35	1.726	0.019	62	1.716	0.019
9	1.711	0.019	36	1.719	0.019	63	1.707	0.019
10	1.700	0.019	37	1.709	0.019	64	1.693	0.019
11	1.685	0.018	38	1.689	0.018	65	1.678	0.018
12	1.669	0.018	39	1.668	0.018	66	1.658	0.018
13	1.642	0.018	40	1.651	0.018	67	1.638	0.018
14	1.616	0.018	41	1.621	0.018	68	1.612	0.018
15	1.579	0.018	42	1.579	0.018	69	1.570	0.018
16	1.516	0.017	43	1.511	0.017	70	1.509	0.017
17	1.375	0.017	44	1.367	0.017	71	1.380	0.017
18	1.056	0.015	45	1.046	0.015	72	1.036	0.015
19	0.649	0.013	46	0.676	0.013	73	0.634	0.013
20	0.385	0.012	47	0.419	0.012	74	0.359	0.012
21	0.172	0.011	48	0.178	0.011	75	0.218	0.011
22	0.074	0.011	49	0.064	0.011	76	0.106	0.011
23	0.012	0.038	50	0.007	0.038	77	0.014	0.038
24	0.024	0.038	51	0.037	0.038	78	0.032	0.038
25	0.002	0.038	52	-0.003	0.038	79	-0.001	0.038
26	0.042	0.038	53	-0.003	0.038	80	-0.015	0.038
27	0.038	0.038	54	-0.003	0.038	81	0.026	0.038

Table 68: Pressure coefficient data at a Mach number of 4.5, ~0° angle of attack, and 180° roll angle.

Mach Number		4.513	**AoA (deg)**		-0.044	**Roll (deg)**		180.0
ID	C_P	UC_P	**ID**	C_P	UC_P	**ID**	C_P	UC_P
0	1.814	0.019						
1	1.799	0.019	28	1.795	0.019	55	1.803	0.019
2	1.779	0.019	29	1.775	0.019	56	1.786	0.019
3	1.759	0.019	30	1.754	0.019	57	1.769	0.019
4	1.726	0.019	31	1.720	0.019	58	1.740	0.019
5	1.718	0.019	32	1.715	0.019	59	1.729	0.019
6	1.724	0.019	33	1.727	0.019	60	1.734	0.019
7	1.725	0.019	34	1.719	0.019	61	1.731	0.019
8	1.718	0.019	35	1.716	0.019	62	1.729	0.019
9	1.711	0.019	36	1.710	0.019	63	1.719	0.019
10	1.700	0.019	37	1.700	0.019	64	1.705	0.019
11	1.683	0.018	38	1.682	0.018	65	1.691	0.019
12	1.667	0.018	39	1.661	0.018	66	1.669	0.018
13	1.641	0.018	40	1.643	0.018	67	1.650	0.018
14	1.613	0.018	41	1.615	0.018	68	1.624	0.018
15	1.576	0.018	42	1.575	0.018	69	1.582	0.018
16	1.510	0.017	43	1.509	0.017	70	1.521	0.017
17	1.367	0.017	44	1.367	0.017	71	1.391	0.017
18	1.042	0.015	45	1.049	0.015	72	1.048	0.015
19	0.627	0.013	46	0.684	0.013	73	0.644	0.013
20	0.365	0.012	47	0.423	0.012	74	0.366	0.012
21	0.157	0.011	48	0.181	0.011	75	0.223	0.011
22	0.068	0.011	49	0.065	0.011	76	0.107	0.011
23	0.015	0.038	50			77	0.011	0.038
24	0.015	0.038	51	-0.006	0.038	78	0.024	0.038
25	0.003	0.038	52	-0.007	0.038	79	-0.002	0.038
26	0.039	0.038	53	-0.003	0.038	80		
27	0.030	0.038	54	-0.004	0.038	81	-0.003	0.038

Table 69: Pressure coefficient data at a Mach number of 4.5, ∼12° angle of attack, and 0° roll angle.

Mach Number		4.501	**AoA (deg)**		12.985	**Roll (deg)**		0.0
ID	C_P	UC_P	**ID**	C_P	UC_P	**ID**	C_P	UC_P
0	1.632	0.018						
1	1.593	0.018	28	1.631	0.018	55	1.708	0.019
2	1.584	0.018	29	1.639	0.018	56	1.729	0.019
3	1.569	0.018	30	1.634	0.018	57	1.735	0.019
4	1.539	0.018	31	1.617	0.018	58	1.732	0.019
5	1.545	0.018	32	1.613	0.018	59	1.728	0.019
6	1.553	0.018	33	1.631	0.018	60	1.726	0.019
7	1.606	0.018	34	1.632	0.018	61	1.723	0.019
8	1.617	0.018	35	1.636	0.018	62	1.723	0.019
9	1.616	0.018	36	1.636	0.018	63	1.717	0.019
10	1.606	0.018	37	1.631	0.018	64	1.709	0.019
11	1.592	0.018	38	1.619	0.018	65	1.700	0.019
12	1.575	0.018	39	1.603	0.018	66	1.687	0.018
13	1.547	0.018	40	1.588	0.018	67	1.673	0.018
14	1.519	0.017	41	1.562	0.018	68	1.654	0.018
15	1.477	0.017	42	1.524	0.017	69	1.624	0.018
16	1.407	0.017	43	1.461	0.017	70	1.578	0.018
17	1.245	0.016	44	1.327	0.016	71	1.484	0.017
18	0.897	0.014	45	1.027	0.015	72	1.216	0.016
19	0.466	0.012	46	0.674	0.013	73	0.888	0.014
20	0.219	0.011	47	0.418	0.012	74	0.564	0.013
21	0.068	0.011	48	0.178	0.011	75	0.343	0.012
22	0.013	0.011	49	0.067	0.011	76	0.186	0.011
23	0.001	0.038	50	0.008	0.038	77	0.051	0.038
24	0.021	0.038	51	0.040	0.038	78	0.028	0.038
25	0.001	0.038	52	-0.010	0.038	79	-0.002	0.038
26	0.040	0.038	53	-0.004	0.038	80	-0.016	0.038
27	0.021	0.038	54	-0.004	0.038	81	0.026	0.038

Table 70: Pressure coefficient data at a Mach number of 4.5, ~12° angle of attack, and 180° roll angle.

Mach Number	4.501	**AoA (deg)**	12.993	**Roll (deg)**	180.0

ID	C_P	UC_P	**ID**	C_P	UC_P	**ID**	C_P	UC_P
0	1.630	0.018						
1	1.758	0.019	28	1.633	0.018	55	1.596	0.018
2	1.785	0.019	29	1.641	0.018	56	1.592	0.018
3	1.793	0.019	30	1.635	0.018	57	1.577	0.018
4	1.792	0.019	31	1.613	0.018	58	1.548	0.018
5	1.792	0.019	32	1.610	0.018	59	1.544	0.018
6	1.785	0.019	33	1.627	0.018	60	1.577	0.018
7	1.782	0.019	34	1.628	0.018	61	1.600	0.018
8	1.776	0.019	35	1.632	0.018	62	1.610	0.018
9	1.770	0.019	36	1.630	0.018	63	1.608	0.018
10	1.764	0.019	37	1.626	0.018	64	1.600	0.018
11	1.754	0.019	38	1.612	0.018	65	1.589	0.018
12	1.745	0.019	39	1.595	0.018	66	1.569	0.018
13	1.729	0.019	40	1.579	0.018	67	1.550	0.018
14	1.712	0.019	41	1.554	0.018	68	1.523	0.017
15	1.690	0.018	42	1.516	0.017	69	1.480	0.017
16	1.649	0.018	43	1.452	0.017	70	1.414	0.017
17	1.558	0.018	44	1.315	0.016	71	1.271	0.016
18	1.330	0.016	45	1.009	0.015	72	0.907	0.014
19	1.014	0.015	46	0.657	0.013	73	0.491	0.012
20	0.699	0.013	47	0.405	0.012	74	0.236	0.012
21	0.398	0.012	48	0.175	0.011	75	0.155	0.011
22	0.238	0.012	49	0.062	0.011	76	0.073	0.011
23	0.090	0.038	50			77	0.004	0.038
24	0.005	0.038	51	-0.007	0.038	78	0.020	0.038
25	0.001	0.038	52	-0.004	0.038	79	-0.004	0.038
26	0.034	0.038	53	-0.004	0.038	80		
27	0.019	0.038	54	-0.006	0.038	81	-0.005	0.038

Table 71: Pressure coefficient data at a Mach number of 4.5, ~20° angle of attack, and 0° roll angle.

Mach Number		4.472	**AoA (deg)**		20.751	**Roll (deg)**		0.0
ID	C_P	UC_P	**ID**	C_P	UC_P	**ID**	C_P	UC_P
0	1.337	0.016						
1	1.340	0.016	28	1.360	0.017	55	1.535	0.018
2	1.379	0.017	29	1.415	0.017	56	1.605	0.018
3	1.394	0.017	30	1.436	0.017	57	1.640	0.018
4	1.395	0.017	31	1.436	0.017	58	1.657	0.018
5	1.407	0.017	32	1.437	0.017	59	1.662	0.018
6	1.413	0.017	33	1.469	0.017	60	1.668	0.018
7	1.500	0.017	34	1.486	0.017	61	1.674	0.018
8	1.538	0.018	35	1.503	0.017	62	1.682	0.018
9	1.550	0.018	36	1.516	0.017	63	1.683	0.018
10	1.550	0.018	37	1.520	0.017	64	1.682	0.018
11	1.541	0.018	38	1.517	0.017	65	1.679	0.018
12	1.527	0.017	39	1.508	0.017	66	1.675	0.018
13	1.502	0.017	40	1.497	0.017	67	1.666	0.018
14	1.475	0.017	41	1.475	0.017	68	1.654	0.018
15	1.435	0.017	42	1.442	0.017	69	1.633	0.018
16	1.365	0.017	43	1.383	0.017	70	1.601	0.018
17	1.206	0.016	44	1.259	0.016	71	1.532	0.018
18	0.858	0.014	45	0.976	0.014	72	1.329	0.016
19	0.433	0.012	46	0.643	0.013	73	1.046	0.015
20	0.191	0.011	47	0.399	0.012	74	0.710	0.013
21	0.050	0.011	48	0.172	0.011	75	0.459	0.012
22	0.002	0.011	49	0.064	0.011	76	0.280	0.012
23	-0.003	0.038	50	0.007	0.038	77	0.114	0.038
24	0.015	0.038	51	0.030	0.038	78	0.025	0.038
25	-0.002	0.038	52	-0.008	0.038	79	-0.005	0.038
26	0.035	0.038	53	-0.007	0.038	80	-0.020	0.038
27	0.033	0.038	54	-0.007	0.038	81	0.021	0.038

Table 72: Pressure coefficient data at a Mach number of 4.5, ∼20° angle of attack, and 180° roll angle.

Mach Number		4.472	**AoA (deg)**		20.750	**Roll (deg)**		180.0
ID	C_P	UC_P	**ID**	C_P	UC_P	**ID**	C_P	UC_P
0	1.331	0.016						
1	1.636	0.018	28	1.365	0.017	55	1.321	0.016
2	1.716	0.019	29	1.422	0.017	56	1.359	0.017
3	1.753	0.019	30	1.442	0.017	57	1.371	0.017
4	1.769	0.019	31	1.438	0.017	58	1.372	0.017
5	1.784	0.019	32	1.438	0.017	59	1.387	0.017
6	1.793	0.019	33	1.471	0.017	60	1.390	0.017
7	1.795	0.019	34	1.488	0.017	61	1.480	0.017
8	1.795	0.019	35	1.505	0.017	62	1.502	0.017
9	1.795	0.019	36	1.517	0.017	63	1.522	0.017
10	1.793	0.019	37	1.523	0.017	64	1.526	0.017
11	1.789	0.019	38	1.518	0.017	65	1.522	0.017
12	1.788	0.019	39	1.508	0.017	66	1.507	0.017
13	1.780	0.019	40	1.496	0.017	67	1.492	0.017
14	1.771	0.019	41	1.475	0.017	68	1.469	0.017
15	1.760	0.019	42	1.442	0.017	69	1.427	0.017
16	1.736	0.019	43	1.383	0.017	70	1.362	0.017
17	1.686	0.018	44	1.256	0.016	71	1.219	0.016
18	1.537	0.018	45	0.967	0.014	72	0.849	0.014
19	1.283	0.016	46	0.635	0.013	73	0.439	0.012
20	0.963	0.014	47	0.391	0.012	74	0.195	0.011
21	0.633	0.013	48	0.170	0.011	75	0.135	0.011
22	0.439	0.012	49	0.061	0.011	76	0.060	0.011
23	0.220	0.038	50			77	0.000	0.038
24	0.010	0.038	51	-0.010	0.038	78	0.018	0.038
25	-0.002	0.038	52	-0.014	0.038	79	-0.007	0.038
26	0.031	0.038	53	-0.007	0.038	80		
27	0.020	0.038	54	-0.009	0.038	81	-0.008	0.038

APPENDIX F

GLENN RESEARCH CENTER 10- X 10-FOOT SUPERSONIC WIND TUNNEL SEMI-RIGID MODEL STATIC AERODYNAMICS RESULTS

F.1 Description

The following presents tabulated values of the data presented in Chapter 3 for testing of the semi-rigid model at the GRC 10- x 10-Foot Supersonic Wind Tunnel. Details of the data reduction and uncertainty analysis are provided in Subsection 3.3.3. The data tables are organized by Mach number, Reynolds number, and type of model (with or without anti-torque panels). Test conditions pertaining to each Mach number are summarized in Table 73. Values of the uncertainty in coefficients C_x, listed as UC_x, are shown at the 95% confidence level for an individual observation.

Table 73: Run averaged test conditions for the GRC 10x10 semi-rigid model tests.

Model without anti-torque panels						
Mach	$Re(10^6)$	P_0**, psf (kPa)**	P_S**, psf (kPa)**	T_0**, R (K)**	T_S**, R (K)**	q_∞**, psf (kPa)**
1.964	1.016	285.30 (13.66)	38.54 (1.85)	540.03 (300.02)	304.80 (169.33)	104.10 (4.98)
2.421	0.544	193.24 (9.25)	12.80 (0.61)	547.96 (304.42)	252.31 (140.17)	52.50 (2.51)
2.441	0.996	351.19 (16.82)	22.52 (1.08)	541.06 (300.59)	246.84 (137.13)	93.96 (4.50)
2.463	1.597	571.88 (27.38)	35.43 (1.70)	542.59 (301.44)	245.10 (136.17)	150.51 (7.21)
2.471	2.106	764.77 (36.62)	46.81 (2.24)	546.23 (303.46)	245.89 (136.61)	200.10 (9.58)

Model with anti-torque panels						
Mach	$Re(10^6)$	P_0**, psf (kPa)**	P_S**, psf (kPa)**	T_0**, R (K)**	T_S**, R (K)**	q_∞**, psf (kPa)**
2.471	2.103	765.41 (36.65)	46.88 (2.24)	547.22 (304.01)	246.38 (136.88)	200.33 (9.59)

Table 74: Static aerodynamic coefficient data for the semi-rigid model without anti-torque panels at a Mach number of 2.0 and a Reynolds number of 1.0 x 10^6.

Mach 1.964			Re 1.016 **x** 10^6			
AoA (deg)	C_A	C_N	C_m	UC_A	UC_N	UC_m
-0.021	1.4305	-0.0125	-0.0009	0.0183	0.0141	0.0040
2.011	1.4336	0.0004	-0.0048	0.0183	0.0141	0.0040
4.002	1.4360	0.0126	-0.0080	0.0183	0.0141	0.0040
6.003	1.4423	0.0254	-0.0109	0.0183	0.0141	0.0040
9.014	1.4402	0.0457	-0.0155	0.0183	0.0141	0.0040
12.023	1.4380	0.0657	-0.0201	0.0183	0.0141	0.0040
15.009	1.4305	0.0874	-0.0247	0.0183	0.0141	0.0040
18.001	1.4147	0.1071	-0.0292	0.0183	0.0141	0.0040
15.007	1.4275	0.0894	-0.0243	0.0183	0.0141	0.0040
12.017	1.4326	0.0688	-0.0194	0.0183	0.0141	0.0040
9.012	1.4412	0.0491	-0.0146	0.0183	0.0141	0.0040
6.001	1.4433	0.0291	-0.0101	0.0183	0.0141	0.0040
3.998	1.4363	0.0159	-0.0070	0.0183	0.0141	0.0040
2.003	1.4307	0.0034	-0.0038	0.0183	0.0141	0.0040
0.012	1.4322	-0.0105	0.0000	0.0183	0.0141	0.0040
-2.015	1.4236	-0.0243	0.0039	0.0183	0.0141	0.0040
-3.998	1.4060	-0.0373	0.0074	0.0183	0.0141	0.0040
-5.009	1.4019	-0.0438	0.0089	0.0183	0.0141	0.0040
-3.990	1.4108	-0.0383	0.0072	0.0183	0.0141	0.0040
-1.996	1.4253	-0.0267	0.0035	0.0183	0.0141	0.0040
0.009	1.4276	-0.0135	-0.0005	0.0183	0.0141	0.0040

Table 75: Static aerodynamic coefficient data for the semi-rigid model without anti-torque panels at a Mach number of 2.4 and a Reynolds number of 0.5 x 10^6.

Mach 2.421			*Re* 0.544 **x** 10^6			
AoA (deg)	C_A	C_N	C_m	UC_A	UC_N	UC_m
-0.014	1.4231	-0.0170	-0.0012	0.0241	0.0271	0.0077
2.006	1.4228	-0.0031	-0.0058	0.0241	0.0271	0.0077
4.022	1.4301	0.0089	-0.0093	0.0241	0.0271	0.0077
6.001	1.4305	0.0206	-0.0125	0.0241	0.0271	0.0077
9.007	1.4340	0.0419	-0.0180	0.0241	0.0271	0.0077
12.010	1.4264	0.0621	-0.0234	0.0241	0.0271	0.0077
15.011	1.4250	0.0827	-0.0289	0.0241	0.0271	0.0077
18.020	1.4212	0.1019	-0.0336	0.0241	0.0271	0.0077
15.018	1.4244	0.0853	-0.0284	0.0241	0.0271	0.0077
11.990	1.4316	0.0660	-0.0227	0.0241	0.0271	0.0077
9.027	1.4280	0.0454	-0.0169	0.0241	0.0271	0.0077
6.010	1.4308	0.0253	-0.0115	0.0241	0.0271	0.0077
4.007	1.4303	0.0129	-0.0083	0.0241	0.0271	0.0077
2.026	1.4257	0.0006	-0.0048	0.0241	0.0271	0.0077
0.005	1.4293	-0.0143	-0.0004	0.0241	0.0271	0.0077
-2.011	1.4403	-0.0298	0.0042	0.0241	0.0271	0.0077
-4.041	1.4246	-0.0431	0.0079	0.0241	0.0271	0.0077
-5.019	1.4237	-0.0486	0.0096	0.0241	0.0271	0.0077
-4.019	1.4289	-0.0439	0.0077	0.0241	0.0271	0.0077
-2.011	1.4169	-0.0322	0.0036	0.0241	0.0271	0.0077
-0.020	1.4266	-0.0185	-0.0010	0.0241	0.0271	0.0077

Table 76: Static aerodynamic coefficient data for the semi-rigid model without anti-torque panels at a Mach number of 2.4 and a Reynolds number of 1.0 x 10^6.

Mach 2.441			*Re* 0.996 **x** 10^6			
AoA (deg)	C_A	C_N	C_m	UC_A	UC_N	UC_m
0.009	1.4298	-0.0037	-0.0049	0.0222	0.0155	0.0044
2.014	1.4324	0.0109	-0.0089	0.0222	0.0155	0.0044
4.004	1.4413	0.0229	-0.0122	0.0222	0.0155	0.0044
6.001	1.4400	0.0347	-0.0149	0.0222	0.0155	0.0044
9.007	1.4382	0.0555	-0.0195	0.0222	0.0155	0.0044
11.988	1.4351	0.0774	-0.0243	0.0222	0.0155	0.0044
15.005	1.4262	0.0987	-0.0289	0.0222	0.0155	0.0044
18.009	1.4267	0.1198	-0.0337	0.0222	0.0155	0.0044
14.991	1.4317	0.1010	-0.0284	0.0222	0.0155	0.0044
11.992	1.4366	0.0801	-0.0231	0.0222	0.0155	0.0044
9.008	1.4379	0.0585	-0.0180	0.0222	0.0155	0.0044
6.012	1.4398	0.0378	-0.0132	0.0222	0.0155	0.0044
3.990	1.4379	0.0252	-0.0103	0.0222	0.0155	0.0044
2.006	1.4350	0.0122	-0.0071	0.0222	0.0155	0.0044
0.016	1.4298	-0.0039	-0.0029	0.0222	0.0155	0.0044
-2.015	1.4314	-0.0203	0.0014	0.0222	0.0155	0.0044
-4.026	1.4400	-0.0350	0.0051	0.0222	0.0155	0.0044
-5.013	1.4385	-0.0410	0.0066	0.0222	0.0155	0.0044
-4.010	1.4326	-0.0360	0.0050	0.0222	0.0155	0.0044
-2.020	1.4333	-0.0234	0.0012	0.0222	0.0155	0.0044
-0.004	1.4325	-0.0084	-0.0031	0.0222	0.0155	0.0044

Table 77: Static aerodynamic coefficient data for the semi-rigid model without anti-torque panels at a Mach number of 2.5 and a Reynolds number of 1.6 x 10^6.

Mach 2.463			*Re* 1.597 **x** 10^6			
AoA (deg)	C_A	C_N	C_m	UC_A	UC_N	UC_m
-0.006	1.4287	-0.0083	-0.0018	0.0216	0.0101	0.0028
2.010	1.4350	0.0073	-0.0058	0.0216	0.0101	0.0028
4.011	1.4408	0.0189	-0.0086	0.0216	0.0101	0.0028
6.014	1.4414	0.0323	-0.0114	0.0216	0.0101	0.0028
9.008	1.4380	0.0537	-0.0159	0.0216	0.0101	0.0028
12.016	1.4360	0.0763	-0.0205	0.0216	0.0101	0.0028
14.998	1.4321	0.0985	-0.0250	0.0216	0.0101	0.0028
18.011	1.4266	0.1205	-0.0294	0.0216	0.0101	0.0028
15.003	1.4304	0.1004	-0.0244	0.0216	0.0101	0.0028
12.016	1.4357	0.0791	-0.0196	0.0216	0.0101	0.0028
9.000	1.4393	0.0572	-0.0147	0.0216	0.0101	0.0028
6.011	1.4410	0.0356	-0.0102	0.0216	0.0101	0.0028
3.993	1.4418	0.0221	-0.0074	0.0216	0.0101	0.0028
2.026	1.4341	0.0097	-0.0045	0.0216	0.0101	0.0028
0.002	1.4266	-0.0070	-0.0005	0.0216	0.0101	0.0028
-1.994	1.4320	-0.0231	0.0034	0.0216	0.0101	0.0028
-3.997	1.4411	-0.0366	0.0066	0.0216	0.0101	0.0028
-4.987	1.4407	-0.0435	0.0079	0.0216	0.0101	0.0028
-4.016	1.4407	-0.0378	0.0064	0.0216	0.0101	0.0028
-2.000	1.4309	-0.0253	0.0030	0.0216	0.0101	0.0028
0.005	1.4274	-0.0101	-0.0009	0.0216	0.0101	0.0028

Table 78: Static aerodynamic coefficient data for the semi-rigid model without anti-torque panels at a Mach number of 2.5 and a Reynolds number of 2.1 x 10^6.

Mach 2.471			*Re* 2.106 **x** 10^6			
AoA (deg)	C_A	C_N	C_m	UC_A	UC_N	UC_m
0.016	1.4271	-0.0091	-0.0006	0.0212	0.0079	0.0022
1.999	1.4378	0.0064	-0.0045	0.0212	0.0079	0.0022
4.030	1.4416	0.0188	-0.0072	0.0212	0.0079	0.0022
6.000	1.4413	0.0326	-0.0100	0.0212	0.0079	0.0022
9.012	1.4385	0.0547	-0.0145	0.0212	0.0079	0.0022
12.003	1.4377	0.0779	-0.0190	0.0212	0.0079	0.0022
15.011	1.4312	0.1004	-0.0235	0.0212	0.0079	0.0022
18.006	1.4309	0.1229	-0.0279	0.0212	0.0079	0.0022
15.013	1.4290	0.1018	-0.0230	0.0212	0.0079	0.0022
12.010	1.4369	0.0801	-0.0183	0.0212	0.0079	0.0022
8.996	1.4394	0.0574	-0.0136	0.0212	0.0079	0.0022
6.005	1.4422	0.0360	-0.0092	0.0212	0.0079	0.0022
3.992	1.4412	0.0218	-0.0064	0.0212	0.0079	0.0022
2.003	1.4357	0.0090	-0.0036	0.0212	0.0079	0.0022
-0.010	1.4277	-0.0077	0.0002	0.0212	0.0079	0.0022
-2.004	1.4314	-0.0236	0.0039	0.0212	0.0079	0.0022
-4.012	1.4403	-0.0381	0.0069	0.0212	0.0079	0.0022
-5.019	1.4427	-0.0449	0.0083	0.0212	0.0079	0.0022
-4.009	1.4409	-0.0388	0.0068	0.0212	0.0079	0.0022
-2.023	1.4303	-0.0257	0.0036	0.0212	0.0079	0.0022
0.025	1.4283	-0.0102	-0.0003	0.0212	0.0079	0.0022

Table 79: Static aerodynamic coefficient data for the semi-rigid model with anti-torque panels at a Mach number of 2.5 and a Reynolds number of 2.1 x 10^6.

Mach 2.471			*Re* 2.103 **x** 10^6			
AoA (deg)	C_A	C_N	C_m	UC_A	UC_N	UC_m
0.011	1.4357	-0.0028	-0.0014	0.0212	0.0079	0.0022
2.010	1.4441	0.0084	-0.0055	0.0212	0.0079	0.0022
4.015	1.4509	0.0178	-0.0083	0.0212	0.0079	0.0022
6.008	1.4495	0.0282	-0.0113	0.0212	0.0079	0.0022
8.998	1.4489	0.0449	-0.0159	0.0212	0.0079	0.0022
12.019	1.4472	0.0625	-0.0208	0.0212	0.0079	0.0022
14.992	1.4400	0.0797	-0.0254	0.0212	0.0079	0.0022
18.013	1.4415	0.0976	-0.0301	0.0212	0.0079	0.0022
15.010	1.4397	0.0822	-0.0248	0.0212	0.0079	0.0022
11.988	1.4451	0.0661	-0.0197	0.0212	0.0079	0.0022
9.016	1.4466	0.0498	-0.0146	0.0212	0.0079	0.0022
6.008	1.4485	0.0336	-0.0097	0.0212	0.0079	0.0022
4.004	1.4488	0.0232	-0.0067	0.0212	0.0079	0.0022
1.999	1.4413	0.0136	-0.0037	0.0212	0.0079	0.0022
0.011	1.4334	0.0015	0.0006	0.0212	0.0079	0.0022
-2.004	1.4388	-0.0099	0.0045	0.0212	0.0079	0.0022
-3.999	1.4458	-0.0204	0.0078	0.0212	0.0079	0.0022
-5.013	1.4481	-0.0259	0.0094	0.0212	0.0079	0.0022
-4.025	1.4462	-0.0215	0.0077	0.0212	0.0079	0.0022
-2.020	1.4375	-0.0122	0.0042	0.0212	0.0079	0.0022
-0.013	1.4328	-0.0020	0.0002	0.0212	0.0079	0.0022

REFERENCES

[1] Alexander, W. C., "Investigation to Determine the Feasibility of Using Inflatable Balloon Type Drag Devices for Recovery Applications in the Transonic, Supersonic, and Hypersonic Flight Regime," ASD-TDR-62-702, Dec 1962.

[2] Anderson, M. S. and Bohon, H. L., "A Structural Merit Function for Aerodynamic Declerators," NASA Technical Note TN D-5535, 1969.

[3] Anderson, M. S., Robinson, J. C., Bush, H. G., and Fralich, R. W., "A Tension Shell Structure for Application to Entry Vehicles," NASA Technical Note TN D-2675, Mar 1965.

[4] Anonymous, "PEPP Ballute Design and Development," NASA Contractor Report CR-66585, 1967.

[5] Arrington, E. A., Spera, D. A., Blumenthal, P., and Thompson, J., "Calibration of the NASA Glenn Research Center 10- by 10-ft Supersonic Wind Tunnel (1993 and 1995 Tests)," NASA Technical Memorandum TM-2000-209799, 2000.

[6] Barton, R. R., "Development of Attached Inflatable Decelerators for Supersonic Application," NASA Contractor Report CR-66613, May 1968.

[7] Beegle, L. W., Wilson, M. G., Abillerira, F., Jordan, J. F., and Wilson, G. R., "A Concept for NASA's Mars 2016 Astrobiology Field Laboratory," *Astrobiology*, vol. 7, no. 4, pp. 545–577, 2007.

[8] Belotserkovskii, O. M., "Flow With a Detached Shock Wave About a Symmetrical Profile," *Journal of Applied Mathematics and Mechanics*, vol. 22, pp. 279–296, July 1958.

[9] Bippes, H., "Experimental Study of the Laminar-Turbulent Transition of a Concave Wall in a Parallel Flow," NASA Technical Memorandum TM-75243, 1978.

[10] Bixby, H. W., Ewing, E. G., and Knacke, T. W., "Recovery Systems Design Guide," Air Force Flight Dynamics Laboratory Technical Report AFFDL-TR-78-151, 1978.

[11] Bloetscher, F., "Aerodynamic Deployable Decelerator Performance Evaluation Program, Phase II," Air Force Flight Dynamics Laboratory Technical Report AFFDL-TR-67-25, Apr 1967.

[12] Bohon, H. L. and Miserentino, R., "Deployment and Performance Characteristics of 5-Foot Diameter (1.5 m) Attached Inflatable Decelerators From Mach Number 2.2 to 4.4," NASA Technical Note TN D-5840, Aug 1970.

[13] Bohon, H. L. and Miserentino, R., "Attached Inflatable Decelerator (AID) Performance Evaluation and Mission-Application Study," *Journal of Spacecraft and Rockets*, vol. 8, pp. 952–957, Sep 1971.

[14] Braun, R. D. and Manning, R. M., "Mars Exploration Entry, Descent, and Landing Challenges," *Journal of Spacecraft and Rockets*, vol. 44, pp. 310–323, Mar 2007.

[15] Brown, G., Epp, C., Graves, C., Lingard, J., and Darly, M., "Hypercone Inflatable Supersonic Decelerator," AIAA Paper 2003-2167, 2003.

[16] Brown, G., Lingard, J., Darley, M., and Underwood, J., "Inflatable Aerocapture Decelerators for Mars Orbiters," AIAA Paper 2007-2543, 2007.

[17] Buning, P. G., Jespersen, D. C., Pulliam, T. H., Klopfer, G. H., Chan, W. M., Slotnick, J. P., Krist, S. E., and Renze, K. J., *Overflow User's Manual*, Apr 2008.

[18] Chaderjian, N. M. and Olsen, M. E., "Grid Resolution and Turbulence Model Effects on Space Capsule Navier-Stokes Simulations," AIAA Paper 2007-4562, 2007.

[19] Charczenko, N. and McShera, J. T., "Aerodynamic Characteristics of Towed Cones Used as Decelerators at Mach Numbers From 1.57 to 4.65," NASA Technical Note TN D-994, 1961.

[20] Cohen, G. A., Foster, R. M., and Dowty, J. R., "Synthesis of Optimum Structural Designs for Conical and Tension Shell Mars Entry Capsules," NASA Contractor Report CR-1365, 1969.

[21] Creel Jr., T. R., "Longitudinal Aerodynamic Characteristics of a Tension Shell Entry Configuration at Mach 20," NASA Technical Note TN D-3541, 1966.

[22] Cruz, J. R. and Lingard, J. S., "Aerodynamic Decelerators for Planetary Exploration: Past, Present, and Future," AIAA Paper 2006-6792, 2006.

[23] Deveikis, W. D. and Sawyer, J. W., "Aerodynamic Characteristics of Tension Shell Shapes at Mach 3.0," NASA Technical Note TN D-3633, Oct 1966.

[24] Deveikis, W. D. and Sawyer, J. W., "Static Aerodynamic Characteristics, Pressure Distributions, and Ram-Air Inflation of Attached Inflatable Decelerator Models at Mach 3.0," NASA Technical Note TN D-5816, May 1970.

[25] Edquist, K. T., Desai, P. N., and Schoenenberger, M., "Aerodynamics for the Mars Phoenix Entry Capsule," AIAA Paper 2008-7219, Aug 2008.

[26] Ewing, E. G., "Ringsail Parachute Design," Air Force Flight Dynamis Laboratory Technical Report AFFDL-TR-72-3, 1972.

[27] Ewing, E. G., Bixby, H. W., and Knacke, T. W., "Recovery System Design Guide," Air Force Flight Dynamis Laboratory Technical Report AFFDL-TR-78-151, 1978.

[28] Faurote, G. L. and Burgess, J. L., "Thermal and Stress Analysis of an Attached Inflatable Decelerator (AID) Deployed in the Mars and Earth Atmospheres," NASA Contractor Report CR-111920, 1971.

[29] Fette, R. B. and Sovinski, M. F., "Vectran Fiber Time-Dependent Behavior and Additional Static Loading Properties," NASA Technical Memorandum TM-2004-212773, Dec 2004.

[30] Flatau, A., Olson, D. N., and Miller, M. C., "The Use of an Attached Inflatable Decelerator for Store Delivery from High Speed Aircraft from Low Altitude," AIAA Paper 1970-1199, 1970.

[31] George E Weeks, "Buckling of a Pressurized Toroidal Ring Under Uniform External Loading," NASA Technical Note TN D-4124, Aug 1967.

[32] Gnoffo, P. A., Weilmuenster, K. J., Braun, R. D., and Cruz, C. I., "Influence of Sonic-Line Location on Mars Pathfinder Probe Aerothermodynamics," *Journal of Spacecraft and Rockets*, vol. 33, pp. 169–177, March 1996.

[33] Harris, C. D., "Transonic Aerodynamic Investigation of Tension Shell and Blunted 100° Conical Shapes for Unmanned Entry Vehicles," NASA Technical Note TN D-3700, 1966.

[34] Houtz, N. E., "Optimization of Inflatable Drag Devices by Isotensoid Design," AIAA Paper 64-437, Jul 1964.

[35] Hughes, S. J., Dillman, R. A., Starr, B. R., Stephan, R. A., Lindell, M. C., Player, C. J., and Cheatwood, F. M., "Inflatable Re-entry Vehicle Experiment (IRVE) Design Overview," AIAA Paper 2005-1636, Jul 2005.

[36] Humble, R. W., Lewis, D., Bissel, W., and Sackheim, R., *Liquid Rocket Propulsion Systems*, ch. 5, pp. 272–279. 1995.

[37] Jackson, C. M., Corlett, W. A., and Monta, W. J., "Description and Calibration of the Langley Unitary Plan Wind Tunnel," NASA Technical Paper 1905, 1981.

[38] Jones, R. A., Bushnell, D. M., and Hunt, J. L., "Experimental Flow Field and Heat-Transfer Investigation of Several Tension Shell Configurations at a Mach Number of 8," NASA Technical Note TN D-3800, 1967.

[39] Kayser, L. D., "Pressure Distributions, Heat Transfer, and Drag Tests on the Goodyear Ballute at Mach 10," AEDC Technical Report AEDC-TDR-62-39, Mar 1962.

[40] Kim, K. H., C, K., and Rho, O. H., "Accurate Computations of Hypersonic Flows Using AUSMPW+ Scheme and Shock-Aligned Grid Technique," AIAA Paper 1998-2442, 1998.

[41] Kirk, D., Intrieri, P., and Seiff, A., "Aerodynamic Behavior of the Viking Entry Vehicle: Ground Test and Flight Results," *Journal of Spacecraft and Rockets*, vol. 15, pp. 208–212, Feb 1978.

[42] Kyser, A. C., "Deployment Mechanics For An Inflatable Tension-Cone Decelerator," NASA Contractor Report CR-929, Nov 1967.

[43] Lee, J. D., Orsini, A., and Ruffin, S. M., "Unstructured Cartesian-Grid Methodology for Non-Equilibrium Hypersonic Flows," AIAA Paper 2007-0548, 2007.

[44] Lee, J. D. and Ruffin, S. M., "Development of a Turbulent Wall-Function Based Viscous Cartesian-Grid Methodology," AIAA Paper 2007-1326, 2007.

[45] Liepmann, H. W., "Investigations of Boundary Layer Transition on Concave Walls," NACA Report NACA-WR-W-87, 1945.

[46] Marko, W. J., "Static Aerodynamic Characteristics of Three Blunted Sixty-Degree Half-Angle Cones at Mach Numbers From 0.60 to 1.30," JPL Technical Report 32-1298, 1968.

[47] Marshall, D. and Ruffin, S. M., "A New Inviscid Wall Boundary Condition Treatment for Embedded Boundary Cartesian Grid Schemes," AIAA Paper 2004-0583, 2004.

[48] Marshall, D. and Ruffin, S. M., "An Embedded Boundary Cartesian Grid Scheme for Viscous Flows Using a New Viscous Wall Boundary Condition Treatment," AIAA Paper 2004-0581, 2004.

[49] Mayhue, R. J. and Eckstrom, C. V., "Flight-Test Results From Supersonic Deployment of an 18-Foot-Diameter (5.49-Meter) Towed Ballute Decelerator," NASA Technical Memorandum TM X-1773, May 1969.

[50] McShera, J. and Keyes, J., "Wind-Tunnel Investigation of a Balloon as a Towed Decelerator at Mach Numbers from 1.47 to 2.50," NASA Technical Note TN D-919, Aug 1961.

[51] McShera, J. T. and Bohon, H. L., "A Summary of Supersonic Decelerators with Emphasis on Problem Areas in Aerodynamics and Structures," AIAA Paper 67-201, Mar 1967.

[52] McShera Jr., J. T., "Aerodynamic Drag and Stability Characteristics of Towed Inflatable Declerators at Supersonic Speeds," NASA Technical Note TN D-1601, Mar 1963.

[53] Menter, F. R. and Rumsey, C. L., "Assessment of Two-Equation Turbulence Models for Transonic Flows," AIAA Paper 1994-2343, 1994.

[54] Mikulas Jr., M. M. and Bohon, H. L., "Development Status of Attached Inflatable Decelerators," *Journal of Spacecraft and Rockets*, vol. 6, pp. 654–660, Jun 1969.

[55] Mitcheltree, R. A., Moss, J. N., Cheatwood, F. M., Greene, F. A., and Braun, R. D., "Aerodynamics of the Mars Microprobe Entry Vehicles," *Journal of Spacecraft and Rockets*, vol. 36, pp. 392–398, May 1999.

[56] Morrisey, D. C., "Historical Perspective: Viking Mars Lander Propulsion," AIAA Paper 1989-2391, Jul 1989.

[57] Murman, S. M., "Dynamic Viscous Simulations of Atmospheric-Entry Capsules," AIAA Paper 2008-6911, Sep 2008.

[58] Murrow, H. N. and Jr., J. C. M., "Summary of Experimental Results Obtained from the NASA Planetary Entry Parachute Program," AIAA Paper 1968-934, 1968.

[59] Nichols, R. H., W, T. R., and Buning, P. G., "Solver and Turbulence Model Upgrades to OVERFLOW 2 for Unsteady and High-Speed Applications," AIAA Paper 2006-2824, 2006.

[60] Olsen, M. E. and Coakley, T. J., "The Lag Model, a Turbulence Model for Non Equilibrium Flows," AIAA Paper 2001-2564, Jul 2001.

[61] Olsen, M. E., Lillard, R. P., and Coakley, T. J., "The Lag Model Applied to High Speed Flows," AIAA Paper 2005-101, Feb 2005.

[62] Powell, R. W., Striepe, S. A., Desai, P. N., Braun, R. D., Brauer, G. L., Cornick, D. E., W, O. D., Petersen, D. M., and Stevenson, R., *Program to Optimize Simulated Trajectories (POST) Utilization Manual, Volume II, Version 5.2*, 1997.

[63] Reynier, P. and Evans, D., "Post-flight Analysis of IRDT Blackout during Earth Re-entry," AIAA Paper 2008-3894, Jul 2008.

[64] Robinson, J. C. and Jordan, A. W., "Exploratory Experimental Aerodynamic Investigation of Tension Shell Shapes at Mach 7," NASA Technical Note TN D-2994, 1965.

[65] Saric, W. S., "Görtler Vortices," *Annual Review of Fluid Mechanics*, vol. 26, pp. 379–409, Jan 1994.

[66] Sawyer, J. W., "Effects of Pressure Distributions on Bluff Tension-Shell Shapes," NASA Technical Note TN D-5636, Feb 1970.

[67] Sawyer, J. W. and Deveikis, W. D., "Effects of Configuration Modifications on Aerodynamic Characteristics of Tension Shell Shapes at Mach 3.0," NASA Technical Note TN D-4080, Aug 1967.

[68] Sawyer, J. W. and Whitcomb, C. F., "Subsonic and Transonic Pressure Distributions Around a Bluff Afterbody in the Wake of a 120° Cone for Various Separation Distances," NASA Technical Note TN D-6569, 1971.

[69] Schneider, S. P., "Erratum on Laminar-Turbulent Transition on Reentry Capsules and Planetary Probes," *Journal of Spacecraft and Rockets*, vol. 44, pp. 464–484, Mar 2007.

[70] South Jr., J. C., "Calculation of Axisymmetric Supersonic Flow Past Blunt Bodies with Sonic Corners, Including a Program Description and Listing," NASA Technical Note TN D-4563, May 1968.

[71] Stein, J. and Sandy, C., "Recent Developments in Inflatable Airbag Impact Attenuation Systems for Mars Exploration," AIAA Paper 2003-1900, May 2003.

[72] Usry, J., "Performance of a Towed 48-Inch-Diameter (121.92-cm) Ballute Decelerator Tested in Free Flight at Mach Numbers From 4.2 to 0.4," NASA Technical Note TN D-4943, Feb 1969.

[73] Walker, B. and Weaver, R. W., "Static Aerodynamic Characteristics of Blunted Cones in the Mach-Number Range from 2.2 to 9.5," JPL Technical Report 32-1213, 1967.

[74] Way, D. W., Powell, R. W., Chen, A., Steltzner, A. D., Martin, A. M. S., Burkhart, P. D., and Mendeck, G. F., "Mars Science Laboratory: Entry, Descent, and Landing System Performance," IEEEAC Paper 2007-1467, 2007.

[75] Yates, L. A. and Chapman, G. T., "Analysis of Data from Ballistic Range Tests of PAI-DAE Vehicles," Final Report Prime Contract GS00T99ALD0209, Dec 2007.

[76] Young, W. C. and Budynas, R. G., *Roark's Formulas for Stress and Strain*, vol. 7th Edition. 2001.